A study of fission in ^{238}U induced by monoenergetic neutrons and heavy ions and of light particle emission in ^{252}Cf spontaneous fission

by

Hossein Afarideh

A thesis submitted to the Faculty of Science

of the

University of Birmingham

for the degree of

Doctor of Philosophy

Department of Physics
University of Birmingham
Edgbaston
Birmingham B15 2TT
England

Synopsis

Fission yield measurements are important for many aspects of applied and basic nuclear physics.
The First chapter gives a brief introduction to the fission yield data and their importance to reactor technology. This chapter also explains the aims of the research project.

In the Second chapter the basic concepts of fission, properties of fission process and finally ternary fission are discussed in detail.

Chapter Three deals with the explanation of different fission yields and describes techniques available for the determination of binary fission yield as well as existing methods for the measurement or calculation of total fission products.
Chapter Four relates to the calibration of detectors used during the course of this project. The measurements of absolute and intrinsic efficiency of the two HP-Ge detectors are described in this chapter. Also, the comparative calibration of a Parallel Plate Fission Chamber (PPC) relative to an absolutely calibrated Harwell Fission Chamber is discussed here.

Chapter Five describes the measurements of cumulative fission yields of about 32 fission products for 5 different neutron energy ranges in ^{238}U, using direct gamma-ray techniques. These yields were measured by the absolute method. From the measured fission yield data for different monoenergetic neutrons, predictions were made for the yield of fission products from reactor neutrons having a Watt spectrum.

Chapter Six is related to the measurements of alpha and triton yields in the ternary fission of monoenergetic-neutron-induced fission in ^{238}U at

two different neutron energies, using a $\Delta E-E$ telescope technique. In addition, we describe the energy spectrum and emission probability of tritons and alpha particles in Cf-252 which were determined by the telescope technique as well as using Solid State Nuclear Track Detectors (SSNTDs).

Chapter Seven deals with the angular distribution of fission fragments, in the neutron induced fission of ^{238}U, with 1-19 MeV neutrons, as registered in Lexan and Mica detectors. This energy range covers first-, second- and third chance fission. The variation between theoretical predictions and experimentally measured values for angular distribution are also discussed here.

In Chapter Eight, interactions of some heavy projectiles, including 14 MeV/amu beams of ^{238}U, with gold targets are studied, using Mica and CR-39 detectors. The measured cross sections for binary, ternary and quaternary fission are also reported. In addition, the quarter point angle for the interaction of several heavy ions with gold target were determined and used in calculations of elastic scattering cross-sections.

Finally chapter Nine discusses the conclusions and suggestions for further work.

(In the name of God, the Beneficent, the Merciful)

To my father, and my son Mohammed

ACKNOWLEDGEMENTS

It is a pleasure for me to express my thanks to my supervisors Dr. S.A. Durrani and Dr. K. Randle for their advice, supervision and guidance in the completion of this work. I am specially indebted to Dr. K. Randle for his continued interst and encouragement and for many useful discussions we had during the whole course of this work and the pains he has taken to go through and correct this manuscript.

I wish to acknowledge the encouragement and interest shown by Professor J. Walker, Head of Applied Nuclear Science, ANS, during the execution of the this work .

I should like to thank Dr. L. G. Earwaker, Manager Radiation Centre, for providing me irradiation facilities on the Dynamitron .

I also take this opportunity to express my deep hearted thanks to all the Radiation Centre staff in general and Messrs. A. Blackband, N. Franklin, J. Lowe and G. Wood, in particular, for providing me warm hospitality in the radiation centre .

I am grateful to Dr. D. R. Weaver and Mrs. J. Blackband for their invaluable assistance and guidance in connection with computer related problems .

The useful discussions with Dr. R. Sokhi, Dr. J. Turnbull on various occasions, during my stay in the radiation centre are also greatly acknowledged.

I am thankful to all my research colleagues in the Radiation Centre and the Applied Radiation Physics group for providing me with their help and cooperation when and where I needed it. Useful discussions on many different occasions with all of them are greatly acknowledged .

I also express my gratitude to Dr. J. B. England for providing me with the special equipment needed during my ternary fission work .

I greatly acknowledge the financial support extended by Atomic Energy Organization of Iran to carry out this work .

My thanks are also to Mrs. E . Gaize for correcting this manuscript .

Last but not least I would like to thank my wife and my parents for their blessings and well wishes. Without these I could have never been able to complete this task .

CONTENTS

CHAPTER 1

INTRODUCTION

The products formed from a fissioning nucleus provide valuable insights into the mechanism of fission and can provide data with which to test proposed models of the fission process.

Most of the work disscussed here concerns various aspects of the fission of ^{238}U. To this end we have studied fast neutron induced fission product yields and ternary fission as well as heavy ion reactions in ^{238}U. In addition we have also studied some aspects of the spontaneous ternary fission in ^{252}Cf, mainly with the aim of clarifying some aspects of the energy distribution of light charged particles. Finally, the work with heavy ions was extended to the nuclei of atoms other than uranium.

Fission product yield data are one of the most important sets of basic information in the nuclear industry. They are important in several crucial areas concerned with both the operation of nuclear reactors and the subsequent processing of the spent fuel.

The needs and requirement for accurate fission yield data have been the subject of several international meetings[1-3]. Fission yield data measurements began almost immediately after the discovery of the fission process. Hahn and Strassman[4] performed the first yield measurements and by the early 1940's fission yield studies had established the asymetric mode of thermal fission. The shape of the mass yield curve, however, was not well defined because of the rather large uncertainties associated with these data.

In the 1960's radiochemical measurements provided more accurate data on the shape of the mass yield curves for thermal fission of ^{233}U, ^{235}U, ^{239}PU and the existence of "fine structure" was established. By the early 1970's, isotope dilution mass spectrometry was widely

used as the most accurate technique for the measurement of stable fission products.

The requirement for accurate "fast" fission yields became increasingly important at this time. The "fast" yield data then currently available covered only a few, selected radioactive fission products measured by radiochemical techniques. With the development of the fast breeder programme, the user requirement for fast yield data became more important and in some cases a value of +1% as an uncertainty for a fast reactor fission yield was considered necessary[2,3]. Thus, it was not only necessary to produce more accurate fast yield data but also to provide a measure of the change in fast yield data as a function of neutron energy.

In spite of the fact that more than 20000 fission-product-yield values have been determined there are still significant gaps in fission yield measurements. This is especially true for fission of ^{238}U induced by reactor or monoenergetic neutrons. It has been known for many years that fission yields change with the incident energy of the fissioning neutron. The general pattern of these changes with increasing neutron energy, is that:

a) the yields of the valley nuclides increase,

b) the yields of those nuclides on the extreme wings of the mass yield curve increase.

In early studies of this phenomenon, neutrons of several MeV were used and, by radiochemical techniques, the yields of a limited number of selected fission products representing the valley, peak and wing regions of the mass yield curve were measured. The variation in the mass yield curve for monoenergetic-neutron-induced fission has been studied in detail for ^{232}Th, ^{235}U, ^{239}PU and ^{238}U.

These experiments have provided important information to facilitate better understanding of the fission process. In addition, yield data

provide fundamental input for the the safe operation of many areas of the nuclear power industry. A number of the more important applications are briefly outlined below.

i) nuclear fuel burn-up- affect of fission product poisons on fuel lifetime

ii) safeguards- the importance and the accuracy requirements of fission product nuclear data for nuclear material safeguards have been reviewed by Weitkamp[1] and Maeck[2].

iii) reactor neutron dosimetry and flux measurements- dependent on accurate knowledge of fission product yields amongst other factors.

iv) reactor design and operation- fission product distributions and their neutron capture cross-sections have consequences for the reactivity of a reactor and for the size of the emergency cooling system required.

v) decay heat studies- this important effect refers to heat generated by gamma radiation following reactor shut-down. It requires detailed knowledge of fission-product gamma-ray spectra.

vi) fuel handling and reprocessing- the details of the reprocessing procedure are very dependent on the concentration and composition of the fission products.

vii) nuclear waste management- The long-term storage and management of reactor waste is critically dependent on its final composition of long-lived isotopes. Many fission products contribute to this problem and consequently their concentration and composition is very important.

The importance of the energy dependence of the absolute mass yield in binary fission of ^{238}U was also studied and is discussed in the following chapters in regard to obtaining fast fission yield data with reasonably high accuracy. An additional requirement for such data arises from the fact that the fission products are used as burn-up

monitors. At the present time ^{148}Nd is used for this purpose. This is measured mass spectrometrically, together with other Nd isotopes. The variation of Nd yield with neutron energy has to be accurately known for ^{238}U in order to enable the selection of the most suitable burn-up monitor nuclides. Such measurements should also include other nuclides in the mass range 140-160 amu to aid in establishing the systematics of the energy dependence of the mass yield.

Ternary fission is here defined as the mode of fission which results in the emission of two, roughly equal mass fragments together with a third, very low mass fragment such as a triton or an alpha particle. There exists no comprehensive theory with which to compare the various observations in ternary fission. There is, however, a framework from which one can examine these observations for their consistency and for their implications about the nature of the scission process. Most of the available experimental data refer to ^{252}Cf or thermal neutron induced fission of fissile material. Although the study of spontaneous ternary fission in ^{252}Cf commenced soon after it became widely available and a significant body of data has been accumulated, there are still discrepancies in the observed energy spectrum of long range alpha particles. There has been some debate about the energy spectrum of alpha particles, as to whether it is really Gaussian shaped and in the following chapters some further work on this subject is presented. In the case of fertile material, especially ^{238}U, there are very limited experimental data available and some of these are inconsistent with each other. In order to examine the existent framework for fission and consequently to produce a comprehensive theory, it is necessary to extend observations to ternary fission of ^{238}U induced by fast, monoenergetic neutrons. Of particular practical importance are tritium production rates to the development of fast reactors because tritium may be produced at a greater rate in fast reactors than in

thermal reactors. This potential increase in tritium from fast reactors is due to:

1) the possibly higher yields of tritium from fast fission than from thermal fission,

2) the possibly higher yields of tritium from fissions in ^{238}U than from ^{235}U fission.

It is estimated that the production of tritium by ternary fission in fast reactors contributes 25% to 50% of the total tritium production.

An order of magnitude increase in the fast, ternary fission yield of tritium compared to that thermal reactors has been reported[5,6]. If it is confirmed, fission will become the dominant source of tritium in fast reactor systems. Taking advantage of the high neutron flux produced by the Dynamitron accelerator in the Department of Physics, it was possible to measure experimentally, for the first time the probability of emission of tritons and alpha particles in the monoenergetic neutron-induced ternary fission of ^{238}U. From the results of these experiments a more detailed evaluation of tritium production from all sources may become possible. This could then lead to an evaluation of the requirement for additional environment control measures in the operation of fast reactors.

The third phase of this work concerns a study of heavy ion-induced reactions. From these it was hoped to gain further insights into the theory of fission. New, but as yet incomplete, theoretical models have been put forward to explain the kinds of fission which result from such interactions. In several of these approaches, however, the validity of some of the assumption used is not certain, nor are the values of some of the parameters accurately known. More experimental results are, therefore, required if a comprehensive theory is to be developed.

The reaction pattern of multibody processes is extremely complex and

a knowledge of the kinematical correlations between the reaction products is therefore very important. In order to understand the reaction mechanisms involved it is essential to determine the correlations between all the parameters involved. All the reaction products need to be registered on a detector, so that the various kinematical variables may be determined from the analysis.

The experimental total reaction cross sections were determined in the reaction of a 14 MeV/amu beam of ^{238}U with a gold target using two independent methods. The results of cross section measurements by these two methods were found to be in good agreement with theoretical predictions. Furthermore, from measurements on elastically scattered events using the interaction of ^{139}La and ^{208}Pb on gold targets, the total reaction cross sections were determined.

The detailed approach to the problems outlined above was:

1) to study the feasibility of using monoenergetic neutron-induced ternary fission of ^{238}U to determine the yields of tritium and alpha particles,

2) to investigate the dependence of the absolute mass yield following binary fission of ^{238}U as a function of incident neutron energy in the range 1.5-6 MeV,

3) to determine the energy distribution of alpha particles and tritons emitted in the spontaneous fission of ^{252}Cf,

4) study and measurements of heavy-ion-induced fission.

References:

1) Weitkamp C., IAEA Panel on Fission Product Nuclear Data, RP-6 Bologna, Italy (1973)

2) Maeck W.J., IAEA Panel on Fission Product Nuclear Data,RP-6 (1977). Published as IAEA-213 (1978)

3) Maeck W.J., IAEA Panel on Fission Product Nuclear Data (1983)

4) Hahn O., F. Strassman, Naturwiss, 27, 89 (1939)

5) Buzzelli G. Trans. American Nuclear Society, 24, 458 (1976)

6) Buzzelli G. and S.Langer. Trans. American Nuclear Society, 27, 283 (1977)

Chapter 2

An overview of the Fission Process

2. Introduction

Nuclear fission is a very complex phenomenon which, although discovered as early as 1938[1], is far from being completely understood yet. A-detailed presentation of the fission properties will not be discussed in this chapter, but is explained in detail else where[2,3]. Nuclear fission is a violent collective phenomenon in which a nucleus undergoes a series of large vibrations until it becomes so strongly deformed that it breaks into two primary fragments of comparable mass and very infrequently, into more than two fragments. This break in the fissioning nucleus is called scission. After scission the fragments repel each other as a result of the long-range, Coulomb, repulsive force. During their mutual repulsion, these fragments de-excite rapidly "in flight" by prompt-neutron and prompt-γ-ray emissions until the residual fragments are left in long-lived states, either isomeric or more frequently the ground states. The residual fragments, usually called the fission products, are generally far from the line of β-stability, even if they are formed in their ground state. Therefore they decay to stable nuclei by emitting β-radioactivity followed by possible γ-ray or even neutron emission; these are called delayed processes.

The total energy released in fission is very large, about 206.24 MeV for fission of ^{238}U induced by 3.1 MeV fast neutrons. The time scale of the various phases is given approximately in Fig. 2.1.

Fission can occur in various manners, from spontaneous fission of an actinide nuclues in its ground state to fission occurring in the interaction of neutrons with complex nuclei. The process can be described as the succession of four distinct phases.

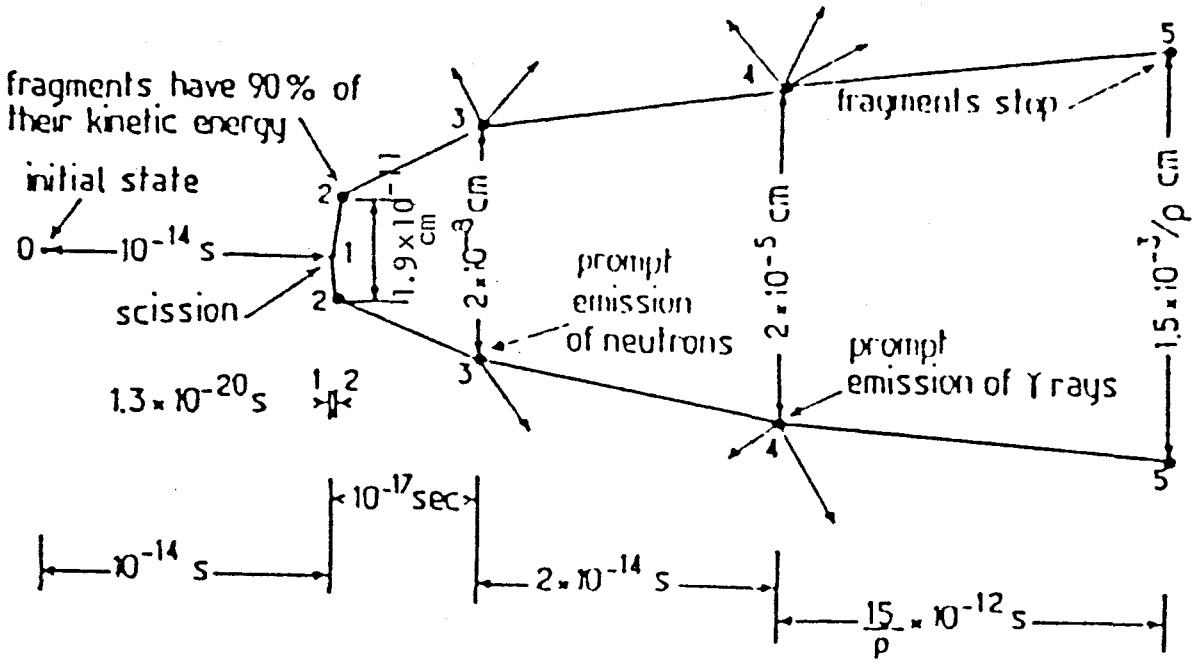

Fig. 2.1 Illustration of fission process in two scales. The horizontal scale indicates the durations of the various phases of the fission process whereas the vertical scale indicates the distance between the fission fragments.

0 - formation of initial state

1 - scission

2 - fragments having 90% of their total kinetic energy

3 - prompt neutron emission

4 - prompt γ-ray emission

5 - fragments stop and decay by delay processes.

1. formation of initial state

2. transition from initial state to scission

3. transition from scission to the formation of fission products by prompt processes

4. De-excitation of the fission products by decay processes.

2.1 Formation of Initial State

In the case of fission induced by neutrons in a target nucleus, (A,Z), in its ground state, the nature of the compound nucleus depends on the energy of incident neutron. At low energies it gives rise to the formation of a compound nucleus, A^*, where

$$A^* = A+1$$

This process is called first chance fission. At higher neutron energies there is the possibility of emission of neutrons prior to fission, so that the fissioning nuclei are either (A,Z) or (A-1,Z). Where (A,Z) is the fissioning species the process is called second chance fission and where it is (A-1,Z) it is called third chance fission. The excitation energy, E^*, of an initial state is determined by

$$E^* = S_n(A^*, Z) + E_n\left(\frac{A}{A+1}\right)$$

$S_n(A^*,Z)$ is the neutron separation energy in the nucleus (A^*,Z), with a value of about 4.8 MeV for ^{239}U (^{238}U+n).

The spin, J, of a compound nucleus is given by

$$J=I+l+s$$

where:

I= spin of target nucleus,

l= angular momentum,

s= spin of incoming neutron and is equal to $\frac{1}{2}$.

2.2 Transition from Initial State to Scission

This phase is very important in the determination of fission

properties, especially the fission probability. The statics of the process are determined from a knowledge of the total energy of the system, usually called potential energy, as a function of deformation. The potential energy at deformation, s, is called V(s). The potential energy surface is the plot of V(s) as function of the n deformation coordinates in a (n+1) dimensional space. The plot is illustrated for two and one deformation coordinates in Figures 2.2(a) and 2.2(b), respectively. The calculation of V(s) is classified as follows:

1. macroscopic,
2. microscopic,
3. hybrid.

2.2.1 Macroscopic Models

In these models the nucleus is assumed as bulk nuclear matter in which a few macroscopic variables such as the shape and the nuclear density can define the nucleus properties. The liquid drop model is the most important model in this category.

2.2.1.1 Liquid Drop Model

In this model, the compound nucleus becomes uniformly excited in a manner somewhat analogous to the warming of a small glass of water upon addition of a spoonful of boiling water. As the nucleii move about and collide with other nucleii, their individual kinetic energies vary with each collision just as those of molecules in a liquid change in molecular collisions. As this process continues, there is an increase in the probability that at least one nucleon will gain kinetic energy in excess of its binding energy. That nucleon is then evaporated (i.e. leaves the nucleus) analogously to the evaporation of molecules from a liquid surfaces. The evaporation of the nucleon decreases the excitation energy of the residual nucleus by

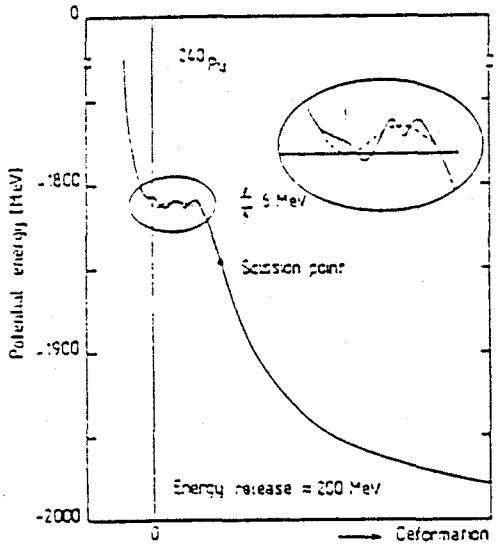

Fig. 2.2(a) Variation of the potential energy of ^{240}Pu as a function of deformation along the fission path. The energy is expressed in MeV with the origin corresponding to the sum of the individual mass energies of the nucleons in ^{240}Pu. The solid line shows the energy variations, including the effect of shells. Fission barrier is very small about 6 MeV compared to the overall range of energy variations during the fission process. The dashed line illustrates the smooth energy variation obtained from LDM calculation (ref. 45).

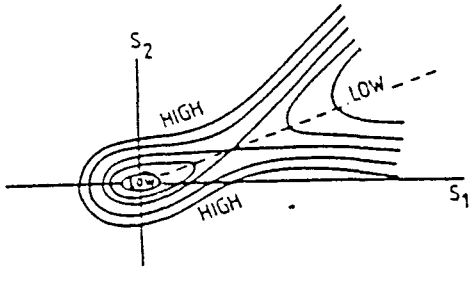

Fig. 2.2(b) Shows the contour lines of V(S) and the fission path for the case of two deformation coordinates S_1 and S_2. Two regions of low potential energy are connected by a saddle and the path to fission is indicated by a dashed line.

an amount corresponding to the binding energy plus the kinetic energy of the released nucleon. The evaporation process continues until the residual excitation energy is less than the binding energy of a nucleon. The excitation energy remaining at this point is removed from the nucleus by emission of γ-rays. This model describes the potential energy variation with shape distortions in terms of the interplay between surface and Coulomb effects. It is assumed that the change in Coulomb and surface energy with distortion are of comparable magnitude but of opposite sign. In order for the charged, liquid drop to be stable against small distortions, the decrease in Coulomb energy, ΔE_C, must be smaller than the increase in surface energy ΔE_S. The drop will become unstable when $|\Delta E_C| / \Delta E_S = 1$.

The surface tension of a liquid causes a droplet to assume a spherical shape, but if energy is supplied in some way, this shape is distorted. If the attractive surface tension force is greater than the distorting force, the drop oscillates between spherical and elongated shapes. If, however, the distorting force becomes larger than the attractive force, the drop elongates past a threshold point and splits (fission). Following Bohr and Wheeler[4], the ratio between the two opposing energies should measure the instability to fissioning of the nucleus.

$$\text{Instability} = \frac{\text{energy of repulsion}}{\text{energy of attraction}} = \frac{(Z^2/A^{1/3})}{A^{2/3}} = \frac{Z^2}{A}$$

The parameter, Z^2/A, is known as the fissionability parameter. Fig 2.3 represents the variation of potential energy as a function of deformation from spherical to prolate shape, by keeping N and Z constant.

The nucleus exists normally in the ground state level of the potential well. In order to undergo fission it must be excited above the fission barrier, which is about 5-6 MeV. As shown in Fig. 2.4, the excitation of the nucleus into the continiuum level region leads to

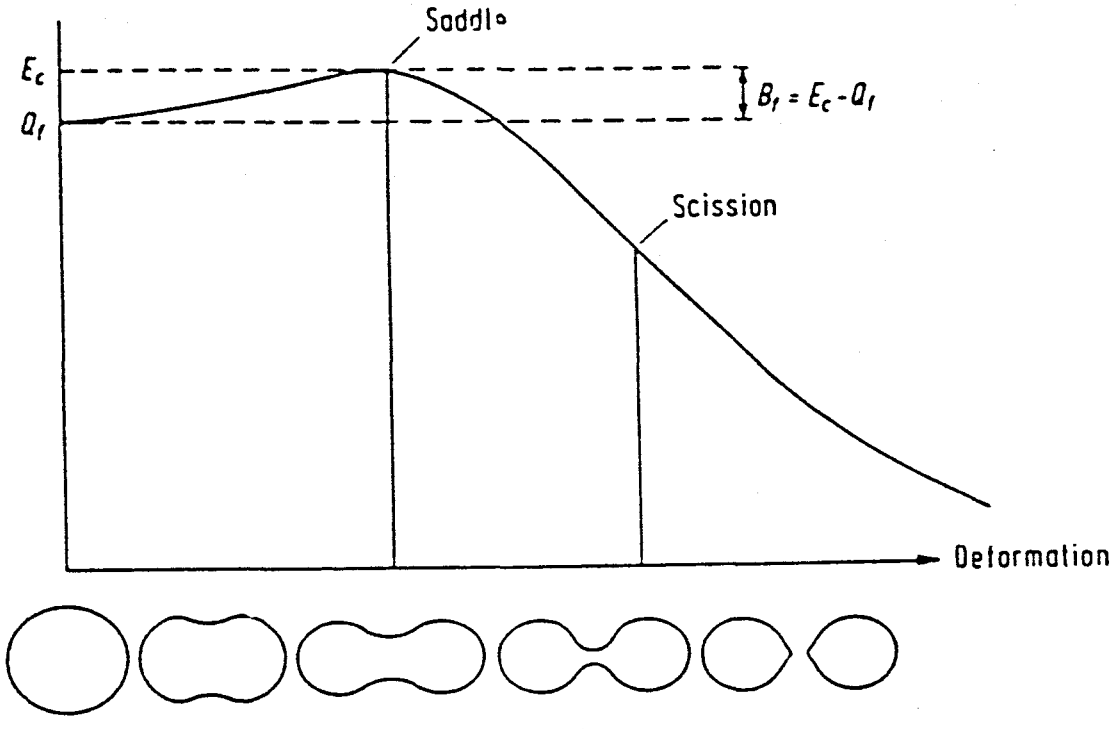

Fig. 2.3 Potential energy as a function of deformation in a simple liquid-drop diagram. The fission barrier B_f, the saddle point (critical deformation), and the scission point (separation into two fragments) are illustrated in the diagram. The distortion of an initially spherical nucleus is schematically shown beneath the potential-energy diagram.

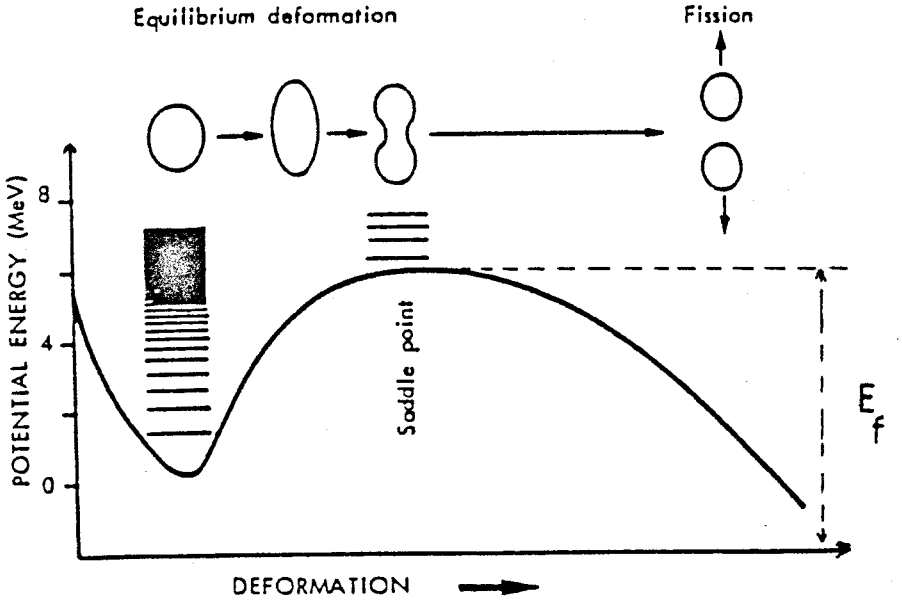

Fig. 2.4 The liquid-drop model potential energy as a function of deformation.

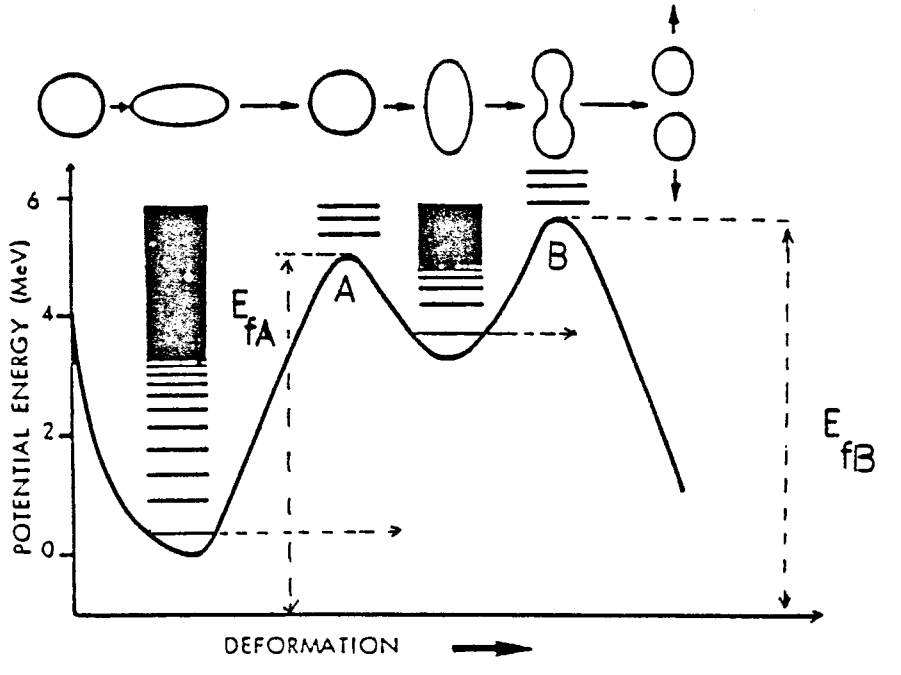

Fig. 2.6 The double-hump fission barrier, the result of combination of the liquid drop model with the shell energy correction.

the assumption that the nucleus shape is associated with the potential well. If, however, the nucleus deforms, some excitation energy is lost as deformation energy. At the top of the barrier, the nucleus is highly deformed and has relatively little internal excitation energy. It exists in well-defined vibrational levels, and fission occurs from such a level. This is known as the saddle point of fission. The difference in the values of potential at the saddle point and at sphericity is called the fission barrier height E_f. The curve in Fig. 2.4 predicts symmetric fission. Although this model is successful in accounting for many gross features of the fission process and forms the principle basis for understanding fission, it is clear that it is not able to calculate absolute heights of fission barriers.

This model is less succesful for highly deformed nuclei lying midway between closed nucleon shells. An additional complication arose when isomers were discovered which decayed by spontaneous fission. Between uranium and californium a number of nuclides were found to decay by spontaneous fission with half-lives of the order of 10^{-2} to 10^{-9} s, millions of times faster than normal spontaneous fission (see Fig. 2.5.). For example ^{242}Cm has a ground state half-life of 106 years for spontaneous fission, while an isomeric state of ^{242}Cm has been found to fission with $t_{\frac{1}{2}}$ of 10^{-7} seconds.

2.2.2 Microscopic Models

These models consider the wave function for all nucleons in detail and should, therefore, provide knowledge of all nuclear properties. The effective nucleon-nucleon interaction in nuclear matter is very complex; in addition the large number of nucleons in actinide nuclei make the calculations extremely long and difficult. The single-particle shell model is one of the best known of the models in this catagory. This model was proposed in 1949 by M.G.Mayer[5] as an explanation of magic numbers. Great progress has been achieved by the

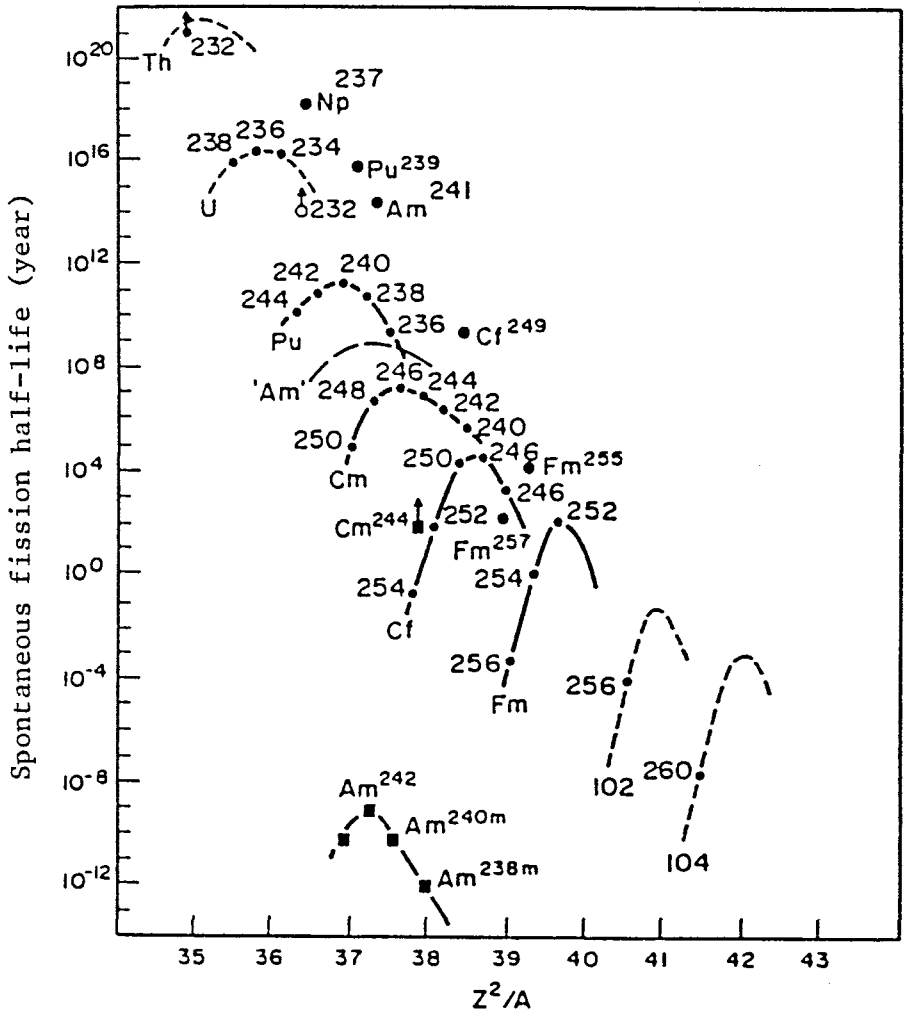

Fig. 2.5 Spontaneous fission life times.

use of the self-consistent field method proposed by Hartree-Fock[6], which allows, with appropriate deformation constraint, the calculation of fission barriers. Purely microscopic models, however, cannot provide for realistic barrier shape, due to the uncertainties in the effective nucleon-nucleon force and limitations in the accuracy of results obtained from a small number of single-particle states used in the calculations.

2.2.3 Hybrid Model

This model, which combines the macroscopic and microscopic aspects of the nucleus was proposed by Strutinsky[7] in 1966, producing extremely interesting results. The model uses the liquid-drop model to represent the smooth, average properties of nuclei but correcting these by the use of separately evaluated, single-particle or shell effects that take account of the non-uniform distribution of nucleons in phase space. The potential energy, $V(s)$, is the sum of the macroscopic energy, $V_M(s)$ (which is more important and can be derived from the liquid-drop model) and a shell-energy correction, $\Delta E_{sh}(s)$, which takes into account the effect of the shell structure of the nucleus at deformation, s. We can therefore write

$$V(s) = V_M(s) + \Delta E_{sh}(s)$$

Strutinsky has found a strong correlation between the shell-energy correction and the ratio of the shell density to the uniform density. Correlation is due to the fact that the Fermi energy is essentially independent of deformation, a decrease of level density at the Fermi surface is associated with the unfilled levels being pushed up (relative to the uniform density distribution) and the filled levels being pushed down. The shell-energy correction is therefore strongly correlated with the density, $g_F(s)$, of single particle states at the Fermi surface. Its values is positive or negative depending on whether

the density, $g_F(s)$, is large or small, respectively. The shell correction presents oscillations along the fission path due to the shell structure variation with deformation. This oscillation is illustrated in Fig. 2.6. The behaviour of the oscillation as a function of deformation for the actinide nuclei is very important. In the case of a spherical nucleus, the density, $g_F(s)$, is high and therefore the shell correction is positive. The first negative correction occurs at the ground-state deformation, and is responsible for the permenant deformation of actinide nuclei in their ground state. The second, negative-energy correction apears in the vicinity of the saddle point and this produces a second well in the fission barrier, between two humps. For heavy actinides the inner well is higher than outer one, whereas it is reversed for light actinides. This shape of the fission barrier for actinide nuclei leads to a better understanding of the fission process.

2.3 From Scission to the Fission Products

The Coulmb repulsion of the two fragments and their prompt de-excitation by neutron and gamma-ray emission are effective in the process leading from scission to the formation of fission products in their ground state. After scission, there is no nuclear force between two fragments and they repel each other due to the Coulomb force. These fragments very rapidly form into a spherical shape when close to their ground state, and the released deformation energy apears in the form of excitaion energy which adds to the excitation energy that existed already at scission. If this excitation energy is greater than the neutron separation energy in the fission fragments, they de-excite in flight by evaporating off neutrons until their excitation energy becomes less than the threshold for neutron evaporation. The evaporation of the neutrons take place at about 10^{-17} seconds from scission. At this time, the fission fragments are fully accelerated

and they would reach infinity if they are separated by a distance of about of 2 A^{o} (see Fig 2.7). If the excitation energy becomes less than the threshold for neutron emission, only gamma-ray emission is possible after a time of about $2x10^{-14}$ sec. The fission fragments when slowed down in a medium are then called fission products.

2.4 De-excitation of the Fission Products

Although the evaporation of prompt neutrons brings the fission products closer to the β-stability line, they are still neutron-rich and far from that line. These nuclides decay by β-emission until they reach the bottom of the valley of β-stability (Fig. 2.8). The process is isobaric and the mass number is conserved during this process, and this is the reason why it is possible to talk about a "mass chain" of fission products. The residual nucleus formed from β-decays, is rarely left in the ground state and therefore, decays to that state by gamma-emission. In a few cases the daughter nuclide is excited above the neutron emission threshold, hence it decays by neutron emission. Such neutrons or gamma-rays, despite occuring promptly after β-emission, are called delayed processes.

2.5 Some Properties of Low-energy Fission of Actinide Nuclei

Briefly described below are some properties of nuclei formed in neutron induced fission at energies up to 20 MeV.

2.5.1 Charge distribution

Inspection of the energy equation shows that for a given mass division, there is a range of values for the nuclear charge of the fragments. Measurement of charge distribution is technically difficult because of the short half-lives of the earlier members of the mass chains. Available data support the view that the range of values for the nuclear charge for a given mass is distributed about a certain probable value for the charge in an approximately Gaussian manner. For low to moderate excitation energies (i.e. less than 30 MeV), the

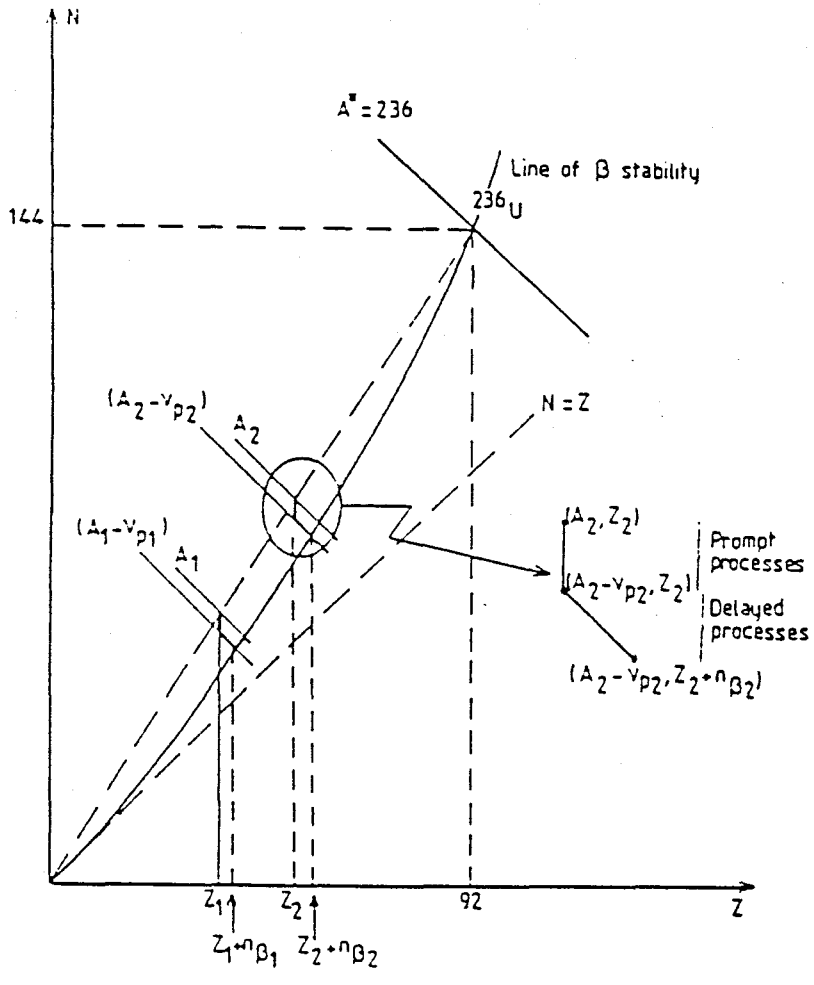

Fig. 2.7 Formation of primary fragments (A_1, Z_1) and (A_2, Z_2) by fission of ^{236}U and decay of these fragments by prompt and delayed processes.

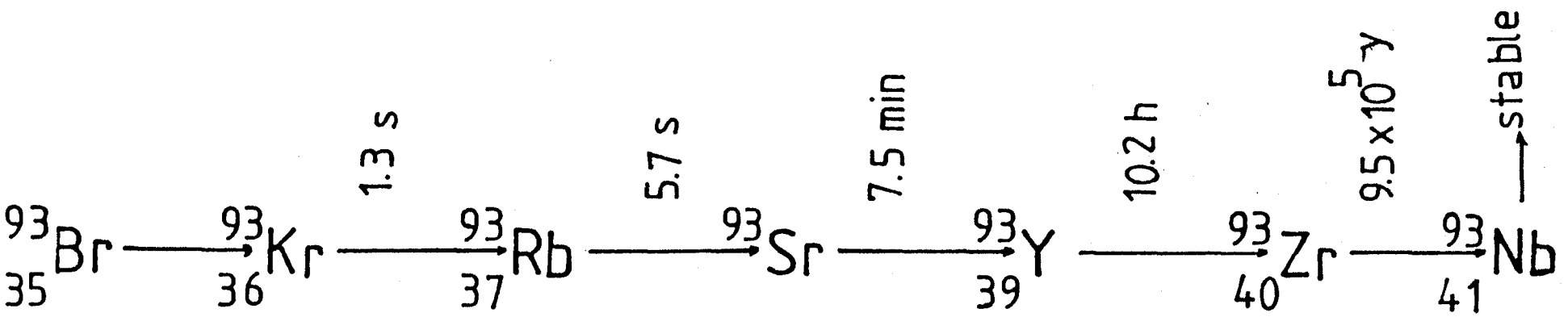

Fig. 2.8 The fission decay chain of A = 93.

charge distribution can be described by the Equal Charge Displacement Hypothesis which originally was proposed by Glendenin etal[8]. This postulates that the most probable charges for complementary fragments are equally for removed from the stable charges for the respective fragments. As suggested by Fong[9], the actual charge distribution is probably related to the energy equation, as the masses of the fission fragment are not known; this can be tested. With the use of sophisticated techniques, such as the measurement of prompt X-rays[10], a more detailed and accurate conception of the effect of excitation energy and nucleon shell-effects on the charge distribution may be realised.

2.5.2 Mass Distribution

The mass of a fission product, A_F, varies from one fission event to another and in order to obtain a proper distribution of mass, it is necessary to study a large number of fission events. The mass distribution of fragments has been investigated for many of the heavier nuclides in the periodic table. Variation in mass distribution with excitation energy has also been examined. A close study of the experimentally-detemined mass distributions reveals several prevalent features. One such feature is the more probable division of a nucleus at low excitation energies into two fragments of unequal mass (asymmetric fission) than division into fragments of equal mass (symmetric fission), as observed in the fission of uranium and heavier elements. As the excitation energy is increased the probability of symmetric fission relative to asymmetric fission increases. At very high excitation energies, symmetric fission is prodominant. Elements lighter than uranium but heavier than bismuth, exhibit essentially the same feature in their mass distributions as do those heavier than uranium. The probability per fission of forming a given mass, A_f, is

(usually expressed as a percentage) called the fission yield and is discussed later in Chapter 3 . The technique of measuring the yield of products is also described in Chapter 3. Mass distributions may be represented graphically as fragment peak width against fragment mass, thus giving rise to the so-called mass yield curves. Whereas the mass-yield curves for uranium and heavier elements exhibit two maxima, those of the group of elements between bismuth and uranium sometimes exhibit three maxima. Several examples of this type of mass distribution have been reported[11], although the majority of systems in which such a distribution has been observed, are those involving charged particle-induced fission at moderate energies (tens of MeV). Mass yield curves exhibiting three maxima resulting from neutron-induced fission are few; evidence for three systems-fission of ^{232}Th[12] and ^{231}Pa[13] induced by 14 MeV neutrons and ^{232}Th[14] by fission spectrum neutrons, has been reported. Bismuth and lighter elements can be induced to undergo fission only at very high excitation energies, where symmetric fission preponderates.There is evidence for the occurrance of "shoulders" in the very asymmetric mass region of ^{238}U[14]. Wahl[15] has shown that in the double-hump mass distribution, the high mass peak remains almost unchanged but the light-mass one is shifted to a higher mass value on increasing the mass of the fissioning nuclide (Fig 2.9). For the fission of on individual nuclide, the mass distribution varies with the compound nucleus excitation energy and this is illustrated in Fig. 2.10 for the neutron induced fission of ^{238}U and ^{232}Th. The yield increases in the symmetric region with increasing neutron energy. Several authors[16,17,18] have developed methods to predict un-measured fission product yields by fitting the sum of up to five Gaussian functions as follows:

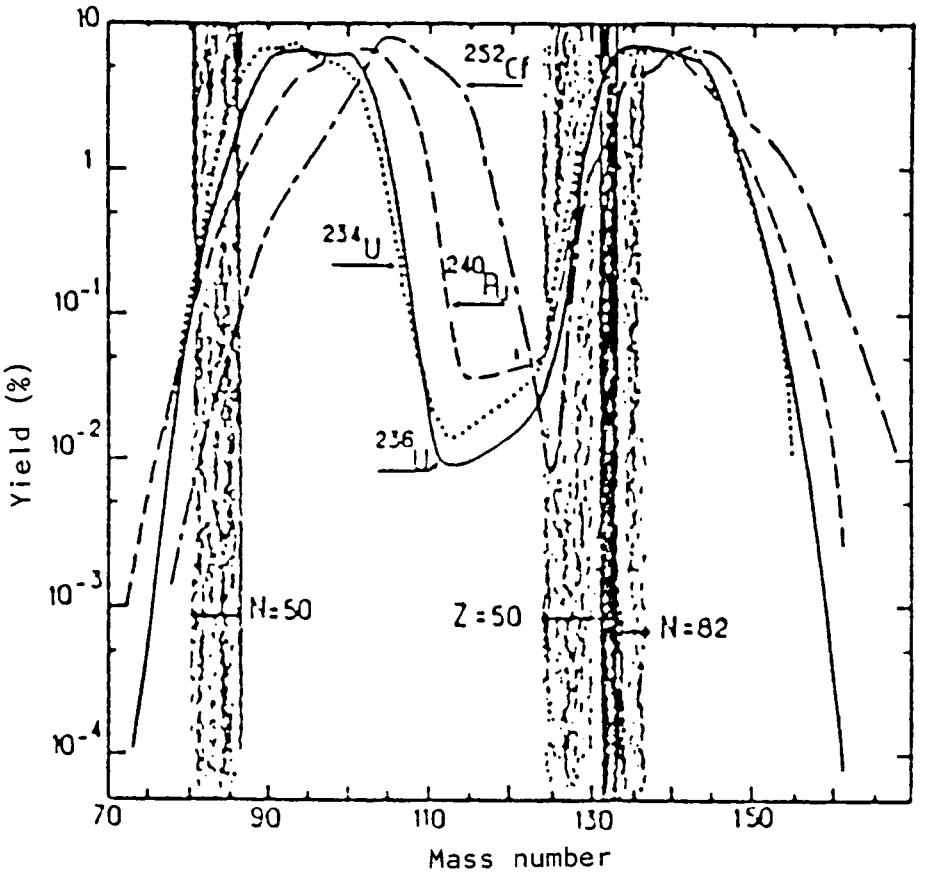

Fig. 2.9 Yield and fission fragment mass distribution for thermal neutron induced fission in ^{233}U, ^{235}U and ^{239}Pu and for spontaneous fission of ^{252}Cf. Shaded areas represent positions of closed shells for neutrons and for protons.

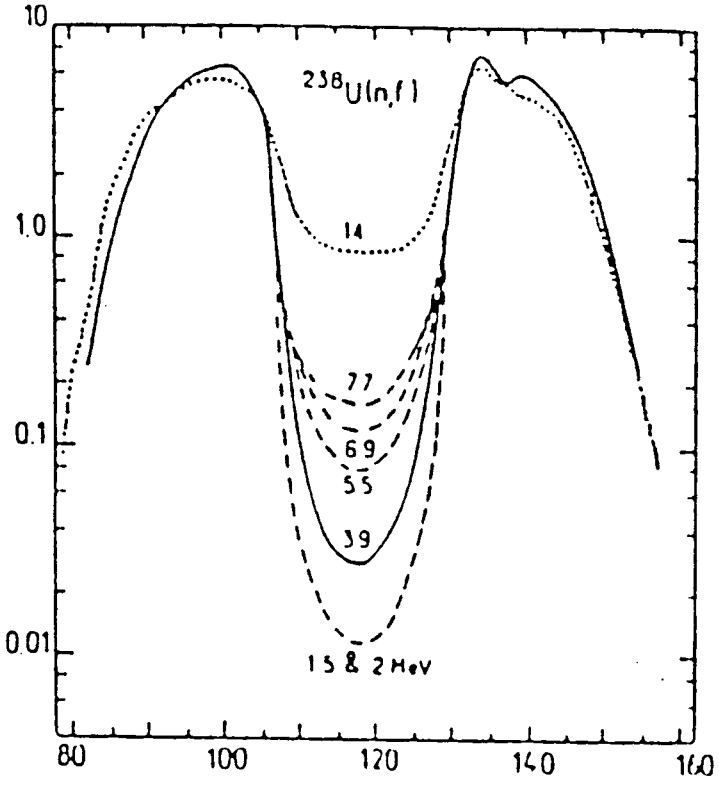

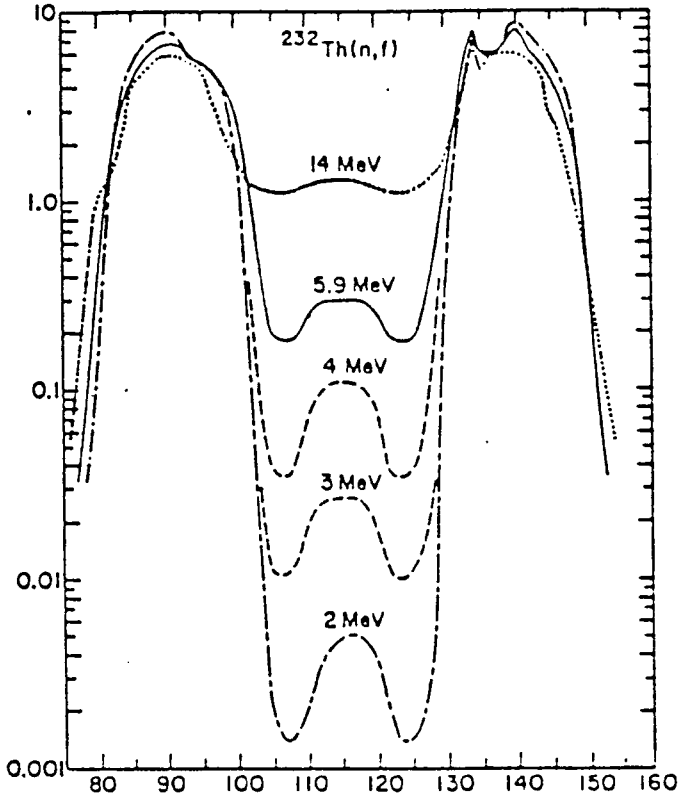

Fig. 2.10 Mass yield curves as a function of incident neutron energy. 2.10(a) for ^{238}U (ref. 18) and 2.10(b) for ^{232}Th (ref. 12).

$$Y(A) = 100. \sum_i \omega_i (2\pi)^{\frac{1}{2}}. \sigma_i . \exp\{-(A-A_i)^2/(2.\sigma_i^2)\}$$

where ω_i, A_i and σ_i are the weight, position, and width parameter of the ith Gaussian, respectively; the subscripts i=1,2 and 4,5 denote the Gaussians corresponding to the light and heavy peaks of the asymmetric fission, respectively, while i=3 denotes the Gaussian describing the symmetric fission. The Liquid-drop model mass equation is used in the calculation of fission masses, but it is less succesful for highly deformed nuclei lying midway between closed nucleon shells.

2.5.3 Prompt Fission Neutrons

As mentioned earlier, the neutrons released in fission can be divided into categories, namely, prompt neutrons and delayed neutrons. The prompt neutrons constitute more than 99% of the total fission neutrons and are emitted by the moving fragments. The average number of neutron, ν, liberated for each fission reaction is given[2] in Table 2.1 for fission induced by .0253 eV neutrons and fast (about 1 MeV) neutrons. The value of, ν, increases linearly with increasing neutron energy, with a slope of .144 neutron/MeV. This is shown in Fig. 2.11 for ^{239}PU. Two spectral shapes are used for the prompt fission neutrons.

2.5.4 The Neutron Spectrum

Two models suggested[20,3] for the neutron spectrum are a Maxwell spectrum and a Watt spectrum. The latter one gives a better fit to the experimental data. In this model all neutrons are emitted by fragments of temperature, T, and moving with velocity, V_k. They are emitted isotropically in the centre of mass system with a Maxwell spectrum. Then by combining the velocities of the emitted neutron and of the fragment in the laboratory system it becomes

$$\Phi(E) = A \exp(E_n/T) \sinh \sqrt{BE_n}$$

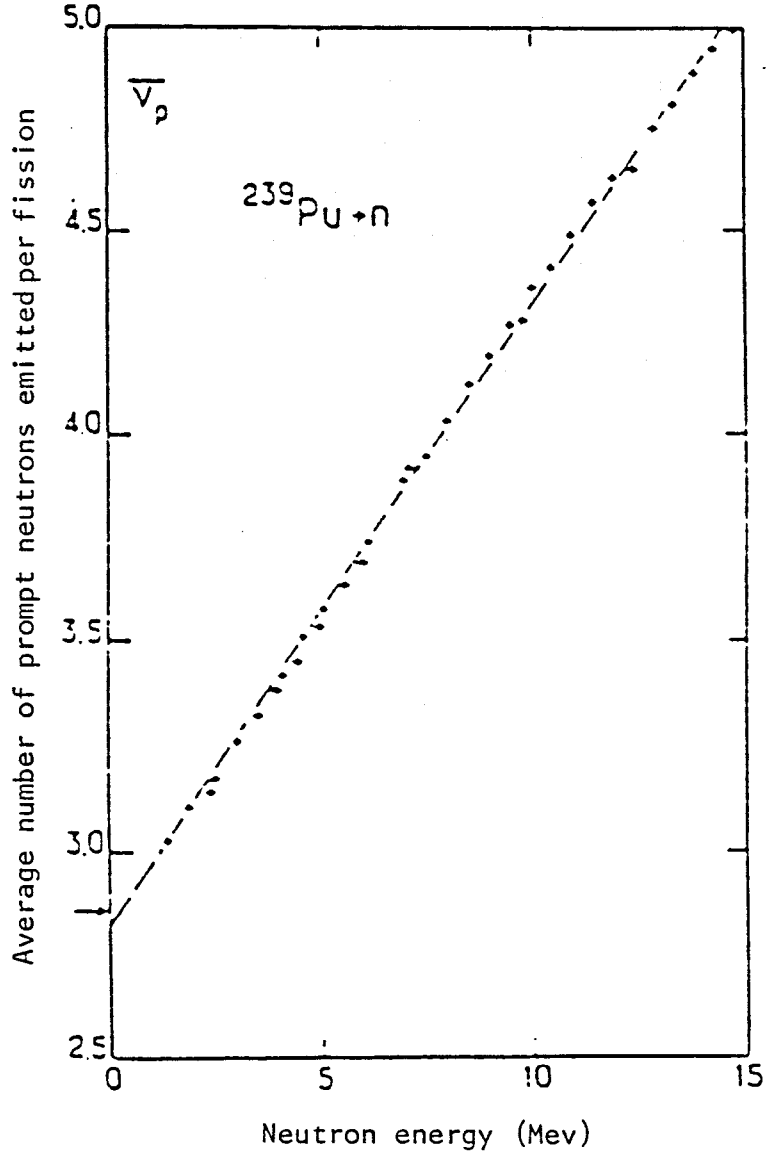

Fig. 2.11 Variation of the average number of prompt neutrons emitted per fission as a function of neutron energy for neutron induced fission of ^{239}Pu.

where A is a normalisation factor and B is a parameter depending on T.

2.5.5 Delayed Neutrons

In addition to the prompt neutrons which are emitted in 10^{-14} s, a much smaller number of neutrons, of the order of 1 to 3 in 100 fissions are emitted with time delays of between 0.08 s and nearly 1 min. These delayed neutrons originate from excited states of the fission products which have decayed by β-emission. Over 60 individual delayed neutron precursors have been identified. Many of the delayed-neutron emitters are clustered just above the N=50 and N=82 closed neutron shells, as a result of the low neutron-binding energies in the β-decay daughters. Among the most prominent delayed-neutron precursors are 4.4 s ^{89}Br, 55.6 s ^{87}Br, 2.8 s ^{94}Rb, 24.5 s ^{137}I, and 1.7 s ^{135}Sb. This subject is reviewed by Rudstam[21] in detail.

2.5.6 Energy Balance in Fission

The average energy released after all prompt and delayed processes are terminated, is given by

$$Q_{tot} = E_k + E_n + E_\nu + E_\beta$$

where E_n, E_β and E_ν are the average energies of all the fission fragments, neutrons, gamma-rays, β-rays and anti-neutrinoes emitted in the fission process. Most of the energy appears in the form of kinetic energy of the fission fragments. The total energy released for different nuclides is shown in Table 2.1.

2.6 Ternary Fission

Ternary fission is classified into two types: one type where one fragment is a light charged particle, and the other type where

Table 2.1

Total energy release per fission and the energy of each particle emitted during the fission process

Fission nucleus	Incident neutron energy (MeV)	neutron emitted per fission	Total kinetic energy (MeV)	Prompt process Kinetic energy (MeV)			Delay process Kenetic energy (MeV)		
				γ	neutron	ff	β	γ	ν
232Th	3.35	2.42	196.11	6.15	4.70	161.79	8.09	7.86	10.87
	14.0	3.92	185.14	6.15	7.37	161.79	7.18	6.99	9.66
233U	thermal	2.48	198.25	7.59	4.90	168.92	5.08	4.94	6.82
	.5	2.51	198.13	7.61	4.90	169.37	5.05	4.91	6.79
	14.0	4.26	184.65	7.61	7.53	169.37	4.26	4.15	5.73
235U	thermal	2.42	202.75	6.96	4.79	169.75	6.41	6.23	8.62
	.5	2.48	202.28	6.96	4.80	169.85	6.38	6.21	8.58
236U	2.82	2.67	202.26	6.30	5.28	170.40	6.92	6.73	9.30
238U	3.10	2.78	206.24	6.30	5.51	170.29	8.21	7.99	11.04
	14.0	4.45	193.21	6.30	7.08	170.29	7.10	6.90	9.54
237Np	2.37	3.1	201.57	6.40	6.14	173.04	5.54	5.38	7.44
239Pu	thermal	2.87	207.24	7.78	5.90	176.07	5.27	5.13	7.09

Table 2.1 (continued)

	.5	2.94	206.66	7.78	5.90	176.09	5.24	5.10	7.05
	14.0	4.90	191.55	7.78	7.51	176.09	4.27	4.16	5.74
240Pu	2.39	3.12	206.68	6.51	6.18	175.98	5.74	5.58	7.72
241Pu	thermal	2.93	210.91	7.86	5.99	175.36	6.54	6.36	8.80
	.5	3.00	210.53	7.87	6.0	175.62	6.49	6.32	8.73
242Pu	2.32	3.73	206.15	6.54	4.59	176.79	6.62	6.44	8.90
252Cf	spontaneous	3.76	225.76	8.36	7.45	189.96	6.03	5.86	8.10

β - bieta particles

γ - gamma rays

ν - neutrino

the masses of three fragments are roughly equal. Fission of the first type ocurs more frequently than the second type.

2.6.1 Fission Involving the Emission of Light, Charged Particles (LCPs)

The details of the ternary fission mechanism are still unclear, but it has been hoped that these particles would provide unique information about the fission process, i.e. the inter-fragment distance D and, as a consequence, the fragment kinetic energy at the moment of scission. It is, however, generally believed that light, charged particles, which accompany fission once every few hundred events, are formed close to the time of scission ($t=10^{-20}$ sec.) and subsequently accelerated and focused almost perpendicularly to the fission axis by the Coulomb field of the fission fragments[22]. Immediately after formation of this charged particle, its motion under the influence of the Coulomb forces exerted by the two major fragments can be followed in trajectory calculations. The final energies and angular distributions of the charged particles emitted in fission are quite sensitive to the separation and speed of the nascent fragments at the time of formation of the particles.

Since these particles are born between the fission fragments at a time close to scission, they therefore appeared to be an excellent probe of the scission configuration. Such studies of the scission configuration in nuclear fission should in principle indicate the dominant mechanism.

The available experimental methods for studying scission configurations are unfortunately very limited. The systematics of the production of long-range charged particles based on kinetic

measurements such as angular distribution, may offer a clue to the mechanism of third-particle production and to the nuclear configuration at the time of scission.

Since the first observation of this rare mode of fission in 1947 by Alvarez[23] and simultaneously by Tsien San-tsiang et al.[24], an extensive body of experimental studies has been built up, particularly with regard to the spontanous fission of ^{252}Cf and the thermal neutron induced fission of ^{235}U[25,26]. Despite these experimental studies a comprehensive theory of light particle ternary fission does not yet exist. Some progress has been made, however, in understanding the mechanism involved and this will now be briefly reviewed.

2.6.2 The Mechanism for Charged Particle Emission During Fission

Early experimental reports on ternary fission based on the observation of tracks in nuclear emulsions showed that the alpha particles were preferentially emitted in a direction orthogonal to the fission axis[23]. The angular distribution for light charged particles indicate that they are produced in the neck region between the two heavy fragments[22].

Estimates have also been given for the energy required to release particles into the region between these fragments and this turns out to be a very large fraction of the total available energy[22].

It has also been suggested that this energy is stored in the deformation of the fragments[2]. If so, it must be stored in some readily convertible form involving only a few degrees of freedom, in order for it to be transferred to the escaping particle on a sufficiently fast time scale.

After the scission process, the energy transfer to the light particle takes place through the sudden snap of the neck stubs[22]. Particle release cannot be considered as a slow thinning of the neck on either side of the particle followed by a slow retraction of the neck stubs into the fragments. For such a process most of the deformation energy would appear as excitation energy of the fragments due to their acquisition of the deformation energy of the slowly collapsing stubs.The energy is insufficient to release both a light particle in a region of high potential energy and at the same time produce a high deformation in the fragments. If one assumes that the process of rupture of the neck and collapse of the stubs is sufficiently rapid i.e. the collapse of the neck takes place in a time much shorter than that required for the light particle being formed to travel a distance of the order of the neck dimension, the rapid change in the nuclear potential of the fragments as felt by the light particle can result in a large change of the potential energy of the light particle with little corresponding change in its kinetic energy. This process has been discussed from the point of view of wave mechanics and is illustrated in Fig. 2.12 by Halpern[22]. This process is independent of the charge of the light particles and Fuller[27] has investigated this mechanism for producing prompt neutrons.The potential change appears less sudden to the neutron than to a heavier particle due its low mass. On the other hand, the energy required to release the neutron is much less and the process has a much higher probability. In a purely classical approach, it is assumed that the forces acting between the fission fragments and light particle may be approximated by an interaction of three charged points; the Newtonian equations of motion of three bodies are numerically intergrated under several assumptions

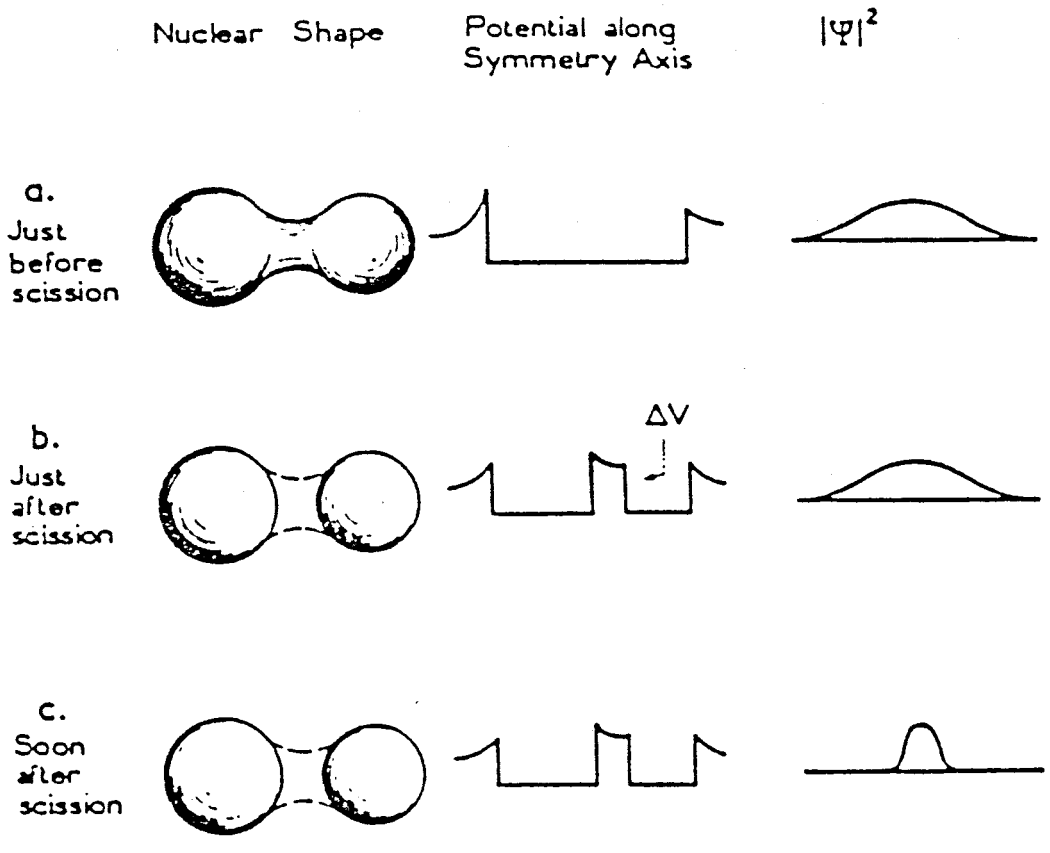

Fig. 2.12 Mechanism for charged particle emission during fission as illustrated by wave mechanics.

concerning the initial conditions, these assumptions being modified until the results are brought into agreement with experimental data.

2.6.3 Relative yield of the Varous Light Particles in Ternary Fission

It is possible for particles with $Z < 8$ to be emitted during a ternary fission event. For these relatively rare events, however, it is found that alpha particles are the most favoured third particle. The experimental data for the yield of these particles for several fissioning systems are given in Table 2.2. The next most abundant particles emitted are tritons, with a frequency roughly 10% of that of the alpha particles. Other nuclei e.g.those of B,C,O have also been detected (Raisbeack and Thomas[42], Natowitz et al[43], Vcrobycv et al[35]. Whetstone and Thomas[39] have shown that a there is a rough correlation between the observed yields and the energy required to form the particle in the region between the two fragments. Their data are shown in Fig. 2.13. This energy is given by the following expression

$$E_R = B_i + \frac{z(Z_1 - z)e^2}{D/2} + \frac{z(Z - Z_1)e^2}{D/2} + \frac{(Z - Z_1)(Z_1 - z)e^2}{D} - \frac{Z_1(Z - Z_1)e^2}{D}$$

Where:

z is the light-particle atomic number,

Z_i is the atomic number of the fragment to which the particle was bound,

B is binding energy,

Z is the atomic number of the fissioning nucleus

Table 2.2

The relative yield of LCPs to alpha-particles emitted in the ternary fission of actinide isotopes

Reaction	Relative yield of different third particles to α-particles (%)												Method	Reference
	p	d	t	3He	4He	6He	8He	7Li	8Li	9Li	7Be	9Be	^{10}Be	
^{241}Pu±n_{th}			8.07 ±.20		100									ΔE-E	30
^{252}Cf	1.8	.7	8.46 ±.28		100	2.6	.09	.13				.21		ΔE-E	26
	1.6	.6	5.9 ±.2	<1	100	2.4	.2	.12				>.01		ΔE-E	40
					100			.3				.65			41
	1.5	.5	7.0		100	1	.06	.12				.2			42
			7.4		100										48
^{233}U±n_{th} 43		.4	4.6 ±.2		100	1.4	.036	.037	.02	.036		.037	.43	Magnetic Mass Spectrometer	28
			3.57 ±.2		100									ΔE-E	29

Table 2.2 (continued)

			5.59 ±.15		100									30
235U		.4	6.3	<.005	100	1.4	.033	.036	.011	.011	.02	.30	Magnetic Mass	25
	1.2	.5	6.2 ±.5		100	1.1							ΔE-E	31
					100						$<10^{-6}$		Radiochemistry	32
					100			.12			.37		ΔE-E	33
			6.67 ±.10		100			.1			.34		ΔE-E	34
			6.73 ±.15		100								ΔE-E	30
2		.5 ±.02	7.2 ±.3	<.01	100	1.91	.082	.041	.018	.03	<10*	.029	.3 ΔE-E	35
			5.29		100								Radiochemistry	36
$^{239}Pu \pm n_{th}$			5.5 ±.5		100								ΔE-E	37
			6.80 ±.30		100								ΔE-E	38
			7.20 ±.30		100								Magnetic Mass Spectrometer	39
			6.79 ±.20		100								ΔE-E	30

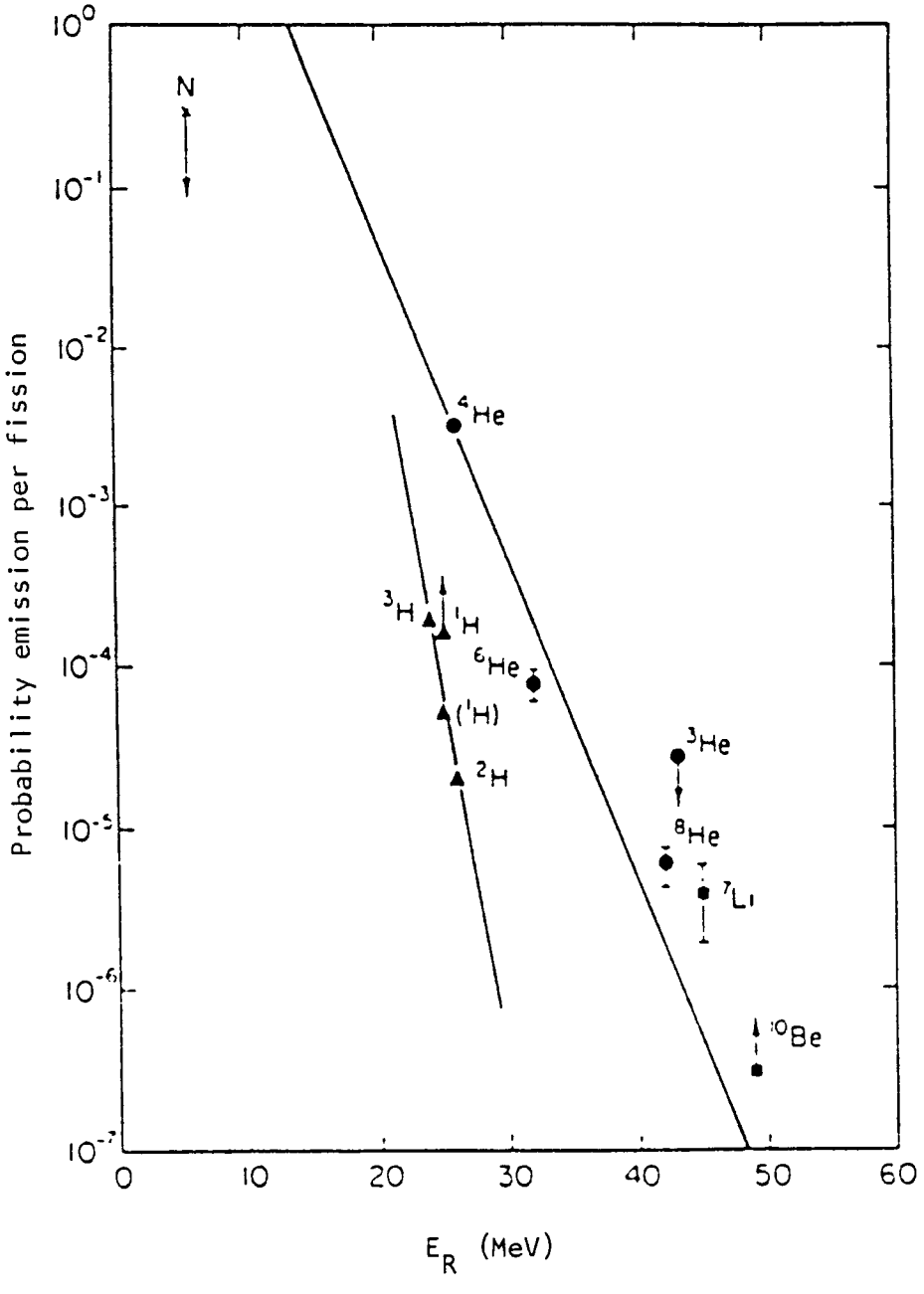

Fig. 2.13 Estimated total LCP yield as a function of the removal energy E_R required for the release of the particle into the space between the fission fragments.

D is the separation of distance the fragments at the time of scission.

The first term on the right hand side of the equation is the separation (binding) energy of the particle, which is the energy required to move a particle to infinity from an isolated fragment. The other terms are the differences in Coulomb energy for a pair of fragments at scission as compared with a configuration of a pair from which a particle has been removed and placed midway between the fragments.

This expression can be simplified to give

$$E_R = B_i + z.V_o[(Z_i - Z - 2.z)/Z_i(Z - Z_i)]$$

Where, $V_o = [Z_i(Z - Z_i)e^2]/D$

is the Coulomb potential energy of the fragments at the time of scission. It is clear from Fig. 2.13 that this removal energy is around 20 Mev or more for all light charged particles and is comparable to the total distortion energy of the ordinary fission event at scission. Fig. 2.13 shows an apparent correlation between yields and mass, and this may be expected on the basis of the uncertainty principle, if the particles are constraind to originiate from the neck region. The uncertainty principle would predict an initial kinetic energy which is inversely proportional to the mass of the light particles. The minimum initial kinetic energy is given[2] by $E = 3\pi^2h^2/2mV^{2/3}$, where V is the volume of the neck region and m is the mass of the light particle. The particle with smallest mass (i.e.the proton) can travel far from the fragment axis in the time during which the just-formed distorted fragments are collapsing to their spherical shape. This implies a larger effective volume for the lightest

particles, which cancels the mass dependence mentioned earlier. So far, trajectory calculations have not produced any evidence for a mass-dependent initial kinetic energy. The fragment direction is the only direction which is relevant to the initial kinetic energies involved in trajectory calculations. Therefore, in considering the spatial localization in the direction prependicular to the fragment direction, it may be necessary to consider also the amplitude and frequency of the bending mode which is responsible for inducing the angular momentum acquired by the fragments.

2.6.4 Dependence of Light-Particle Yield on Nuclear Species and Excitation Energy

It is difficult to distingush the dependence of yield on mass (A) and charge (Z) from the dependence on excitation energy, on the basis of existing data for light-particle-accompanied fission. This is because for the heaviest elements only spontaneous fission and for lighter elements only energetic-particle-induced fission have been studied. The yields of light particles as a function of the excitation energy, E^*, of the initial compound nucleus are shown in Fig. 2.14. They decrease by about 25% for thermal neutron induced fission (E^*=7 MeV) as compared to spontaneous fission (E^*=0). At higher excitation energies e.g. above 15 Mev, the yield increases again. Thus the emission of light charged particles is relatively insensitive to excitation energy and this confirms that these particles are not evaporated from the nucleus. If they were evaporated,their yield would depend sensitively on the excitation energy. The total kinetic energy of the fragments is approximately constant with initial excitation energy. The

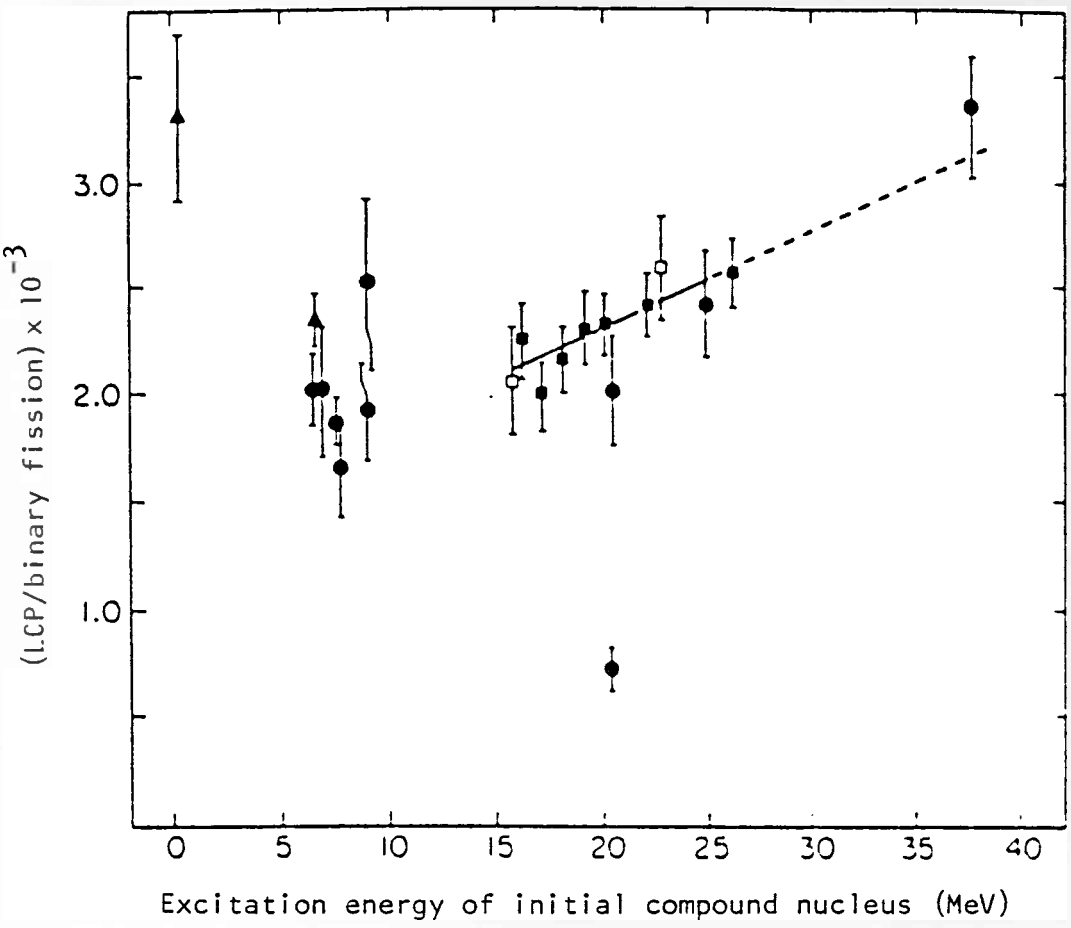

Fig. 2.14 The ratio of light charged particles (LCP) to binary fissions versus the excitation energy of the initial compound nucleus (from ref. 40).

- ^{236}U
- ^{240}Pu
- ^{237}Np

additional increment in the excitation energy of the fissioning nucleus therfore appears as internal energy at scission. The near constancy of the kinetic energy and angular distributions in fission indicate that the average deformation at scission is independent of the initial excitation energy. This supports the mechanism for the ejection of light particles at scission by converting some of the deformation energy at scission into a separation energy.

The correlation between the number of long-range alpha particles (LRA) per 1000 fission events and Z^2/A was observed by Nobles[44]. The quantity Z^2/A appears in the liquid drop model as the ratio of the electrostatic to the surface energy of the drop. So Z^2/A is a measure of the fissility of the fissioning system considered. Hence it has been widely correlated with all the fission observables.

Halpern[22] on the other hand correlated the LRA/B values with a parameter, $4Z-A$, where B is the number of binary fission events. In both methods the proton number, Z, of the fissioning system is the dominant factor. The obseved increase of the light particle yield with increasing Z^2/A is inconsistent with the idea that the yield is dependent on the amount of deformation at scission. Conversly, the liquid drop model calculation by Nix[45] indicated an increase in the deformation energy at scission with increasing Z^2/A, so that the observed increase of LRA/B with Z^2/A is consistent with this model.

The correlation of ternary-particle-emission probability and the deformation energy has been found by Wild et al[46] for several spontaneously fissioning isotopes. Since the internal heating in the case of spontaneus fission is expected to be very small, they approximated the deformation potential energy at scission by

Q-<TKE>.

where

Q = calculated Q value from mass excess for fission

<TKE> = averaged total kinetic energy

Such an approximation is, however, not valid for thermal neutron-induced fission, as Wagemans et al[47] have shown becase the fission mode appears to be strongly damped below the barrier.

2.6.5 Energy and Angular Distribution of the Light Charged Particles

It was pointed out previously that light charged particles are emitted approximately in the normal direction to the fission fragment axis. Cumpstey etal[48] studing the fission of ^{252}Cf, obtained a most probable angle of emission for the alpha particles of 85+1^{o} to the axis of the light fragment and a width (FWHM) of 17+1^{o}. They also found that the most probable angle of emission for tritons from ^{252}Cf was 86.5^{o}, with a width (FWHM) of 17+1^{o}. For the thermal neutron induced ternary fission of ^{235}U, Guet etal[49] found the most probable value of 81.3+0.01^{o} with a width (FWHM) of 18.5+ 0.8^{o} to 20.1+ 0.8^{o}, depending on the low alpha energy cut-off value.. Table 2.3 shows the angular distribution of alpha particles produced in the ternary fission of ^{235}U and ^{252}Cf. Angular distribution is defined by the angle with respect to the light or heavy fragments. The sum of the most probable angles of emission with respect to the light and to the heavy fragments is slightly larger than 180^{o}, because the momentum of a 18 MeV alpha particle increases the angle between

Table 2.3

The angle of emission of alpha-particles relative to the light fission fragment in the ternary fission of ^{235}U and ^{252}Cf at different cut-off energies for the alpha-particles

Fissioning nucleus	Minimum α-particles energy(MeV)	$(\theta_{\alpha-L})$ degree	FWHM of $(\theta_{\alpha-L})$ degree	Reference
^{235}U		83	29	50
"	10	81	24	51
"	12.5	81	22	52
"	4	81.0 ± .6	22.4 ± 1.2	53
"	7.5	81.3 ± .4	18.5 ± .8	49
"	9.5	81.5 ± .4	18.5 ± .8	49
"	12.5	82.2 ± .4	20.1 ± .8	49
^{252}Cf	11.0	84	32	54
"	13.0	92	34	55
"	7.0	82	23.5	56
"	11.0	84.3	18.5 ± .1.0	57
"	12.5	84.3	18.3	58
"	13.3	85.0 ± 1.0	17.0 ± 1.0	48

the two fragments by 4° compared to binary fission. Cumpstey etal[48] detemined the yield of alpha particles and tritons for ^{252}Cf using an energy cut-off of 13.3 MeV and 5.5 MeV respectively, at each angle and these variations with angle are shown in Fig. 2.15. For light particles with E>7.5 MeV the angular distribution with respect to the light fragment for thermal neutron-induced fission of ^{235}U is illustrated in Fig. 2.16 (afte Guet et al[49]). The variations of the most probable angles of emission and the width of the distribution with energy are shown in Figs. 2.17 & 2.18 for alpha emission in ^{252}Cf and ^{235}U, and in Fig. 2.19 for triton emission in ^{252}Cf. There is a positive correlation between the average kinetic energy of both alpha particles and tritons and the angle of emission. The kinetic energy of the alpha particle increases as the angle changes from the most probable angle. Conversely, this effect can be described as a broadening of the angular distribution for alpha particles with energies considerably above the average energy. Piaseki et al[59,60] found that a certain proportion of light particles are emitted along the fission axis, which is difficult to interpret assuming the usual tripartition mechanism. Such particles must come from the poles of the fragments rather than from the neck region, and this phenomenon is called polar emission (PE). Table 2.4 shows the intensity and energy of these polar emission particles (p,d,t, ^{4}He, ^{6}He).The kinetic energies of these polar particles are definately greater than those emitted perpendicular to the fission axis. Piasecki et al[60] have put forward eight hypotheses that could be responsible for PE. These are:

i) bending of the trajectory by the nuclear force,

ii) reactions induced by scission neutrons,

iii) the rotating remanants of the necks,

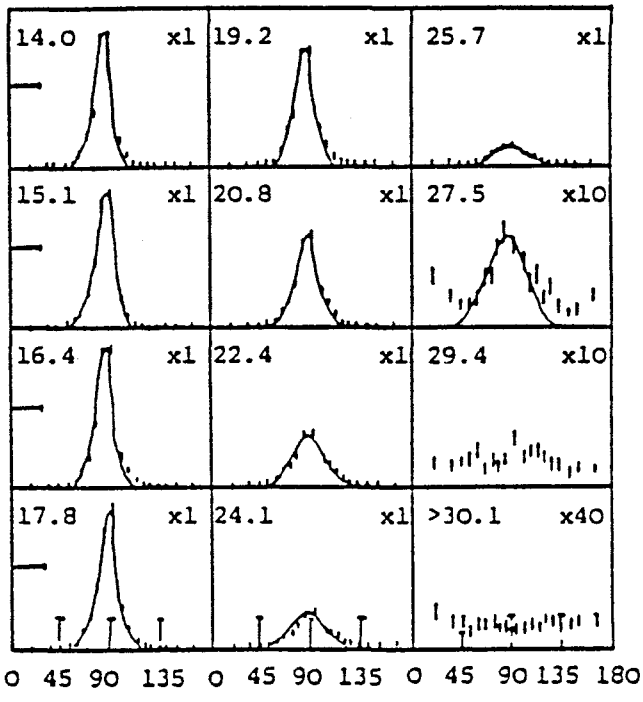

Fig. 2.15(a) The angular distributions of the ^{4}He particles within selected ^{4}He energy ranges identified by the mean energy in MeV. These correspond to the following ranges (in MeV): 14.0 (13.3-14.3), 15.1 (14.3-15.5), 16.4 (15.5-16.8), 17.8 (16.8-18.3), 19.2 (18.3-19.9), 20.8 (19.9-21.5), 22.4 (21.5-23.2), 24.1 (23.2-25.0), 25.7 (25.0-26.6), 27.5 (26.6-28.4), 29.4 (28.4-30.1) and lastly energies > 30.1.

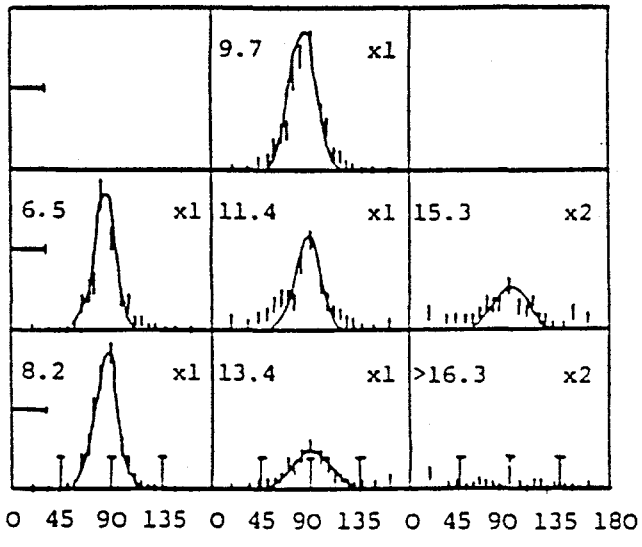

Fig. 2.15(b) The angular distributions of the ^{3}H particles within selected ^{3}H energy ranges identified by the mean energy in MeV. These correspond to the following ranges (in MeV): 6.5 (5.5-7.1), 8.2 (7.1-8.8), 9.7 (8.8-10.5), 11.4 (10.5-12.4), 13.4 (12.4-14.3), 15.3 (14.3-16.3) and lastly energies > 16.3 MeV.

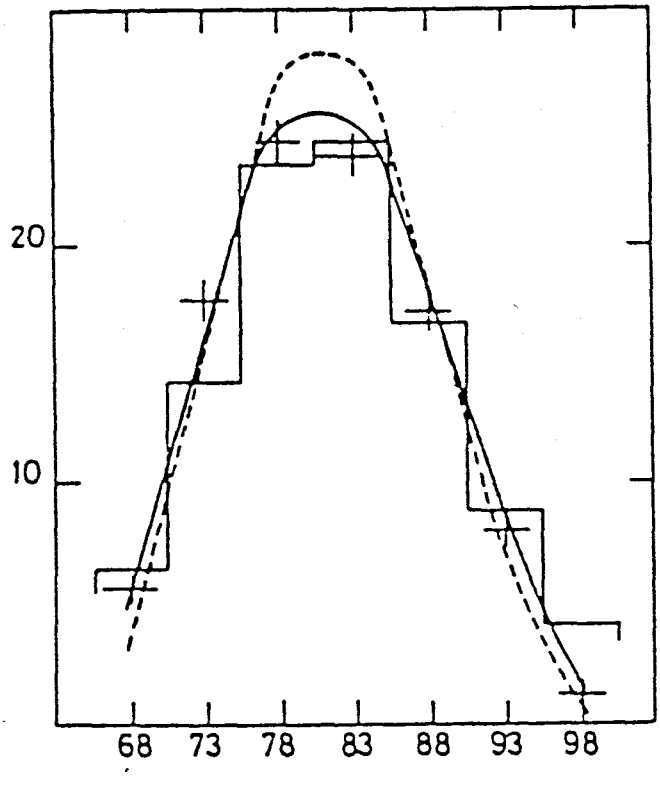

Fig. 2.16 Angular distribution of the alpha-particle with respect to the light fragment. The histogram refers to measured data. The full and dashed lines are the calculated values and differ with respect to the neck configuration (see ref. 49).

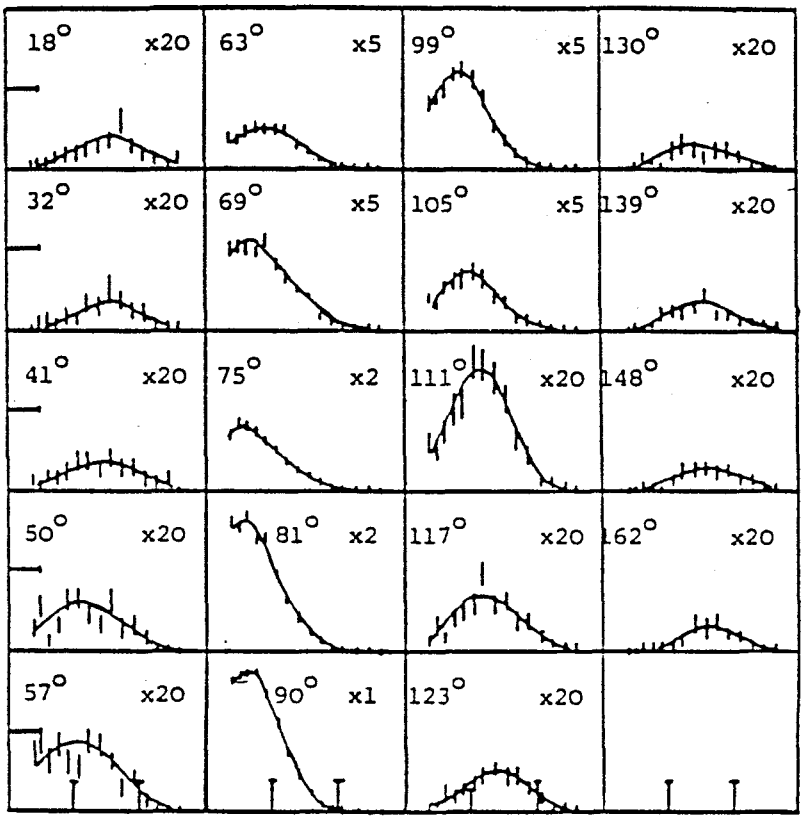

Fig. 2.17 The energy distributions of the ^{4}He particles emitted with the mean angles specified in the ternary fission of ^{252}Cf (ref. 48).

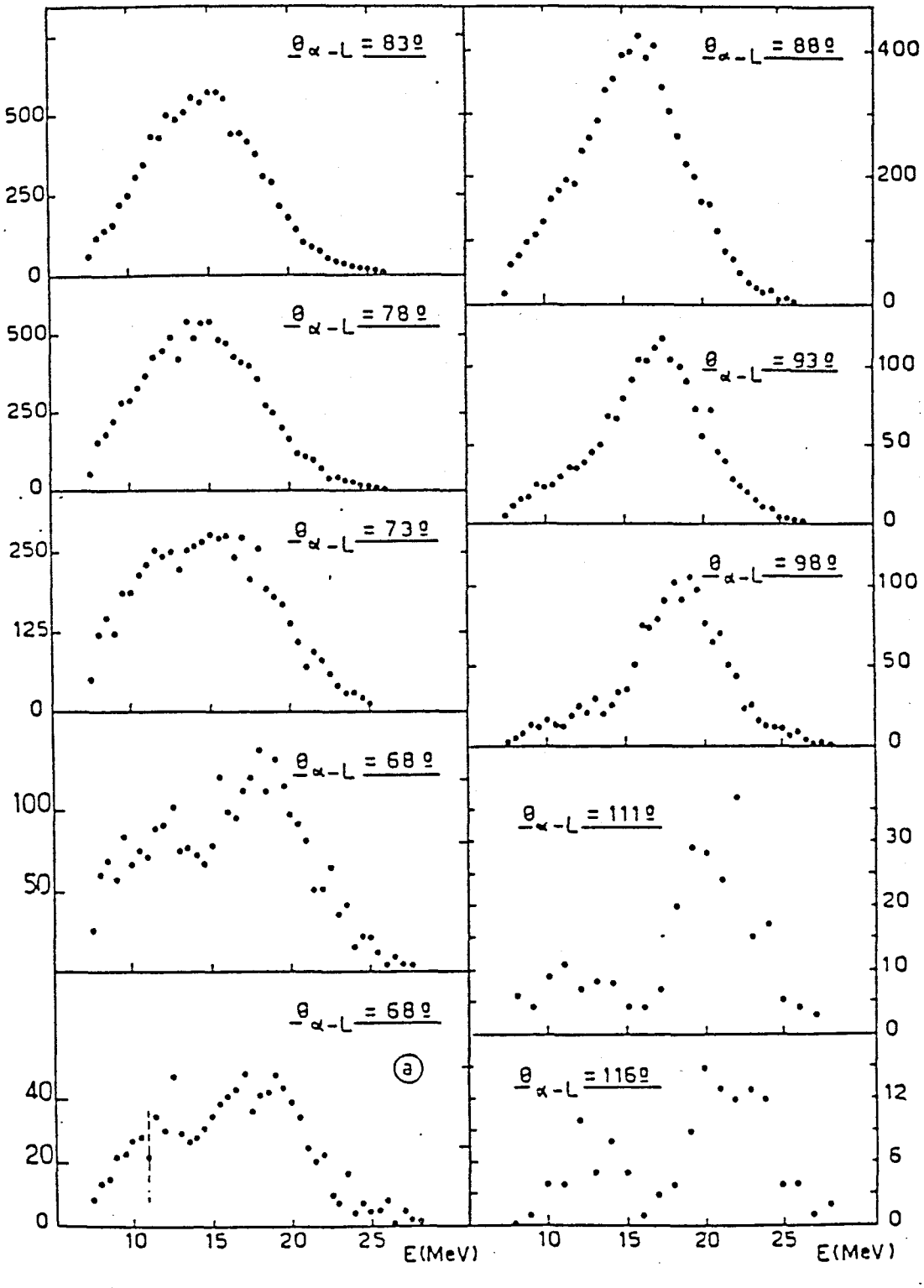

Fig. 2.18 The energy distributions of ^{4}He particles emitted with the mean angles specified in thermal neutron induced fission of ^{235}U (ref. 49).

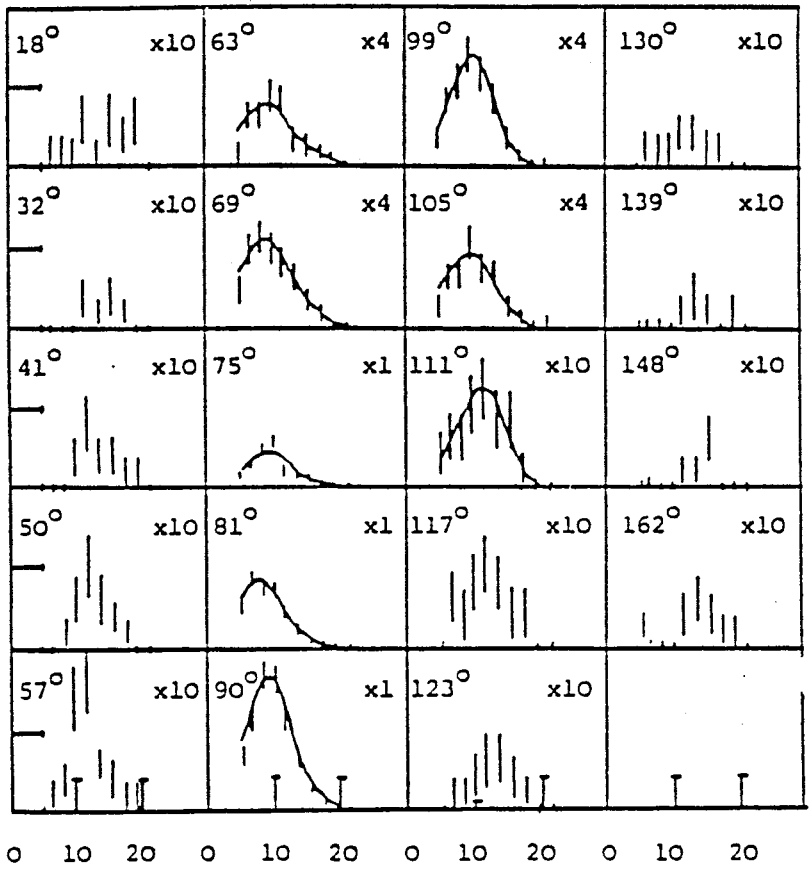

Fig. 2.19 The energy distributions of the ^{3}H particles emitted with the mean angle specified (ref. 48).

Table 2.4

Polar emission of LCPs relative to the light and heavy fission fragments in the ternary fission of ^{235}U and ^{252}Cf

	^{236}U					^{252}Cf			
	ternary fission ref.31	polar emission ref. 60			P/E ratio	ternary fission ref.40	polar emission ref. 61		
		L- emission	H- emission	L/H ratio			L- emission	H- emission	L/H ratio
p	1.15 ±.15	30.5 ±2	44.5 ±4	2.0 ±.2	.17 ±.03	1.6 ±.2	35.0 ±2	33.0 ±3	3.9 ±.3
d	.50 ±.1	2.80 ±.5	3.4 ±.9	2.4 ±.9	.03 ±.01	.63 .03	7.2 ±.6	5.7 ±1.1	4.8 ±1
t	6.2 ±.5	9.2 ±1.2	8.0 ±1.5	3.3 ±.6	.0072 ±.0015	5.9 ±.2	13 ±1	18 ±2	2.7 ±.3
4He	100	100	100	2.9 ±.4	.005	100	100	100	3.8 ±.2
6He	1.1 ±.2	<.06	<.2	-	-	2.4 ±.5	<.05	<.2	-

iv) delayed tripartiation,

v) evaporation from fission fragments,

vi) snapping of the nuclear surface,

vii) pre-scission emission from the fragment polar tips and

viii) diffraction and transmission through fission fragments.

They came to the conclusion that four of them are false, namely postulates i to iv. One (viii) is able to describe some experimental data quite well, which is quite surprising since the hypothesis is apprarently also wrong. Pre-scission emission and wave phenomenon are both in a preliminary stage and do not agree with experimental data. In fact, none of the above hypotheses was able to adequately account for all of the existing data for PE.

2.6.6 Three-Point Charge Model for Ternary Fission

In ternary fission light charged particles are emitted at, or immediately after, the onset of scission and are then accelerated and deflected by the Coulomb field of the two heavy fragments. Their motion is controlled by the state of the nucleus at scission or at the moment of light particle emission. The quantitative imformation on the state of the nucleus at the onset of scission can be obtained if the relations between the initial condition (or the parameters which describe the state of the nucleus at the instant of scission) and the final parameters can be measured experimentally. To relate the final properties of the emitted particle to those of the initial system,it is necessary to perform trajectory calculations, which link the two situations.

In this model, there are three particles: a light fission fragment, F_1, a heavy fission fragment F_2, and a third

particle, A, which is a light charged particle. These three point charges interact by Coulomb forces, and this interaction is explained by the following differential equation

$M_i \, d^2X_{ij}/dt^2 = F_{ij}$

where M_i is the mass of the ith particle, X_{ij} is the jth spatial coordinate of the ith particle and F_{ij} is the jth component of the force on the ith particle. These equations can be solved numerically by the expectation-value method[62]. In this method the initial value of the time increment and the maximum allowable difference between the set of values computed in successive iterations and those expected, are assumed. In addition, the integration period must also be assumed. These equations are integrated until a time when the Coulomb force becomes negligible. In an early account of this model Boneh et al[63] assumed fixed values for initial conditions. The model has been modified by Tsuji etal[58] and Gavron[64], who used a Monte-Carlo procedure for determining the set of initial conditions. The final energies and their mutual angles can be obtained for the set of initial conditions at the time of release of the light particle, which are defined as the initial conditions. Eighteen variables are required to express the motions of the three particles, namely three coordinates and three momentum or velocity variables for each particle. There are six conditions between these variables:three variables for conservation of linear momentum and three variables for conservation of angular momentum. In the case of spontaneous fission or fission with thermal neutrons, there is no preferred direction for the fission axis in space, and therefore the number of variables can be reduced to ten. If it is assumed that the momenta of the three particles lie in a plane, this reduces the number of variables to

seven and it then becomes a two dimensional problem. Tsuji etal[58] selected the initial position of the light particle on the fission axis, and introduced another two conditions. One was that the conservation of the total energy of the system (the sum of the total kinetic and potential energies). The second assumption was that the light fragment was initially on the fission X-axis.They described the initial conditions using the following five quantities (see Fig. 2.20):

(1) the distance, D_f, between the two fragments F_1 and F_2,

(2) the distance, D_α, between the light fragment, F_1, and the foot, H, of the vertical line from the third particle, A, to the fission axis, F_1 F_2,

(3) the distance, H, of the third particle, A, from the fission axis,

(4) the initial kinetic energy ,E, of the particle, A and

(5) the initial emission angle of the particle, A, with the fission axis.

Gavron[64] in a determination of the initial parameter distribution (scission-point parameters) used a trajectory calculation in order to fit experimental data on light particle emission from ^{252}Cf, which empolyed the uncertainty principle for selecting the initial position and momentum of the light particles. He calculated a fit for both LRA and ^5He experimental data simultaneously and found that there is not a correct time scale for particle emission. This result indicates that different light particles must be fitted with different sets of parameters and that none of these sets are consistent with the kinetic energy distribution in binary fission. In this study it was assumed that there was no dependence between the alpha particle and the heavy fragment energies, other than conservation of the total energy,

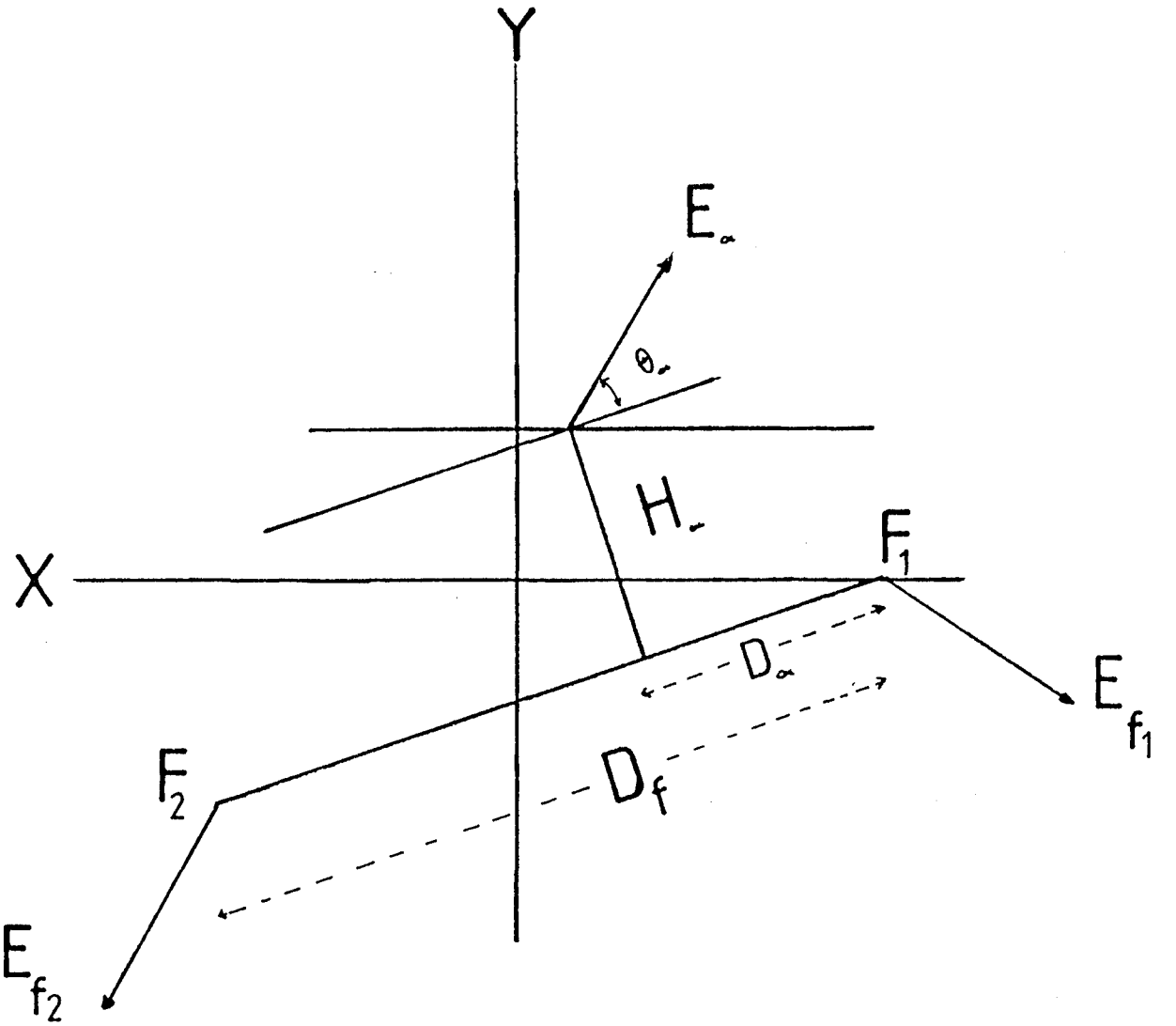

Fig. 2.20 Schematic scission configuration.

$E_\alpha + E_k$. As a result, $d\langle E_k\rangle/dE_\alpha$ equals -1, contrary to various experimental results which indicate that this derivative is approximately[65] -0.5. Further, he also tried to fit his scission-point parameter to experimental data on protons and tritons obtained by Raisbeck etal[41] and found that triton-accompanied fission could be fit with scission point parameters similar to those of LRA fission except for the value of E^o_k (the initial fragment kinetic energy) which was approximately twice that of LRA-fission for the same value of the initial inter-fragment distance, D. His calculations, however, did not fit the data with any set of parameters involving distances, D, in the range of 21-23 fm. Guet etal[66] also used this model, with initial parameters which were selcted by a trial and error method in order to try and fit the experimental results. They have shown that it is possible to fit most of the typical features of alpha-accompanied fission of $^{235}U(n_{th},f)$, by assuming that the fission fragments are already moving apart when the alpha-particle is released but have a relatively low kinetic energy of 8 MeV. This corresponds to approximately five percent of their final total kinetic energy, E_k. Table 2.5 shows a comparison of calculated parameters with those measured for the case of ^{252}Cf fission.

2.6.7 Energy Balance in Alpha-Accompanied Fission

According to Nardi and Frankel[67] the difference between total fragment energy in binary fission and in alpha particle-accompanied fission is about 12.8 MeV for ^{252}Cf. The total kinetic energy of ternary fission is greater than the total kinetic energy in binary by 3 MeV. The number of prompt neutrons

Table 2.5

Comparison of calculated parameters by trajectory calculation with those experimentally measured for ^{252}Cf

Method	Mean total f. fragment kinetic energy Ek(MeV)	Mean α-particle kinetic energy Eα (MeV)	Mean angle $\theta_{\alpha-L}$ degree	Angular width FWHM of $\theta_{\alpha-L}$ degree
measured	174.5[a]	16.0[b]	84.3[c]	18.5[c]
calculated	175.4	15.7	83.6	18

[a] reference 67

[b] reference 26

[c] reference 58

emitted in ternary fission of ^{252}Cf is about .65 less than the binary fission[67,68]. By using the value of 8.7 MeV for average neutron production in binary and ternary, the excitation energy of fragments appears to be 5.7 MeV less in ternary fission than binary fission.

2.7 Fission in which Three Fragments of comparable Mass are produced

Since the discovery of fission, scientists have long considered the possibility that a heavy, excited nuclues may divide into three fragments of comparable mass. Muga[69] has investigated this form of ternary fission of uranium and plutonium induced by thermal neutrons. He used three fission detectors, separated by 120^{o} from each other, in the coincidence mode. He found that the probability of emission for such rare decays was one in 10^{5} or 10^{6} binary fissions. Their results indicated the appearance of two peaks at masses 30 and 60, but such peaks failed to be observed in the radiochemical method[70]. In superheavy systems of very high charges, generated by fusion of heavy ions, there is very clear evidence[71,72] for this phenemenon. The technique used in the investigation of ternary fission and its theory has been reviewed by by Brandt[73] in detail. He discussed the formation of ternary fission by thermal neutrons, light charged particles of energies in the range 10–50 MeV and protons of 20 GeV with counters and the Solid State Nuclear Track method. The first model put forward for ternary fission was proposed by Muzychka et al[74]. This model is represented schematically in Fig. 2.21 which consists of two decay modes.

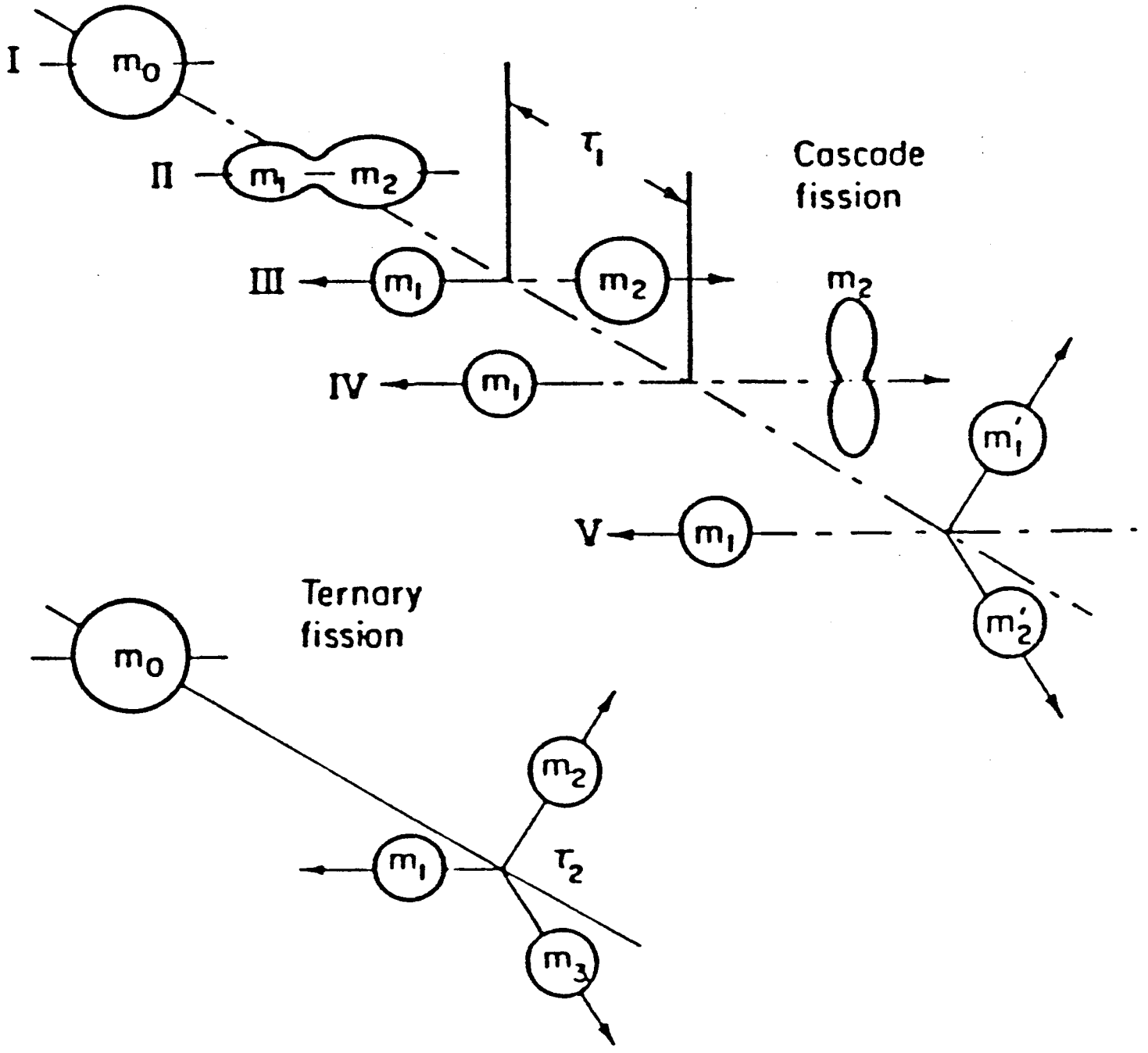

Fig. 2.21 Schematic representation of (a) cascade-type ternary fission and (b) direct ternary fission.

2.7.1 Direct Ternary Fission

Target and projectile form a compound nucleus and two necks are formed essentially simultaneously, which decay in one step into three fragments of approximately equal size. It has already been shown[75] that there are two possible direct modes, the oblate and prolate ones for fission into three fragments and, moreover, that the barrier height for prolate fission is much lower than that for oblate ternary fission (see Fig. 2.22).

2.7.2 Cascade Fission

In this kind of fission, first the compound nucleus undergoes fission and divides asymmetrically into one light and one very heavy fragment, with mass approximately 200. This heavy fragment may have sufficient excitation energy to decay by fission once more into two fragments, within a period of 10^{-21} second. Such a ternary fission is therefore produced in two steps. This mode is often responsible for the ternary fission observed except for systems with both low Z^2/A and low excitation energy.

Recently, the dynamics of ternary fission for the system of $^{238}U+^{238}U$ was investigated[76] in detail with the help of the liquid-drop model. The dependence of potential energy surface for ternary fission on mass asymmetry was exhibited in this study. They also discussed when and where necks are formed and where ruptures occur.

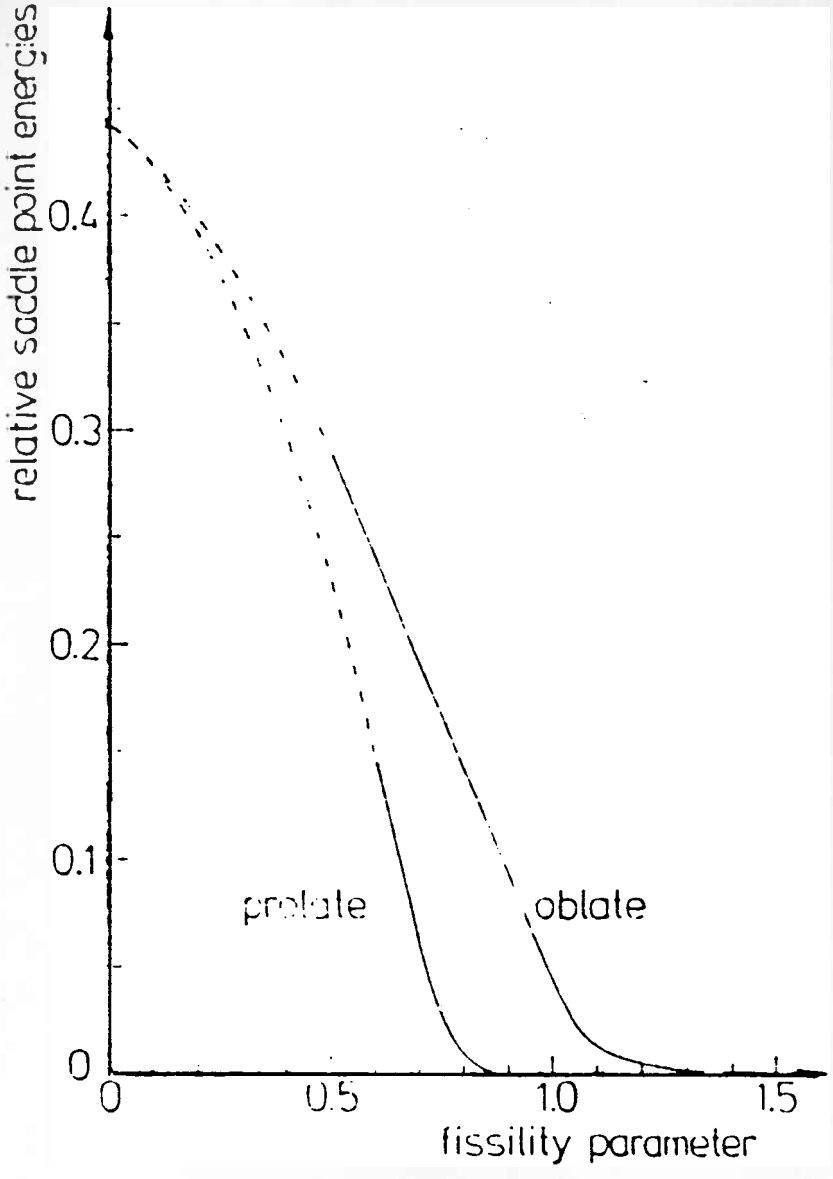

Fig. 2.22 The barrier energies for oblate and prolate ternary fission as a function of fissility parameter.

References

1- Huhn and F.Strassman, Natuwissenschaften 26, 755(1938)

2- Vandenbosch R. and J.R. Huizenga, Nuclear Fission, Academic press London 1973

3- Michaudon A., chapter II, Nuclear fission and neutron-induced fission cross sections, Pergamon press, 1980

4- Bohr N., J.A. Wheeler, phys. Rev. 56, 426(1939).

5- Mayer M.G. and J.H.D.Jensen, Theory of Nuclear Shell Structure, Wiley, New York, 1955

6- Flocard H., P.Quentin, D. Vautherin and A.K. Kerman, Conf. Phys. and Chemi. of Fission, Rochester,I, 221(1973)

7- Strutinsky V.M., Nucl. Phys. A95, 420(1967).

8-Glendenin L.E., C.D. Coryell and R. Edwards, Nat. Nucl. Energy Ser., McGraw-Hill, New York (1951).

9- Fong P., Phys. Rev., 135, B 1338.

10- Nifenecker K., Proceeding of physics and chemistry of fission, IAEA, 435 (1973)

11- Unik J.P., and J.R. Huizenga Phys. Rev. B 90, 134(1964)

12- Glendenin L.E., J.E. Gindler, I. Ahmad, D.J. Henderson, and J.W. Meadows, Phy. Rev., C 22, 152(1980)

13- Sellars J., PhD. thesis, Durhm university, 1967-68

14-Iyer R.H., V.K.Bhargava, V.K. Rao, S.G. Maranthe, S.M. Sahakundu, Proc. Phys. Chem. Fission 1979, IAEA, Vienna (1980)

15-Wahl A.C., Symp. on Physics and Chemistry of fission, Salzburg, I, 317(1965).

16- Musgrove A.R., J.L. Cook and G.D. Trimble, Pannel on FPND, Bologna, Italy, IAEA-169, Vol. II, 163(1973)

17- Cook J.L., E.K. Rose, and G.D. Trimble, Austral, J. Phys., 29, 125(1976)

18- Nagy S.,S. Daroczy, P. Raics, I. Boda, and I. Matajsz, Nucl. Science and Engineering 88, 154(1984)

19- Soleilhar, J. Frehant and J. Gauriau, J. Nucl. Energy 23, 257(1969)

20- Lamarsh J.R. "Introduction to nuclear reactor theory", Addison-Wesley inc, USA, 1966

21- Rudstam G., IAEA Report 213, vol.II., 567 (1978)

22 Halpern I., Ann. Rev. Nucl. Sci. 21, 21(1971)

23 Alvarez L.W., Phys. Rev. 71, 327(1947)

24 Tsien San-Tsiang, Hozah-vei, Vigneron L., Chastel R., Nature 159, 773(1947).

25- Vorobiev A.A., V.T. Grachev, A.P. Komar, I.A. Kondurov, A.M. Nikitin and D.M. Seleverstov, Sov. J. At. Energy 27, 713(1969)

26- Cosper S.W., J. Cerny, and R.C. Gatte, Phys. Rev. 154, 1193 (1967)

27- Fuller R.W.,Phys. Rev. 126, 884 (1962)

28- Vorobiev A.A., D.M. Seleverstov, V.T. Grachov, I.A. Kondurov, A.M. Nikitin, I.A. Yegorov, and Yu.K. Zulite, Phys. Lett B 30, 332 (1969)

29- Cambinghi M., F. Fossati and T. Pinelli, Nuovo Cimento 59B, 236(1969)

30- Wagemans C., P. Dhoundt, P. Schilebecckx, R. Brisot, Phys. Rev. C33, 943(1986)

31- Dokowski M., J. Chwaszczweska, T. Krogulski, E. Piasecki, and M. Sowinski, Phlett. 25B, 213(1967)

32-Roy J.C., Can. J. Phys. 39, 315(1961)

33-Blocki etal, Nucl. phys. A127, 495(1969)

34-Andreev V.N., V.G. Nedopekin, V.I. Rogov, Sov. J. Nucl. Phys. 8, 22(1969)

35-Vorobyev A., D. Seleverstov, V. Grachov, I. Kondurov, A.

Nihitin, N. Smirnov and Y. Zalite, Phys. Lett. 40B 102(1972)

36-Fluss M.J., N.D. Dudey and R.L. Malewicki, Phys. Rev. C6, 2252(1972)

37- Cavallari F., M. Cambiaghi, F. Fossati and pinetti, in Proceedings of symposium on the Phys. and Chem. of fission, Vienna, 891(1969)

38- Krogulski T., J. Chwaszczewska, M. Dakowski, M. Sowinsky and J. Tys., Nucl. Phys. A128, 219(1969)

39- Vorobiev A., V. Grachov, I. Kondurov, Y. Miroshnichenko, A. Nikitin, D. Seliverstov and smirnov, Sov. J. Nucl. Phys. 20, 248(1975)

40- Whelstone S.L. and T.D. Thomas, Phys. Rev. 154, 1174(1967)

41- Gazit Y., E. Nardi, S.Katcoff, Phys. Rev. c1, 2101(1970)

42- Raisbeck G.M., and T.D. Thomas, Phys. Rev. 172, 1272(1968)

43- Natowitz J.B., A Khodai-Joopari, J.M. Alexander, and T.D. Thomas, Phys. ReV. 169, 993(1968)

44- Nobles R., Phys. Rev. 126, 1508(1962)

45- Nix J.R. Nucl. Phys. A130, 241(1969)

46- Wild J.F., P.A. Baisden, R.J. Dougan, E.K. Hulet, R.W. Lougheed and J.H. Landrum, Phys. ReV. 32, 488(1985)

47- Wagemans C., E. Allaect, A. Deruytter, R. Barthelmy and P. Schillebeeckx, Phys. Rev. C30, 218(1984)

48- Cumpstey D.E., D.G. Vass, Proc. Phys. Chem. Fission, IAEA, 1979, IAEA,Viena (1980)

49- Guet C., Signarbieux C., Perrin P., Nifenecker H., Ssghar M., Caitucolli F., Leroux B., Nucl. Phys. A 314, 1(1979)

50- Carles C., Asghar M., Doan T.P., Chastel R., Proc. second symp. on physics and chemistry of fission, Vienna, 119(1969) ,IAEA, Vienna, 1969

51- Gazit Y., Kataze A., Ben-David G., Moreh R., Phys. Rev. C 4,

223(1971)

52- Piasecki E., and J. Blocki, Nucl. Phys. A208, 381(1973)

53- Grachov V.T., Yu.I. Gusev, D.M. Seliverstov and N.N. Smirnov, Sov. J. Nucl. Phys. 32, 612(1980)

54- Fraenkel Z., Phys. ReV. 156, 1283(1967)

55- Adamov V.M., L.V. Drapchinskii, S.S. Kovalencko, K.A. Petrazhak and I.I. Tyutyugin, Sov. J. Nucl. Phys. 13, 540(1971)

56- Rajagopulan M., T.D. Tomas, Phys. Rev. C5, 2064(1972)

57- Fluss M.J., S.B. Kaufman, E.P. Steinberg, B.D. Wilkins, Phys. Rev. c 7, 353(1973)

58- Tsuji K., A. Katase, Y. Yoshida, T. Katayama, F. Toyofuku, H. Yamamoto, Proc. Symp. on chemistry and physics of fission, Rochester, volume 2, 405(1973), IAEA, Vienna, 1974.

59- Piasecki E., J. Blocki, Nucl. Phys. A208, 381(1973), Nucl. Phys. A212, 628(1973)

60- Piasecki E., L. Nowicki, Proc. Phys. Chem. Fission, IARA, 1979, IAEA, Viena (1980)

61- Nowicki etal

62- Moriguchi S., ALGOL Nyumon, 69(1962)

63- Boneh Y., Z. Frankel, I. Nebenzahl, Phys. Rev. 156, 1305(1976)

64- Gavron A., Phys. Rev. c 11, 580(1975)

65- Mehta G.K., J. Poitou, M. Ribrag, Signarbieux, Phys. Rev. c 7, 373(1973)

66- Guet C.R., H.A. Nifenecker, C.Signarbieux, M. Asghar, Proce. Phys. Chemi. Fission, IAEA, 1979, IAEA, Viena (1980)

67- Nardi E., and Z. Frankel, Phys. Rev. c2 1156(1970)

68- Piekartz H., J. Blocki, T. Krogulski and E. Piasecki, Nucl. Phys. A 146, 273(1970)

69- Muga M.L., Proc. IAEA symp. Phys. Chem. Fission, Salzburg,

1965,2, p. 409(1965), IAEA, Vienna.

70- Stoenner R.W. and M. Hillman, Phys. Rev. 142, 716(1966)

71- Fleischer R.L., P.B. Price, R.M. Walker and E.L. Hubbard, Phys. Rev. 143, 943(1966)

72- Perelygin V.P., N.H. Shadieva, V.P. Tretiakova,A.H. Boss, and R. Brandt, Nucl. Phys. A127, 577(1969)

73- Brandt R., Angew Chem. 10, 890(1971)

74- Muzychka Yu.A., Yu.Ts. Oganesyan, B.I. Pustylnik and G.N. Flerov, Sov. J. Nucl. Physics 6, 222(1968).

75- Diehl W.D. and W. Greiner, Nucl. Phys. A 229, 29(1974)

76- Xi-Zhen Wu., J.A. Maruhn and W. Greiner, Nucl. Phys. 10, 645(1984)

CHAPTER 3

REVIEW OF TECHNIQUES FOR BINARY YIELD DETERMINATIONS

3. Introduction

In this chapter we discuss the various definitions of fission yields and then outline the available techniques for their determination. Finally, we describe the methods used for estimating the total number of fissions induced during an irradation.

3.1 Definitions of Fission Yield

There are three kinds of fission-product yields, which are defined in the following sections.

3.1.1 Chain Yield

The chain yield is the probability of formation in fission of all stable nuclides of a given mass number after prompt and delayed neutron emission and after beta decay of all precursors. It is the sum of the independent yields of all the precursors in the beta decay chain of the given mass number and it is also the cumulative yield of the stable members of the decay chain. Since original fission products are neutron rich, the yield of the stable nuclide with greatest neutron number N and smallest charge Z is much greater than the yield of the one or two stable nuclides in even chains with lower N and higher Z. The yields of the latter can be produced by direct formation of even-even "shielded" nuclides or by decay of their immediate odd-odd neighbours. If any chain member is preceded by a nuclide of very long half-life, that nuclide is said to be "shielded".

3.1.2 Cumulative Yield

A cumulative[1] yield is the probability of formation of a nuclide of

a given mass number after prompt and delayed neutron emission and after decay of its shorter-lived precursors. In fact, a cumulative yield is the sum of all the independent yields of nuclides of the same mass number with atomic number less than and including that of the specified nuclide. A fractional cumulative yield is a cumulative yield expressed as a fraction of the chain yield of the given mass number.

3.1.3 Independent Yield

An independent (or direct) yield is the probability of formation in fission of a nuclide of a given mass number after neutron emission before any radioactive decay of itself and of its precursors. A fractional independent yield is an independent yield expressed as a fraction of the chain yield of the same mass number.

3.2 Available Techniques for Measuring Fission Yields

3.2.1 Mass Spectrometry

Mass spectrometry is the most accurate technique used in the determination of fission products yields. In this technique the fission fragments are separated in the succesive electrostatic and magnetic fields of the spectrometer, corresponding to Eqs. (3.1) and (3.2)

$$Mm_o(V^2 / a_e) = e\ e_o\ F \qquad (3.1)$$

$$Mm_o\ (V^2 / a_m) = e\ e_o\ V\ B \qquad (3.2)$$

where

M = mass number

m_o = atomic mass unit

V = fragment velocity

e = ionic charge number

e_o = elementary charge

F = electrical field strength

B = magnetic flux density

a_e = mean deflection radius in the electrostatic field

a_m = deflection radius in the magnetic field

By eliminating V there follows

$$\frac{M}{e} = \frac{a_m^2}{a_e} \cdot \frac{B^2}{F} \cdot \frac{e_o}{m_o}$$

Particles are deflected to an extend representative of their M/e values.

This technique has the problem of requiring long irradiation times and possible variations of the neutron spectrum during irradiation. These problems are serious and make it difficult to know how to evaluate such yields when carried out in different reactors. Mass spectrometry was widely used in the early days of fission yield measurments[2,3]. Davies[2] used this technique and obtained the number of fission products which had occured in his samples due to the consumption of the target material during the irradiation. Isotope dilution mass spectrometry is one of the most accurate techniques used in the measurement of fuel burn-up.

3.2.2 Radiochemical Separation Followed by β-Counting or γ-Ray Spectrometry

Different techniques can be distinguished here:

i) classical, manual, radiochemical separation techniques,

ii) fast, automatic separation methods based on classical radiochemistry,

iii) on-line separation with a chemically selective ion source,

iv) mass separation with a chemically selective ion source,

These techniques are used in measurements of independent fission yield and recently have been reveiwed in detail by Denschlag[4].

3.2.3 Time-of-Flight Measurement

Fission of fissile or fertile material is induced by a pulsed beam of monoenergetic, fast neutrons. A heavy-ion, surface barrier detector is used for the detection of fission fragments. Fragment mass is determined from measured fragment energy and fragment flight time[5,6].

3.2.4 Direct γ-Ray Spectrometery

This method consists of using different irradiation times of fissile material and following the decay of the fission products by recording sequential, gamma-ray spectra with a high-resolution Ge detector. The gamma-ray spectra obtained by this method are quite complex, especially when short irradiation and counting time are required to obtain information on independent yields rather than chain yields. In spite of the complexity of these gamma-ray spectra, with a knowledge of gamma ray intensities, half-lives, irradiation, counting and decay times it is posible to analyse such spectra for those radionuclides produced with reasonable yields. Precise calibration of the gamma-ray detector is required for this technique to be succesful.

The advantages of the method are:

i) a fission yield distribution is possible in a relatively short time,

ii) chemical separation of radionuclides is not necessary,

iii) only a small amount of fissile material is required,

iv) handling of the fissile is quite easy, which is an important

consideration when handling highly toxic nuclides.

The disadvantages are:

i) the accuracy of the method is limited to no better than ±10% ,

ii) it does not provide imformation on the low-yield regions, which can only be studied if some chemical or physical separition technique is available and

iii) the information necessary for data analysis i.e. gamma-ray line intensities, branching ratios and half-lives is often not well known.

Direct γ-ray spectrometry has been widely used in recent years. Some laboratories developed fast techniques of irradiation and counting, necessary for the determination of independent yields. The most advanced one with respect to speed and instrumental character has been developed at Oak Ridge National Lab. by Dikens etal[7-11]. They irradiated the fissile material for a very short time (4 s to 6 min), and by analysis of growth and decay curves of daughters and parents, they determined fractional-independent or cumulative yields of thermal-induced fission of ^{229}Th[7,8], ^{239}Pu[9,10], ^{241}Pu[11]. Hamelin et al.[12] determined the isomeric ratio of ^{136m}I to ^{136}I by using a fast pneumatic system for short irradiations (4, 15 and 90 s) of ^{235}U, ^{238}U and ^{232}Th by 3-MeV neutrons. Toppare et al[13] have determined the spontaneous fission of ^{252}Cf, and Laurec et al[14] have studied the fission of ^{233}U, ^{235}U,^{238}U and ^{239}Pu by fission neutrons and 14 MeV neutrons.

The Argone National Lab. developed a method based on a combination of direct gamma-ray spectrometry and radiochemical separation after both short and long irradiation times[15-22]. They investigated the variations of cumulative yields as a function of neutron energy in the range of .17 to 8.1 MeV. The following nuclides where investigated: ^{232}Th[15], ^{235}U[16], ^{238}U[17] and ^{239}Pu[18]. They also studied ^{229}Th(n_{th},f)[19], ^{236}Np(n_{th},f)[20], ^{245}Cm(sp.f)[21] and ^{249}Cf(n_{th},f)[22].

A similar technique was used by the Livermore group to study the fission of ^{235}U and ^{238}U induced by neutrons of 6.0, 7.1,8.1 and 9.1 MeV[23]. Pure gamma-ray spectrometry was used to follow the growth and decay of mother-daughter systems and to determine fractional cumulative yields of ^{135}I and ^{140}Ba in $^{245}Cm(n_{th},f)$[24] and $^{229}Th(n_{th},f)$[25]. The fractional cumulative yield of ^{134}Te and ^{135}I in the spontaneus fission of ^{252}Cf, and ^{138}Xe in ^{252}Cf(sp. f) was obtained by the growth and decay of its daughter, ^{138}Cs[26].

3.3 Estimation of Total Fissions in the Sample

Total fissions in the sample can be determined by a variety of methods.

1) Heavy Element Mass Difference

The number of fissions in this method are derived from the relationship

$F=U^{o}-(U+U_{cp})$

where:

U^{o} = is the accurately determined number of heavy element atoms irradiated,

U = is the determined number of heavy element atoms remaining after the irradiation,

U_{cp} = is the number of atoms of U_{o}, which converted to other elements by processes other than fission.

By this method, for an irradiation giving a burnup of 20%-40% , the number of fission can be determined to better than 1% .

This technique is based on the fact that the sum of the fission products in one peak of the mass curve is equal to the number of fission events. The accuracy of this method depends on the fraction of total fission products measured in the peak. Measurement of fission products in the heavy peak is easier than for the light one. The preferred measurement technique for individual fission product atoms is that of isotope dilution mass spectrometry. The number of un-measured fission products is obtained by interpolation and extrapolation. Accuracy of the method is about 2-3 % . It requires large number of fissions to be produced in the sample and therefore, long irradiation times in a high flux are necessary.

3) Fission Counting

In this method two target foils are used; one is a bare, thin foil from which the fission fragments escape and are counted in a gas proportional chamber; the other is a heavy target, usually wrapped in aluminium foil to contain the fission fragments. The heavy target is analyzed for the desired fission products. The number of fissions occuring in the thin foil are counted directly and the number of fission occuring in the sample can be calculated from the relative amount of the fissile nuclide in the foil. This method may be used as

i) A fission chamber

Its accuracy is about 2-4 % and this depends chiefly on uncertainties in the fissile or fertile cross-section of the reaction being used. It requires careful calibration.

ii) A fission track detector

This method allows for operation in quite high fluxes by adjustment of the amount of fissile material used. It is simple and reliable but

the amount of fissile material used. It is simple and reliable but tedious to obtain the data unless an automatic counting method is used. The accuracy depends on the number of tracks counted but is not better than 1-2 % .

4) Calculational Methods

The number of fissions can be calculated using some measured quantities such as a cross-section and relevant neutron flux. The accuracy in this method depends mainly on the accuracy of the measurement of the cross-section.

References

1- Crouch E.A.C., Atomic Data and Nuclear Data Tables 19, 417 (1977)

2- Davies W., Radiochim. Acta 12, 173 (1969)

3- Lisman F.L., R.M. Aibernathey, W. Maeck and J.E. Rein, Nucl. Sci. Engng. 42, 191 (1970)

4- Denschlag H.O., Nucl. Sci. and Eng. 94, 337 (1986)

5- Lam S.T., L.L. Yu, H.W. Fielding, W.K. Dawson, G.C. Neilson and J.T. Sample, Phys. Rev. C 22, 2485 (1980)

6- Muller R., A.A. Naqvi, F.Kappeler and J.K.Dickman, Phys. Rev. C 29, 885 (1984)

7- Dickens J.K., J.W. McConnell and K.J. Northcutt, Nucl. Sci. Eng. 80, 455 (1982)

8- Dickens J.K. and J.W. McConnell, Phys. Rev. C27, 253 (1983)

9- Dickens J.K. and J.W. McConnell, Nucl. Sci. Eng. 73,42 (1980)

10- Dickens J.K., J.W. McConnell and K.J. Northcutt, Nucl. Sci. Eng. 77, 146 (1981)

11- Dickens J.K., Nucl. Sci. Eng. 70, 177 (1979)

12- Hamellin CH., J. Crancon, J. Blachot, G. Lhospice, J.P. Bocquet and A. Moussa, J. Phys. (Paris) Lett. 41, 233 (1980)

13- Toppare L., H.N. Erten and N.K. Aras, Can. J. Chem. 61, 649 (1982).

14- Laurec J., A. Adam and T. Debruyne, CEA-R-5147, Commissariat a l'Energie Atomique Saclay (1982)

15- Glendenin, J. E. Gindler, I. Ahmad, D.J. Henderson and J.W.Meadows, Phys. Rev. C 22, 152 (1980)

16- Glendenin L.E., J.E. Gindler, D.J. Henderson and J.W. Meadows, Phys. Rev. C 24,2600 (1981)

17- Nagy S., K.F. Flynn, J.E. Gindler, J.W. Meadows and L.E. Glendenin, Phys. Rev. C 17, 163 (1978).

18- Gindler J.E., L.E. Glendenin, D.J. Henderson and J.W. Meadows, Phys. Rev. C 27, 2058 (1983)

19- Gindler J.E., L.E. Glendenin and D.J. Henderson, J. Inorg. Nucl. Chem. 43, 1433 (1981)

20- Gindler J.E., L.E. Glendenin, E.L. Krapp, S.J. Fernndez, K.F. Flynn and D.J. Henderson, J. Inorg. Ncl. Chem. 43, 445 (1981)

21- Gindler J.E.,D.J. Henderson and L.E.Glendenin, J. Inorg. Nucl. Chem. 43, 895 (1981)

22- Gindler J.E., L.E. Glendenin and D.J. Henderson, J. Inorg. Nucl. Chem. 43, 1743 (1981)

23- Chapman T.C., G.A. Anzelon, G.C. Spitale and D.R. Nethaway, Phys. Rev. C 17, 1089 (1978)

24- Datta T., S.P. Dange, S.B. Manohar, A.G.C. Nair, S. Prakash and M.V. Ramaniah, Phys. ReV. C 21, 1411 (1980)

25- Rattan S.S., A.V.R. Reddy, R.J. Singh, S. Prakash and M.V. Ramaniah, Radiochim. Acta 33, 189 (1983)

26- Ramaswami A., B.K. Srivastava, S.B. Manohar, S. Prakash and M.K. Ramaniah, Radiochim. Acta 30, 15 (1982).

CHAPTER 4

EFFICIENCY DETERMINATIONS OF γ-RAY DETECTORS AND FISSION CHAMBERS

4. Introduction

The accuracy of the yield determination are dependent on the accuracy with which the efficiency of the hyperpure Ge detector and the fission chambers are known. This is because the absolute fission yield (see Section 5.3.8) is dependent on both the absolute gamma ray disintegration and total number of fission events.

4.1 The Efficiency Calibration of a Ge Detector

Both a small volume and large volume, hyperpure Ge detectors were used as spectrometers in the course of this project. In order to obtain absolute fission yield data it was necessary to determine the absolute counting efficiency of these two detectors. The smaller of the detectors was an Ortec GLP series, which is coaxial type, of 10 mm diameter, 80mm^2 area and 7μm depletion depth. It had a measured resolution (FWHM) of 180 ev at 5.9 KeV and 485 ev at 122 Kev. This detector was calibrated over a range of photon energies from 20-350 KeV. The large detector was an Ortec model GLI, also of the coaxial type, with a diameter of 49.0 mm, 18.85 cm^2 area and 49.4 mm depletion depth. It was considered necessary to carry out efficiency determinations using both calibrated point sources and sources with diameters comparable to the foils used in the irradiations i.e. about 10 mm. The 'absolute' and the 'comparison' techniques were used for the measurement of the efficiency of the small detector, whilst only the 'absolute' technique was employed for the large one.

4.2 Absolute Technique

Because of the high cost of calibrated sources a compromise was made between using several sources, each emitting just a few gamma rays and a small number of sources, each of which emits many gamma rays covering the energy range of interest. In this study a single, multi-gamma ray source was used so that the coincidence summing effect correction had to be taken into account to obtain accurate efficiency results.

4.2.1 Coincidence Summing Effects:

The effect results from the simultaneous detection of truly coincident gamma rays (or x-rays). The consequences depend on whether each photon deposits its full energy (F) in the detector or only part of it (P). There are three posible combinations for a simple cascade of two gamma rays:

i)- F_1+F_2 which results in a well-known "coincidence sum peak",

ii)- F_1+P_2 or P_1+F_2 which give rise to important effects which are referred to as the "coincidence summing correction",

iii)- P_1+P_2 which contributes only to the background and does not influence the intensities of the full-energy peaks.

A cascade involving more than two gamma rays gives rise to further terms. Random coincidence corrections, because of low count rate were very small and therefore were not taken into account.

4.2.2 Theory of Coincidence Summing Corrections

Consider the decay scheme shown below.

The observed area A'_3 of the peak corresponding to γ_3 will be larger than the "true" area A_3. This arises from the fact that lifetimes of nuclear levels for γ-ray decay are usually much shorter

than the charge collection time in a Ge detector. Thus the two γ-rays, γ_1 and γ_2 may both deposit their energy in the detector within the charge collection time and hence give rise to a pulse indistinguishable from that due to the single event of γ_3. Other radiations such as x-rays, beta particles (and their bremsstrahlung) and annihilation radiation from β^+ decay may also be in true coincidence. The observed area will include a term from the simultaneous counting of γ_1 and γ_2 so that

$A'_3 = I_3\epsilon_3 + I_1\epsilon_1 b_2\epsilon_2 W_{12}(0^o)$

where

ϵ_i = full-energy peak efficiency for γ_i

I_i= intensity of γ_i in units such that $A_i = I_i\epsilon_i$

b_i = fraction of the decays from the level from which γ_i originates which produce γ_i photons, and

$W_{12}(0^o)$= directional correction of the γ-rays γ_1 and γ_2 averaged over the solid angle subtended by the detector.

This equation can be written as:

$I_3\epsilon_3 = I'_3\epsilon_3(1-(I_1\epsilon_1 b_2 W_{12}(0^o)/I'_3\epsilon_3))$

where $(I_1\epsilon_1 b_2\epsilon_2 W_{12}(0^o)/I'_3\epsilon_3)$ is the fraction of the observed peak that is due to coincidence summing. Following from this discussion it is clear that the observed areas A'_1 and A'_2 for γ_1 and γ_2 are less than the true areas, A_1 and A_2 due to the same coincidence summing. Thus we can write

$A'_1 = A_1 - A_1 b_2\epsilon_2 W_{12}(0^o)$

$A'_2 = A_2 - A_2 f_1\epsilon_2 W_{12}(0^o)$

where

ϵ_1 = the total efficiency for detecting a photon of γ_i and

f_i = the fraction of the events populating the level to which γ_i de-excites that are γ_i photons.

Corrections for coincidence summing for more complex schems are based on these equations. For the Ge detector and source distances used in these experiments $\epsilon << 1$ and all terms containing $\epsilon_i\epsilon_j$, $\epsilon_j\epsilon_k$ etc. were therefore neglected. $W(0^o)$ was set to 1.0 in all the calculations[1].

4.2.3 Experiment Procedure

The procedure used for determing the absolute counting efficiency at a specific gamma-ray or x-ray energy involved

(1) preparing a suitable calibrated source of known activity,

(2) counting the source at a precise and known distance from the detector,

(3) measurement of the net peak area at the given peak energy,

(4) correcting the peak area for decay, counting time, coincidence summing and for attenuation in any absorbers,

(5) knowledge of the decay scheme for the nuclide so that the precise branching ratio for each γ-ray was known and finally,

(6) comparing the corrected count rate with the known disintegration rate.

Two types of sources were used, either a point source of mixed nuclides or an extended source of ^{152}Eu. The point source consisted of ^{109}Cd, ^{57}Co, ^{139}Ce, ^{203}Hg, ^{113}Sn, ^{85}Sr, ^{137}Cs and ^{88}Y, prepared by dispensing an accurately weighed aliquot of a calibrated solution of these nuclides on to polyester tape and then drying and covering with a second layer of tape. This was finally mounted on an aluminium annulus. The actual source used was obtained from Amersham International plc.

The initial, total activity of the source was 37 kBq but by the time these experiments were performed it was weak, because most of the

radionuclides had decayed due to their short half-lives. This source provides γ-rays in the energy range from 22 KeV to 1.333 MeV with reasonably equal distribution of γ-rays between these extremes. The number of γ-rays at each energy was known to at least 4.0% in all cases and in several cases to better than 1.0% . The relevant γ-ray energies and the emission rates are given in Table 4.1.

The extended sources were of nominal diameter 10 mm and consisted of either ^{152}Eu or ^{60}Co. The ^{60}Co obtained from Amersham International plc. had an activity of 46.25±4.0 KBq at a specified date and the ^{152}Eu had a 41.66±4.0 KBq on the same date. Due to the long half-lives of both nuclides these were close to the activities used in the experiment. Sources were again prepared by dispensing weighed aliquots onto a polyster film but dispersing it over a circular area about 10 mm diameter. After drying the sources were then covered with a second layer of tape and then mounted on an aluminium annulus of inner diameter 20 mm and outer diameter 25mm. Again, the complete sources were obtained from Amersham International plc.. Because of the use of activation foils and uranium disks of 10mm diameter in binary fission experiments it was considered necessary to determine the efficiency of such sources and to check these data with those from the nominal point source. For counting, the sources were located precisely in front of the detector with their centre on the cylinderical axis of the detector. The source to detector distance was measured from the polyester film to the front covers of the detectors. The front face of the detectors were about 2.1 mm and 3.0 mm behind these covers for the large and small detector, respectively. After counting the source for an appropriate time, spectra were stored, first on disc and then on magnetic tape. Peak area calculations were performed with the SAMPO 80 program (discussed in chapter 5) on the H-P computer. In the case of ^{152}Eu and ^{60}Co, several of the peak

Table 4.1

The mixed radionuclide gamma-ray reference point source

Radionuclide	Gamma-ray energy(KeV)	Gamma-rays per second	Random uncertainty	Systematic uncertainty	Overall uncertainty
Cadmium-109	88	764	±.2%	±3.0%	±3.2%
Cobalt-57	122	771	±.2%	±2.1%	±2.3%
Cerium-139	166	941	±.3%	±3.4%	±3.7%
Mercury-203	279	2262	±.3%	±2.3	±2.6%
Tin-113	392	2418	±.1%	±3.9%	±4.0%
Strontium-85	514	4654	±.3%	±2.0%	±2.3%
Caesium-137	662	2916	±.2%	±2.7%	±2.9%
Yttrium-88	898	7239	±.1%	±3.8%	±3.9%
Cobalt-60	1173	3988	±.2%	±.7%	±.9%
Cobalt-60	1333	3992	±.2%	±.7%	±.9%
Yttrium-88	1836	7718	±.1%	±2.8%	±2.9%

Reference time: 1200 GMT on 15 June 1983

areas required small corrections for coincidence peak summing in the manner described in section 4.2.2. Calculated peak areas, after correction due to decay were then converted to count rate. The latter could then be compared with the number of γ-rays of a particular energy emitted by each source in unit time. Intensity data for ^{152}Eu were taken from Iwata et al[2] and Debertin[3]. The intensity data for ^{60}Co were taken from the seventh Edition of the Table of Isotops[4]. Table 4.2 shows the energies of the gamma rays emitted from ^{152}Eu and ^{60}Co and their intensities. Using these intensities and the known activities of ^{60}Co and ^{152}Eu, it was possible to calculate the number of γ-rays emitted at each energy. In this way the absolute counting efficiency at each gamma ray energy was determined. From the calculation of the solid angle, Ω, for a point isotropic source and detector with a circular aperture

$$\Omega = \tfrac{1}{2}\left[1 - \frac{d}{(d^2+R^2)^{\frac{1}{2}}}\right]$$

where R was the radius of detector and d was the source-detector distance.

The intrinsic efficiency, E_{int}, can be calculated from

$$E_{int} = E_{abs}/\Omega \qquad 4.1$$

where E_{abs} is the absolute detection efficiency.

4.2.4 Results and Discussion

The absolute efficiency data for a source-detector distance of 4.8 cm are given in Table 4.3 for the large detector. Table 4.4 shows absolute and intrinsic efficiencies for the small detector for the point sources. A plot of the experimental data for the intrinsic efficiency of this detector versus energy for the point source is shown in Fig 4.1. In order to define the best interpolation function through the experimental efficiency data for the large detector, a

Table 4.2

Energies and intensities of gamma rays emitted by a ^{152}Eu source

Gamma-ray energy (keV)	Relative intensity (%)	Intensities per decay (%) Iwata[2]	Debertin[3]
121.8	136.9 ± 1.3	28.80 ± .28	28.37 ± .2
244.7	36.16 ± .25	7.61 ± .05	7.51 ± .05
295.9	2.13 ± .04	.448 ± .009	
329.4	.707 ± .015	.149 ± .003	
344.3	127.1 ± .7	26.74 ± .12	26.58 ± .18
367.8	4.13 ± .04	.869 ± .009	
411.1	10.84 ± .07	2.28 ± .016	2.234 ± .013
443.9	15.01 ± .11	3.158 ± .025	3.121 ± .017
488.7	2.031 ± .015	.427 ± .003	
503.5	.768 ± .018	.162 ± .004	
564.0	2.43 ± .04	.511 ± .009	
566.6	.64 ± .06	.135 ± .013	
586.3	2.19 ± .08	.461 ± .017	
656.5	.71 ± .05	.149 ± .011	
674.6	.94 ± .05	.198 ± .011	
678.6	2.28 ± .05	.480 ± .011	
688.6	4.20 ± .04	.884 ± .009	
719.3	1.67 ± .03	.351 ± .006	
764.8	.95 ± .05	.200 ± .011	
778.8	62.16 ± .22	13.08 ± .06	12.96 ± .07
810.4	1.56 ± .04	.328 ± .008	
841.5	.837 ± .023	.176 ± .005	
867.3	20.33 ± .10	4.277 ± .024	
901.2	.40 ± .05	.084 ± .011	
919.3	2.08 ± .06	.438 ± .013	
926.2	1.38 ± .06	.290 ± .013	
930.5	.37 ± .06	.078 ± .013	
963.3	70.14 ± .23	14.76 ± .06	14.62 ± .06
1005.1	3.078 ± .024	.648 ± .005	
1085.8	48.15 ± .16	10.13 ± .04	10.16 ± .05
1089.7	8.35 ± .04	1.756 ± .010	
1108.9	1.00 ± .05	.210 ± .011	
1112.0	64.67 ± .21	13.60 ± .05	13.56 ± .06
1212.0	6.85 ± .05	1.441 ± .011	
1249.9	.875 ± .024	.184 ± .005	
1292.7	.46 ± .03	.097 ± .006	
1299.2	7.80 ± .05	1.641 ± .012	
1408.0	100.0 ± .3	21.04 ± .08	20.85 ± .08
1457.6	2.391 ± .029	.503 ± .006	
1528.1	1.346 ± .013	.2832 ± .0028	

Table 4.3

The absolute efficiency of the large HP-Ge detector for a point and extended source

Gamma-rays Energy (KeV)	Absolute Efficiency*	
	Point Source	Extended Source
88	204±8	-
121.8	-	218±21
122.1	234±7	
-		
165.9	215±11	-
244.7	-	142.5±13.9
279.2	135±4	-
344.3	-	105±10
391.7	96±5	-
411.1	-	85.8±8.7
443.9	-	80.0±7.7
514	72±2	-
586.3	-	57.8±5.6
661.6	57.1±1.9	-
688.6	-	49.2±4.7
778.8	-	47.0±4.6
867.3	-	43.3±4.2
898.0	43.0±1.9	-
1085.8	-	36.5±3.5
1112.0	-	34.0±3.3
1173.2	32.8±.7	27.9±1.4
1299.2	-	29.5±2.9
1332.5	29.4±.6	24.9±1.2
1408.0	-	27.0±2.8

* $\times 10^{-5}$

Table 4.4

The absolute and intrinsic efficiencies for the small HP-Ge detector

X-ray or γ-ray Energy (KeV)	Ω	Intrinsic Efficiency (%)
22.16	0.096	45.75
32.19	=	30.20
88	=	35.83
121.97	=	20.5

Table 4.5

The value of the fitted parameters of the multi-element point source and extended source for the large HP-Ge detector

Parameter	Point Source	Extended Source
A	$(1.083\pm.25)\times10^{-2}$	$(1.208\pm.32)\times10^{-2}$
B	$(6.151\pm2.4)\times10^{-4}$	$(7.632\pm.84)\times10^{-3}$
C	$(2.847\pm.46)\times10^{-2}$	$(3.402\pm.54)\times10^{-2}$
D	$(3.541\pm.31)\times10^{-3}$	$(4.754\pm1.0)\times10^{-3}$
F	$-(1.327\pm.56)\times10^{-2}$	$-(5.915\pm3.28)\times10^{-3}$
G	$(1.761\pm.41)\times10^{-3}$	$(5.798\pm4.52)\times10^{-4}$

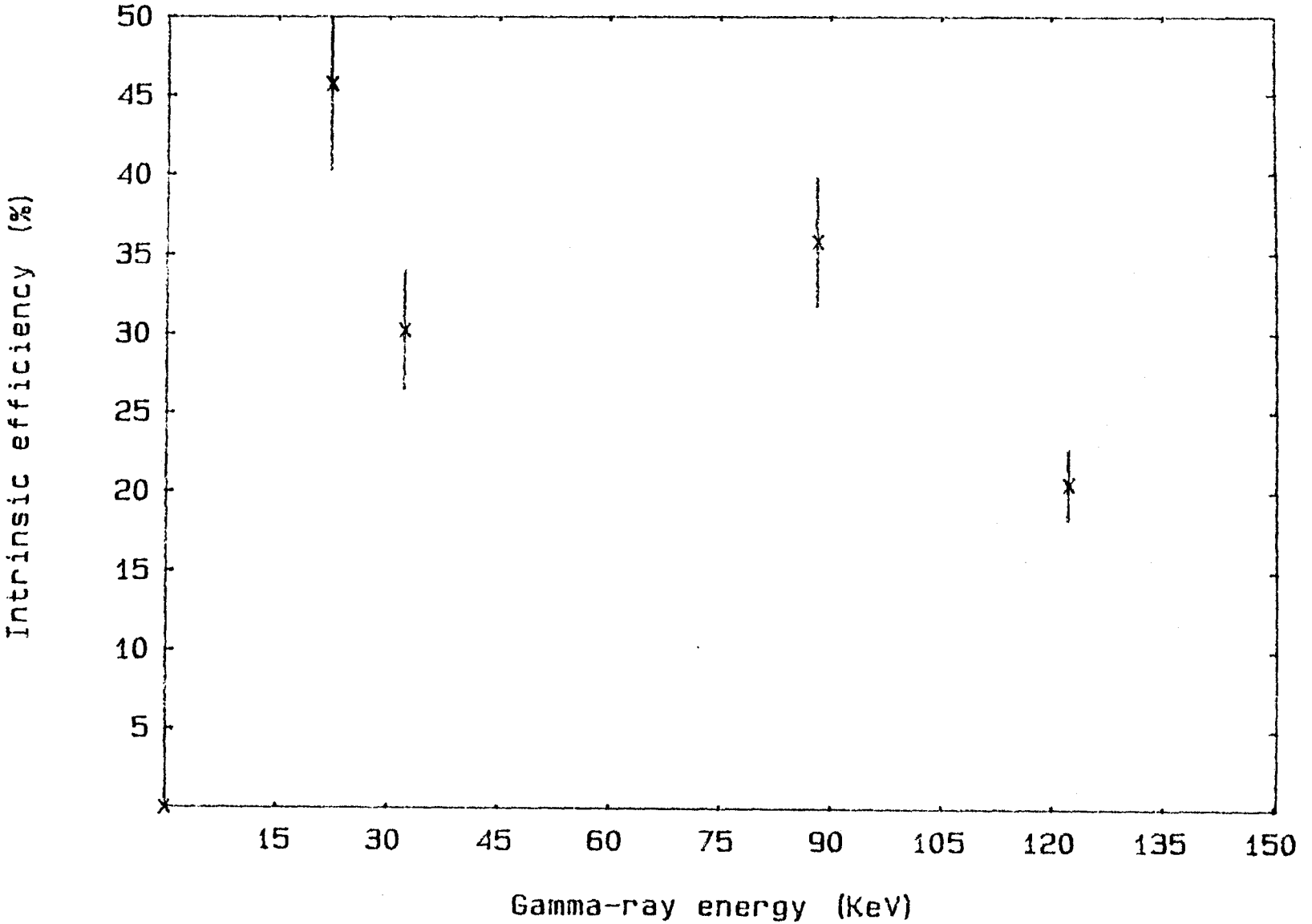

Fig. 4.1 Intrinsic efficiency versus γ-ray energy of the small Ge detector determined with a multi-element, standard point source.

number of functions were examined including a simple exponential, an exponential with a correction term and a linear combination of these exponentials. The latter function is of the form

$\epsilon = A.\exp(-E_n) + C.\exp(-E_n) + F.\exp(-E_n)$

where

ϵ = detector efficiency

E_n = γ-ray energy

A,B,C,D,F,G =fitted parameters.

The values of the fitted parameters were determined using a computer program based on a least-sqaure fit using the Marquart method[5] to fit the functions to the experimental data. The plot of the experimental data and the fitted function are given in Figures 4.2 and 4.3. The values of the fitted parameters for the multi-element source and for the combined ^{60}Co-^{152}Eu extended sources are given in Table 4.5. The solid angle for an extended disc source parallel to a detector with a circular aperture (Fig. 4.4) was calculated from equation Ap.1 in (appendix 1) to be .05476±.00054 srd..

Knowing the solid angle, Ω and using equation 4.1, the intrinsic efficiency for the large detector for a point or an extended source was determined and the results are shown in Table 4.6.

4.3 Comparison Technique

In this method, the small HP-Ge detector is compared to that of a NaI(Tl) detector whose efficiency is known or can be calculated. The advantage of this method is that the incident flux of photons does not have to be known absolutely.

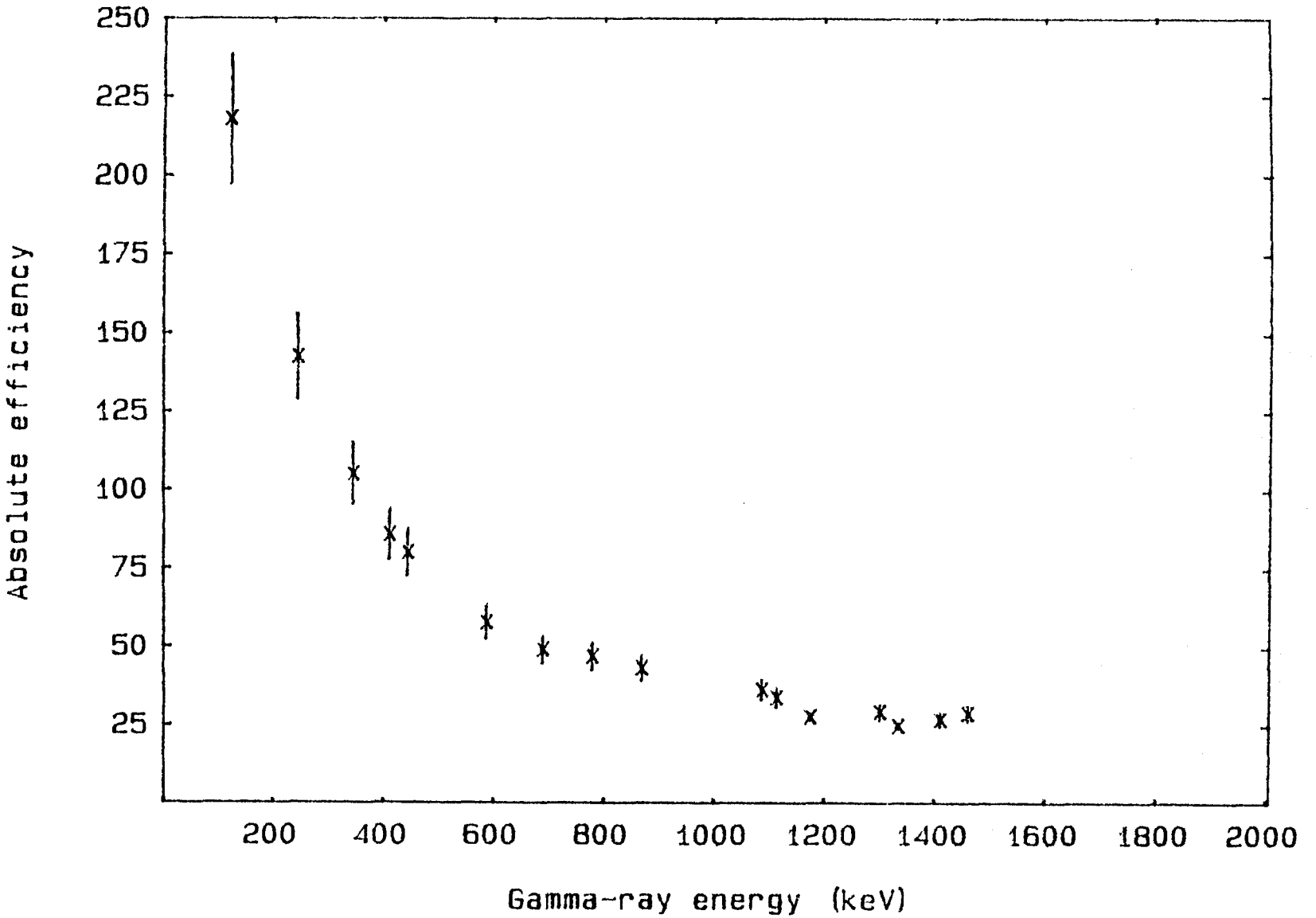

Fig. 4.2 Absolute efficiency as a function of γ-ray energy for the large Ge detector determined with the multi-element, standard point source.

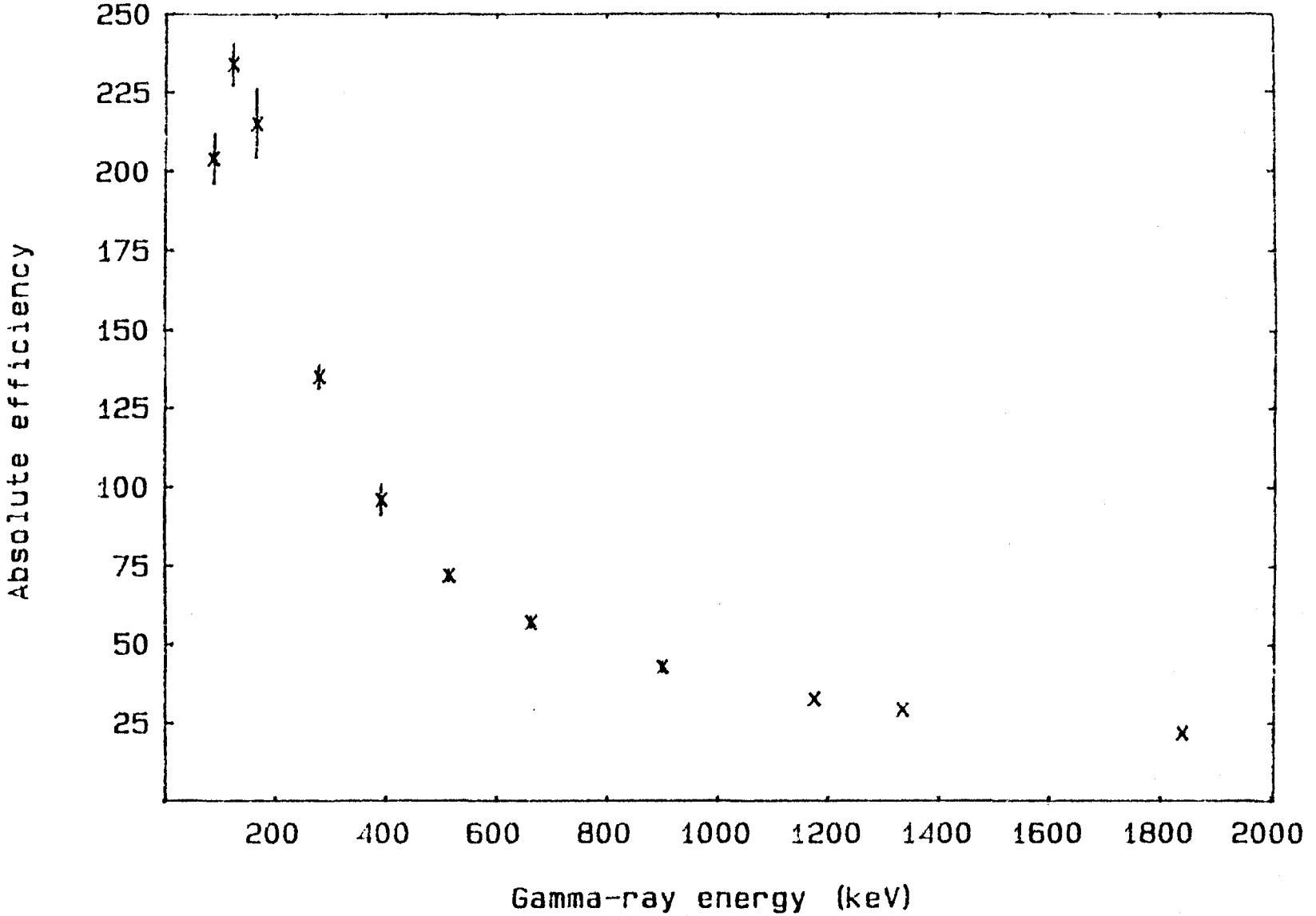

Fig. 4.3 Absolute efficiency as a function of γ-ray energy for the large Ge detector determined with an extended, calibrated source.

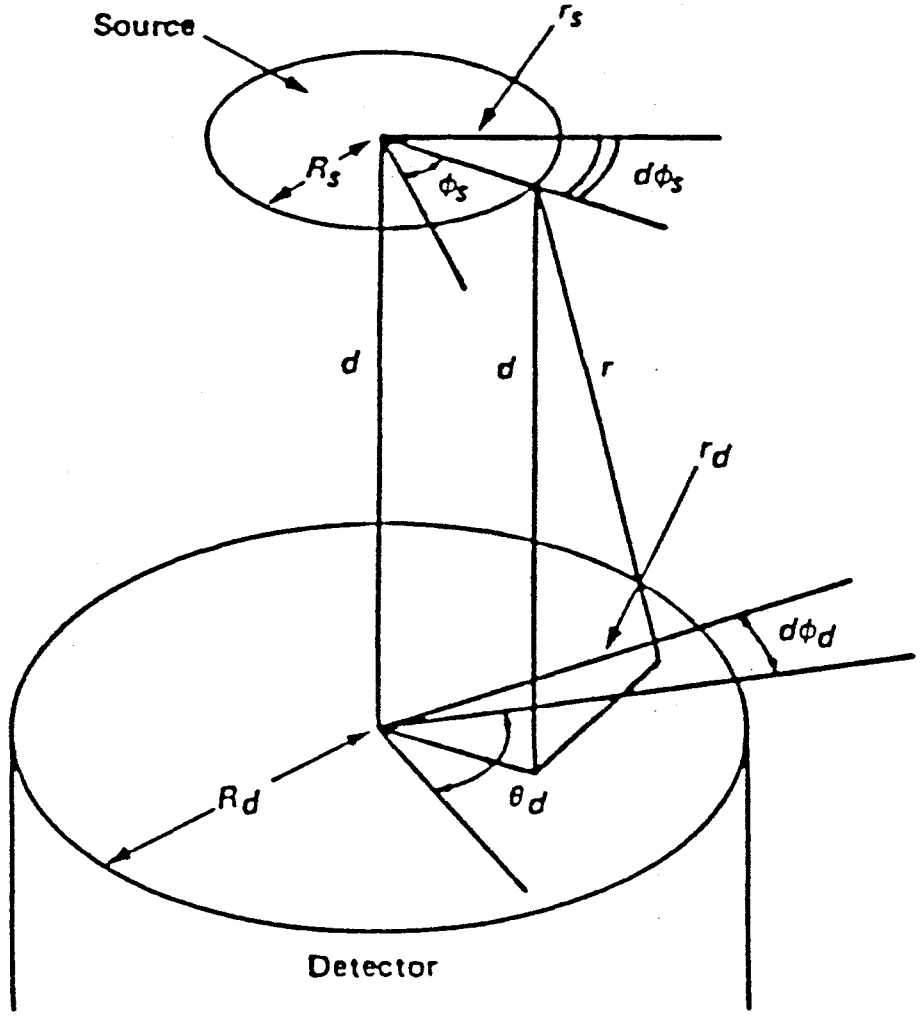

Fig. 4.4 Diagram of the geometry for a disc source counted with a cylinderical detector.

Table 4.6

The intrinsic efficiency of the point and extended source for the large HP-Ge detector

Gamma-rays Energy (KeV)	Intrinsic Efficiency* Point Source	Extended Source
88	37.32±1.46	-
121.8	-	39.8±3.83
122.1	42.81±1.28	-
165.9	39.33±2.01	-
244.7	-	26.02±2.53
279.2	24.69±.73	-
344.3	-	19.17±1.82
391.7	17.56±.91	-
411.1	-	15.66±1.58
443.9	-	14.6±1.40
514	13.17±.36	-
586.3	-	10.55±1.02
661.6	10.44±.34	-
688.6	-	8.98±.85
778.8	-	8.58±.84
867.3	-	7.90±.76
898.0	7.86±.34	-
1085.8	-	6.66±.63
1112.0	-	6.20±.60
1173.2	6.0±.12	
1299.2	-	5.38±.53
1332.5	5.38±.1	
1408.0	-	4.93±.51

4.3.1 Experimental Procedure

A standard, variable x-ray energy source consisting of Cu, Rb, Mo, Ag, Ba and Tb targets, fluoresced by 60 KeV γ-rays from a 10 mci ^{241}Am source was used to provide the photons in the energy range 10-60 KeV. For higher energies the reference gamma-ray sources of ^{57}Co, ^{152}Eu and ^{133}Ba were used. Table 4.7 lists the sources and the energies of the characteristic x-rays or emitted gamma rays. The energies quoted are the weighted K x-rays energies from Storm and Israel[6] instead of the individual K_α and K_β energies.

A Bicron NaI(Tl) detector with a 7.5cm X 7.5cm crystal and a Nuclear Enterprises detector with a 3.8cm X 3.8cm crystal were used. These detectors have a detection efficiency of close to 100% for photons in the energy range of 10-300 KeV[7]. The NaI(Tl) detectors had a .01" aluminium window and consequently a sheet of aluminium of the same thickness was placed in front of the Ge detector to give the same absorption in all of the detectors.

The geometrical arrangement for both counting systems and the electronics for the NaI(Tl) system are shown in Figure 4.5. All of the detectors were exposed to the sources for a sufficient time to obtain satisfactory counting statistics. Both detectors were apertured by 1cm thick lead with a .5 cm diameter hole to try to ensure that the photons were incident normally at the crystal, fairly central and did not interact with the edges of the crystal.

The scintillation pulses from the NaI(Tl) detector were processed and amplified by a preamplifier and a Ortec 572 amplifier. These pulses and those from Ge detector were fed into a H-P multichannel analyser (Figure 4.5).

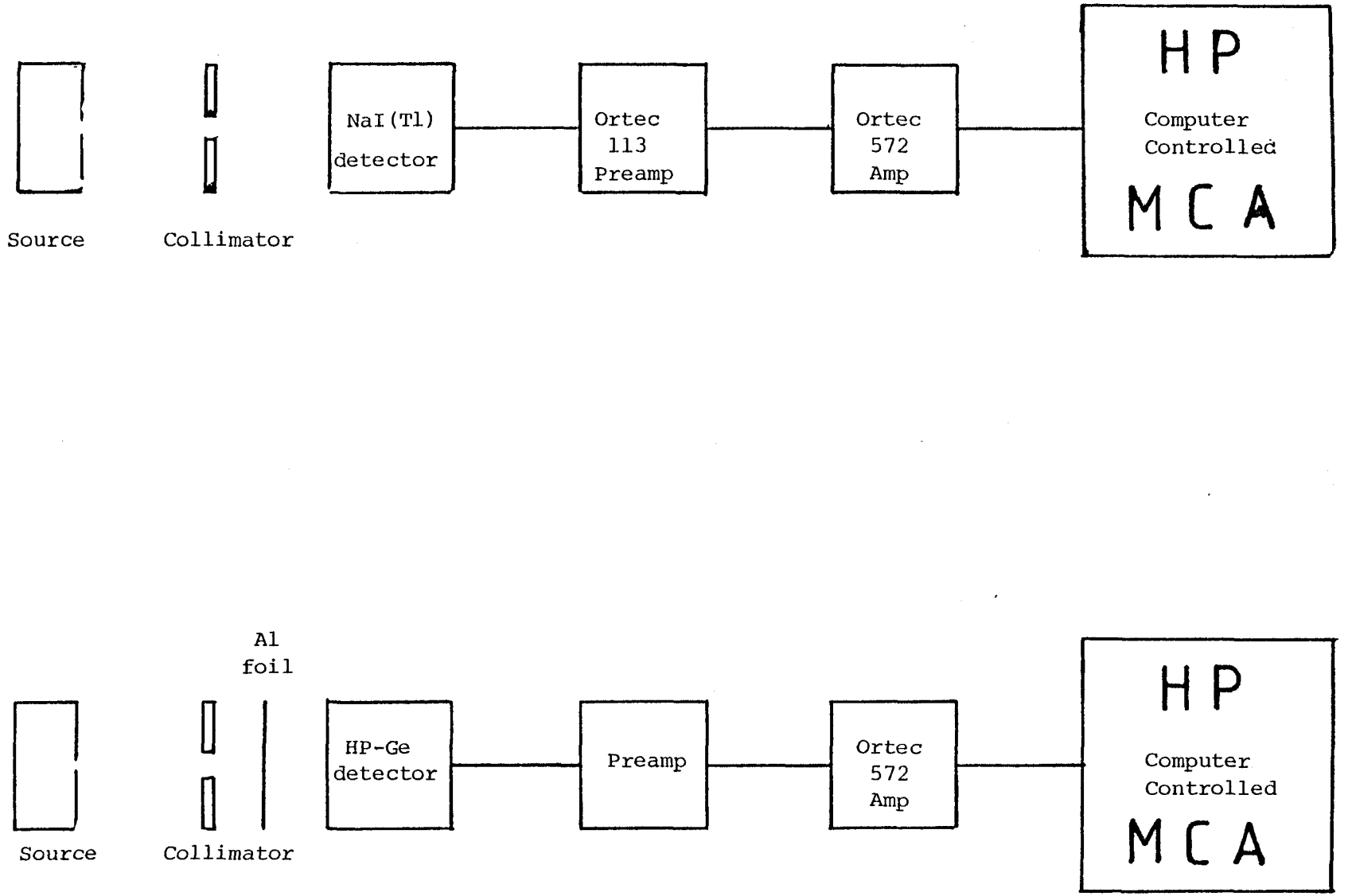

Fig. 4.5 The experimental arrangement of the HP-Ge and NaI(TL) detector with their associated electronics used for the relative efficiency determination.

4.3.2 Results and Discussion

Figures 4.6 and 4.7 show Ag K x-rays detected by the HP-Ge and the NaI(Tl) detectors, respectively. In the x-ray energy range (8 to 18 KeV), the NaI(Tl) spectrum is complicated compared to that from the HP-Ge detector. The number of x-rays detected by the HP-Ge detector, for a given collection time were simply obtained by summing the counts under the characteristic peaks and subtracting the appropriate background, assumed linear. The procedure was somewhat more complicated in the case of NaI(Tl) spectra. The K_α and K_β components of the x-rays are not resolved by the NaI(Tl) detector. Furthermore the 26.4 KeV and 16.9 KeV iodine x-ray escape peaks resulting from the 60 KeV ^{241}Am gamma ray and its 50 KeV Compton-scattered peak and Np L X-rays with energy of nearly 17.7 Kev also contributes completely or partially to the K X-ray peak of all elements up to Mo. For the elements with the higher K X-ray energies than Mo, their photopeaks were completly separated from the iodine escape peaks. The escape peak contributions were subtracted from the x-ray peak area by using Al absorbers of thicknesses up to 10 mm. This served to prevent any of the X-rays fluorsced by the ^{241}Am source from reaching the detector. The resulting spectrum was accumulated until the peak areas under the 60 KeV photopeak plus the Compton peak were identical to those obtained in the original X-ray experiment. Hence, it was now possible to determine the iodine escape peak contributions from the ^{241}Am source alone to the 26.4 and 16.4 KeV escape peaks. The contribution of the escape peak to the photopeak, however, cannot be removed completely by this method, with consequent large increase in the uncertainties of the results. Therefore, we have not used the data for elements prior to Ag obtained by this method. Counting times varied from 15 to 30 minutes and the statistical uncertainties were about 1% . The uncertainty in the detector solid

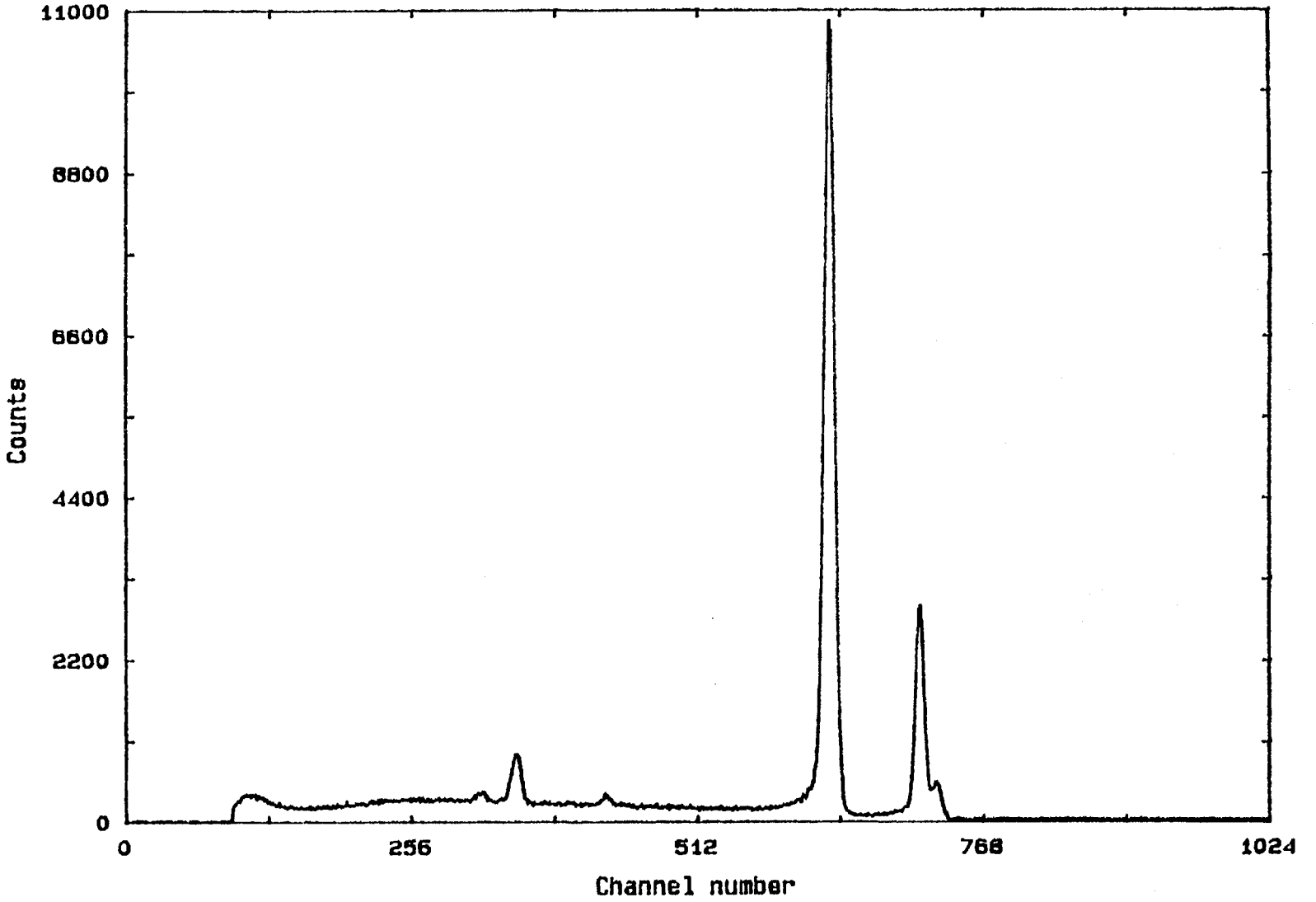

Fig. 4.6 The spectrum of Ag K X-rays obtained with the HP-Ge detector.

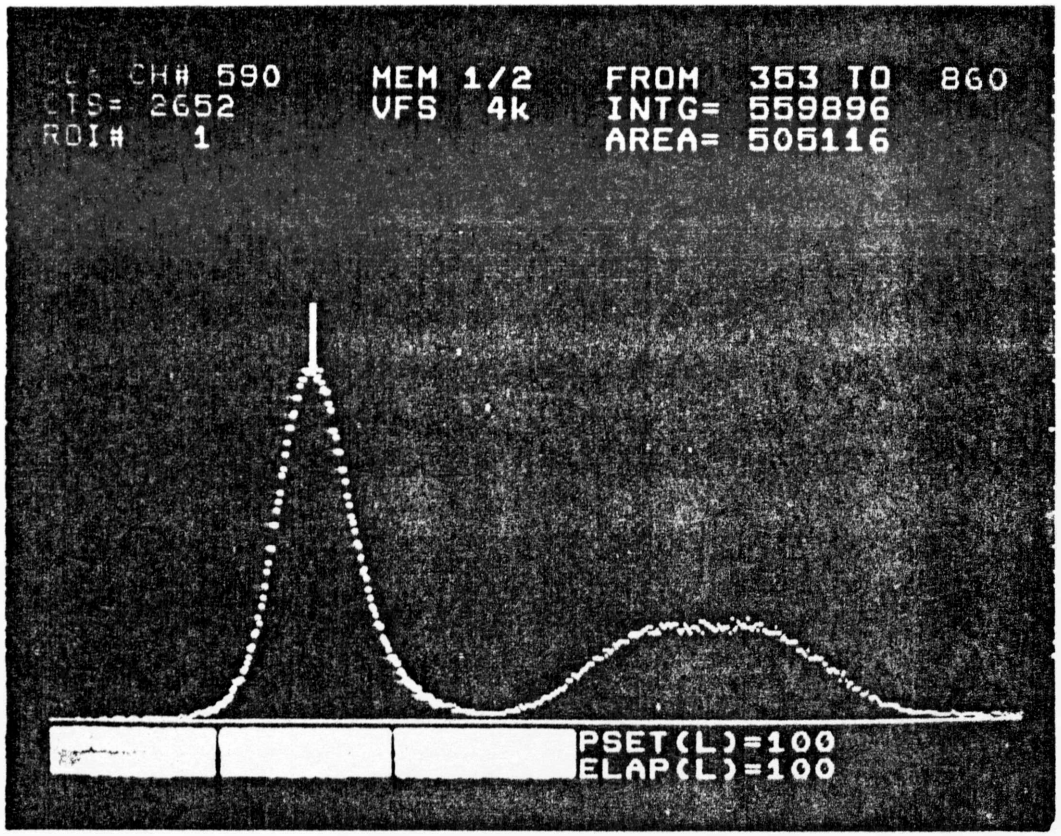

Fig. 4.7 The same spectrum obtained with the NaI(Tl) detector.

Table 4.7

The X-ray sources and their weighted K X-ray energies

Source	Weighted X X-rays Energy* (KeV)
Cu	8.136
Rb	13.596
Mo	17.781
Ag	22.581
Ba	32.89
Tb	45.469

* Storm and Israel

angle was about 2% . The efficiency of the HP-Ge detector, ϵ_{Ge} can be determined from the expression

$$\epsilon_{Ge} = \frac{Y_{Ge}}{Y_{NaI}} \cdot \frac{\Omega_{NaI}}{\Omega_{Ge}} \cdot \frac{\exp[-\mu/\rho(\rho t)]^{NaI}_{air}}{\exp[-\mu/\rho(\rho t)]^{Ge}_{air}} \qquad 4.2$$

where

Y_{Ge} and Y_{NaI} are the photon fluxes detected by the HP-Ge and NaI(Tl) detectors respectively; the exponential terms represent the correction for absorption by air for both detectors;

t is the source -detector distance (air gap) and

Ω_{Ge} and Ω_{NaI} are the solid angles subtended by the two detectors.

The mass absorption coefficients, μ/ρ were taken from Storm and Israel[6]. The uncertainties in the value of μ/ρ is 3% . the total uncertainty in the efficiency calculations were in the range 3 to 4% . The intrinsic efficiency of the HP-Ge detector determined by this method is shown in Fig 4.8.

4.4 A Comparative Study of a Harwell and a Parallel Plate Fission Chamber

For determining high neutron fluxes the fission chamber is an eminently suitable detector because it does not easily saturate, unlike other detectors (e.g. long counters). Therefore, it provides the possibility of measuring absolute fission yields for radionuclides. We have studied the behaviour of a parallel plate, pulse fission chamber and compared it to the Harwell fission chamber, which was used as an absolute standard. The purpose of these experimental studies was to investigate the possible application of the Parallel Plate Chamber (PPC) for absolute fission yield

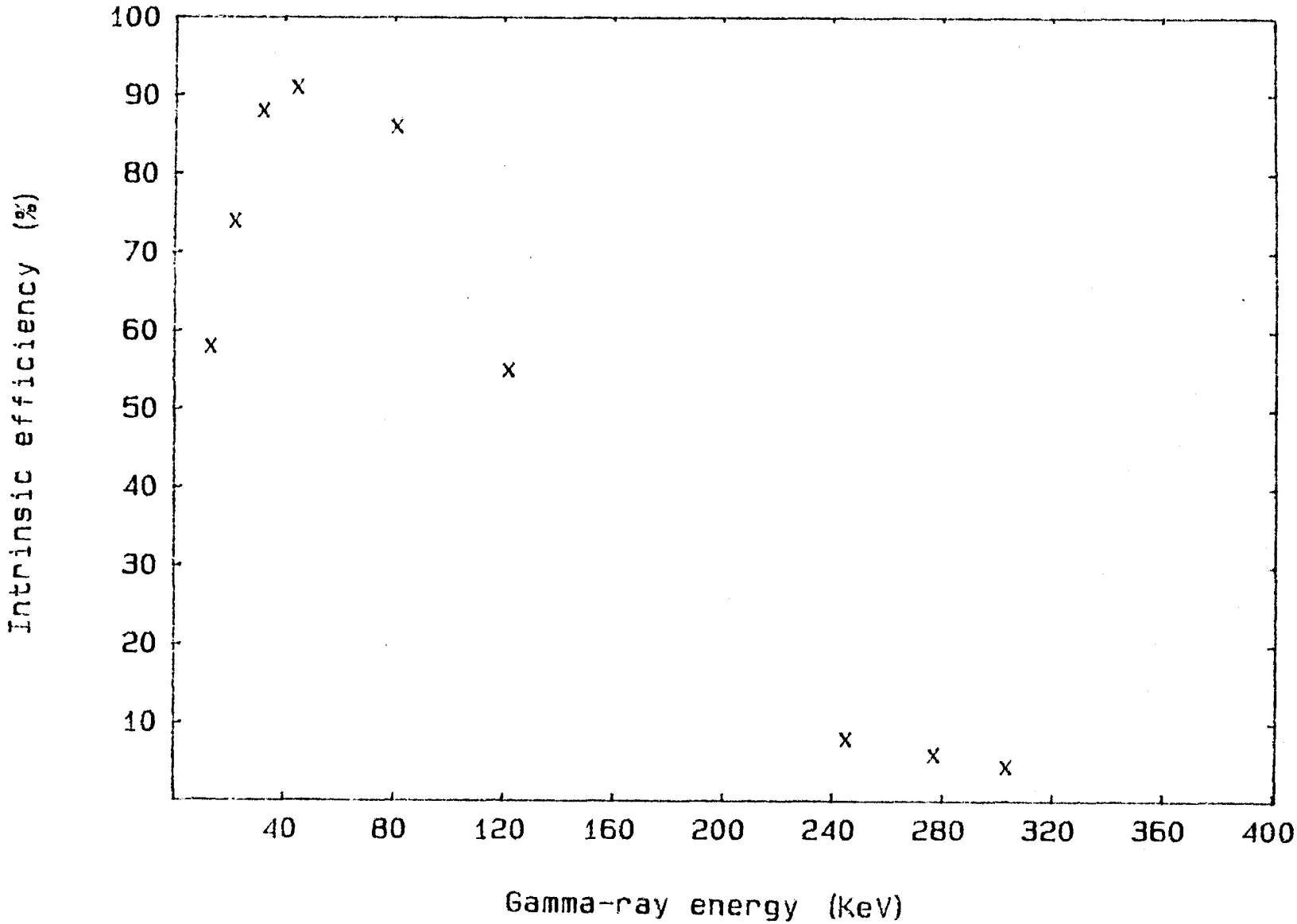

Fig. 4.8 The intrinsic efficiency of the small HP-Ge obtained by the comparison technique relative to NaI(Tl).

measurements.

4.4.1 The Parallel Plate Chamber

The parallel plate fission chamber (PPC) used in this experiment was a type PFC 16B/1000/ ^{238}U , from 20th Century Electronics. This chamber had a fissile foil diameter of 44.5 mm and the weight of fissile material was 15.52 mg with an isotopic composition of 99.96% uranium-238 and .04% uranium-235. Fig 4.9 is a diagram of the construction of the chamber. It had an external diameter of 66.5 mm and was 19.0 mm deep, with a nominal sensitive area of 16 cm. The latter consisted of one uranium oxide-coated electrode with a surface density equivalent to 1000 $\mu g/cm^2$ of uranium metal[8]. The coating was specified by the manufacturer as being 'reasonably uniform', having been formed by 10-20 individual depositions of thinner oxide coats. The manufacturer's specifications assumes a 100% pulse collection efficiency for the PPC fission chamber, but it needed to be confirmed. The necessity for this arose from the possibility of a thick coating of oxide causing a less than 100% efficiency of the detector due to fission events deep within the uranium deposit which either give rise to pulses severely attenuated (and thus undistingushable from alpha events) or which do not produce a pulse at all, owing to complete absorption of the fission fragments within the deposit. Some uncertainty also arose as to whether the fissionable mass content specifications referred to the mass of oxide or the equivalent mass of uranium metal. Additional uncertainty was present in the optimum discrimination level to be used, due to incomplete separation of pulses arising from alpha decay and those arising from attenuated fission fragment ionisation, caused by the finite thickness of the oxide coating.

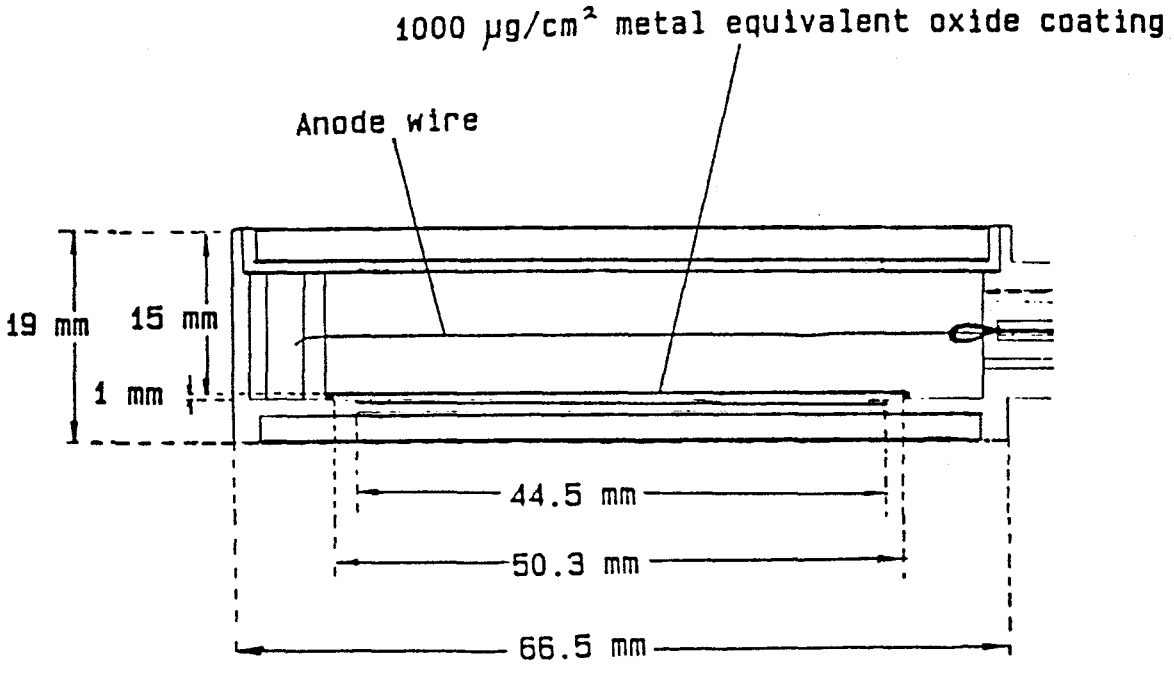

Fig. 4.9 The design of the PPC fission chamber.

4.4.2 The Harwell Fission Chamber

This was constructed as shown in Fig 4.10 at Harwell. It has a total, fissionable mass of 63.7±1.3 μg, consisting of a deposit of 99.999% ^{238}U painted on to a .127 mm thick, platinum plate located on the inside surface of the chamber wall. The deposit had a diameter of 10.03 mm. This detector was a standard, parallel-plate ionisation chamber made from 1 mm thick stainless steel and with a plate separation of 9.5 mm to discriminate against alpha particles. The chamber was operated with a continuous flow of P-10 gas (90% argon, 10% methane). The fissile deposit was prepared and its mass assayed in the Chemistry Division, Harwell. The deposit mass was determined by alpha-counting in 2π-geometry with a calibrated ion chamber. The following corrections were necessary to the results obtained by this chamber:

(i) loss of fragments in the fissile deposit (0.6 %) and

(ii) loss of events below the pulse height discriminator level (0.5%).

The counting efficiency of the fission chamber with the ^{238}U deposit was calibrated against its efficiency with a ^{235}U deposit and was found to be about 100±0.8 %[9].

4.4.3 Investigation of the Response of the PPC

Measurements with the PPC fission chamber used a Canberra 200E preamplifier, a type specifically designed for use with fission chambers, and an Ortec 572, spectroscopy amplifier with suitably chosen gain and time constant settings. In measurements with the Harwell chamber an Ortec 142B preamplifier and an Ortec 460 delay amplifier were used.

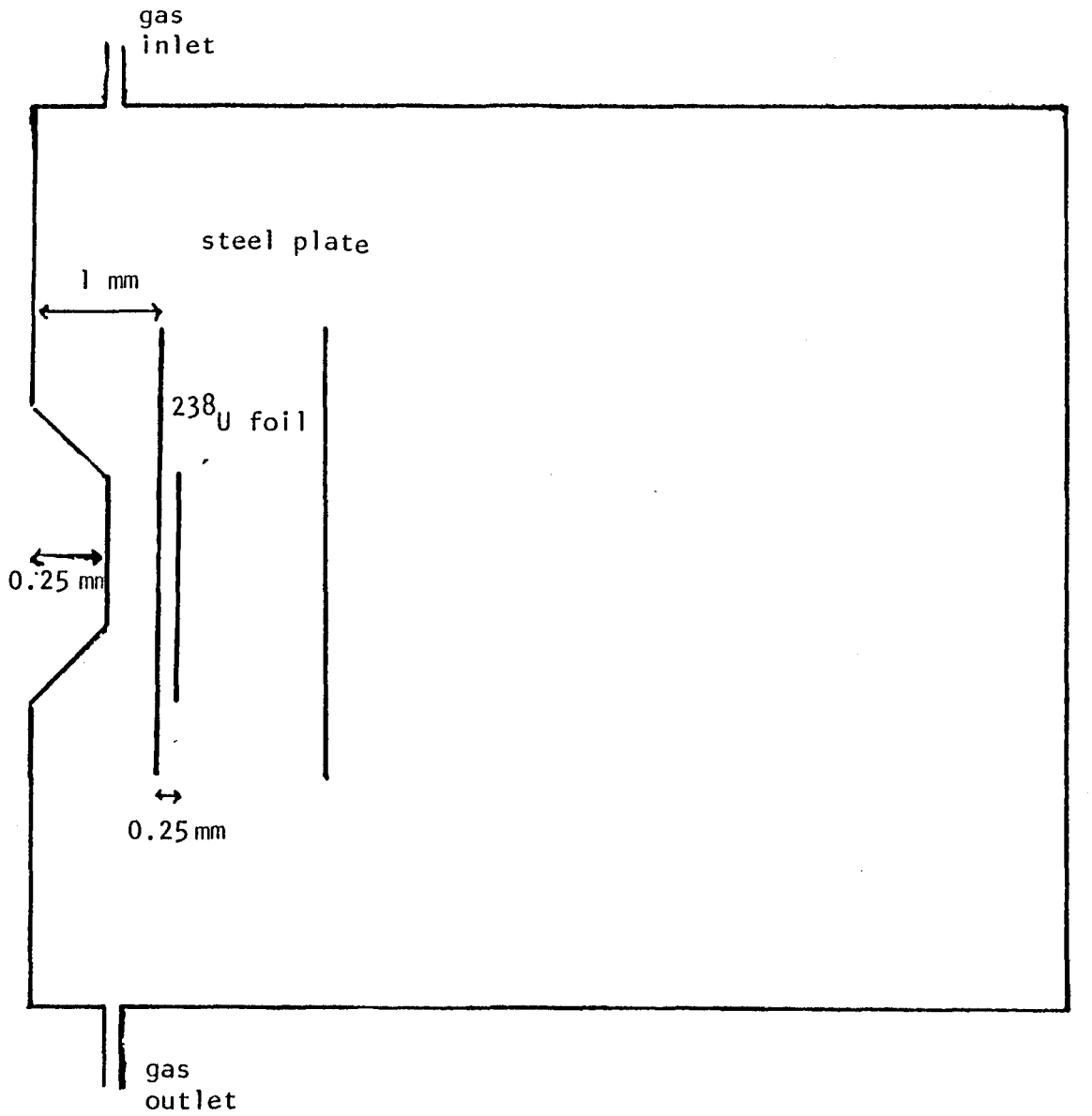

Fig. 4.10. Schematic diagram of Harwell fission chamber.

The lower, discriminiation-level cut-off against pulses from alpha-particle emission was taken close to the centre of the dip between the main fission pulse distribution and the alpha-particle pulse distribution (Fig 4.11a and 4.11b). The total fission events from the chamber, produced as a result of neutron interactions were collected over 1024 channels, using the H-P counting system. In addition, they were simultaneously counted by a scalar. Neutrons used in this comparative experiment were produced via the $^{2}H(d,n)^{3}He$ reaction, using the Dynamitron accelerator in the Department of Physics Radiation Centre.

4.4.4 Results

The meaurements were made for each fission chamber at various distances from the deuterium target in the 0^{o} direction. This gave the maximum neutron flux and also avoided employing geometrical correction factors. It was informative to study the response of the PPC as a function of neutron flux. The chamber was exposed to different fluxes of neutrons by varying the particle beam current in the range 10 - 200 μA (neutron fluxes in the range 3.2×10^{6} to 6.4×10^{7} n/cm^{2}/sec.). The results obtained are shown in Fig. 4.12. As can be seen, the fission count per unit charge was constant over this range of beam currents. The response of the chamber as a function of distance from the target for two different beam currents is shown in Fig. 4.13. This shows that a similar response was obtained for both the beam currents. In order to determine the detection efficiency of the PPC, both "activation" and "comparison" techniques were employed. Fig. 4.14 shows the response of the Harwell chamber as a function of its distance from neutron target. As can be seen from the figures 4.12 to 4.14 the behaviour of both chambers are highly linear.

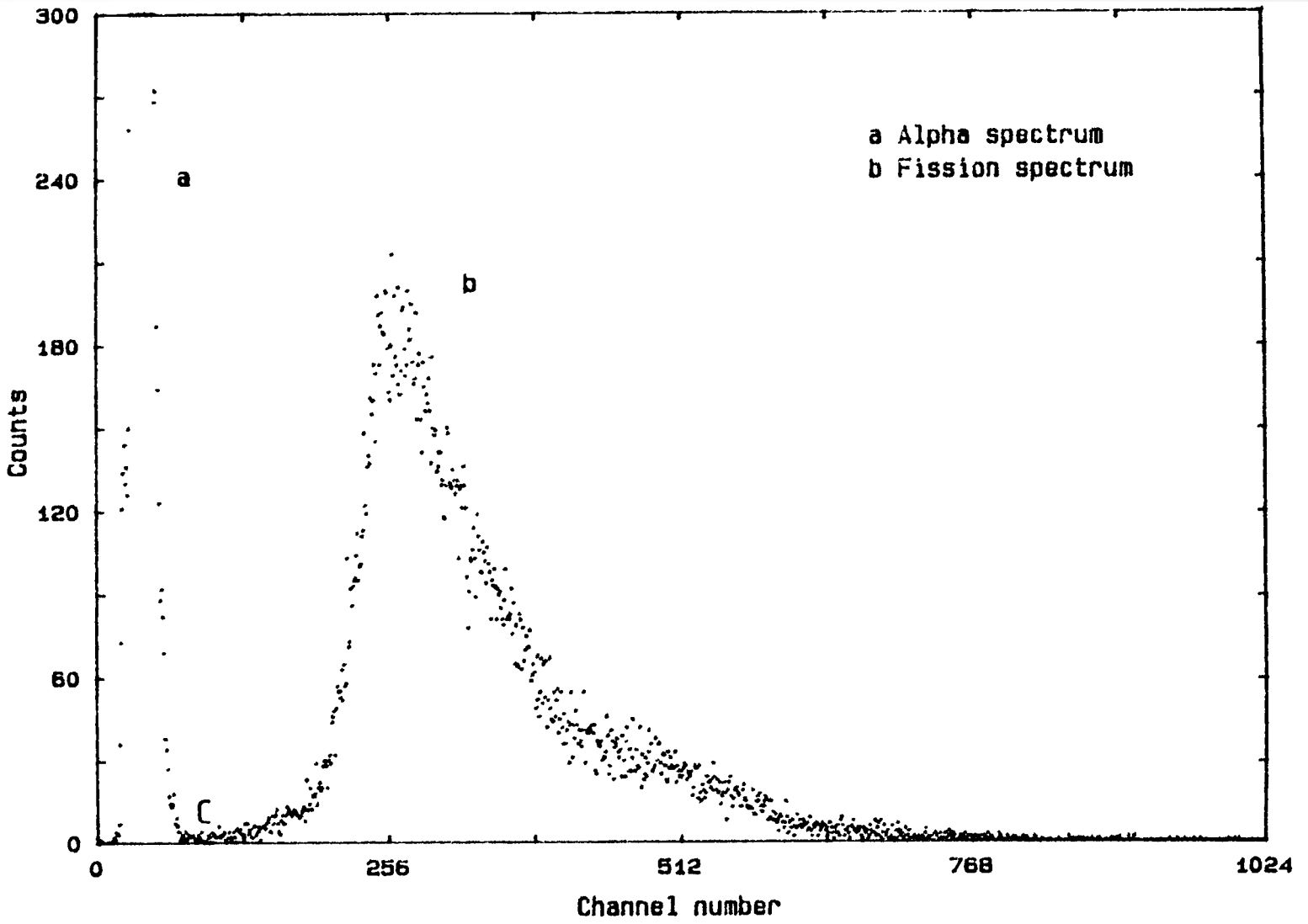

Fig. 4.11 A typical spectrum obtained with the fission chamber, showing the alpha-particle peak (a) and the fission spectrum (b). The cut-off by the lower level discriminator is shown at C.

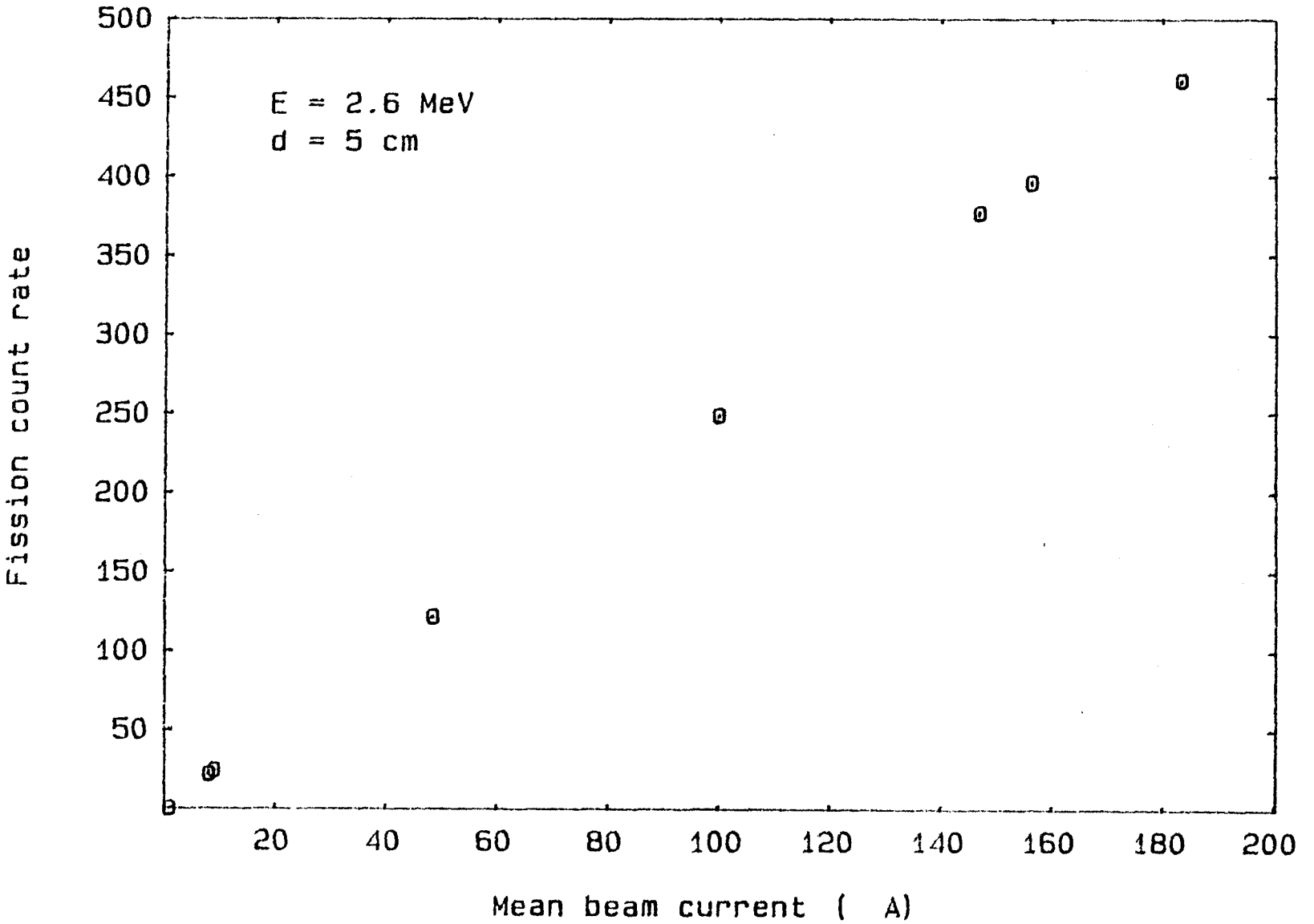

Fig. 4.12 The PPC fission chamber response versus mean beam current (neutron flux).

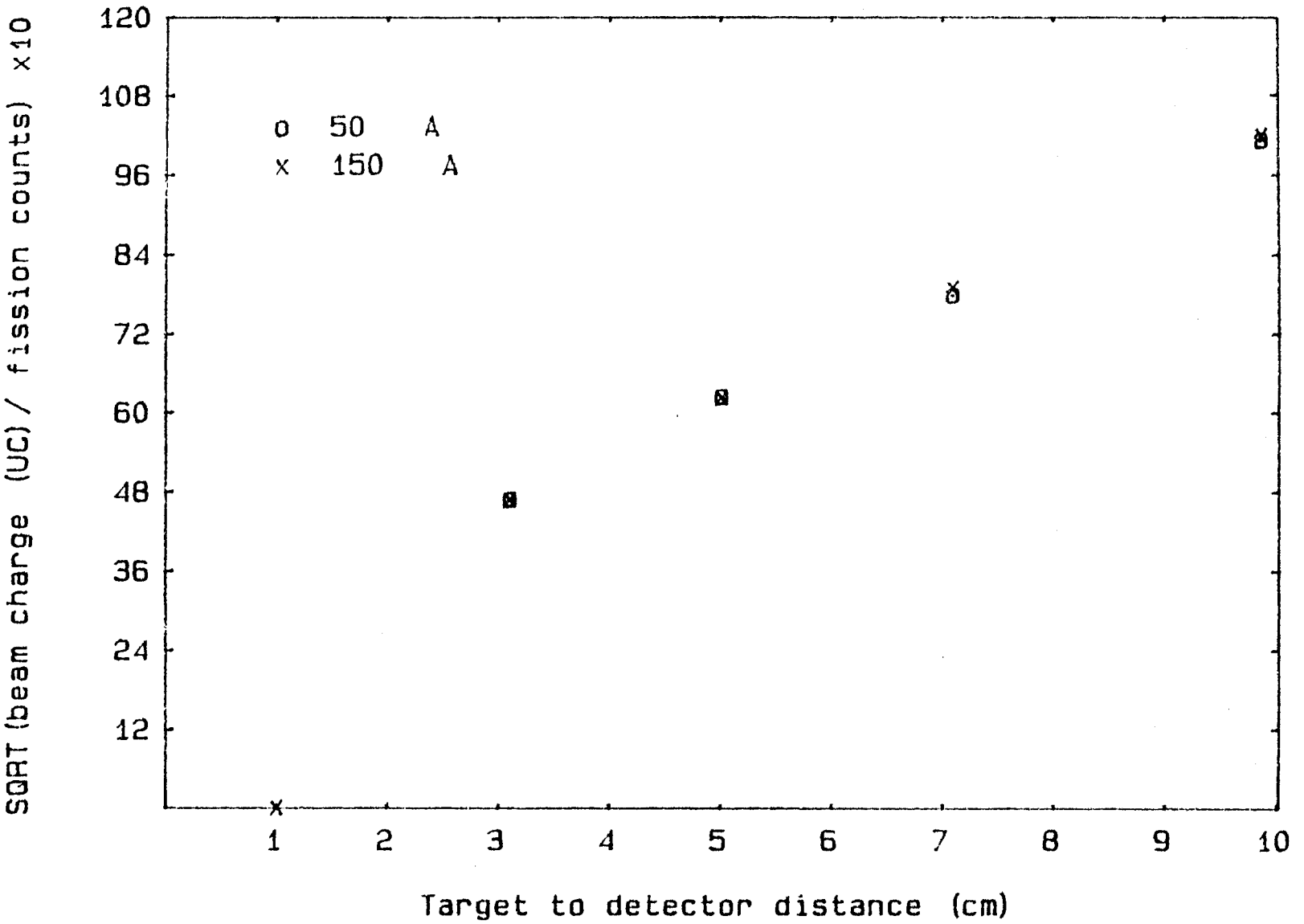

Fig. 4.13 The response of the PPC fission chamber as a function of its distance from the target in the 0^{o} direction, for two different beam currents.

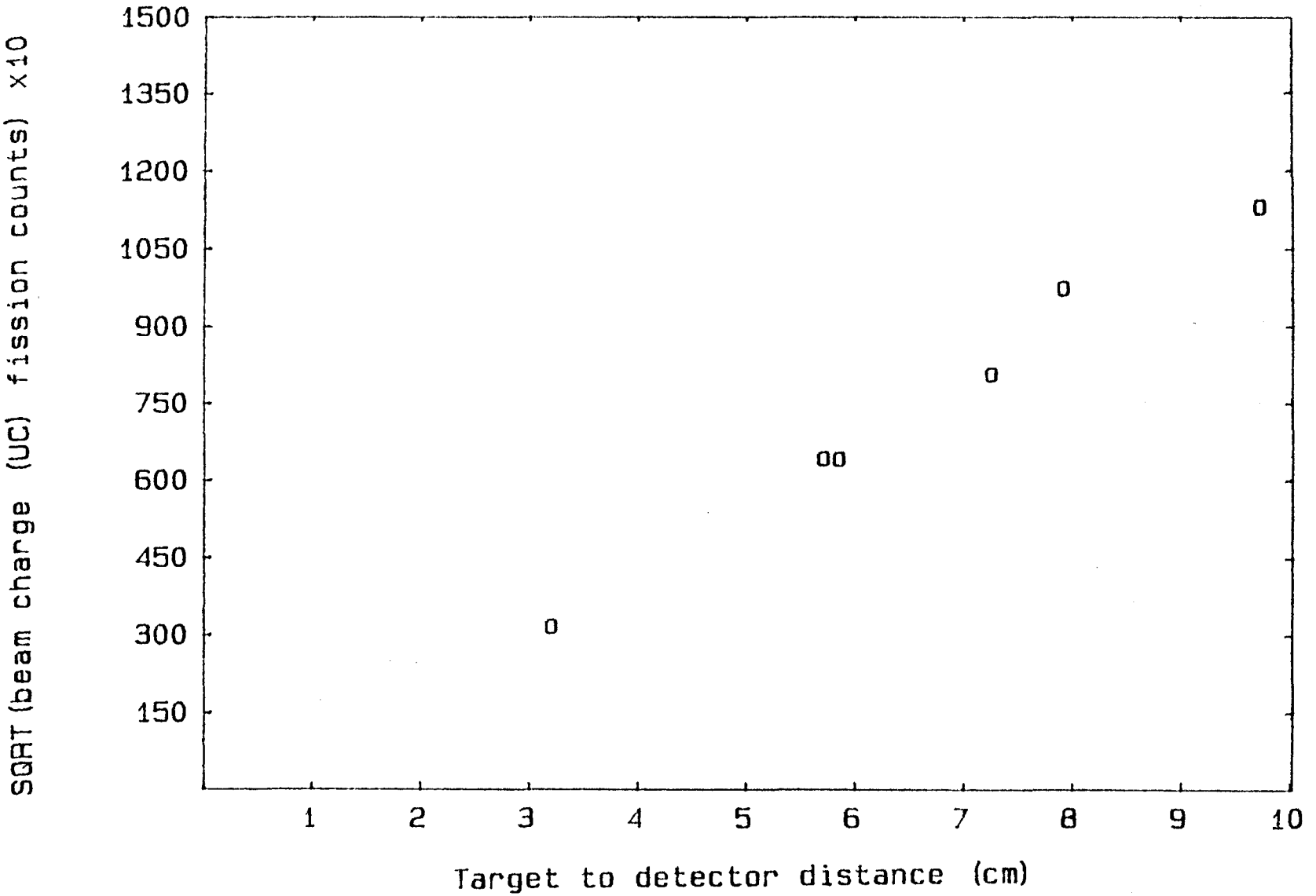

Fig. 4.14 The response of the Harwell fission chamber as a function of its distance from the neutron target.

4.4.4.1 Determination of the Efficiency of the PPC

a) Comparison Method

In this method, the efficiency of the PPC was determined by comparing it with the efficiency of the calibrated Harwell chamber. In order to be sure that the relation between integrated current and neutron yield was constant, a small fission chamber was placed at a fixed angle of 90° to the beam axis and about 10 cm from the target, to act as a relative flux monitor (see Fig. 4.15). Both calibrated and uncalibrated chambers were then irradiated for a fixed number of counts of the small flux monitor chamber which led to more accurate results. It was found that the plot of integrated current versus fission counts for small chamber was quite linear. Therefore, the fission counts per unit charge were calculated from the curve for both the PPC and the Harwell chambers . The efficiency of the PPC, ϵ_u, was determined from the following relationship

$$\epsilon_u = \epsilon_{cal} \cdot (M_{cal}/M_u) \cdot (Y_u/Y_{cal}) \cdot K \qquad 4.3$$

where

ϵ_{cal} is the efficiency of the calibrated chamber

M_{cal}, M_u are the masses of the fissile material in the calibrated chamber and the PPC respectively.

Y_{cal}, Y_u are the total counts per unit charge at a given distance for the calibrated chamber and the PPC, respectively.

K is the geometrical correction factor for the PPC, taking into account the large area of the fission foil compared to that in the calibrated chamber.

A computer program, SCDDFLX, written in Basic was used to calculate this correction[10]. By supplying the value of parameter in equation 4.3 the ϵ of PPC was found to be .98±.03. The biggest uncertainty in

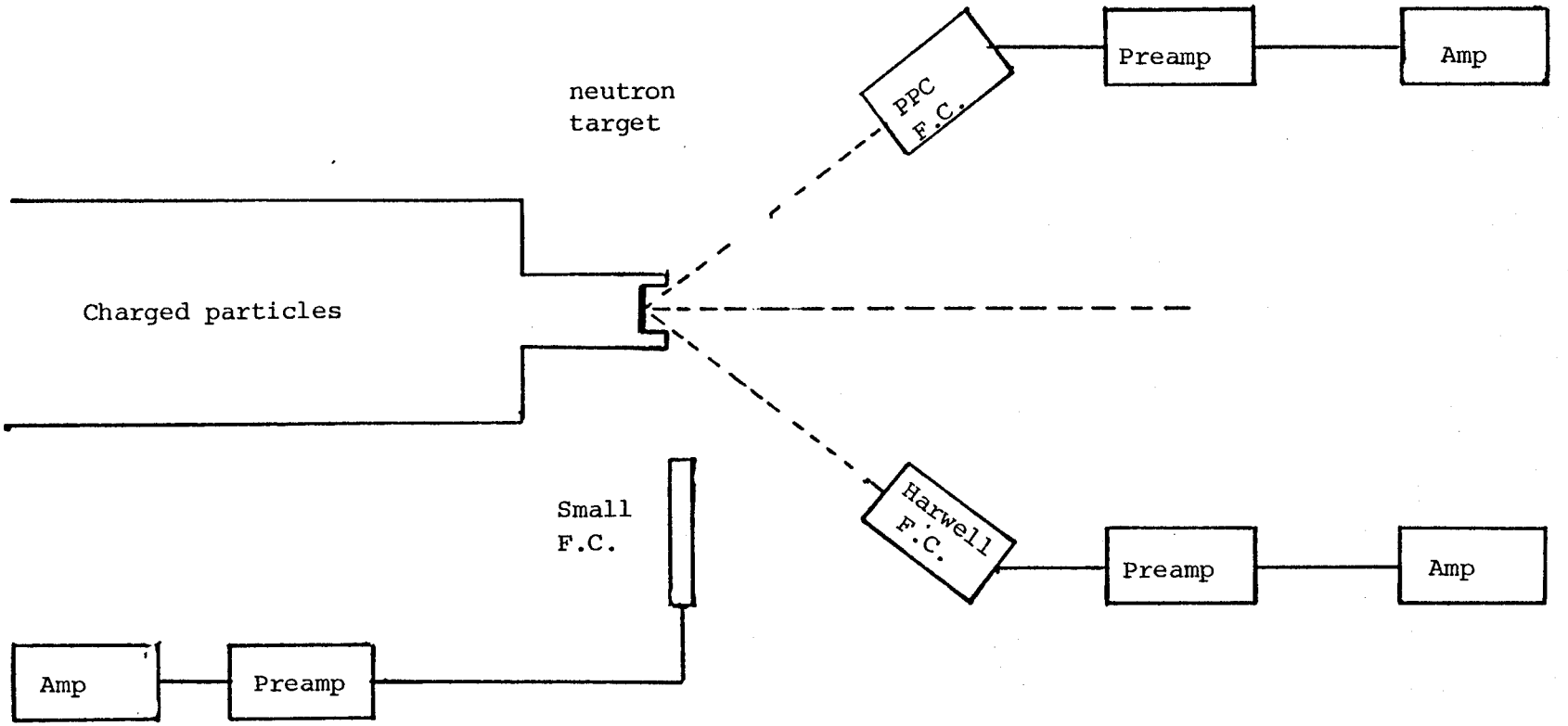

Fig. 4.15 Experimental arrangement for the calibration of the PPC against the Harwell fission chamber.

this calculation was 3% due to mass of calibrated chamber. The actual mass of PPC obtained to be 15.20±.46 by product of ϵ_u at nominal mass of chamber.

b) Activation Foil Technique

In order to check the efficiency of the PPC as a function of neutron energy, In foils were placed in contact with the chamber in a central position. These foils where 75 μm thick and 10 mm diameter and were irradiated with fast neutrons. The reaction used was $^{115}In(n,n')^{115m}In$. ^{115m}In has a half-life of 4.486h and emits a gamma ray of energy 336 KeV. Hence, the 336 KeV photo peak was measured using a HP-Ge detector and the peak area calculated using the computer program SAMPO80[11]. The neutron flux, Φ_{foil}, was calculated from the measured activity in the usual way[12], using published values for the reaction cross section[13]. The flux, $\Phi_{F.C.}$, from the fission count rate in the fission chamber was calculated using the relationship

$$\Phi_{F.C.} = F/\sigma.N$$

where

σ is the fission cross section for ^{238}U at the given neutron energy,

N is the number of atoms of ^{238}U and

F is the fission count rate.

In order to determine the response of the PPC as a function of neutron energy and hence obtain an efficiency value, it was necessary to determine the ratio, R, of the fluxes obtained by the indium foil and PPC i.e. $\Phi_{F.C.}/\Phi_{foil}$. This ratio was plotted as a function of neutron energy and is shown in Fig. 4.16.

Since the In foils had a much smaller area than the fission foil in

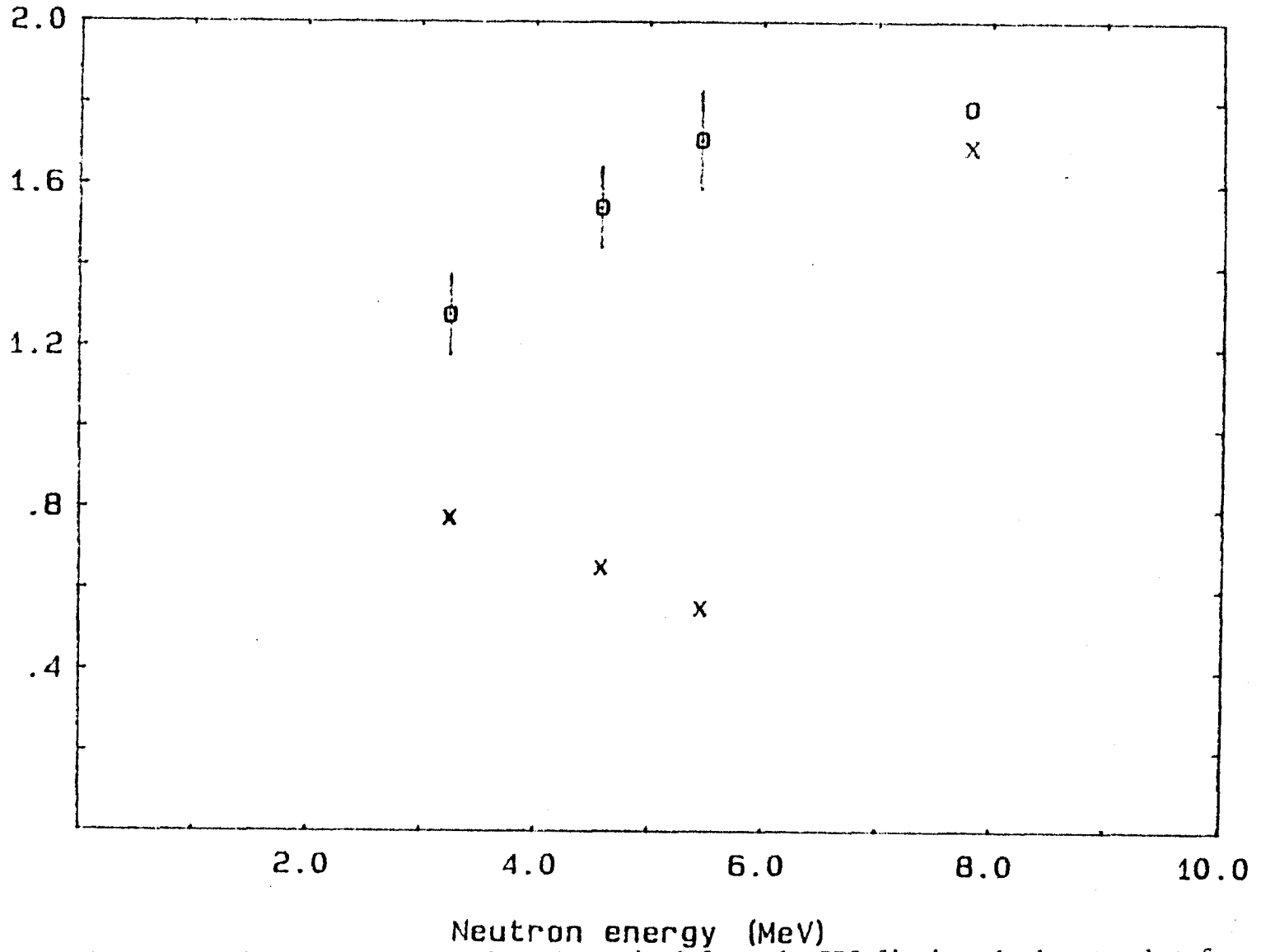

Fig. 4.16 (a) The ratio of the neutron flux determined from the PPC fission chamber to that from the indium foils as a function of the neutron energy (b) the geometry correction as a function of the neutron energy.

the PPC, they will not give the same response even for a monoenergetic neutron source.

In order to obtain the efficiency of the chamber one must correct for the diffrent geometries of the In and fission foils. The efficiency, ϵ, of the chamber is given by

$$\epsilon = R.K$$

where K is the geometry correction and described in section 4.4.4.1 (a). This geometry correction for different neutron energies is also plotted in Fig. 4.16.

The response of the PPC was also checked by irradiating a series of foils arranged across the diameter of the chamber. The foils were then removed and counted and the corresponding fluxes determined. In this way flux variations across the diameter of the chamber were determined to be 32% flux reduction from centre of chamber to the place very close to outer edge of ^{238}U foil. The variation of the response of the PPC fission chamber over the surface of the large fission foil was investigated for neutrons produced from deuterons in the energy range 2.5 - 2.75 MeV bombardment of a thick beryllium target. This response was determined by comparison with a small fission chamber having a diameter of about 0.635 cm and active length of 2.49 cm (Centronics FC4A). The small fission chamber placed as close to the surface of the PPC as possible and perpendicular to the face as shown in Fig. 4.17. This small chamber could be scanned across the face of the PPC in steps of 0.5 cm by being fixed to a holder located on the sample table of a microprocessor -controlled, stepping motor driven X-Y table (see Fig. 4.18) which was controlled from outside the beam room. The results obtained are shown in Figs. 4.19 and 4.20. Due to the polyenergetic neutron output of the Be target only a few percent variation in the flux distribution was found on moving from the centre of the PPC to the outer edge. The variation, however, is more obvious for 2.75 MeV deuterons than for 2.5 MeV. This

Fig. 4.17 Experimental arrangement of PPC and small fission chamber (FC4A) during bombardment of deuterium with a thick Be target

(a) Be target

(b) PPC

(c) FC4A.

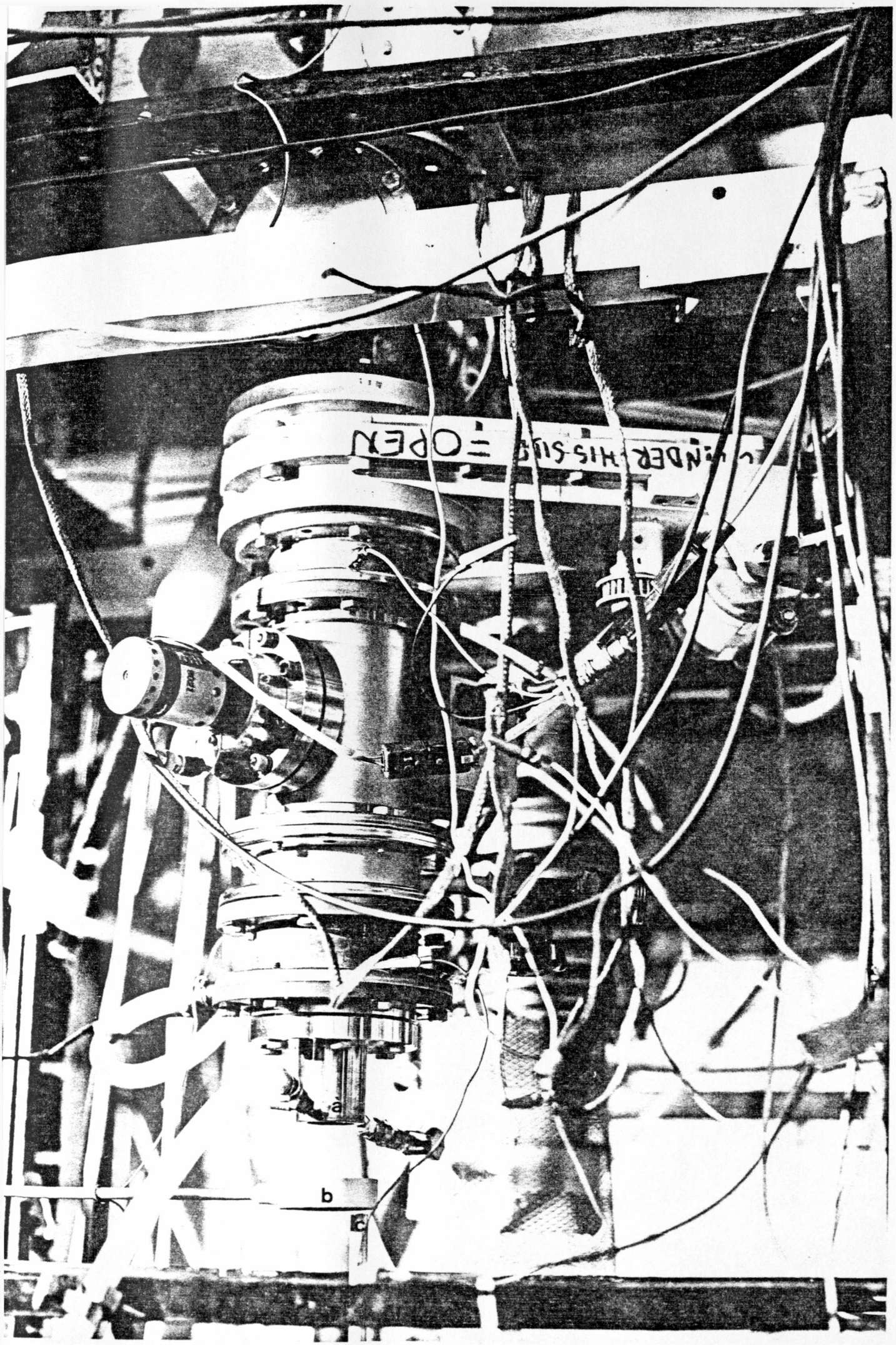
a
b
c

Fig. 4.18 Photograph of microprocessor-controlled, stepping motor driven X-Y table

(a) sample table

(b) stepping motor

(c) detector holder.

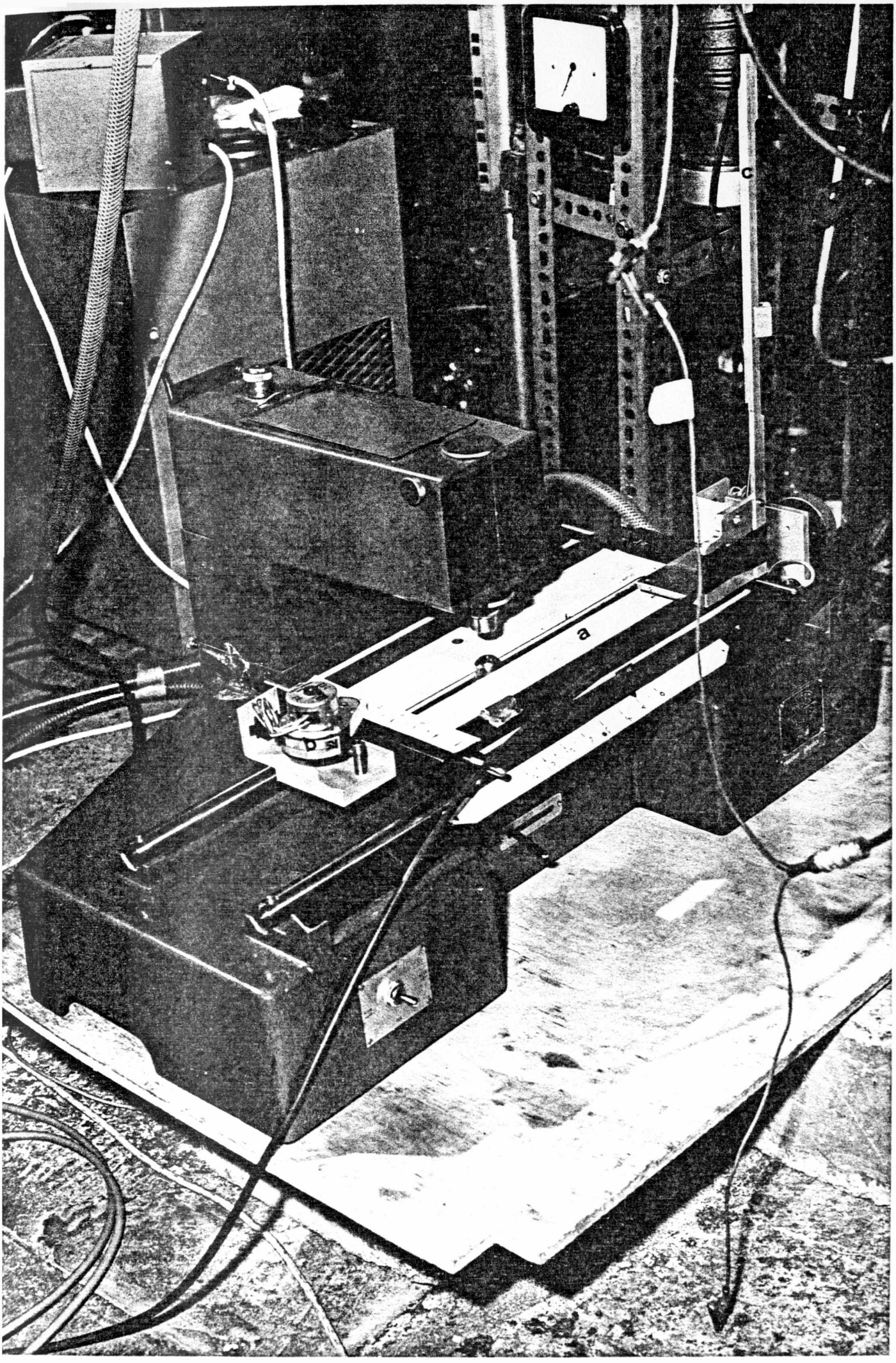
a
c

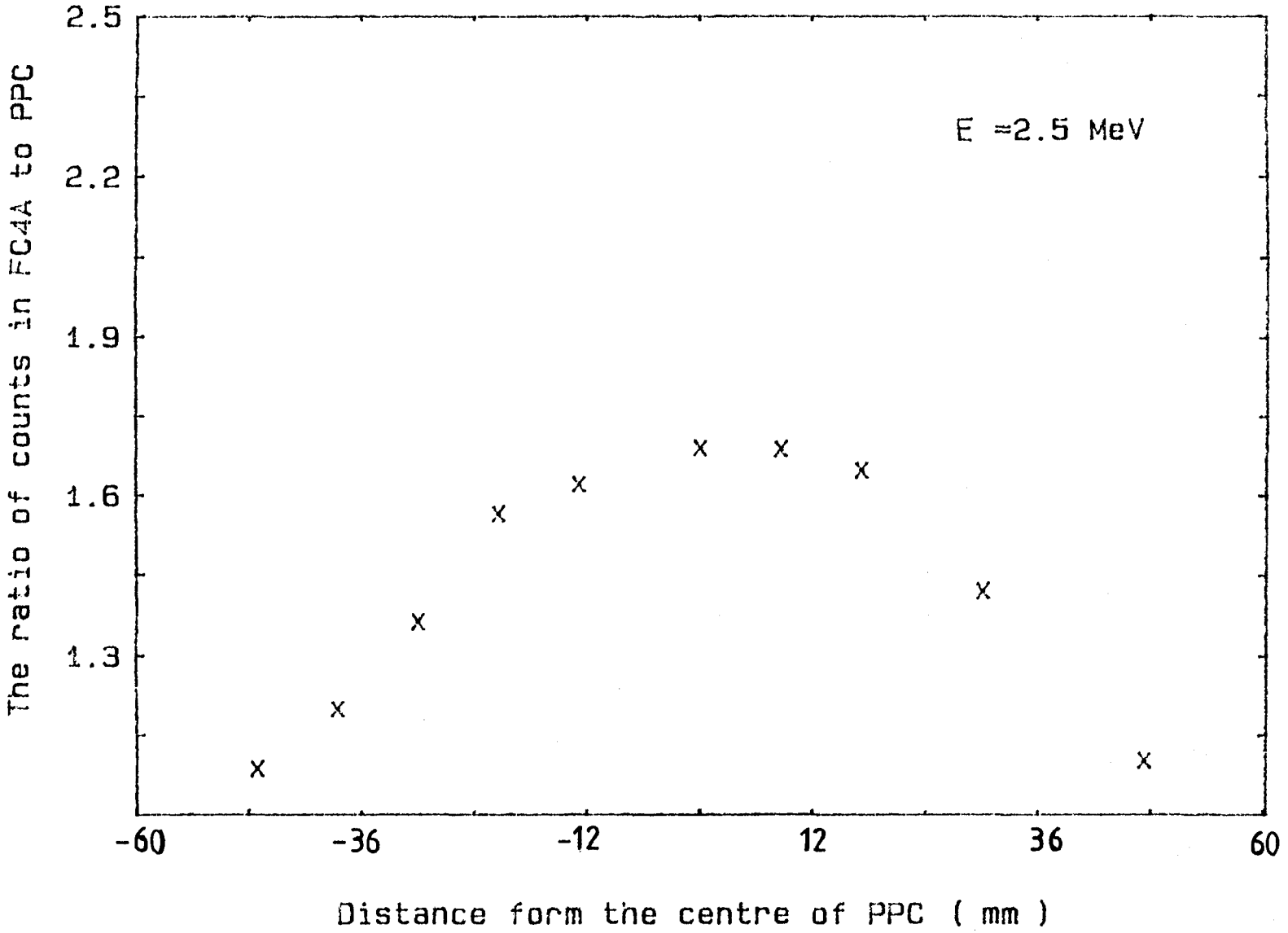

Fig. 4.19 The response of FC4A to PPC fission chamber from neutrons produced by bombardment of 2.5 MeV deuterium on a thick Be target.

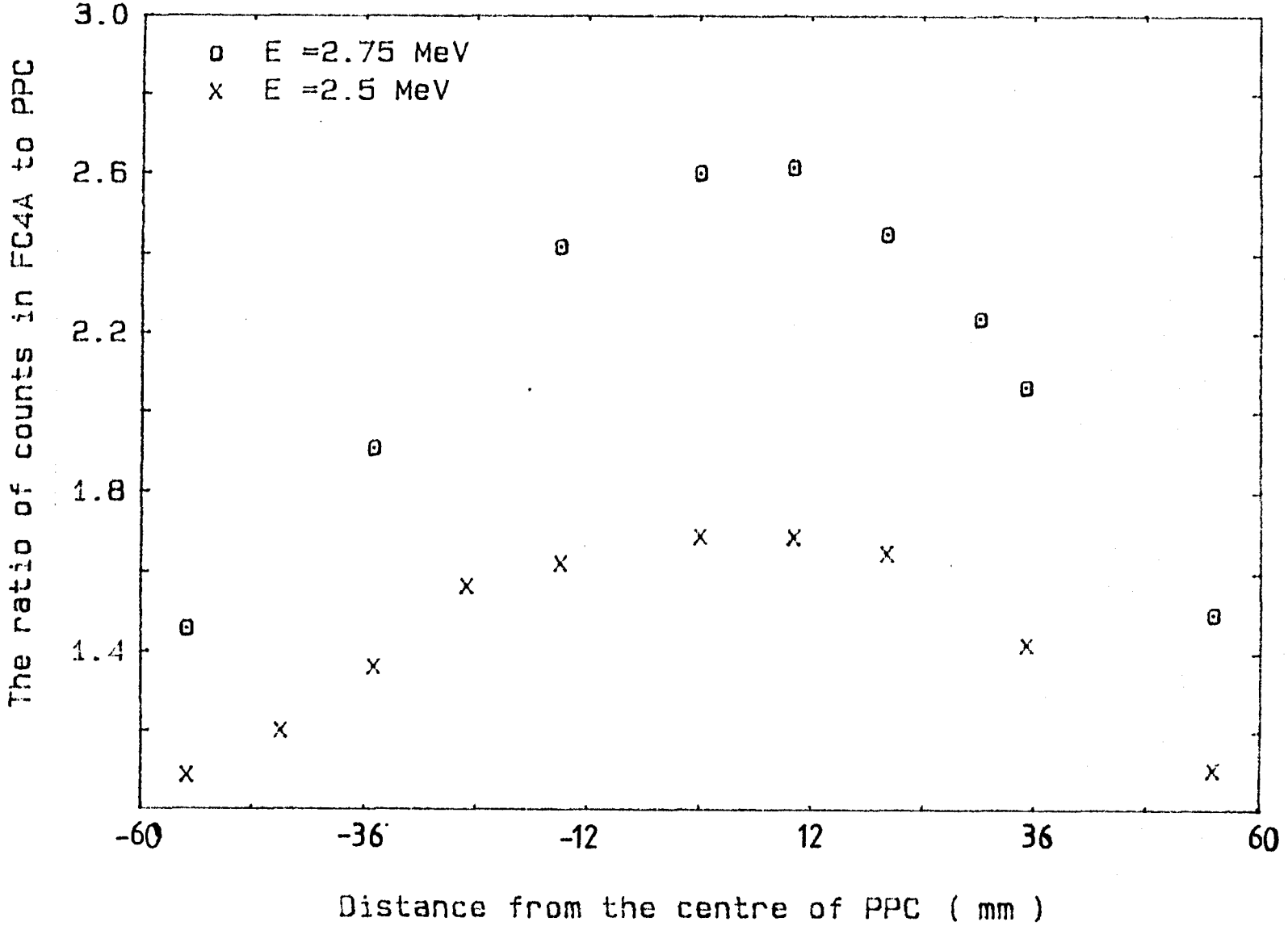

Fig. 4.20 Same as Fig. 4.19 but for 2.5 and 2.75 MeV.

is because the neutrons are more forward peaked in energy distribution at the higher, incident deuteron energy. A similar set of results were obtained by replacing the small chamber with indium activation foils. The results from the foil experiments are shown in Figs. 4.21 and 4.22 for the same incident deuteron energies.

References:

1- Gehrke R.J., R.G. Helmer and R.C. Greenwood, Nucl. Instr. and Meth. 147,405 (1977)

2- Iwata Y., M.Yasuhara, K.Maeda and Y. Yoshizawa, Nucl. Instr. and Meth. 219, 123 (1984)

3- Debertin K., Nucl. Instr. and Meth. 158,479 (1979)

4- Tables of isotopes, seventh edition, edited by C.Michael Lederer and V.S. Shirley published by J. Wiley and sons, Inc., New York, (1978)

5- Marquardt D.W., J. Soc. Ind. Appl. Math., 11, 431 (1963)

6- Storm E. and H.I. Israel, Nuclear Data Tables A7, 565 (1970).

7- Bicron NaI(Tl) scintillator detectors editted by J.O. Bellian and R.Dayton, Pub. Bicron Inc.

8-Mobbs D.J., Technical Manager, Nuclear Division Centronic Limited, Private communication.

9- Gayther D.B., M.F. Murphy, K. Randle, W.H. Taylor and C.A. Uttley, AERE Report No. AERE-R 12612, May 1987

10- Croft S., Ph.D. Thesis, Physics Department, University of Birmingham 1988.

11- Blackband J. and K. Randle, Birmingham Radiation Centre Annual Report, BRC 82/04, 72 (1982).

12- DeSoete D., R. Gijbels and J. Hoste, Neutron Activation Analysis, Wiley-Interscience, 1972.

13- Liskien H., F. Arnotle, R. Widera and A.Paulsen. Nucl. Science and Engineering 67, 334 (1978).

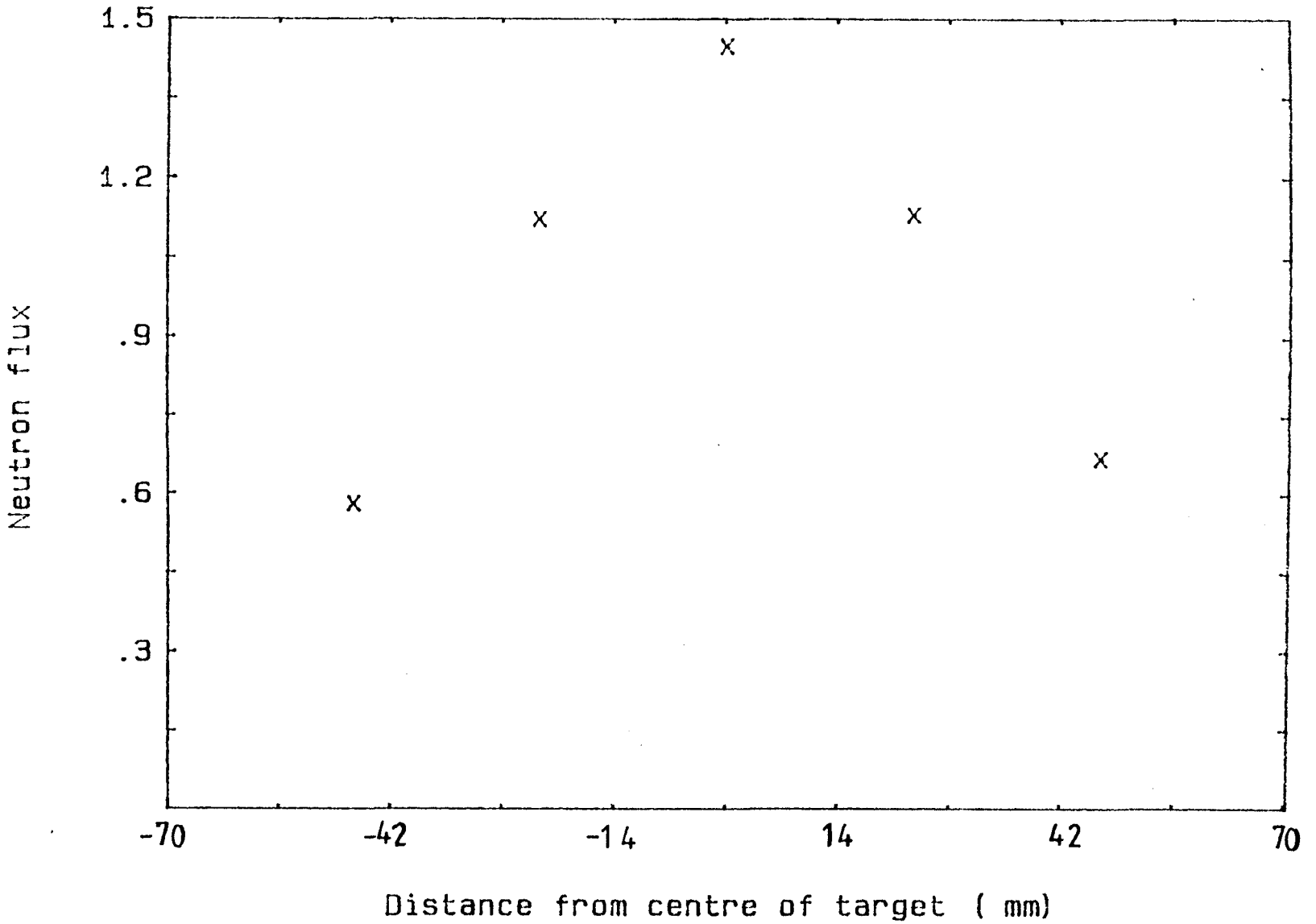

Fig. 4.21 The neutron flux distribution across the PPC produced by bombardment of 2.5 MeV deuterium on Be target.

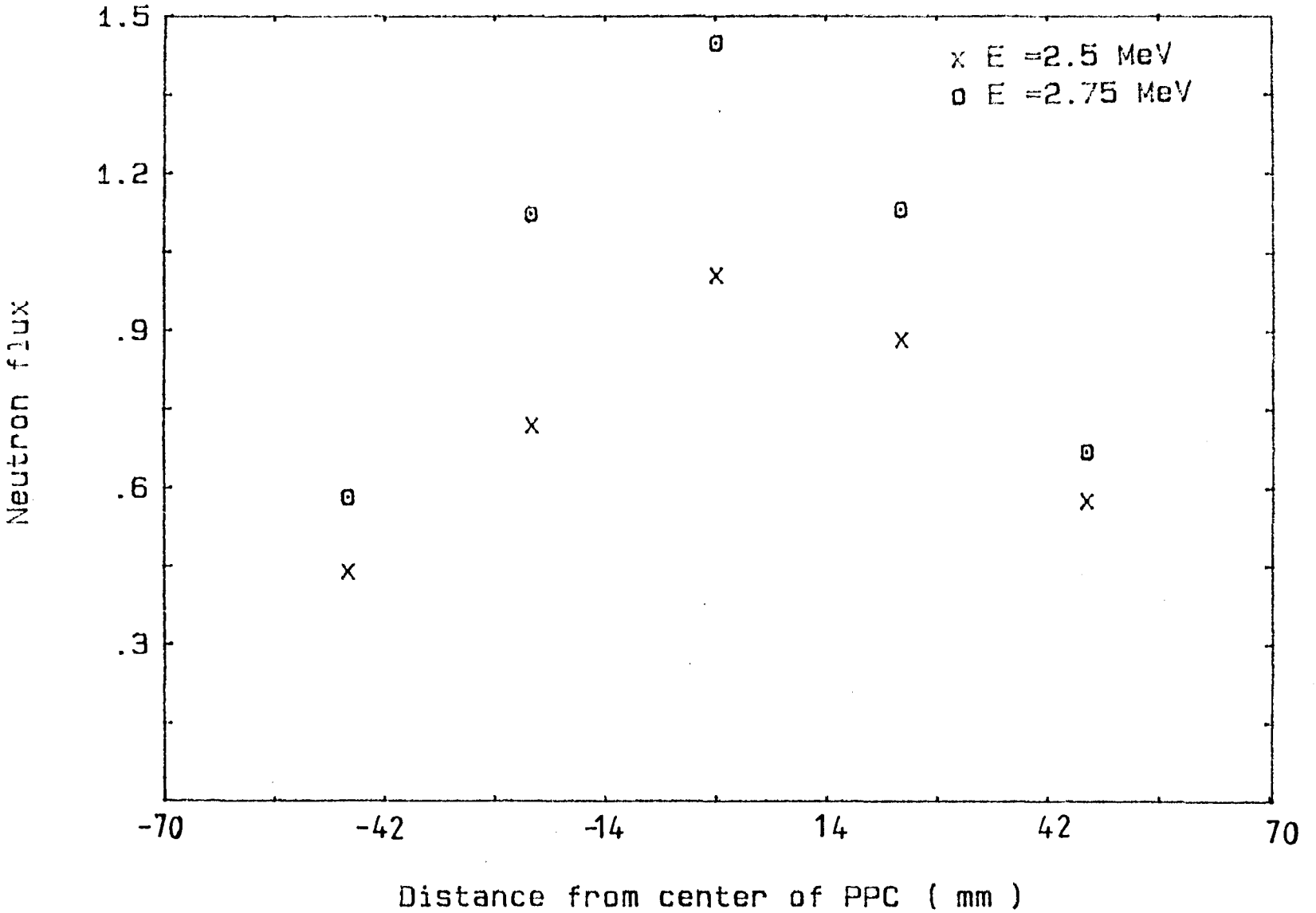

Fig. 4.22 Neutron flux distribution across the PPC fission chamber produced by 2.5 and 2.75 MeV deuterium on a thick Be target.

Chapter 5

BINARY FISSION EXPERIMENTS

5. Introduction

A survey of the literature[1] reveals a lack of data on fission product mass distributions for monoenergetic, neutron induced fission of ^{238}U, particularly as a function of incident neutron energy, E_n. Several authors[2-4] have determined the relative or absolute yield of some fission fragments at E_n values in the range of 1.5 to 18 MeV. Nagy etal[5] have determined the mass distribution of nearly 44 fission products at six E_n values in the range 1.5 to 7.7 MeV by employing both chemical separation and direct gamma spectrometry. In this work we measured the absolute cumulative yield of nearly 32 fission products in five different neutron energy in the range of 1.75 to 5.9 MeV.

5.1 Experimental Techniques

5.1.1 Irradiation Procedure

The investigation of mass distribution following the fission of ^{238}U was carried out using discs of natural uranium which contained 99.78% ^{238}U. Discs for irradiation were 10 mm diameter and .178 mm thick.

5.1.2 Neutron Production

The irradiations were performed in the Low Scatter Cell (LSC) of

the Physics Department Radiation Centre using the Dynamitron accelerator facility. The LSC dimensions are 9.25 m high, 9 m long and 8 m wide, with a gridded floor supported 4.25 m above the concrete floor. The beam line is constructed approximately 1 m above the gridded floor and approximately mid-way between the two walls, with the target position close to the centre of the room. The design of the cell is specifically intended to provide a suitable low-scatter environment for experiments in which it is important to minimise contributions from room-return neutrons. In fact, the scattering of neutrons within this beam room is not negligible and must be accounted for in many experiments by separate measurements, calibrations or calculations. The Dynamitron accelerator can produce beam currents of protons or deutrons up to ≈ 1mA, and thus high fluxes of "monoenergetic" neutrons using the $^{3}H(p,n)^{3}He$ and $^{2}H(d,n)^{3}He$ reactions. Solid targets of tritium or deuterium absorbed in titanium were used, each with a diameter of 25.4 mm and of different thicknesses. The titanium was evaporated on to silver backings prior to absorption forming a layer, .5 mm thick and 31 mm diameter. The relatively high beam power on the target was dissipated by cooling the silver backing with a .5 mm thick stream water. A uniform beam spot of 11 mm diameter was achieved by sweeping the beam across a water-cooled, gold-plated copper collimator situated in front of the target. Details of the target assembly along with the uranium disc and other foils to be irradiated are shown in Fig. 5.1.

5.1.3 Irradiation Geometry and Neutron Fluence Monitoring

The uranium disc, together with the neutron fluence monitor foils was placed about 20-30 mm from the neutron source as a

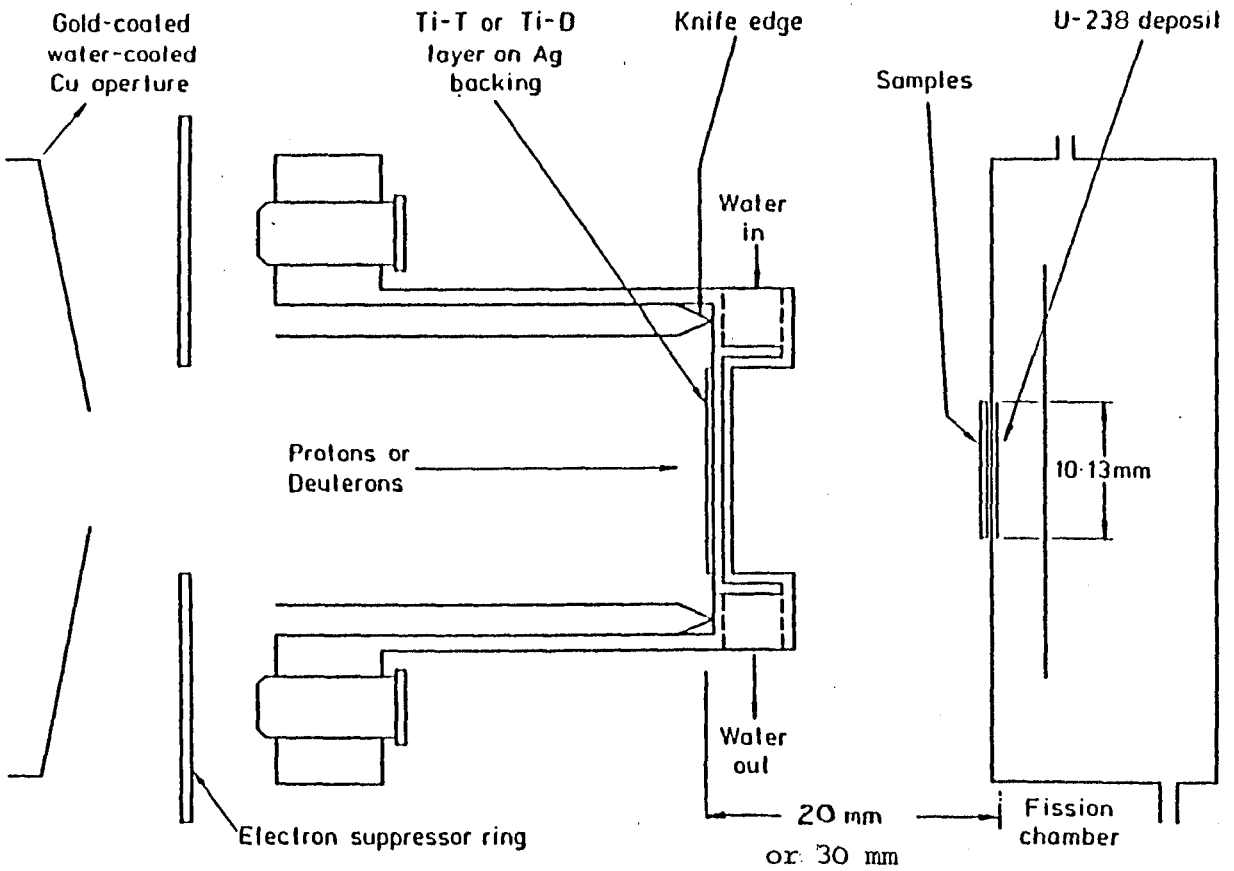

Fig. 5.1 Irradiation geometry on the Dynamitron.

suitable compromise between maximising the neutron fluence and minimising the angular spread of neutrons intercepting the samples. Irradiations at such a short distance do not allow an independent measurement of the neutron fluence to be made with a detector of known efficiency, because the effective solid angle subtended by the foil at the source cannot be determined with sufficient accuracy. It was therefore necessary to determine the fluence by detecting a neutron-induced reaction with a cross-section which is a standard. The fission cross section of ^{238}U was chosen for this purpose. A fission chamber was used, as shown in Fig.5.2 (known as the Harwell fission chamber), with a 63.7±1.3 μg deposit of 99.999% ^{238}U painted on a .127 mm thick platinum plate located on the inside surface of the fission chamber wall. The deposit had the same diameter as the samples, which were positioned in a circular recess on the outer wall of the chamber immediately in front of the ^{238}U deposit and held in the recess by thin spring clips. Otherwise, the detector was a standard parallel-plate ionisation chamber made from 1 mm thick stainless steel and with a plate separation of 9.5 mm to discriminate against alpha particles. This chamber was discussed in Chapter 4. Foils of indium or rhodium, which provide additional fluence monitoring in the event of fission chamber failure were included with the uranium discs in sample packs. A diagram of a typical pack and its location relative to the fissile deposit in the chamber is given in Fig.5.3. Each pack was a multi-layer sandwich of thin discs wrapped in thin aluminium, the uranium disc was sandwiched between aluminium, catcher foils to retain the fission products. This pack was coverd with a separate cadmium sheet in order to stop thermal neutrons reaching to the uranium disk. Therefore, contributions to the

Fig. 5.2 Irradiation geometry on the Dynamitron

(a) Fission chamber

(b) Neutron producing target

(c) Beam line.

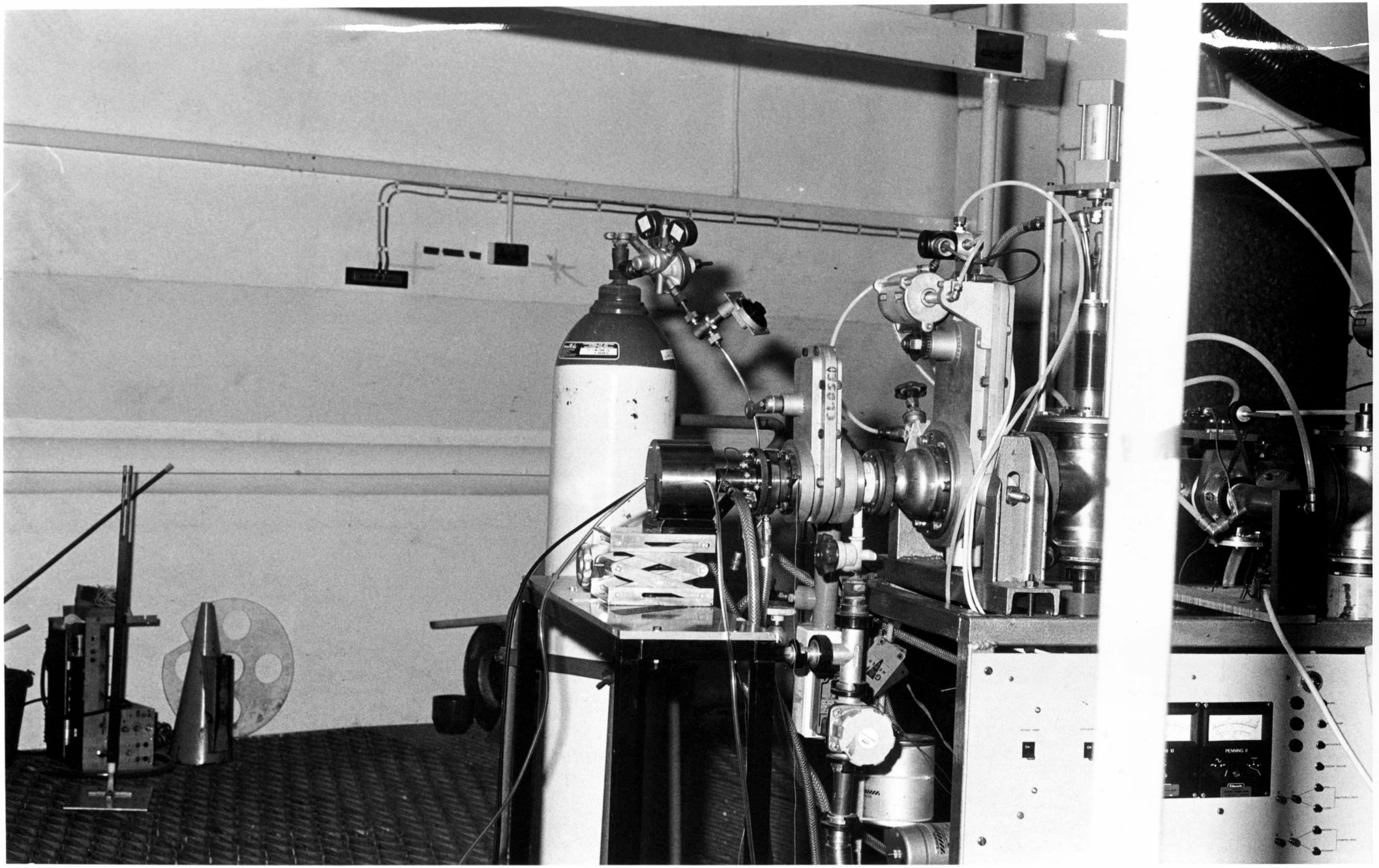
PENNING

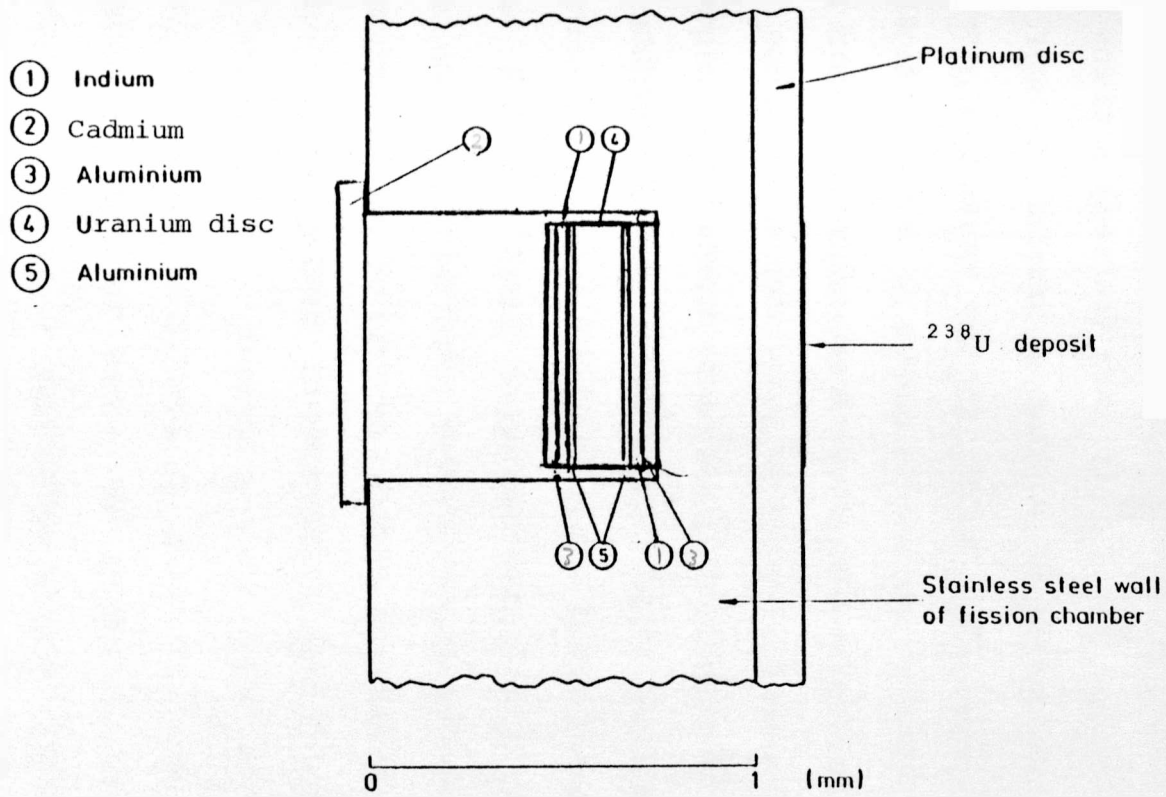

Fig. 5.3 Arrangement of ^{238}U and monitor foils in typical sample pack and position relative to the uranium deposit in the fission chamber.

count rate due to thermal-neutron-induced fission in ^{235}U found to be negligable. The foil packs are shown in more detail in Fig.5.4. The relative significance of room-return neutrons compared to direct neutrons from a source or target varies considerably with the positioning and type of detector, as well as the anisotropy of the particular neutron source used. For a uranium-238 fission chamber the scattering contribution to the total counts is essentially zero, due to the insensitivity of that type of detector to neutrons with energy less than 1 MeV. Recently, calculations with the Monte Carlo code, MORSE, for scattered neutrons in a room showed that the absolute scattered flux from an isotropic source was approximately independent of the position in an unoccupied, concrete-lined room, with a scale in approximately inverse proportion to the volume of the room[6]. In addition, it was found to be virtually independent of the neutron-source energy provided that the source energy was above about 100 keV. Small corrections were made for the effects of these neutrons on the fission yields of masses that are sensitive to neutron energy. To optimise the detection efficiency for both short- and long-lived fission products, short (20 min to 3 h) and long (6-24 h) irradiations were made at each neutron energy. Detailed information is given in Table 5.2. The variation of the flux during the irradiation period were monitored by using a multiscalling system, which recorded the total fission detector count for fixed intervals of time. A parallel plate fission chamber (PPC) was used for monitoring the fluctuations of the flux and is described in detail in Chapter 4.

Fig 5.5 shows the electronic arrangement used during the irradiations for fluence monitoring by the Harwell fission chamber and the PPC fission chamber.

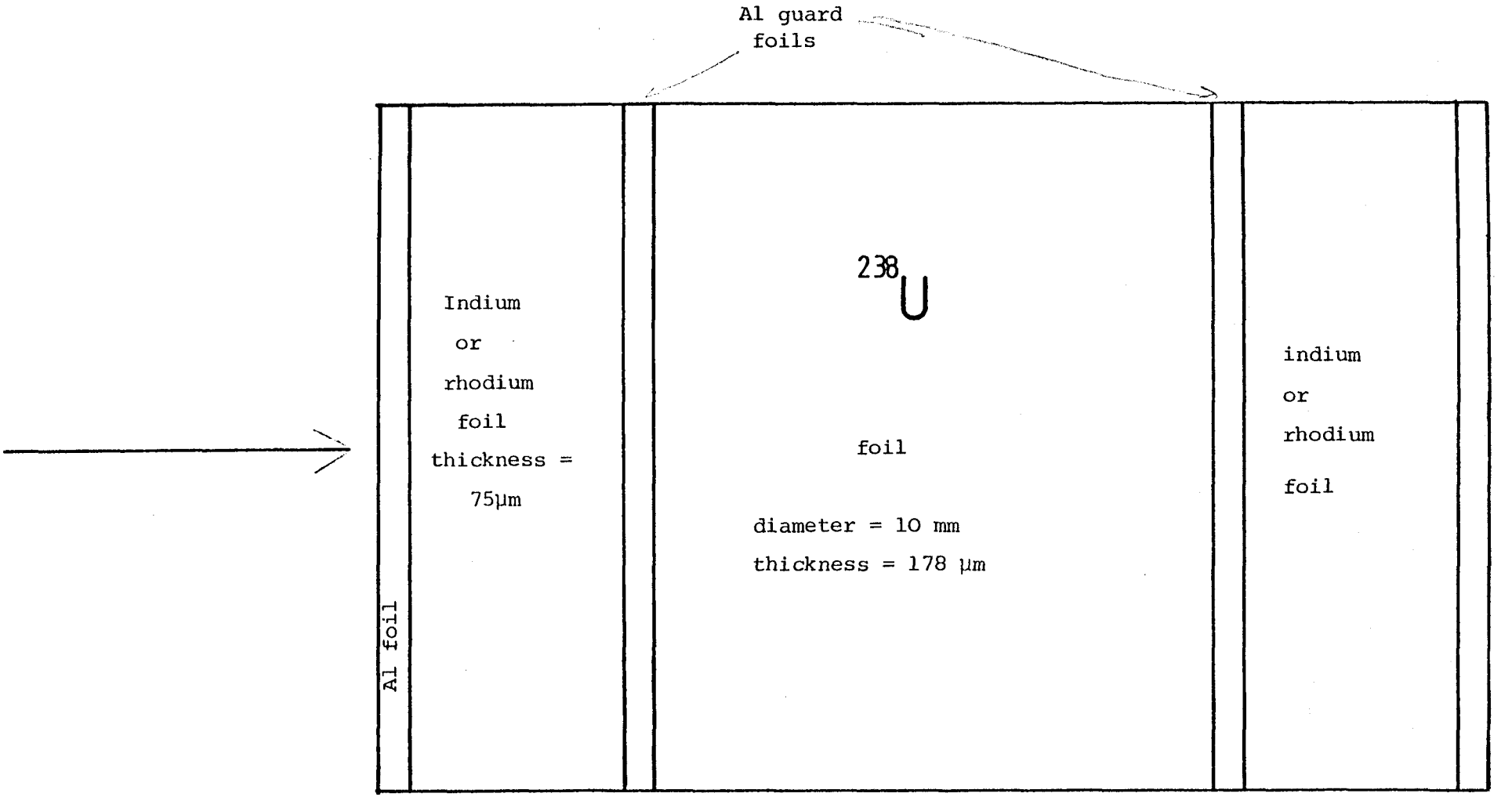

Fig. 5.4 Schematic representation of irradiation foil packs.

Table 5.2

Irradiation times at different neutron energies

Neutron Energy KeV	Irradiation time (min) short	intermediate	long
1722	112	397	709-1385
2160	40.5	153.14	399
3726		210	594
4782	65	120-155.5	338-1102
5982	23	72	402

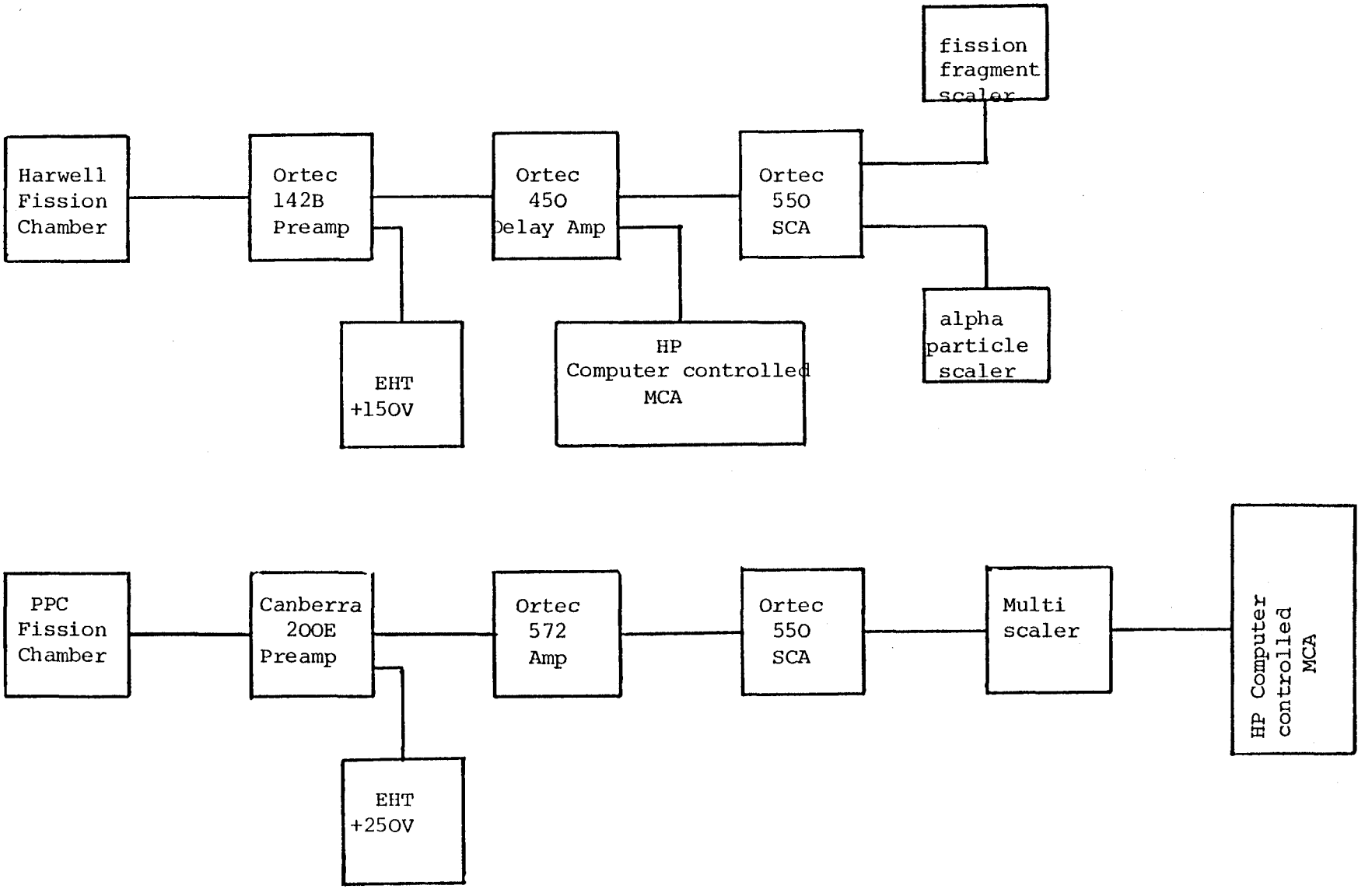

Fig. 5.5 The electronic arrangement used during irradiations for the Harwell and PPC fission chamber.

5-1.4 Neutron Energy Resolution

The neutron energy resolution function of the irradiation, $R(E_n)$, is defined as the relative probability that a neutron of energy, E_n, emitted from the target intercept the foil assembly. It is required to define the weighted mean energy of the measurement and to determine the weighted mean cross-sections of the standard reactions used to measure the neutron fluence. The resolution is dependent on both the thickness of the neutron producing target and the geometrical arrangement used in the irradiation. These factors need to be considered in detail.

(a) Effect of Irradiation Geometry

The incident beam particles (proton or deutron) in irradiations on the Dynamitron fall uniformly over a target area by scanning the beam on target. The exposed target area was approximately equal to the areas of the uranium discs or activation foils and the ^{238}U deposit in the fission chamber. Thus, the maximum angle of emission of neutrons that can intercept the sample was nearly 27^{o} and 18.5^{o} respectively, for a separation distance of 2 or 3 cm between the target and the sample. Such neutrons are of lower energy than those emitted at 0^{o} in the direction of the incident beam. The neutron energy resolution function due to the angular spread of emitted neutrons from a circular distributed source intercepting a circular foil was obtained by using the DWFXA2 computer program[7], based on the procedure discussed by Gotoh and Yagi[8]. The relative number of neutrons, $N(\theta)$, emitted from the source at an angle θ to $\theta+d\theta$ to the forward direction which intercept the axially mounted discs, can be deduced from analytical expressions. The diffential neutron production cross-section for the

source reaction was then combined with the kinematic relation between the emitted neutron energy (E_n) and the angle of emission (θ) to produce the expression

$$N(E) = N(\theta). \frac{d\theta}{dE} .$$

A plot of $N(E_n)$ against E_n allows one to determine the relative number of neutrons intercepting to the sample disc for a suitable energy interval, dE_n. The resolution function is a maximum for neutrons emitted at 0^o and decreases smoothly to zero for the maximum angle of emission at which neutrons intercept the foil for a circular source irradiating the disc. The resolution function becomes narrower if the source size is reduced to a point source. These resolution functions were used to determine the weighted, mean neutron energy.

(b) Effect of Target Thickness

The thicknesses of the neutron targets used in these measurements were chosen as a compromise between neutron yield and energy loss of the beam particles traversing the target. The energy loss of the beam in the target causes an increase in the energy spread of the neutrons intercepting the foils and must be combined with the intrinsic resolution function due to the properties of the source reaction and irradiation geometry as described above. Details of the targets are shown in Table 5.3. Since the targets used were relatively thick, both the stopping power (SP) and the neutron production cross-section ($\sigma(\theta)$) of the incident beam particles passing through the target material may change. Thus the effect of the target thickness on broadening the intrinsic resolution function is not, in general rectangular but is proportional to the relative neutron yield ($\sigma(\theta)$/SP) as the beam particles interact in increasing depths of the target material. The energy loss in the target is usually more

Table 5.3

The reaction used for producing neutrons, together with their energies and fluxes as function of the experimental parameters

Reaction	Target $\mu g/cm2$	Distance cm	incident particle energy	Mean neutron KeV	Energy spread KeV	FWHM KeV	Neutron flux n/cm2/μA
D(d,n)3He	1800	3	2900	5982	451.5	260	3.06
	2200	3	1800	4782	521	420	2.30
	2200	2	1800	4750	650	435	4.48
	2200	3	1000	3726	820	-	1.32
T(p,n)3He	900	2	2600	1722	238	125	1.08
	900	3	3000	2160	146	57	6.71
	900	2	3000	2147	246	67.5	1.24

significant than the energy spread due to irradiation geometry; therefore, the FWHM of the total neutron energy resolution function listed in Table 5.3 is correlated with the difference between the maximum and minimum neutron energy emitted from the target in the forward direction. However, with reduction of the energy of charged particles emitted from the accelerator the energy loss increases in target with a consequent large reduction in neutron yield with increasing depth of irradiation. There is considerable suppression in the relative number of lower energy neutrons in the resolution function, and this reduces the FWHM value of the energy distribution.

A typical example of the energy resolution function for a circular target irradiating disc foils of the same diameter at a distance of 30 mm is shown in Fig. 5.6(a). The incident deutron beam energy was 2.9 MeV and the thickness of the titanium tritide target was 1.8 mg/cm^2 (Table 5.3). The equivalent resolution function for a point source of neutrons in this irradiation is shown in Fig.5.6(b) and is much more symmetrical, although both have the same half-width of 260 KeV.

5.1.5 Activation foils

The indium and rhodium foils were used for flux measurements. The reactions of interest in indium and rhodium were $^{115}In(n,n')^{115m}In$ and $^{103}Rh(n,n')^{103m}Rh$.

^{115}In has an abundance of 95.72 % in natural indium whereas ^{103}Rh is 100% abundant. ^{115}In has an excited, metastable, state and decays to the ground state with a half-life of 4.486 hours, emitting 336 KeV gamma-rays with an emission probability of 45.9% . The contribution to the ^{115}In activity due to the reaction $^{115}In(n,p)^{115}Cd$, with a 54 hour half-life was found to be negligible. Indium has a relatively flat excitation function in the energy range 2-6 MeV[9]. This reaction, with its low threshold of 339 Kev was very suitable for these

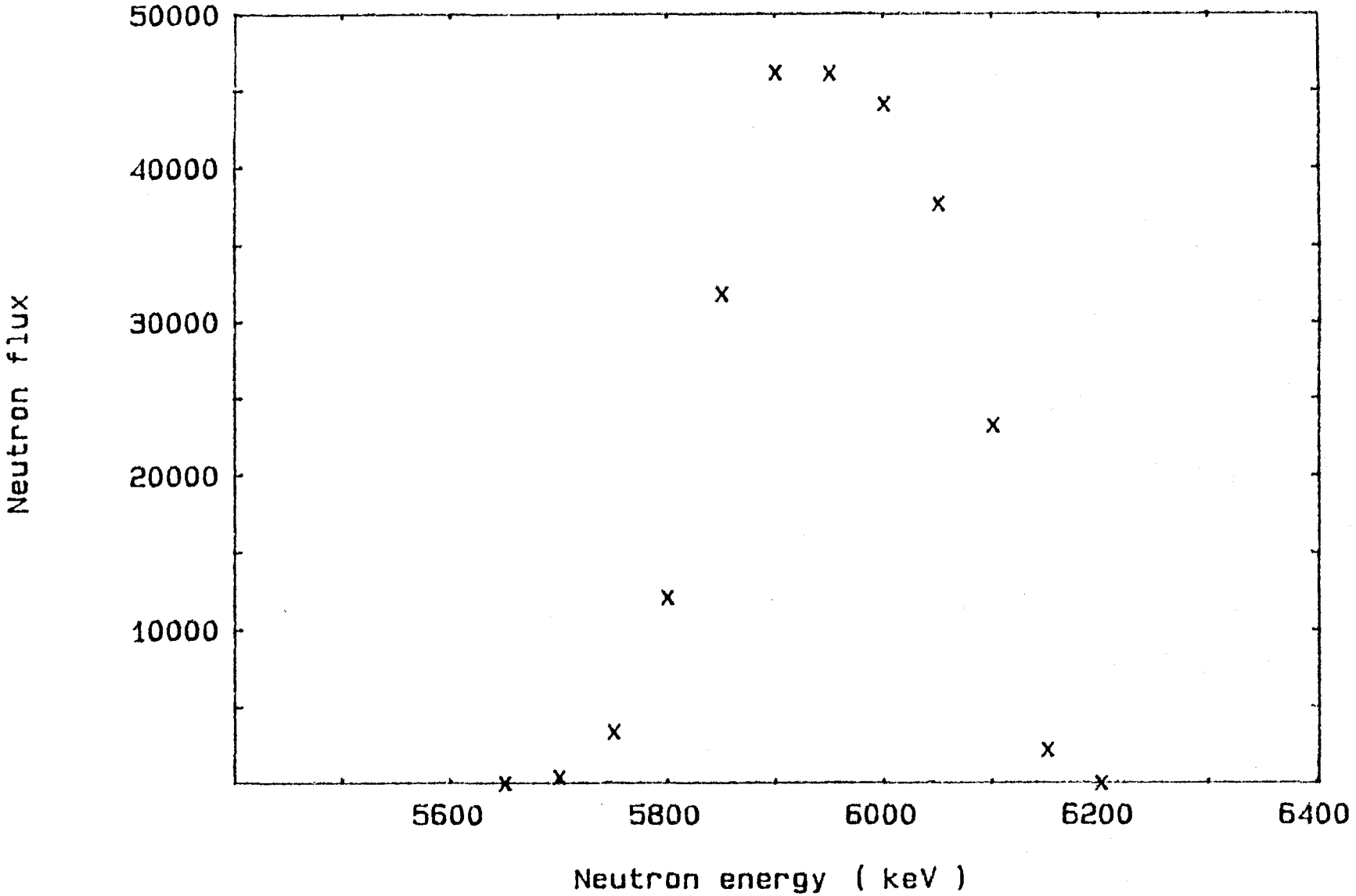

Fig. 5.6(a) Calculated energy resolution spectrum at a disc placed 30 mm from the circular target used during the irradiation.

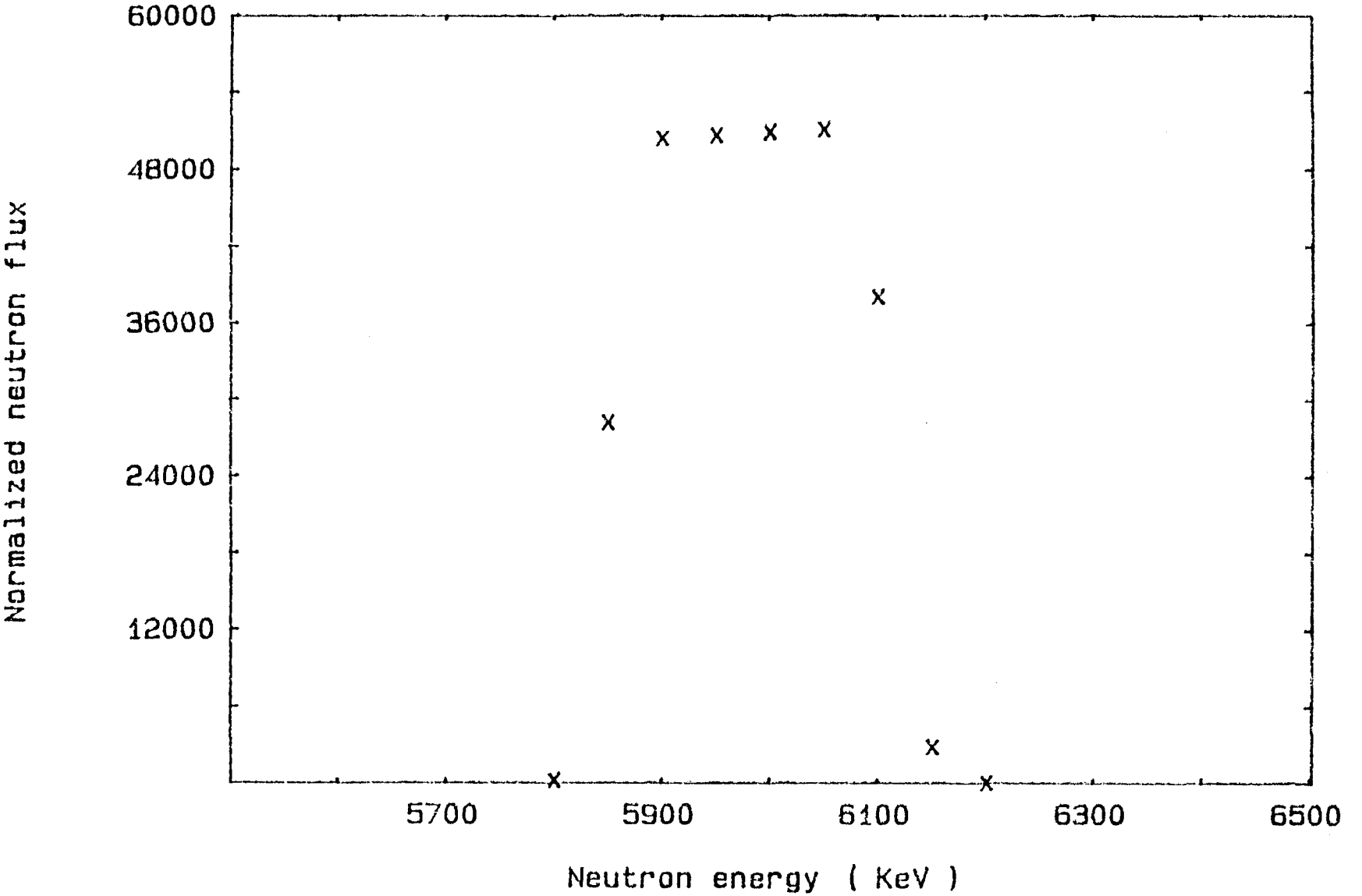

Fig. 5.6(b) Same as Fig. 5.6(a) for a point source.

measurements.

The rhodium reaction is suitable for lower neutron energy measurements since it has a threshold of only 40 KeV and a relatively constant cross section in the energy range 1.5 to 2.5 MeV[10]. ^{103m}Rh has a half-life of 56 minutes and decays with the emission of 40 KeV gamma rays to the ground state of ^{103}Rh. Unfortunately, this gamma transition is highly internally converted so that the ^{103m}Rh activity was measured by counting the resultant 20 Kev, K X-rays. The short half-life of this isomer, however, makes this reaction very suitable for monitoring short irradiations.

5.2 Fission Yield Determination.

5.3.1 Gamma Decay

Gamma emission frequently accompanies a beta decay process. The latter may leave the nucleus in an excited state and as the gamma rays are emitted the nucleus decays to the ground state. This may take place via one or more intermediate energy states or directly to the ground state. In either case the energy of the gamma ray emitted is simply the difference in energy between the two levels concerned. Where the excited state has a measurable life-time such a level is known as an Isomeric state and the subsequent gamma ray transition an Isomeric Transition. Not all transitions lead to the emission of gamma rays. For quantum mechanical reasons it may be that the energy is used to eject an orbital electron. This process is known an Internal Conversion. Obviously, in cases of 100% internal conversion no gamma rays are emitted. At the other extreme the internal conversion ratio is zero. Any given transition will have an internal conversion factor

associated with it, lying between 0 and 1.

5.2.2 Gamma-Ray Counting and Calibration Procedures.

The Gamma ray spectrometer system used in this work was based on a 93 cm^3 hyperpure germanium (Ge) detector with a resolution of 1.8 KeV (full width at half maximum (FWHM)) for the 1.33 MeV gamma ray of ^{60}Co. This detector was shielded with two inch thick lead bricks in order to reduce background counts. Amplifier time constants of 6 μsec were used for good energy resolution. Pulses from the detector were amplified and fed into a 4096 channel pulse-height analyser, based on an H-P 2100A computer. The system was calibrated with a ^{152}Eu source and the gain of the system (.37 KeV/channel) was checked periodically with a reference sources of gamma rays.

Samples to be counted were mounted on a sample holder at a distance of 4.8 cm from the front face of the Ge detector. The full-energy photopeak counting efficiency of the detector as a function of gamma ray energy, E at 4.8 cm was determined as previously described in chapter 4. Typical spectra obtained with this detector are shown in figs 5.7(a), 5.7(b), 5.7(c) and 5.7(d).

5.2.3 Corrections due to Cascade Coincidence Summing.

The correction for losses from the photopeak caused by gamma cascade coincidence summing in the decay of nuclides in which two or more gamma rays are emitted in coincidence, is necessary. The correction factors for this effect were discussed in Chapter 4 Section 4.2.1 and 4.2.2.

Fig. 5.7 Three successive γ-ray spectra following irradiation of a Uranium disc by 5.98 MeV neutrons.

Irradiation time 23 min

Decay and counting time as follows:

Spectra 1 6.5 min 3.128 min

Spectra 2 6.5 min 10.181 min

Spectra 3 6.5 min 26.036 min

In the Figs. 5.7 a-d, the same spectrum is shown over four separate energy ranges in order to provide improved resolution and identification of photopeaks.

Energy ranges are

a) 20 - 380 keV

b) 380 - 760 keV

c) 760 - 1140 keV

d) 1140 - 1520 keV.

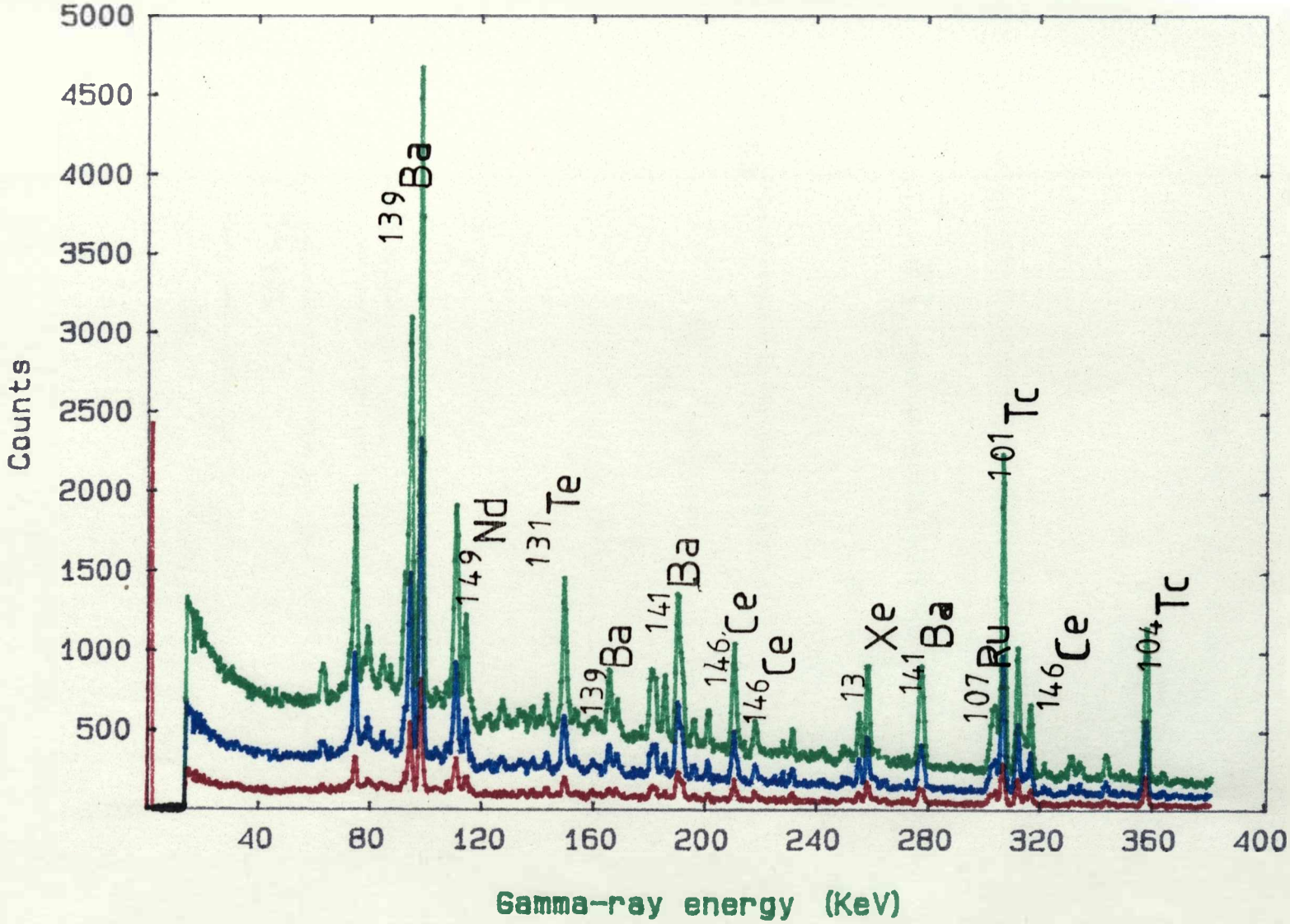
Counts
5000
4500
4000
3500
3000
2500
2000
1500
1000
500
40
80
120
160
200
240
280
320
360
400
Gamma-ray energy (KeV)
139Ba
149Nd
131Te
139Ba
141Ba
146Ce
146Ce
13
Xe
141Ba
107Ru
101Tc
146Ce
104Tc

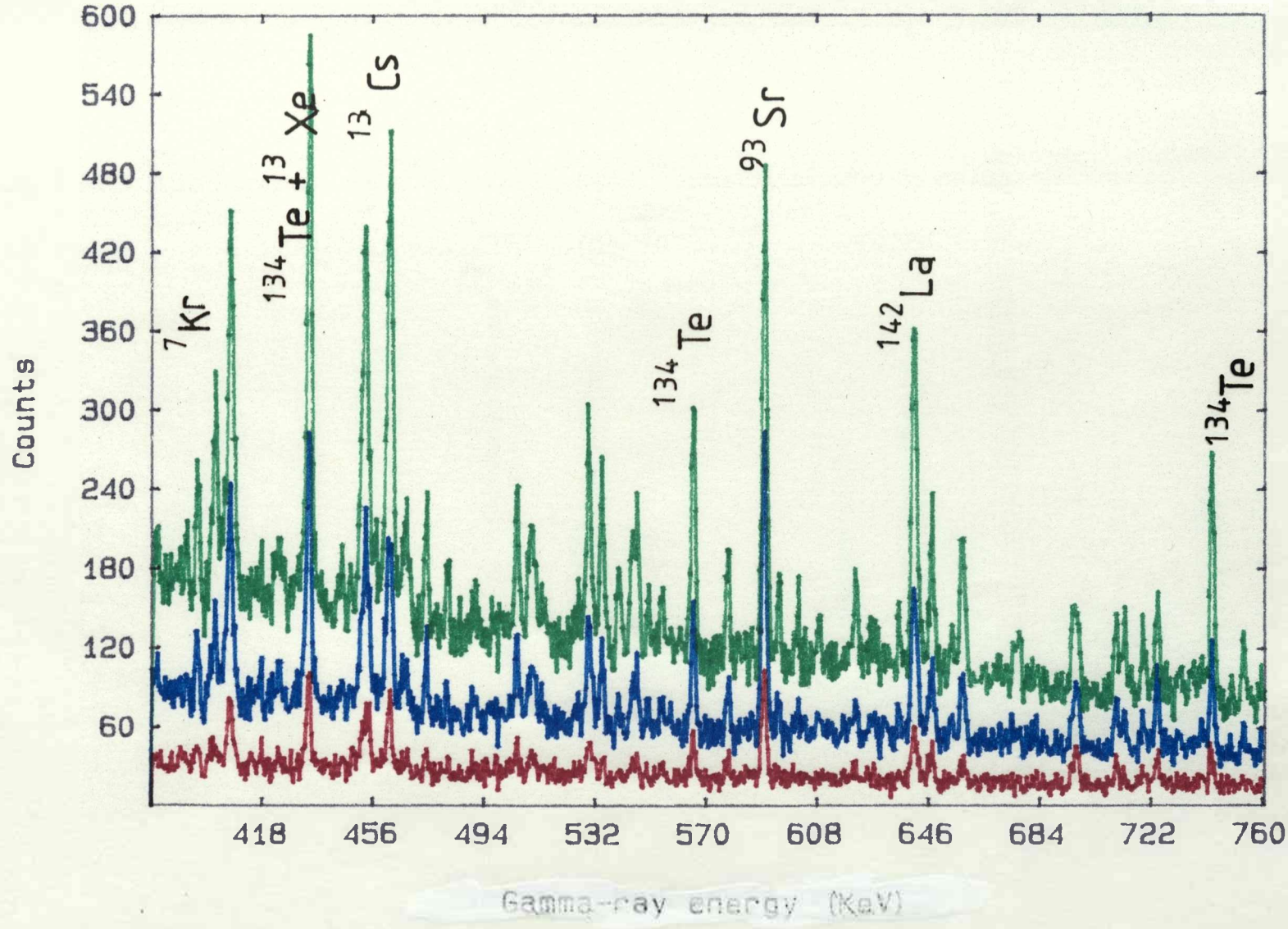
600
540
480
420
360
300
240
180
120
60
Counts
^{7}Kr
^{134}Te + ^{13}Xe
^{13}Cs
^{134}Te
^{93}Sr
^{142}La
^{134}Te
418
456
494
532
570
608
646
684
722
760
Gamma-ray energy (KeV)

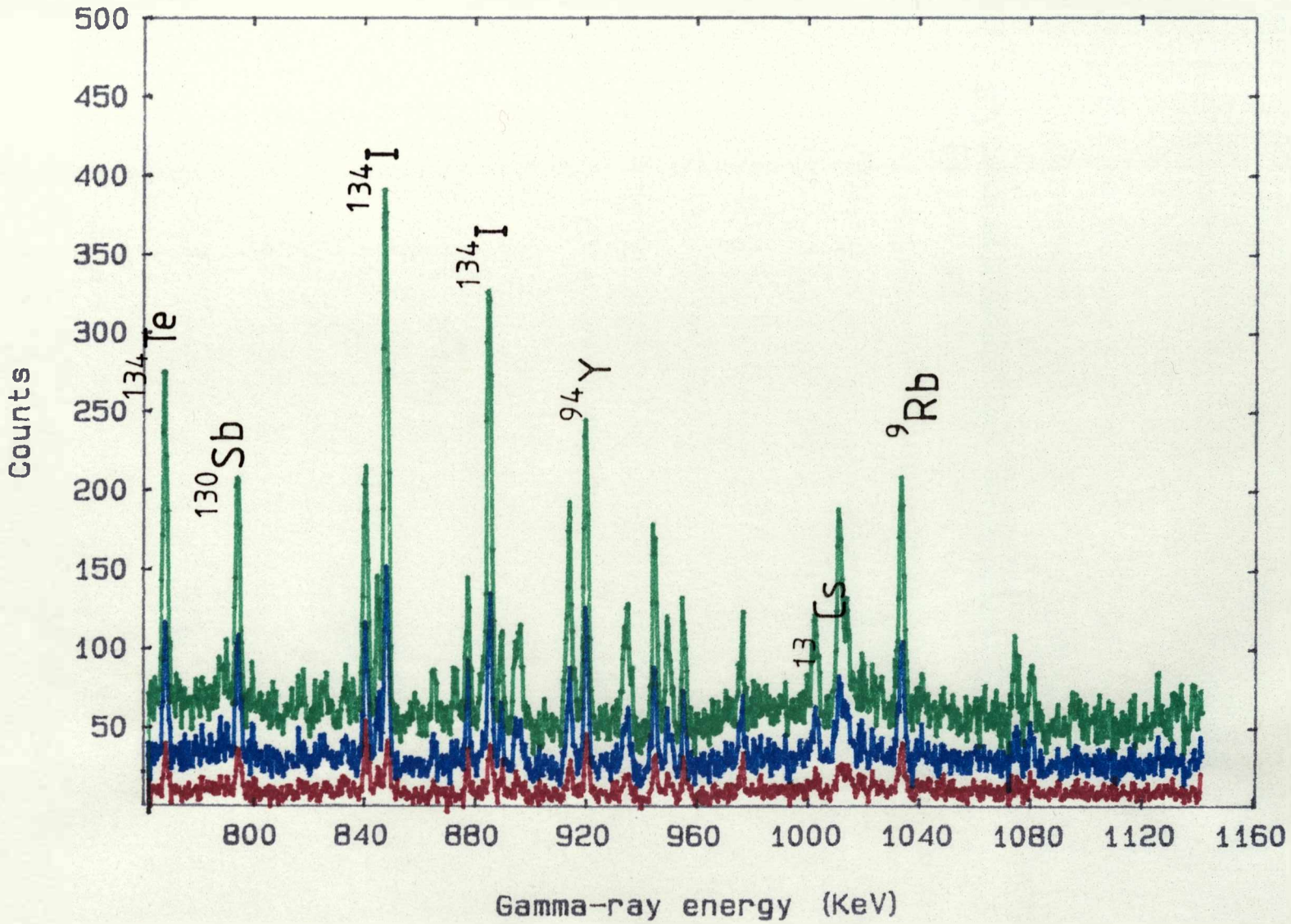
500
450
400
350
300
250
200
150
100
50
Counts
^{134}Te
^{130}Sb
^{134}I
^{134}I
^{94}Y
^{13}Cs
^{9}Rb
800
840
880
920
960
1000
1040
1080
1120
1160
Gamma-ray energy (KeV)

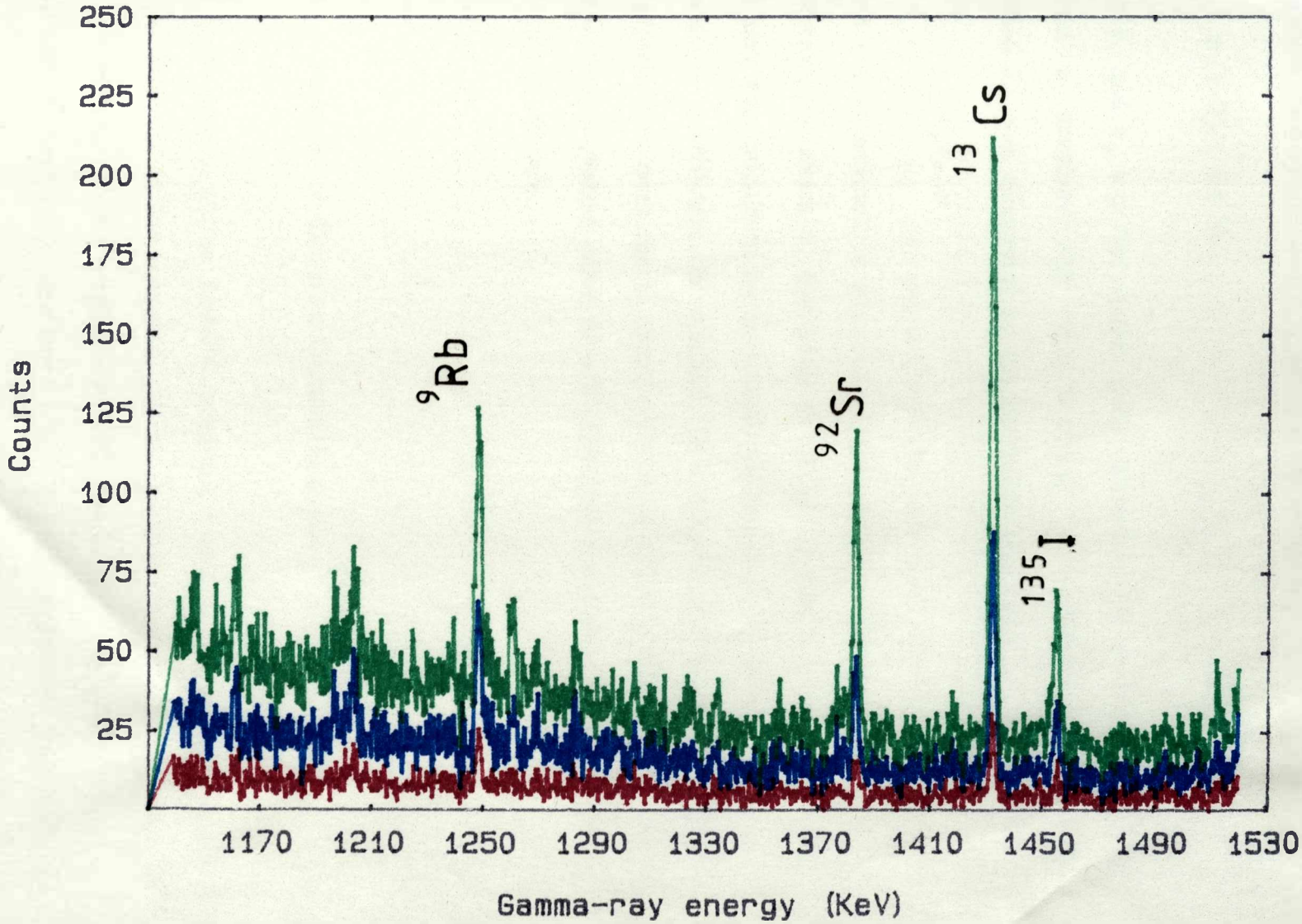
250
225
200
175
150
125
100
75
50
25
Counts
^{9}Rb
^{92}Sr
^{13}Cs
^{135}I
1170
1210
1250
1290
1330
1370
1410
1450
1490
1530
Gamma-ray energy (KeV)

5.2.4 Self-Absorption of Gamma Rays in the Uranium Target Discs.

This correction was determined by measuring the transmittance T through the disc as a function of E using a ^{152}Eu extended source. The self-absorption correction S, given by the relation

$$S = \frac{\Phi_2}{\Phi_0} = (1-T)/(-\ln T) \qquad 5.1$$

The Φ_1 and Φ_2 was the count rate obtained respectively with and without a uranium disk in each energy. Then the value of T in the equation 5.1 was calculated by the following relation

$$T = \frac{\Phi_1}{\Phi_2} = e^{-(\mu/\rho)\rho t}$$

Which was substituted in equation 5.1, in order to calculate the self absorption, by which Φ_2 had been divided to obtain true count rate Φ_0. This also was calculated by using the published[11,12] value of mass attenuation coefficient for uranium. Its values ranged from 86 to 99.9% for gamma rays over the E range of 0.15 to 1.5 MeV. Fig. 5.8 shows the obtained experimental value of self-absorption versus energy along with calculated one.

5.2.5 Analysis of Complex Gamma Spectra.

The H-P version of the SAMPO program[13] and μVAX version was used for the analyses of the complex, gamma spectra. This program, based on the new version of the original SAMPO program[14] was called SAMPO80[15] and was coded for a DEC11 minicomputer with 32K of

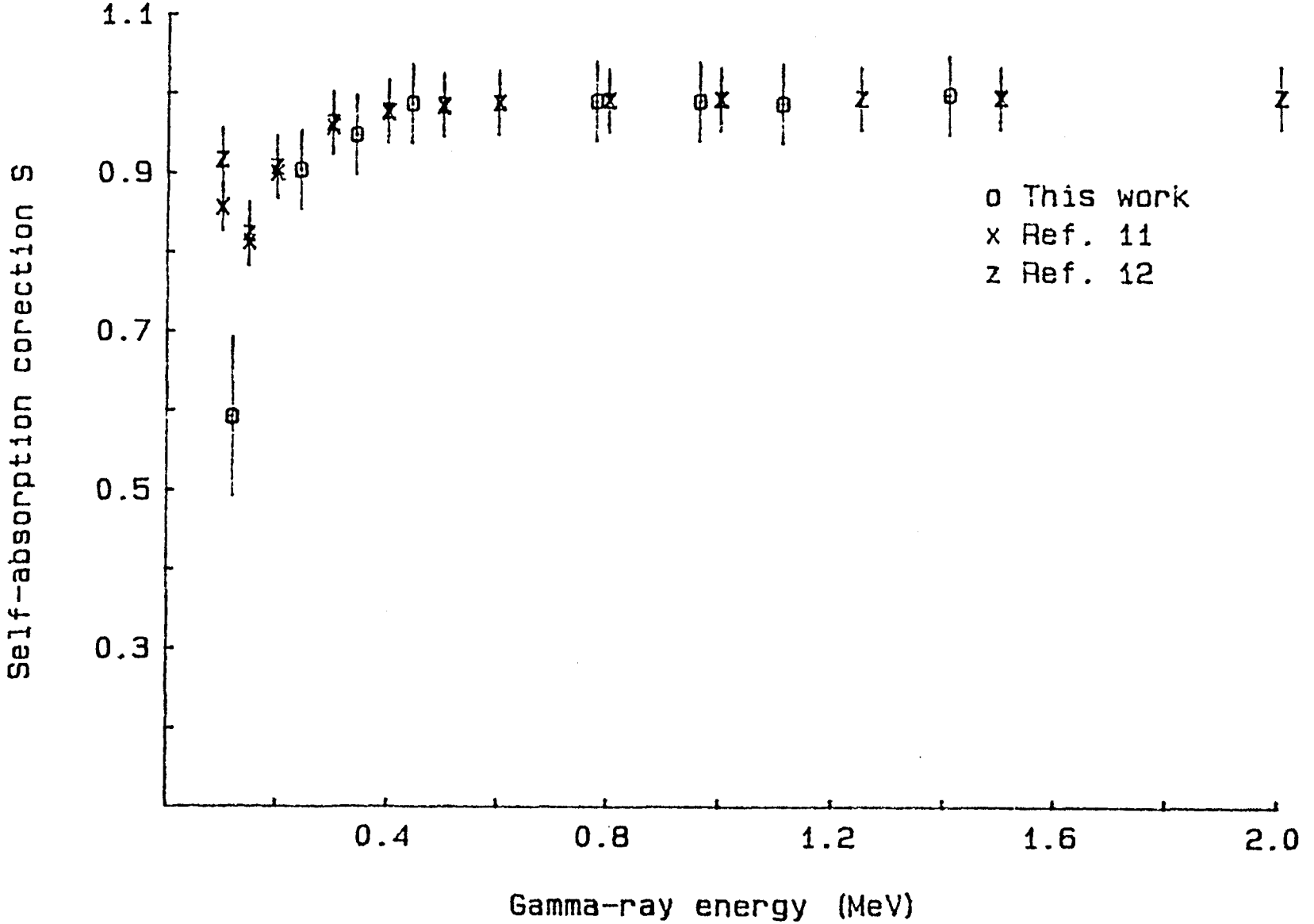

Fig. 5.8 The variation of self-absorption versus gamma-ray energy.

memory. The whole program requires more than 32K of system memory and therefore had to be run in two parts:

i) a shape calibration procedure,

ii) a peak search and fitting routine. The general features of the program will be briefly described here.

i) The peak shape calibration procedure

In this procedure the functional representation for the peak is assumed to be Gaussian with an exponential tail on both sides. The exponentials are joined to the Gaussian in such a way that both the function and its first derivative are continuous. The background under the peak is assumed to be linear. The peak shape is characterized by seven parameters; two background parameters, the peak height and its location, the peak width (CW) and the distances from the peak centroid to the starting point of the exponentials on either side (CL and CH). The last three are used as calibration data for subsequent analysis since they vary smoothly with energy. These shape parameters are determined separately only for a relatively few well defined peaks. To analyse other peaks in the spectra the values of the parameters are obtained by interpolation from the reference values. It has been found that for a 4096 channel spectrum 10 to 12 peaks, [redacted]mately evenly spaced throughout the spectrum are sufficient and less are needed if the spectrum is smaller. This part of the program minimizes the weighted, nonlinear least squares expression

$$\chi^2 = \sum_{i=k-1}^{k+m} (n_i - f_i)^2/n_i$$

Where

i= is the channel number,

n_i= is the counts in channel i,

k= is the approximate center channel of the peak,

l,m= are the channels specified by the user to be the fitting interval. The minimization is done with respect to peak parameters[14] and this is performed by a VARMIT subroutine package with an iterative gradient algorithm. Minimization is terminated if all components in the next step change by less than 10 , or if four, succeeding values of χ^2 are the same, or if 100 iterations have been completed. An example of the printout produced for the shape calibration of one peak and its semilogarithmic printer plot is shown in Fig. 5.9. Some error parameters are also calculated and printed out, in order to show whether the performed shape calibration is acceptable or not. The first error parameter is called CHI/DRG FREE, which is the conventional χ^2 per degree of freedom, the second is its square root and called SIGMA and the last one is ERROR CORRELATION defind as

$$R = \frac{1}{(n-m)} \sum_{i=1}^{n} \Delta'_i \Delta'_{i+1}$$

Where

n= is the number of channels in the fitting interval,

m= is the number of parameters fitted and Δ'_i is defined as

$$\Delta'_i = (n_i - f'_i)/(f'_i)^{\frac{1}{2}}$$

where n_i is the number of counts in channel i, f'_i is the value of the fitted function at channel i. As a rule of thumb, SIGMA values below 5 and ERROR CORRELATION values from -1 to +1 can be considered to be acceptable. In practice it is found that, within at most four attempts it is possible to obtain an acceptable fit.

ii) The peak search and fitting routines:

This part is run separately after acceptable fits have been found for the peaks in the calibration spectrum. In this routine the smoothed second difference is used to find the peaks in the spectrum. The

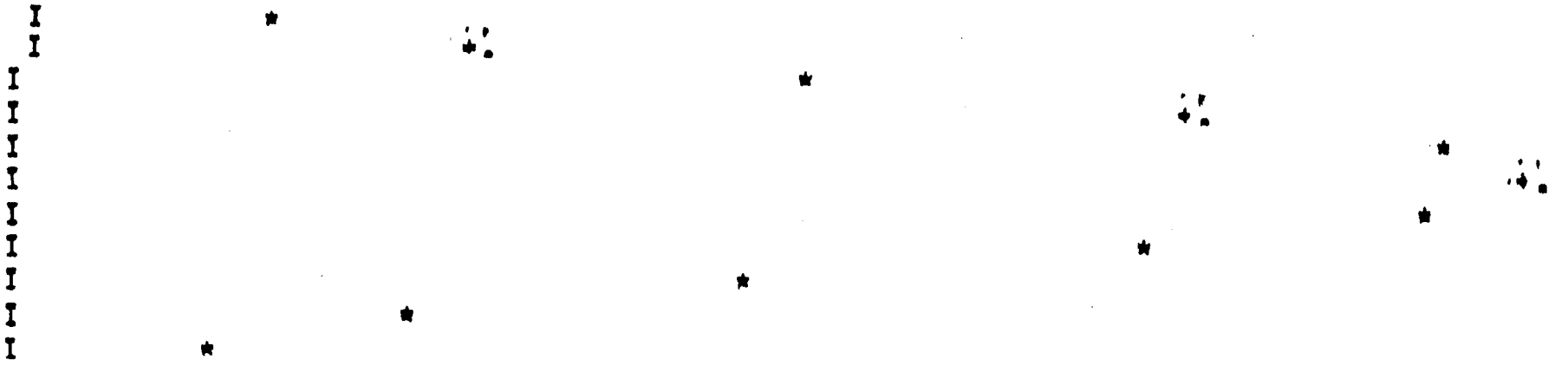

SYMBOLS: I = CONTINUUM . = DATA + = FIT * = . AND +
) = I AND . (= I AND + $ = I AND . AND +

SUMDATA= .758477E+05 SUMCALC= .758423E+05

SHAPE CALIBRATION RESULTS
CHI/DEG.FREE = .143E+01 SIGMA= 1.197 ERROR CORRELATION= -1.000

CP =	1844.934	+/-	.107
CL =	2.716	+/-	.095
CH =	2.935	+/-	.656
CW =	1.837	+/-	.031

Fig. 5.9 A typical fit of a calculated function to the 662 keV photopeak provided as output from the SAMPO 80 program.

method is particularly good in detecting small peaks on a high or low background. Multiplets are detected with a reasonable accuracy. The details of the procedure are to be found in the original SAMPO80 procedure[16]. The accepted peaks for fitting are required to pass two checks. One is based on the absolute value of the significance which is set by the user and the other on the width of the peak. The peak centroid is determined by the expression

$$CH = \frac{\sum_i i \cdot ss_i}{\sum ss_i}$$

The summing is done over the channels i where the significance value SSi is negative, i.e. the location is found as the weighted average of those channels. The peak areas are calculated by fitting the precalibrated, modified Gaussian to the data with a weighted least squares formula using a parabolic background. The fitting intervals are determined automatically by the program. Peaks separated by less than four times the average FWHM are fitted together. The background and peak height are fitted by a linear algorithm. The errors for the peak areas are calculated from the errors given for the peak height parameters. The matrix of the least squares minimization is solved by Gaussian elimination and back substitution. The diagonal elements of the putative inverse of the matrix are calculated in a subroutine called DIAG. Errors for the peak locations are calculated in the peak search routine using the normal equation for the standard deviation of the mean. A conversion factor of 1.3 was found necessary to give consistent and accurate results. The calculated peak locations and areas are finally corrected with energy calibration data (if given by the user) to yield peak energies. The energy calibration is a linear interpolation on a linear scale. The major limitation, due to lack of space on the HP system, is that only a maximum of 1024 channels can be analysed at one time. Thus a 4K spectrum requires the program to be

run at least four times, processing one region at a time. Further more, the maximum number of peaks that can be analysed in one run is only 25 and if more than this number of acceptable peaks are present in a given region, then the program has to be run more than once for this region. In μVAX computer can run 4k spectrum at once stage.

5.2.6 Measurement of Activity at the End of Irradiation

To enhance statistical accuracy in the determination of the fission product gamma-ray activities, a large number of 4K spectra ($\simeq$ 1000 spectra) were recorded over a sufficient period of time to encompass the wide range of half-lives involved. These complex spectra were analysed with the computer program SAMPO, as described earlier, to obtain the intensities of the resolved photo-peaks. Experience with this computer code indicated that for a single, large peak such as 641.2 Kev in Fig 5.7(b), the peak area determined using the computer routine usually differed from that obtained manually by less than the normally assigned statistical uncertainties. Doublet peaks, such as for 302.8 and 306.9 KeV peaks in Fig 5.7(b), are also adequately analyzed, at least for the larger peak. The measured gamma-ray activities were assigned to the relevant fission product from their energies and half-lives. In addition, a Least-Squares decay computer program (discussed in 5.2.7) was used to determine the activity of a given nuclide based on several spectra and was found to give a more accurate value than could be determined from a single spectrum.

5.2.7 The Least-Square Decay Computer Program

A computer program for the analysis of multicomponent decay curves by a least-squares procedure was written for both a μVAX and a H-P

computer in FORTRAN IV. The mathematical method employed in this program is as follows. If m independent fission products are present in the n measurments of the counting rates f_i, of the sample at the time t_i, then the set of data satisfy n equations of the form

$$f_i = \sum x_j e^{-\lambda_j t_i} + V_i \qquad 5.3$$

where an individual term in the sum, $X_j\ e^{-\lambda_j t_i}$, represents the contribution of the jth component to the total activity at time t_i. The residual, v_i, is due to statistical fluctuations and experimental errors. If samples under measurement have counting time periods of count, and irradiation time of t_{irr}, the X_i in the above equation becoming as follows

$$X_j = X_j\ (1-e^{-\lambda_j t_{irr}})(1-e^{-\lambda_j t_{count}})$$

Since the m coefficients x_j enter these equations linearly, a solution by the least squares method is possible. The condition for such a solution is that

$S^2 = \sigma w_i(F_i - f_i)^2 = \text{minimum} = \sigma w_i v_i^2$

where w_i is the weight assigned to the square of each residual. In terms of the standard deviation, σ, of the ith counting rate

$P_i = 1/\sigma_i^2$

It is convenient to use matrix notation when equation 5.3 becomes

$F_{ni} = A_{ni}\ X_{ni} + V_{ni}$

and

$V'_{ni}\ P_{nm}\ V_{ni} = \text{minimum.}$

The above equations are solved by the Gaussian elimination method[17]. The listing of this program is provided in Appendix 2.

5.2.8 Absolute Fission Yield Measurements.

The value of the saturation activity was necessary for an absolute

fission yield measurement. Saturation activity is defined as the ratio of activity at the end of irradiation to the saturation factor as discussed in Section 5.3.1. It could be calculated if the information regarding counting efficiency, absolute gamma emission intensities, I (listed as photons per 100 disintegrations in Table 5.4), genetic relationships, and irradiation time were all available. Saturation activities are related to the fission yield by the expression:

fission yield = saturation activity/fission rate.

The fission rate refers to the count rate of the fission chamber or alternatively from counting the indium and/or rhodium foils with the Ge detector.

5.3 Treatment of Fission Yield Data

The following corrections are necessary for obtaining accurate fission yield data:

(i) corrections made to account for the variation in the neutron flux during the irradiation,

(ii) allowance must be made for the decay of the precursors of the nuclide under observation during the irradiation and for the cooling time when the gamma spectrum is recorded,

(iii) corrections applied to allow for the independent yields of members of the decay chain under investigation.

5.3.1 Variations in Neutron Flux

When a uranium foil is irradiated by neutrons that induce fission, a steady state can be reached in which fission products disintegrate at just the rate at which they are formed. If the irradiation is

Table 5.4

Fission product γ-decay data used in fissions yield measurements

Nuclide	Half-life	Gamma Energy (KeV)	I(%)	Reference
85mKr	4.48 h	151.2	78.6 ± 5.2	21
87 Kr	76.3 Min	402.6	49.5 ± 1.6	22
88 Kr	2.84 h	196.3	26.0 ± 1.3	22
89 Rb	15.2 min	1031.9	59.0 ± 6.0	22
		1248.1	43.0 ± 4.0	22
91 Sr	9.6 h	653.0	12.0[a]	23
		749.8	24.0[a]	23
		1024.3	33.0[a]	21
91mY*	45.7 min	555.6	95.1 ± 0.1	
92 Sr	2.71 h	1383.9	90.0[a]	23
93 Y	10.2 h	267.0	6.4[a]	23
94 Y	19.2 min	919.2	49 ± 5	21
95 Zr	64.4 day	724.2	44.2 ± .5	24
		756.7	54.8 ± .5	24
97 Zr	16.9 h			
97mNb*	60 sec	743.4	92.7±1	21
97bNb*	72.1 min	657.9	98.3 ± .1	22
99 M0	66.0 h	140.5	5.7 ± .5	22
		181.1	6.5 ± .2	22
		739.5	13.0 ± .4	22
99m Tc*	6.02 h	140.5	89.0 ± .9	22
101 Tc	14.1 min	306.9	88.7[a]	25
103 Ru	39.36 day	497.1	90 ± 2.3	21
104 Tc	18.0 min	357.8	84.4[a]	24
105 Ru	4.44 h	316.5	10.2[a]	23
		469.4	17.5[a]	23
		676.3	15.0[a]	23
		724.2	44.5[a]	23
105Rh	35.6 h	319.2	19.6[a]	23
107Rh	21.7 min	302.8	66.0[a]	25
127Sb	92.0 h	473.2	24.8[a]	25
		684.9	36.8[a]	25
129Sb	4.35 h	812.6	42.6[a]	25
131I	8.04 day	364.5	81.2 ± 1.2	22
132Te	78.2 h	228.2	88.2 ± .2	22
132I*	2.30 h	522.6	16.1 ± .6	22
		630.2	13.7 ± .6	22
		667.7	98.7 ± .2	22
		772.6	76.2 ± 1.8	22
		954.6	18.1 ± .6	22
133I	20.8 h	529.9	87.3 ± .2	22
134Te	41.8 min	210.5	22.4 ± 1.1	22
		278.0	21.8 ± 1.1	22
		435.1	19.0 ± 1.3	22
		566.0	19.3 ± 1.1	22
135I	6.61 h	1038.8	7.9 ± .3	22
		1131.5	22.5 ± .8	22
		1260.5	28.6 ± 1.0	22
		1457.6	8.6 ± .3	22
135mXe*	15.3 min	526.6	81.0 ± .4	22
138 Xe	14.2 min	258.3	31.5 ± 1.3	22

Table 5.4 (continued)

		434.5	20.3 ± .9	22
138 Cs	32.2 min	1435.9	76.3 ± 1.6	22
139 Ba	83.0 min	165.8	23.8 ± 0.3	21
140 Ba	12.79 day	537.3	24.0[a]	23
140 La*	40.23 h	328.8	21.6[a]	23
		487.0	46.5[a]	23
		815.8	24.0[a]	23
141 Ba	18.2 min	190.3	46.0[a]	26
		276.9	23.3[a]	26
		343.7	14.2[a]	26
141 Ce	32.5 day	145.4	48.0 ± 2.0	22
142 La	93.4 min	641.2	46.5[a]	23
143 Ce	93.0 h	293.2	43.5[a]	23
146 Ce	14.1 min	218.3	21.0[a]	25
		316.8	53.0[a]	25
147 Nd	11.0 day	531.0	13.1 ± .8	22
149 Nd	1.76 h	211.3	27.3 ± 1.8	22
130 Sb		793.4	99.8 ± .1	21

[a] Error of ±5% assumed
* In equilibrium with the parnet nuclide

terminated before the steady state is achieved, then the disintegration rate of a particular radionuclide is less than its rate of formation, R. The number of atoms, N, present at time, t, during an irradiation is governed by the following differential equation:

$$dN/dt = R - \lambda N \qquad 5.4$$

The solution of which is

$$R = N\lambda/(1-\exp(\lambda t_{irr})) \qquad 5.5$$

The factor $1-\exp(-\lambda t_{irr})$ is often called the saturation factor. Thus, the rate of formation of a radionuclide in fission could be obtained by dividing its disintegration rate at the end of a steady bombardment of known duration by this saturation factor. In practice, however, the rate of formation R was not constant during the irradiation, because of variations of beam current and condition of the target during the bombardment. Fig. 5.10 shows fluctuations of neutron output with time, recorded by a multiscaler, electronic system. These variations were corrected for by dividing the bombardment period into time intervals Δt during each of which the rate R_i was approximately steady. Therefore the equation of 5.5 was modified to

$$N = \frac{1}{\lambda} \sum R_i (1-e^{-\lambda \Delta t_i}) e^{-\lambda (t_{irr} - t_i)} \qquad 5.6$$

where t_i was the time at the end of the ith interval. The computer program KRACP[18], based on equation 5.6 was used to correct for this neutron flux variation.

5.3.2 Correction for the Decay of the Precursors.

Consider an irradiation of duration, t_1, and the gamma spectrum recorded at time t_2 (decay time), after the end of the irradiation. At time t, the amount of nuclide (A,Z) will depend on the fraction of its

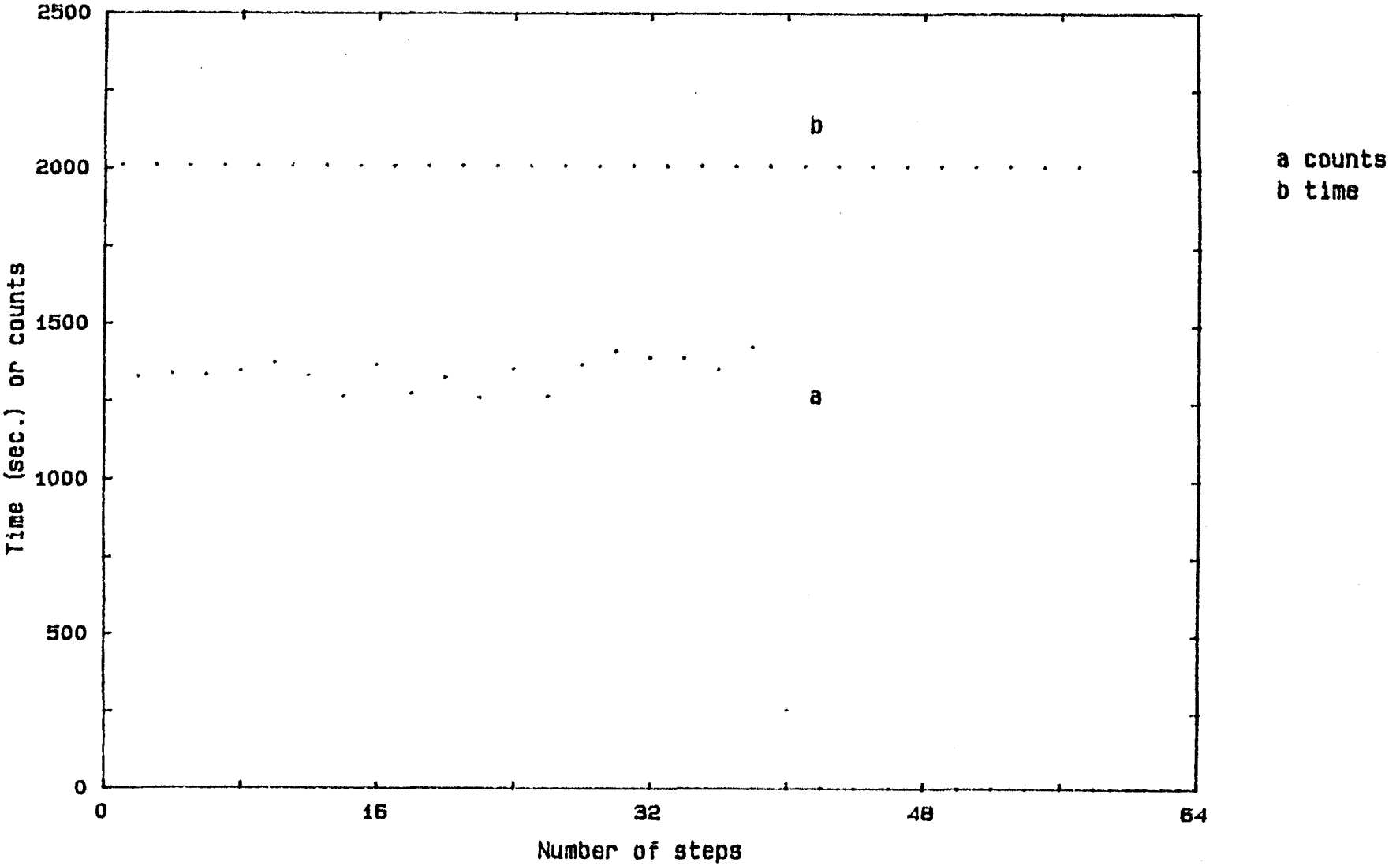

Fig. 5.10 Fluctuations of neutron output with time during an irradiation obtained with the PPC fission chamber and a multiscaler, electronic system.

precursors that have decayed to this nuclide and also on the fraction of the nuclide that has not decayed. The decay correction for fission products of interest depend to genetic relationship and their half-lives and it is applied by the following way:

i) Nuclide (A,Z) is shielded or has short-lived precursors.

This is the simplest case and most of the fission fragments under study in these experiments come under this category. In this case, the nuclide may be considered to be produced at an irregular rate during the irradiation; it therefore requires a correction factor, d, for this irregularity. The absolute independent or cummulative yield, Y(A,Z), of this nuclide can be calculated from the relation

$$Y_i(A,Z) = \frac{S_i}{E_i . I_k} \cdot \frac{F.d}{FCR}$$

Where

S_i is the peak area,

E_i and I_k denote the detector efficiency and absolute intensity for the Kth gammma ray of the studied nuclide respectively.

I_k is the product of the branching ratios of the parent and daughter nuclides leading to the gamma ray of interest. FCR represents the fission chamber count rate during the irradiation or that from a monitor foil, and

F is a function of irradiation time(t_1), decay time(t_2) and counting time (t_3), and of the corresponding decay constant λ.

F is calculated from

$$F = \frac{\lambda}{(1-\exp(-\lambda t_1))\exp(-\lambda t_2)(1-\exp(-\lambda t_3))} \qquad 5.8$$

The relative independent or cumulative yield can be determined with following expression

$$Y_x(A,Z) = Y_R \cdot \frac{(S_i/E_i I_i)_x}{(S_j/\epsilon_j I_j)_R} \cdot \frac{F_x}{F_R} \qquad 5.9$$

where R indicates the reference nuclide.

ii) Nuclide (A,Z) has one precursor of a half-life comparable to the irradiation and/or decay time, which is shielded or has short lived precursors. The absolute or cumulative fission yield for both $Y(A,Z)=Y_2$ and $Y(A,Z-1)=Y_1$ can be determined from the following equation

$$Y_2 = [(\frac{S_i}{E_i I_i})_2 \cdot \frac{F_2}{FCR} - BK\ (\frac{S_i}{E_i I_i})_1 \cdot \frac{F_i}{FCR} \cdot \frac{d_1}{d_2}] \cdot d_2 \qquad 5.10$$

Where B is the branching ratio of the precursor and K accounts for the build up from (A,Z-1) during the irradiation and decay time

$$K = \frac{1}{\lambda_2 - \lambda_1} [\lambda_2 \frac{1-\exp(-\lambda_1 t_1)}{1-\exp(-\lambda_2 t_1)} \cdot \exp((\lambda_2 - \lambda_1) t_2) - \lambda_1] \qquad 5.11$$

d_1 and d_2 denote the correction for neutron irregularity.

The relative independent or cumulative yield can be determined[19] as follows

$$\frac{Y_2}{Y_R} = \frac{(S_i/E_i I_i)_2}{(S_j/W_j I_j)_R} \cdot \frac{F_2}{F_R} \cdot d_2 - BK \frac{Y_1}{Y_R} \cdot d_1 \qquad 5.12$$

Where Y_1 can be calculated by Eq. 5.7.

iii) In the calculation of the fission yield for two isobars (A,Z-1) and (A,Z), the following equation can be used

$$\frac{Y_1}{Y_2} = \frac{(S_i/E_i I_i)_1}{(S_j/E_j I_j)_2} \cdot \frac{F_1}{F_2} - \frac{B}{\lambda_1 - \lambda_2} (\lambda_1 \cdot \frac{F_1}{F_2} - \lambda_2) \qquad 5.13$$

where Y_1 is for (A,Z-1) and Y_2 is for (A,Z). This equation can also be used for isomer ratio in which, by substituting the subscript 1 by m and 2 by g and B by P, the transition probability from metastable (m) to groundstate (g)

$$\frac{\sigma_g}{\sigma_m} = \frac{Y_g}{Y_m} = \frac{(S_i/E_i I_i)_g}{(S_g/E_g I_g)_m} - \frac{F_g}{F_m} - \frac{P}{\lambda_g - \lambda_m}\left(\lambda_g \frac{F_g}{F_m} - \lambda_m\right) \qquad 5.15$$

In the above equations Y_2 and Y_m are calculated by Eq. 5.7.

iv) Nuclide (A,Z) has two precursors of comparable half-lives, i.e. a fission product chain of the (1) B_1 (2) B_2 (3). The yield of the three isobars using the Bateman equations, are related by the following relations

$$Y_3 = \left(\frac{S_1}{E_1 I_i}\right)_3 F_3 - B_2 K Y_2 - B_1 B_2 L Y_1 \qquad 5.15$$

where

$$L = \frac{1}{1-\exp(-\lambda_3 t_1)}\{1 + \frac{\lambda_2 \lambda_3}{(\lambda_2-\lambda_1)(\lambda_3-\lambda_1)}[(1-\exp(-\lambda_1 t_1))\exp((\lambda_3-\lambda_1)t)-1]$$

$$+ \frac{\lambda_1 \lambda_3}{(\lambda_1-\lambda_2)(\lambda_3-\lambda_2)}[(1-\exp(-\lambda_2 t_1))\exp((\lambda_3-\lambda_2)t)-1] -$$

$$- \frac{\lambda_1 \lambda_2}{(\lambda_1-\lambda_3)(\lambda_2-\lambda_2)}\exp(-\lambda_3 t_1)\}$$

The value of Y_1 and Y_2 can be calculated by Eqs. 5.7 and 5.10 respectively.

5.5 Results and Discussion

The fission-products gamma decay data selected for use in these measurements are presented with references in Table 5.4. For data involving gamma-ray counting, a major source of error arises from the values taken for the absolute gamma emission intensities, I (listed for photons per 100 disintegration in Table 5.4). This error is an inherent one and depends upon the best data available. To minimize the overall error, however, we took data for each of the fission products from more than 20 spectra at each neutron energy but the yield for a given fission product was deduced only from those spectra having decay times comparable to the half-life of that product. The presence of a

given fission product in the other spectra served to verify the true identification of the specific product measured, by observing its respective half-life. The total numbers of counts recorded in a complete γ-ray spectrum obtained during the course of these experiments are given in Table 5.5 for short decay times.

Fission product yields obtained at different neutron energies are given in Tables 5.6 and 5.7 for 32 fission products and are compared with the only available, published values in Tables 5.8-5.12. In Table 5.6 two values for each fission product are quoted in each column. The value on the left-hand side is that obtained experimentally without any correction. That quoted on the right hand side is the value after correction for the self-absorption of gamma rays in the uranium disc. Values of the mass absorption coefficients used for these corrections were taken from Fig. 5.8. Table 5.7 shows the corrected fission yield values with their calculated errors. The uncertainties in the present work include those outlined below.

1- The uncertainty assigned to the absolute emission intensities of the gamma rays.

2- A 10% uncertainty assigned to the Ge detector efficiency calibration.

3- A 2% uncertainty assigned to the fission chamber detection efficiency and a 6% uncertainty in the case of activation foils.

4- Uncertainties in the peak areas calculated for each irradiation time and counting period taken from the output of the SAMPO program. The sets of peak areas so derived for each nuclide were then fitted by a least-squares program, taking the peak area as a function of the product of the radiation, counting and decay times. This then allows the overall error in the peak areas to be calculated with values ranging between .5% and 19% .

Table 5.5 The total count and count rate recorded after a short irradiation and for short decay times

Irradiation time	Decay time	Counting time	Total counts	Counts/Rate
40.5	5.5 min	373.3 sec	263821	706.726
"	"	638.8 sec	412358	645.5
"	"	987.0 "	577639	585.3
"	"	1324.9 sec	713941	538.8
"	28.5 min	4074.3	890640	218.6
"	98 min	3715.5 sec	437791	117.8
153	30.5	955.4 sec	478100	500.4
"	"	1886.2 sec	846522	448.7
"	"	2743.9 sec	1129981	411.8
"	"	3735.8 sec	1409642	377.3

Table 5.6

Fission products yields obtained with and without a self-absorption correction for different neutron energies

Fission Product	Gamma energy (KeV)	Neutron Energy (KeV) 1722		2160		3726		4782		5982	
85mKr	151.2	.49	.71	.57	.83	.55	.801	.67	.98	.73	1.06
87 Kr	402.6	1.16	1.22	1.02	1.06	1.33	1.38	1.46	1.524	1.47	1.52
88 Kr	196.3	1.32	1.6	1.22	1.48	1.46	1.77	1.65	2.0	1.68	2.04
89 Rb	1031.9	3.21	3.26	2.97	3.02	2.90	2.95	3.60	3.66	3.1	3.15
89 Rb	1248.1	2.84	2.87	3.0	3.03	2.9	2.93				
92 Sr	1383.9	4.27	4.38	4.41	4.45	4.86	4.91	3.44	3.475	3.71	3.74
94 Y	919.2	4.32	4.37	4.44	4.47	4.51	4.57	4.71	4.77	4.86	4.92
101Tc	306.9	7.28	7.83	6.51	6.99	6.97	7.49	6.1	6.56	5.86	6.3
104Tc	357.8	4.54	4.82	4.44	4.73	3.88	4.13	4.70	5.0	3.64	3.87
134Te	566	6.48	6.65	6.38	6.54	5.96	6.11	6.13	6.28	5.17	5.31
138Xe	258.3	-		4.65	5.29	4.71	5.36			4.95	5.64
						4.65	5.29				
138Xe	434.5			5.77						4.68	
138Cs	1435.9	6.11	6.18	6.02	6.08	5.85	5.91	5.9	5,96	6.46	6.52
139Ba	165.8							5.53			
141Ba	343.7	4.71	4.98	4.67	4.94	4.72	4.99	4.81	5.09	4.92	5.21
142La	641.2	4.93	5.04	4.68	4.78	4.99	5.10	3.73	3.81	4.52	4.62
146Ce	218.3	3.063	3.64	3.97	4.72	3.57	4.25	3.64	4.33	3.27	3.89
				3.51	4.17						
146Ce	316.8	3.16	3.39	3.29	3.54	3.21	3.45	3.31	3.55	3.14	3.38
						3.11	3.34				
91 Sr	653							3.53			
91 Sr	749.8	3.56	3.63	3.51	3.57	3.30	3.36	3.56	3.62	3.44	3.50
91 Sr	1024.3	3.87	3.92	4.27	4.32	3.99	4.04			3.71	3.76
91mY	555.6	3.72	3.82	3.26	3.34	3.37	3.46				
93 Y	267	4.59	5.16	4.1	4.55	4.66	5.23	3.66	4.11	3.81	4.28

Table 5.6 (continued)

105Ru	316.5	4.32	4.65	3.72	3.99	4.49	4.83			3.61	3.88
105Ru	469.4	3.52	3.65	3.2	3.32	3.21	3.33			4.36	4.52
105Ru	724.2	4.29	4.37	4.0	4.07	3.74	3.81	3.65	3.71	3.63	3.69
129Sb	812	.43	.44	.43	.43	.61	.62	.74	.75	1.09	1.11
135I	1038.8	7.26	7.35	6.96	7.04	6.62	6.69	6.52	6.59	6.12	6.19
135I	1131.5	6.65	6.73	7.42	7.51	6.97	7.05	6.69	6.77	6.22	6.29
135I	1260.5	7.25	7.32	6.87	6.95	7.05	7.12	6.50	6.56	6.23	6.30
										6.27	
97mNb	743.4	5.13	5.22	5.44	5.54	5.36	5.46	5.23	5.32	5.03	5.12
97gNb	657.9	5.38	5.48			5.81	5.93	5.47	5.58	5.57	5.68
133I	529.9	6.88	7.08	6.77	6.97	6.32	6.50	6.0	6.17	6.74	6.93
143Ce	293.2	4.27	4.60	4.17	4.49	4.08	4.39	4.15	4.47	4.31	4.64
127Sb	473.2							.24	.24	.26	.27
127Sb	684.9							.38	.39	.36	.37
132I*	522.6	5.31	5.47	5.23	5.38	4.46	4.59	4.19	4.31	4.43	4.56
132I*	630.2	4.52	4.62	6.01	6.14	4.59	4.69	4.26	4.35	4.39	4.48
132I*	667.7	4.91	5.01	5.93	6.05	5.96	6.08	5.08	5.18	5.21	5.32
132I*	772.6	4.82	4.90	5.6	5.70	5.06	5.15	4.81	4.89	4.66	4.74
132I*	954.6			5.17	5.24	4.96	5.02	4.78	4.84	4.87	4.93
105Rh	319.2	4.43	4.74	4.40	4.71	4.32	4.63			4.53	4.85
140Ba	537.3	5.52	5.67	5.57	5.73	5.43	5.58	5.9	6.06	5.70	5.86
140La*	328.8	5.46	5.82	5.75	6.13	5.17	5.51	5.81	6.20		
140La*	487.0			5.42	5.59	5.46	5.63			5.67	5.85
140La*	815.8	5.61	5.69	5.55	5.64					5.75	5.84
147Nd	531	2.58	2.64	2.67	2.73	2.71	2.77	2.68	2.74	2.86	2.93
103Ru	497.1	6.5	6.68	6.3	6.48	6.1	6.27	5.7	5.86	5.8	5.96
95 Zr	756.7	5.28	5.37	5.24	5.33	5.66	5.75	5.2	5.29	5.3	5.39
149Nd	211	1.38	1.65	1.41	1.68	1.54	1.84	1.43	1.71	1.35	1.61
107Rh	302.8	.62	.67	.76	.82	.75	.81	.85	.92	1.09	1.17
131I	364.5	3.35	3.57	3.32	3.53	3.43	3.65	3.63	3.86	3.49	3.72

Table 5.7

Fission products yields obtained from determination of all the γ-rays emitted from a specific nuclide for different neutron energies

Fission Product	Gamma Energy (KeV)	Neutron Energy (KeV) 1722	2160	3726	4782	5982
85mKr	151.2	.71 ± .07	.83 ± .12	.80 ±.08	.99 ± .10	1.06 ±.14
87 Kr	402.6	1.22 ± .15	1.06 ± .13	1.39 ±.16	1.52± .16	1.54 ±.20
88Kr	196.3	1.60 ± .17	1.48 ± .22	1.77 ±.19	2.0 ± .21	2.04 ±.23
89Rb	1031.9	3.26 ± .36	3.02 ± .39	2.95 ±.45	3.66± .50	3.15 ±.39
89Rb	1248.1	2.87 ± .36	3.03 ± .43	2.93 ±.40		
91Sr	749.8	3.63 ± .37	3.57 ± .41	3.36 ±.40	3.62± .38	3.50 ±.41
91Sr	1024.3	3.92 ± .40	4.32 ± .48	4.04 ±.41		3.76 ±.41
91mY	555.6	3.82 ± .39	3.34 ± .40	3.46 ±.35		
92 Sr	1383.9	4.38 ± .40	4.45 ± .47	4.90 ±.51	3.48± .38	3.74 ±.38
93Y	267	5.16 ± .54	4.55 ± .47	5.23 ±.57	4.11± .43	4.28 ±.47
94Y	919.2	4.37 ± .53	4.47 ± .55	4.57 ±.56	4.77± .52	4.92 ±.50
95 Zr	756.7	5.37 ± .57	5.33 ± .57	5.75 ±.63		5.39 ±.55
97mNb	743.4	5.22 ± .57	5.54 ± .58	5.46 ±.56		5.12 ±.52
97gNb	657.9	5.48 ± .63		5.93 ±.61		5.68 ±.58
101Tc	306.9	7.83 ± .93	6.99 ± .77	7.49 ±.79	6.56± .68	6.30 ±.74
103Ru	497.1	6.68 ± .70	6.48 ± .67	6.27 ±.64	5.86± .62	5.96 ±.62
104Tc	357.8	4.82 ± .52	4.73 ± .54	4.13 ±.45	5.0 ± .53	3.87 ±.46
105Ru	469.4	3.65 ± .41	3.32 ± .38	3.33 ±.37		4.52 ±.47
105Ru	676.3	4.37 ± .41	4.45 ± .47	3.58 ±.39	3.71 ± .40	
107Rh	302.8	.67 ± .21	.82 ± .23	.81 ±.18	.92 ± .20	1.17 ±.15
127Sb	473.2	-	-	-	.24 ± .05	.27 ±.06
127Sb	684.9	-	-	-	.39 ± .04	.37 ±.04
129Sb	812	.44 ± .7	.43 ± .05	.62 ±.08	.75 ± .09	1.11 ±.12
132I*	772.6	4.90 ± .50	5.69 ± .59		4.89 ± .51	4.74 ±.48
132I*	667.7	5.01 ± .71	6.05 ± .62	6.08 ±.63	5.18 ± .53	5.32 ±.54
132I*	630.2	4.62 ± .58	6.14 ± .69	4.69 ±.53	4.35 ± .46	4.48 ±.46
132I*	522.6	5.47 ± .59	5.38 ± .59	4.59 ±.53	4.31 ± .46	4.56 ±.47
131I	364.5	3.57 ± .37	3.53 ± .37	3.65 ±.37	3.86 ± .39	3.72 ±.38
133I	529.9	7.08 ± .71	6.96 ± .72	6.50 ±.67	6.17 ± .63	6.94 ±.76
134Te	566	6.64 ± .74	6.54 ± .71	6.11 ±.75	6.28 ± .72	5.31 ±.61
135I	1038.8	7.35 ± .77	7.04 ± .76		6.59 ± .73	6.19 ±.65
135I	1131.5	6.73 ± .67	7.51 ± .83	7.05 ±.75	6.77 ± .70	6.29 ±.80
135I	1260.5	7.32 ± .78	6.95 ± .73	7.12 ±.94	6.56 ± .68	6.53 ±.69
138Cs	258.3		5.29 ± .57	5.36 ±.60		5.64 ±.59
				5.29 ±.58		
139Ba	165.8				5.53 ± .71	
140Ba	537.3	5.67 ± .61	5.73 ± .63	5.73 ±.60	6.06 ± .63	5.86 ±.64
140La*	328.8	5.82 ± .62	6.13 ± .64	5.51 ±.58	6.20 ± .66	
140La*	487.0		5.59 ± .59	5.63 ±.73		5.84 ±.87
140La*	815.8	5.69 ± .62	5.64 ± .64			5.21 ±.63
141Ba	343.7	4.98 ± .65	4.67 ± .51	4.99 ±.79	5.09 ± .55	5.21 ±.63
142La	641.2	5.04 ± .59	4.79 ± .52	5.10 ±.53	3.81 ± .39	4.62 ±.48
143Ce	293.2	4.60 ± .55	4.49 ± .50	4.39 ±.45	4.47 ± .46	4.64 ±.55
146Ce	316.8	3.29 ± .39	3.54 ± .46	3.45 ±.45	3.55 ± .39	3.38 ±.45
				3.34 ±.43		
147Nd	531	2.64 ± .42	2.73 ± .44	2.77 ±.43	2.74 ± .34	2.93 ±.30
149Nd	211	1.65 ± .25	1.68 ± .26	1.84 ±.28	1.71 ± .22	1.61 ±.20

* in equilibrium with parnet nuclide

Table 5.8

Comparison of experimental fission product yields determined at E_n = 1.72 with those reported at E_n = 1.5 MeV

Fission Product	Yield This work	Nagy etal[5]
85mKr	.71 ± .07	.79 ± .05
87 Kr	1.22 ± .15	1.6 ± .10
88 Kr	1.6 ± .18	1.71 ± .13
89 Rb	3.26 ± .36	
	2.87 ± .36	
		2.34 ± .31
91 Sr	3.63 ± .37	
	3.92 ± .40	
91mY	3.82 ± .39	

	3.78 ±	3.93 ± .22
92 Sr	4.38 ± .46	4.18 ± .24
93 Y	5.16 ± .54 *	4.36 ± .31
94 Y	4.37 ± .53	4.45 ± .33
95 Zr	5.37 ± .57	5.31 ± .21
97mNb	5.22 ± .57	
	5.48 ± .63	

97Zr(Nb)	5.34 ± .42 *	5.36 ± .16
101 Tc	7.83 ± .93	6.41 ± .56
103 Ru	6.68 ± .70	6.96 ± .31
104 Tc	4.82 ± .52	5.17 ± .33
105 Ru	4.65 ± .57	
	3.65 ± .41**	
	4.37 ± .48	
105Rh	4.74 ± .71	

105Ru(Rh)	4.54 ± .26	4.68 ± .26
107Rh	.67 ± .20	.54 ± .47
129Sb	.44 ± .07	.43 ± .06
131I	3.57 ± .37	3.24 ± .13
132I	4.90 ± .50	
	5.01 ± .71	
	4.62 ± .58	
	5.46 ± .59	

	4.98 ± .29	5.40 ± .14
133I	7.08 ± .71	7.15 ± .22
134TE	6.64 ± .74 *	8.12 ± .40
135I	7.35 ± .77	
	6.73 ± .67	
	7.32 ± .78	

	7.1 ± .42	7.23 ± .22
138CS	6.17 ± .65 *	
138CS,XE		5.27 ± .19
140Ba	5.67 ± .61	

Table 5.8 (continued)

140La	5.82 ± .62	
140La	5.69 ± .62	

140Ba(La)	5.72 ± .36	6.01 ± .18
141Ba	4.98 ± .65	-
142La	5.04 ± .59	4.69 ± .29
143Ce	4.60 ± .55	4.63 ± .29
146Ce	3.64 ± .65	
	3.29 ± .39	

	3.38 ± .33	3.82 ± .32
147Nd	2.64 ± .42	2.65 ± .35
149Nd	1.65 ± .25	1.74 ± .37

Table 5.9

As for Table 5.8, for experimental values at E_n = 2.16 MeV compared to reported values at 2.0 MeV

Fission Product	This work	yield Nagy etal[5]	Flynn[27]
85mKr	.83 ± .12	.77 ± .03	.75 ± .11
87 Kr	1.06 ± .13	1.57 ± .07	1.53 ± .22
88 Kr	1.48 ± .22	1.95 ± .09	1.79 ± .26
89 Rb	3.02 ± .39		
	3.03 ± .43	2.26 ± .30	
89Sr			2.48 ± .37

89Rb,Sr	3.02 ± .29	2.26 ± .30	2.48 ± .37
91 Sr	4.32 ± .41		
	3.34 ± .48		
91mY	3.34 ± .39		

91Sr(Y)	3.69 ± .33	3.94 ± .21	3.97 ± .60
92Sr	4.45 ± .47	4.1 ± .23	
93 Y	4.55 ± .47	4.80 ± .31	4.58 ± .69
94 Y	4.47 ± .55	4.40 ± .30	
95 Zr	5.33 ±	5.14 ± .19	5.11 ± .77
97mNb	5.54 ± .58		
	---		
97 Zr	5.54 ± .58	5.58 ± .14	5.79 ± .86
101Tc	6.99 ± .77	6.45 ± .49	
103Ru	6.48 ± .67	7.03 ± .22	6.85 ± 1.03
			4.76 ± .71
104Tc	4.73 ± .54	4.88 ± .31	
105Ru	3.99 ± .46		4.44 ± .66
	3.32 ± .39**	4.52 ± .31	4.51 ± .67
	4.45 ± .47		
105Rh	4.71 ± .50		

105Ru,Rh	4.36 ± .32	4.52 ± .24	
107Rh	.82 ± .23	1.05 ± .27	
129Sb	.43 ± .05	.40 ± .05	.46 ± .07
		.38 ± .05	.33 ± .05
131I	3.53 ± .37	3.25 ± .09	3.37 ± .50
			2.46 ± .37
132I	5.38 ± .59		4.59 ± .69
	6.14 ± .68		4.16 ± .62
	6.05 ± .62		
	5.69 ± .59		

132Te(I)	5.78 ± .31	5.23 ± .14	4.59 ± .69
			4.16 ± .62
133I	6.96 ± .72	7.12 ± .21	7.05 ± 1.06
			6.6 ± .99
134Te	6.54 ± .71	7.78 ± .37	
135I	7.04 ± .76	7.20 ± .20	6.24 ± .93
	7.51 ± .83		5.34 ± .80
	6.95 ± .73		

Table 5.9 (continued)

	7.14 ± .44		
138Cs	5.29 ± .57		
138Xe		5.69 ± .19	
138Cs,Xe	5.29 ± .57	5.69 ± .19	
140Ba	5.73 ± .63		5.77 ± .86
140La	6.13 ± .64		5.97 ± .89
	5.59 ± .59		
	5.64 ± .64		

140Ba(La)	5.76 ± .31	6.1 ± .13	
141Ba	4.67 ± .51	5.73 ± .30	
141Ce		5.55 ± .36	5.69 ± .85
			5.61 ± .84
141Ba,Ce			
142La	4.79 ± .52	4.66 ± .29	4.54 ± .68
143Ce	4.49 ± .50	4.62 ± .25	4.28 ± .64
		4.71 ± .29	4.92 ± .74
146Ce	4.72 ± .62		
	4.17 ± .55		
	3.54 ± .46		

	3.86 ± .43	3.72 ± .27	
147Nd	2.73 ± .44	2.82 ± .37	
149Nd	1.68 ± .26	1.72 ± .20	

Table 5.10

As for Table 5.8, for experimental values at E_n = 3.72 MeV compared to reported values at 3.9 MeV

Fission Product	yield This work	Nagy etal[5]
85mKr	.801 ± .08	.88 ± .04
87 Kr	1.39 ± .16	1.78 ± .08
88 kr	1.77 ± .19	2.09 ± .15
89 Rb	2.95 ± .45	
	2.93 ± .40	
	2.94 ± .45	2.57 ± .29
91 Sr	3.36 ± .40	
	4.04 ± .41	
91mY	3.46 ± .35	
91 Sr(Y)	3.59 ± .22	3.96 ± .28
92 Sr	4.91 ± .51	4.24 ± .25
93 Y	5.23 ± .57	4.91 ± .32
		4.31 ± .29
94 Y	4.57 ± .56	5.13 ± .39
95 Zr	5.75 ±	5.34 ± .19
97mNb	5.46 ± .56	
97gNb	5.93 ± .61	
97 Zr	5.67 ± .40	5.62 ± .15
101Tc	7.50 ± .79	7.08 ± .51
103Ru	6.27 ± .64	6.12 ± .18
104Tc	4.13 ± .45	4.74 ± .29
105Ru	4.83 ± .52	
	3.33 ± .37**	
	3.58 ± .39	
105Rh	4.63 ± .52	
105Ru,Rh	4.20 ± .40	4.40 ± .27
107Rh	.81 ± .18	1.1 ± .22
129Sb	.62 ± .08	.78 ± .07
		.61 ± .09
131I	3.65 ± .37	3.36 ± .10
132I	4.59 ± .53	
	4.69 ± .53	
	6.08 ± .63**	
132Te(I)	4.64 ± .37	4.89 ± .12
133I	6.50 ± .67	6.95 ± .25
134Te	6.11 ± .75	7.76 ± .42
135I	7.05 ± .75	6.45 ± .40
	7.12 ± .94	
	7.0 ± .58	6.45 ± .40
138Cs	5.91 ± .58	
138Xe	5.36 ± .59	
	5.29 ± .58	
138Cs,Xe	5.62 ± .41	5.82 ± .18

Table 5.10 (continued)

140Ba	5.58 ± .60	
140La	5.51 ± .58	
	5.63 ± .73	

140Ba(La)	5.56 ± .36	6.17 ± .48
141Ba	4.98 ± .79	5.85 ± .56
141Ce		5.64 ± .32
141Ba,Ce	4.99 ± .79	5.69 ± .30
142La	5.10 ± .53	4.85 ± .28
143Ce	4.39 ± .45	4.60 ± .28
		4.74 ± .29

		4.66 ± .27
146Ce	4.25 ± .54	
	3.45 ± .44	
	3.34 ± .43	

	3.60 ± .26	3.44 ± .31
147Nd	2.77 ± .34	2.70 ± .20
		3.23 ± .25
149Nd	1.84 ± .22	1.94 ± .20
		1.95 ± .24

Table 5.11

As Table 5.8, for experimental values of E_n = 4.78 MeV

Fission Product	yield This Work
85mKr	.99 ± .10
87 Kr	1.52 ± .16
88 Kr	2.0 ± .21
89 Rb	3.66 ± .50
91 Sr	3.62 ± .38
92 Sr	3.47 ± .38
93 Y	4.11 ± .43
94 Y	4.77 ± .52
99 M0	6.77 ± .70
101Tc	6.56 ± .68
103Ru	5.86 ± .62
104Tc	5.0 ± .53
105Ru	3.71 ± .40
107Rh	.92 ± .2
127Sb	.24 ± .05
	.39 ± .04

	.33 ± .03
129Sb	.75 ± .09
131I	3.86 ± .39
132I	4.89 ± .51
	5.18 ± .53
	4.35 ± .46
	4.31 ± .46

	4.63 ± .24

Fission Product	yield This work
133I	6.172 ± .63
134Te	6.28 ± .72
135I	6.59 ± .73
	6.77 ± .70
	6.57 ± .68

	6.64 ± .40
138Cs	5.96 ± .62
139Ba	5.53 ± .71
140Ba	6.06 ± .63
140La	6.2 ± .66

	6.14 ± .45
141Ba	5.09 ± .55
142La	3.81 ± .39
143Ce	4.47 ± .46
146Ce	4.33 ± .45
	3.55 ± .38

	3.86 ± .29
147Nd	2.74 ± .34
149Nd	1.71 ± .22

Table 5.12

As Table 5.8, for experimental values of E_n = 5.98 MeV compared to reported values at 5.5 MeV

Fission Product	Yield This work	Yield Nagy etal[5]
85mKr	1.06 ± .14	1.03 ± .06
87 Kr	1.54 ± .20	1.90 ± .11
88 Kr	2.04 ± .23	2.05 ± .15
89 Rb	3.15 ± .39	2.86 ± .37
91 Sr	3.50 ± .41	3.76 ± .41
91 Sr(Y)	3.62 ± .29	3.63 ± .21
92 Sr	3.74 ± .38	3.96 ± .25
93 Y	4.28 ± .47	4.93 ± .34
94 Y	4.92 ± .50	5.11 ± .37
95 Zr	5.39 ± .55	5.59 ± .19
97mNb	5.12 ± .52	
97gNb	5.68 ± .58	
97 Zr(Nb)	5.37 ± .38	5.44 ± .15
101Tc	6.30 ± .74	6.53 ± .55
104Tc	3.87 ± .46	4.49 ± .29
105Ru	3.88 ± .42	
	4.52 ± .47	
105Rh	4.85 ± .57	
105Ru(Rh)	4.33 ± .29	3.87 ± .31
107Rh	1.17 ± .15	1.40 ± .59
127Sb	.266 ± .06	.28 ± .04
	.369 ± .04	.40 ± .04
	.33 ± .05	
129Sb	1.11 ± .12	1.10 ± .17
		.74 ± .11
131I	3.72 ± .38	3.72 ± .14
132I	4.56 ± .47	
	4.49 ± .46	
	5.32 ± .54	
	4.74 ± .48	
132I(Te)	4.74 ± .22	5.05 ± .15
133I	6.94 ± .76	6.77 ± .20
134Te	5.31 ± .61	7.0 ± .50
135I	6.19 ± .65	
	6.29 ± .80	
	6.30 ± .70	
	6.25 ± .41	6.49 ± .19
138Cs	6.52 ± .69	
138Xe	5.64 ± .59	
138Cs,Xe	6.0 ± .45	5.8 ± .18
140Ba	5.86 ± .64	
	5.84 ± .63	
140Ba,La	5.85 ± .40	5.61 ± .15
141Ba	5.21 ± .63	5.30 ± .36
142La	4.62 ± .49	4.58 ± .28

Table 5.12 (continued)

143Ce	4.64 ± .55	4.75 ± .29
146Ce	3.89 ± .44	
	3.38 ± .45	
	3.64 ± .32	3.64 ± .30
147Nd	2.93 ± .30	2.96 ± .29
149Nd	1.61 ± .20	1.51 ± .24

5- The uncertainty assigned to $T_{\frac{1}{2}}$ is small and hence neglected.

These uncertainties were quadratically combined to give an overall error for each fission yield determination. It would be a simple matter to redetermine the fission yields or their uncertainties due to changes in the input-gamma ray branching ratio, detector efficiency or the error calculation.

Fission product yields were obtained for nuclides having half-lives between 14.1 min and 64.4 day and yields 0.33% . Yields were not obtained for every nuclide within this defined range. In particular, those which decay almost entirely by beta emission were not measured. Those whose primary gamma-ray energy was very close to an intense gamma-ray from another nuclide having a similar half-life were measured but with poor accuracy. A few gamma-rays were observed but which had doubtful provenance e.g. because only one gamma ray was observed although others were expected but not seen and were, therefore not used in yield calculations. All of the gamma rays associated with the decay of a given fission product were analysed. In general, it was found that gamma rays with higher branching ratios gave the acceptable results. As can be seen from Table 5.8 (E_n=1.726 MeV) the fission yield determinations in this work are, for most of the fission product (in good agreement) within the statistical limits, with those reported by Nagy etal[5]. There are, however, a few exceptions where the values determined in this work are different by amounts greater than the quoted standard deviation. For example, the yield determined here for ^{93}Y is higher by 15% whereas that for ^{134}Te is lower by about 18% . There are other examples of such discrepancies included in Table 5.8 and are marked with a *. For some of the products more than one value is reported for the yield, which arises from the poly-energetic nature of gamma ray emission from that particular isotope. In such cases, if all of the values lay within the

statistical error then the weighted mean of the yield was chosen as the representative value. For this purpose the χ^2 test was applied to the data set, in order to determine whether or not the spread in the data values about their weighted mean differed significantly from that expected on the basis of their individual experimental errors. As an example, the value of χ^2 per degree of freedom for the ^{91}Sr data in Table 5.8 was found to be 1.836, which corresponds to a probability value of about 16% . The spread in values of the calculated means was thus insufficient to warrant the rejection of any of the data. In contrast if any of the values were outside the statistical error (possibly attributable to the intereference from some other gamma-rays, whose origin is unknown to us at this stage), the mentioned value was considered as suspicious and not included in the calculation of the mean value. The representive mean value was then calculated using only the other values for that isotope. For example in the case of ^{105}Ru, where four values are reported, of which three are statistically reasonable but one, with the value of 3.65 ± 0.41 (marked **) is not within the statistical error limit and was rejected. In Table 5.9 (E_n=2.16 MeV), the present values seem to be in good agreement, witin statistical limits, with those reported by Nagy etal[15] and Flynn etal[21]. It is, however, worthwhile mentioning, that the errors quoted by Nagy are extremely small (about 4-5%). Such small errors seem unreasonable when considering the type of experiment he discusses. As already mentioned, it is almost impossible to reduce the overall error to less than 10% even in the most favourable cases. Unfortunately no error values were quoted by Flynn etal[27] and hence we arbitarily assigned a 15% error to all their quoted values. Table 5.13 shows the recommended fission yield values obtained in this experiment for different neutron energies.

Fig. 5.11 shows the mass distribution of fission products as a function of neutron energy, E_n. As Fig. 5.11 indicates, the mass distributions for the heavy and light mass groups in the regions near the peaks of the distribution are nearly independent of E_n. For comparision, the data for the valley region, from reference Nagy et al[5] and evaluated data for fission at 14 MeV, are shown in Figure 5.11. The data in Table 5.13 and mass distributions shown in Fig. 5.11 support the following points:

a) that there exists a strong dependence of fission yields on E_n in the valley region, which results from an increase in fission probability with increasing excitation energy,

b) that there is only a weak dependence of peak yields on E_n and these yields decrease somewhat with increasing neutron energy,

c) that there exists a mass shift at E_n=14 MeV due to increasing neutron emission in fission with increasing excitation energy and

d) the continued existence of enhnanced yield ("fine structure peak") near mass 134 at E_n=14 MeV.

Nagy etal[5] have shown that in the valley region, the variation of fission yield versus neutron energy behaves exponentially (see Fig. 5.12). They were able to fit three, separate exponential terms to the available data for the E_n ranges associated with first chance fission (1.5 to 6 MeV), second chance fission (6 to 14 MeV), and third chance fission (14 to 18 MeV). With the aid of Fig. 5.12, it is possible to describe the observed fission yield, when second-chance and third-chance fission become energetically possible, by the following equation

$$Y(E_n) = \frac{\sigma_f^1}{\sigma_f} Y_1(E_n) + \frac{\sigma_f^2}{\sigma_f} Y_2(E_n - \epsilon_n) + \frac{\sigma_f^3}{\sigma_f} Y_3(E_n - \epsilon'_n)$$

The relative amounts of first-, second- and third-chance fission yields are given by the ratio of first-, second- and third-chance

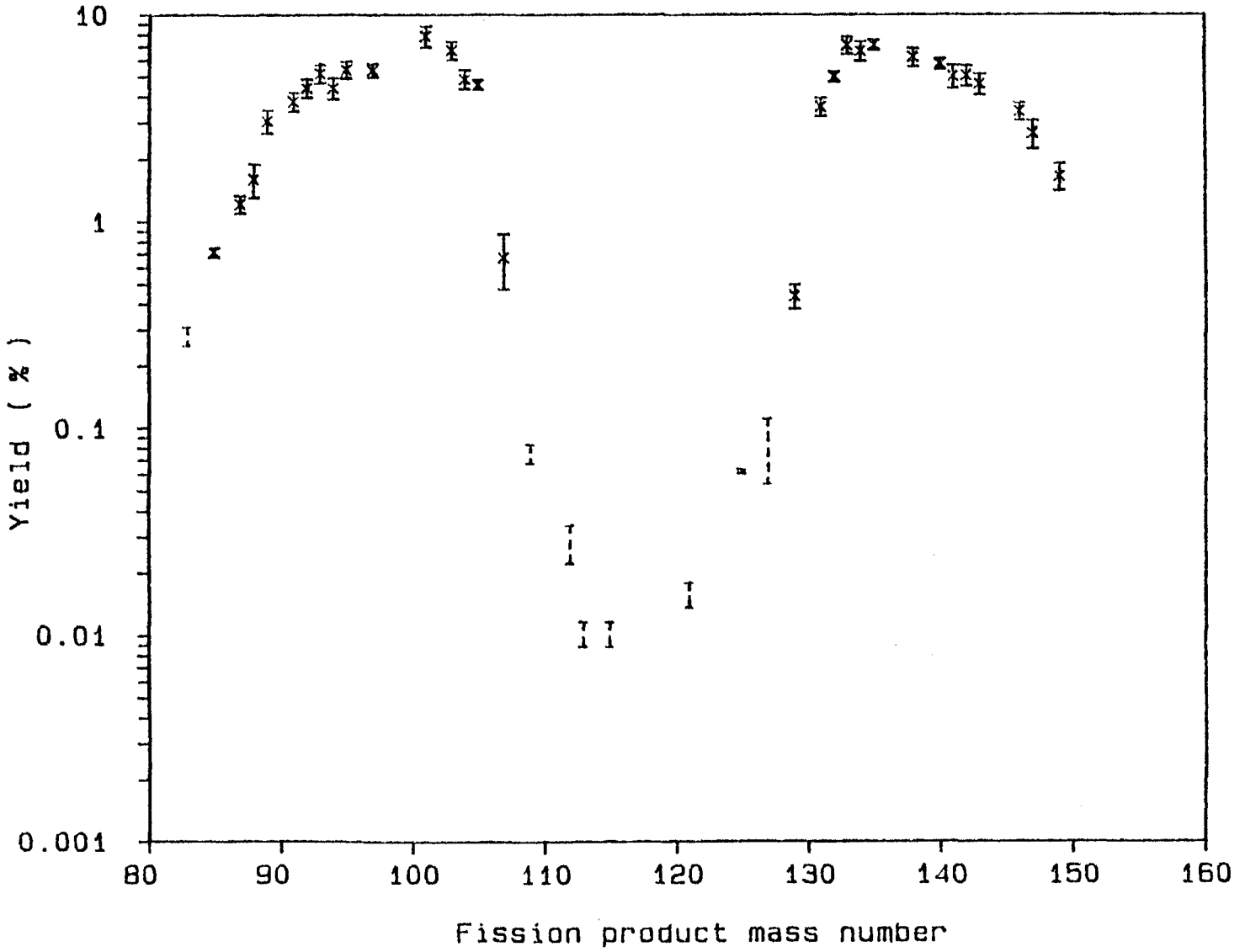

Fig. 5.11 Mass yield curve for fission of ^{238}U with 1.72 MeV neutrons.

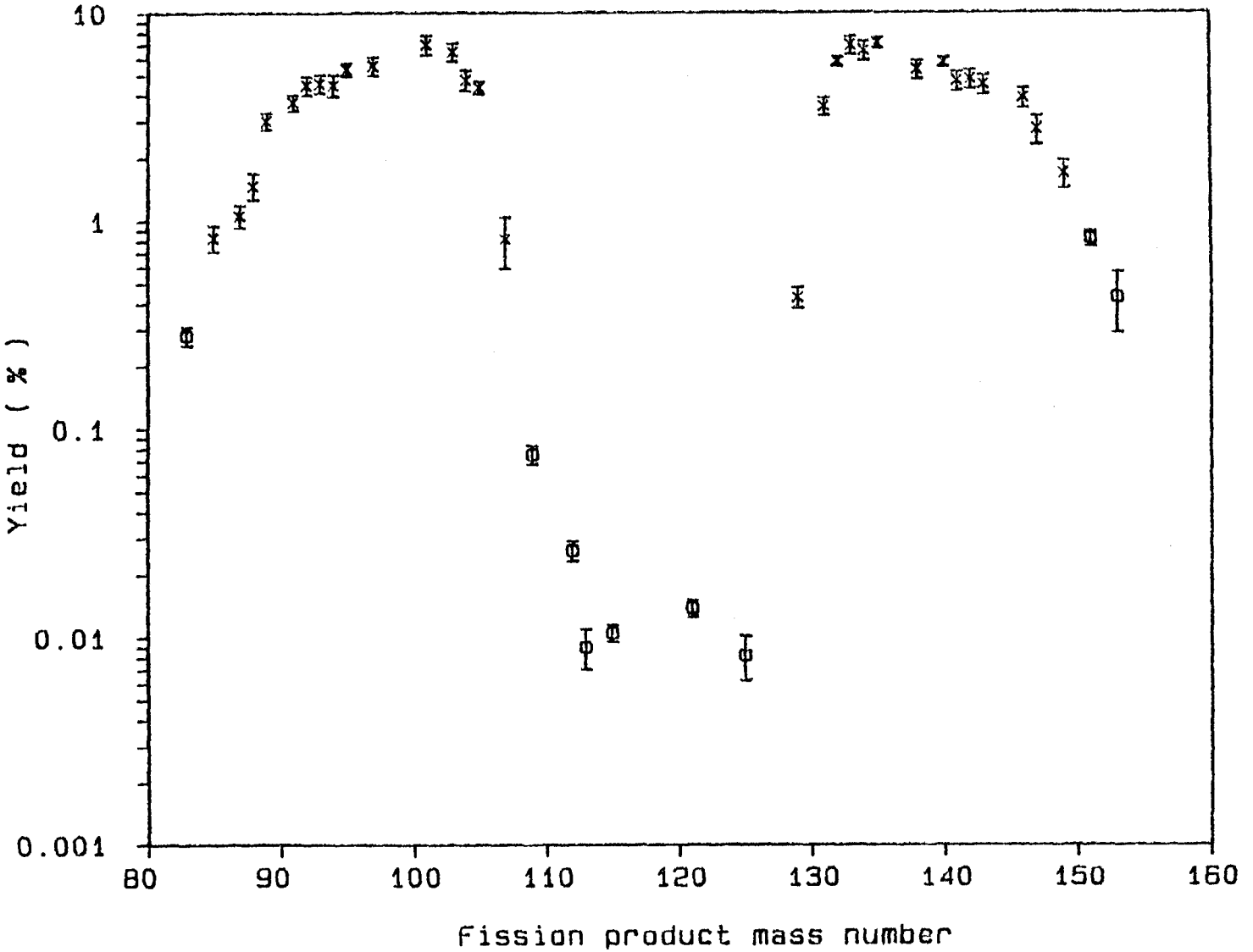

Fig. 5.12 Same as Fig. 5.11 for 2.16 MeV neutrons.

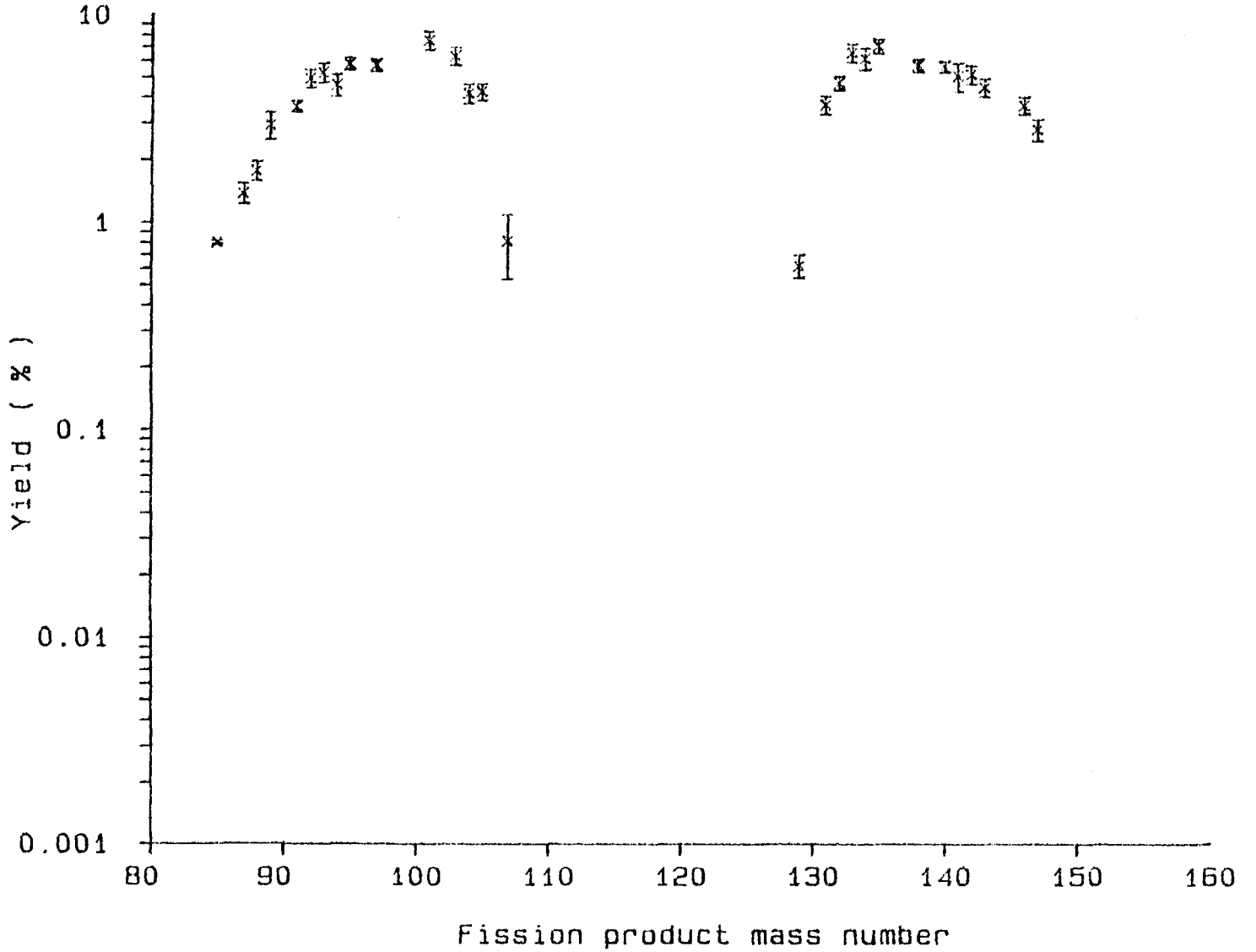

Fig. 5.13 Same as Fig. 5.11 for 3.72 MeV neutrons.

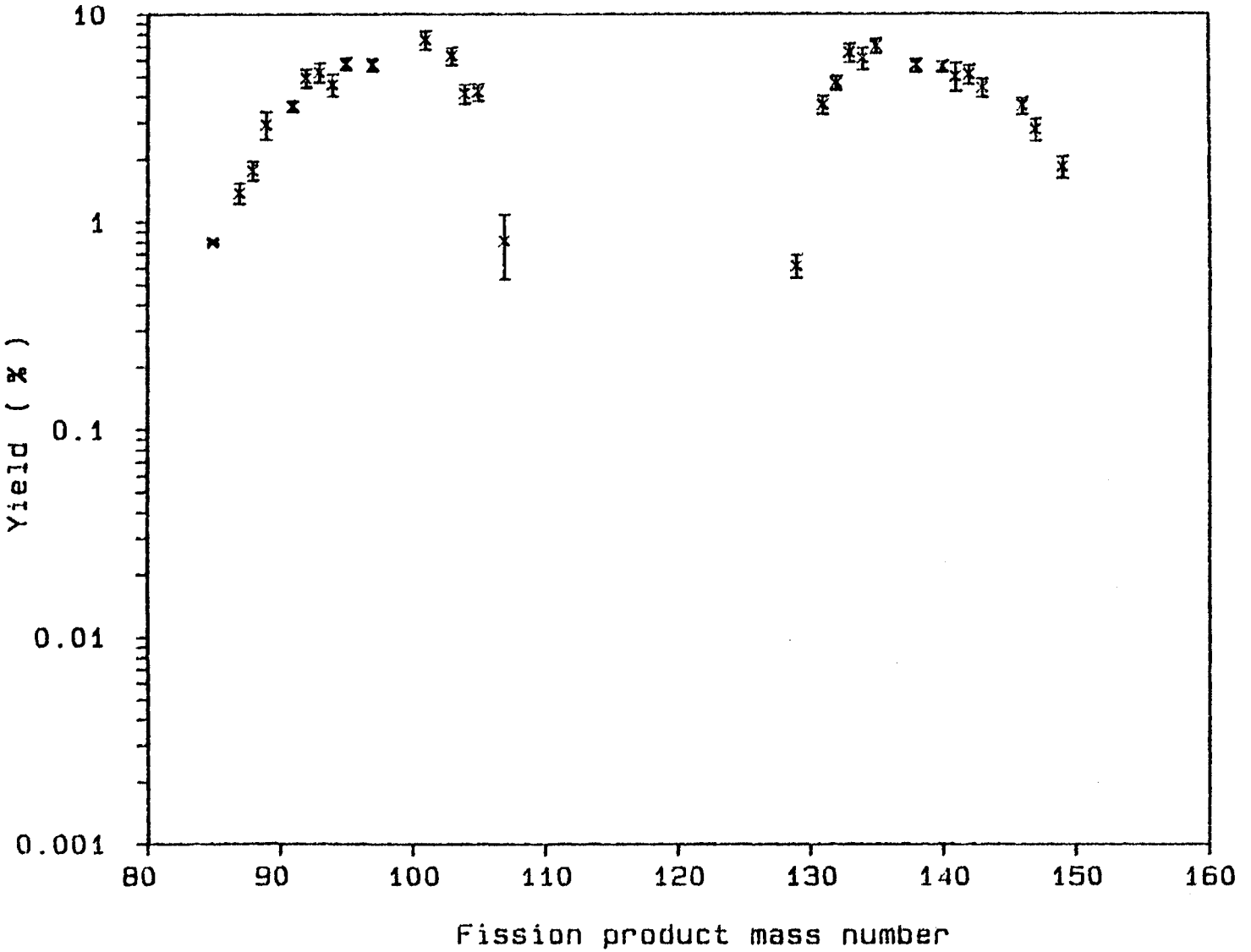

Fig. 5.14 Same as Fig. 5.11 for 4.78 MeV neutrons.

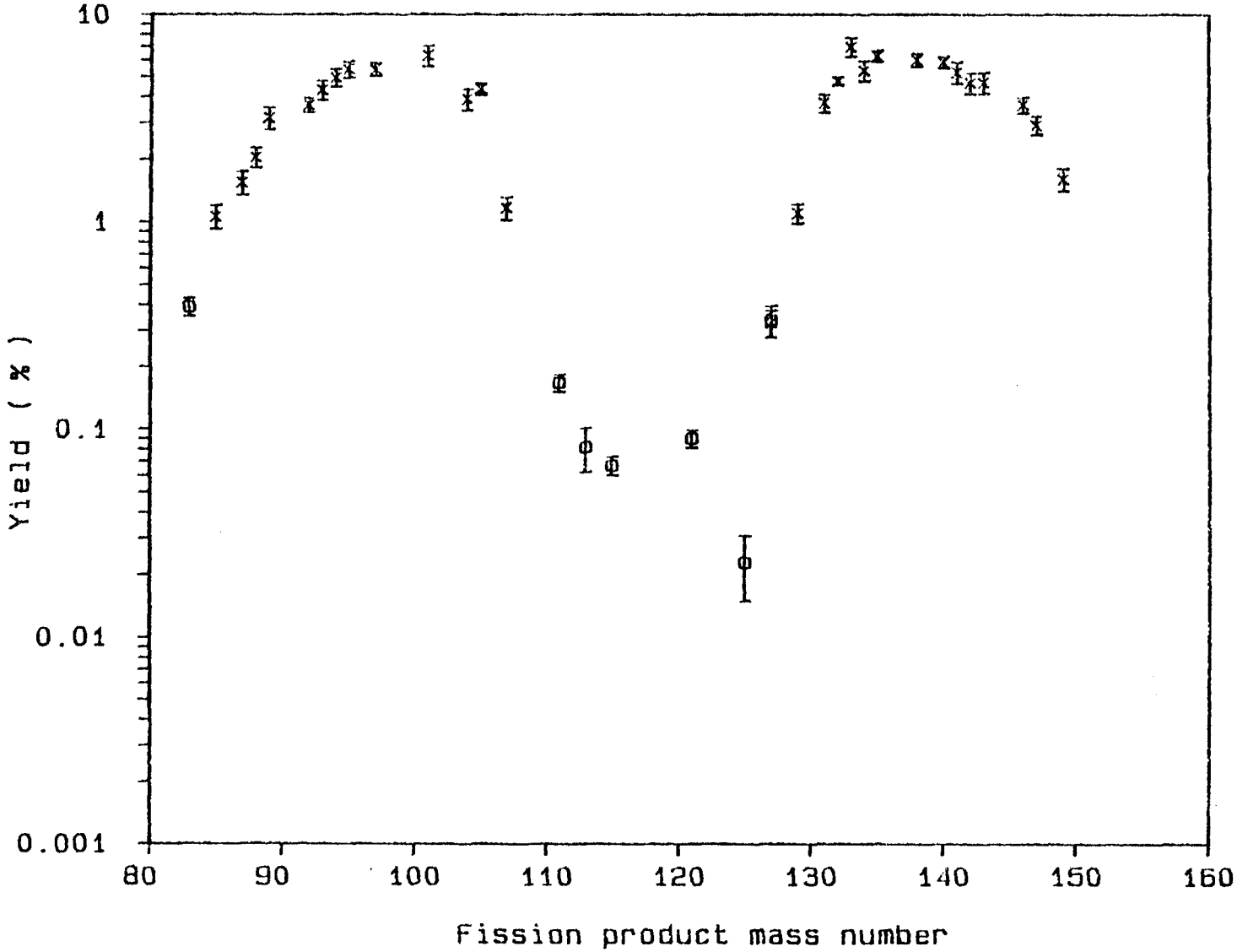

Fig. 5.15 Same as Fig. 5.11 for 5.98 MeV neutrons.

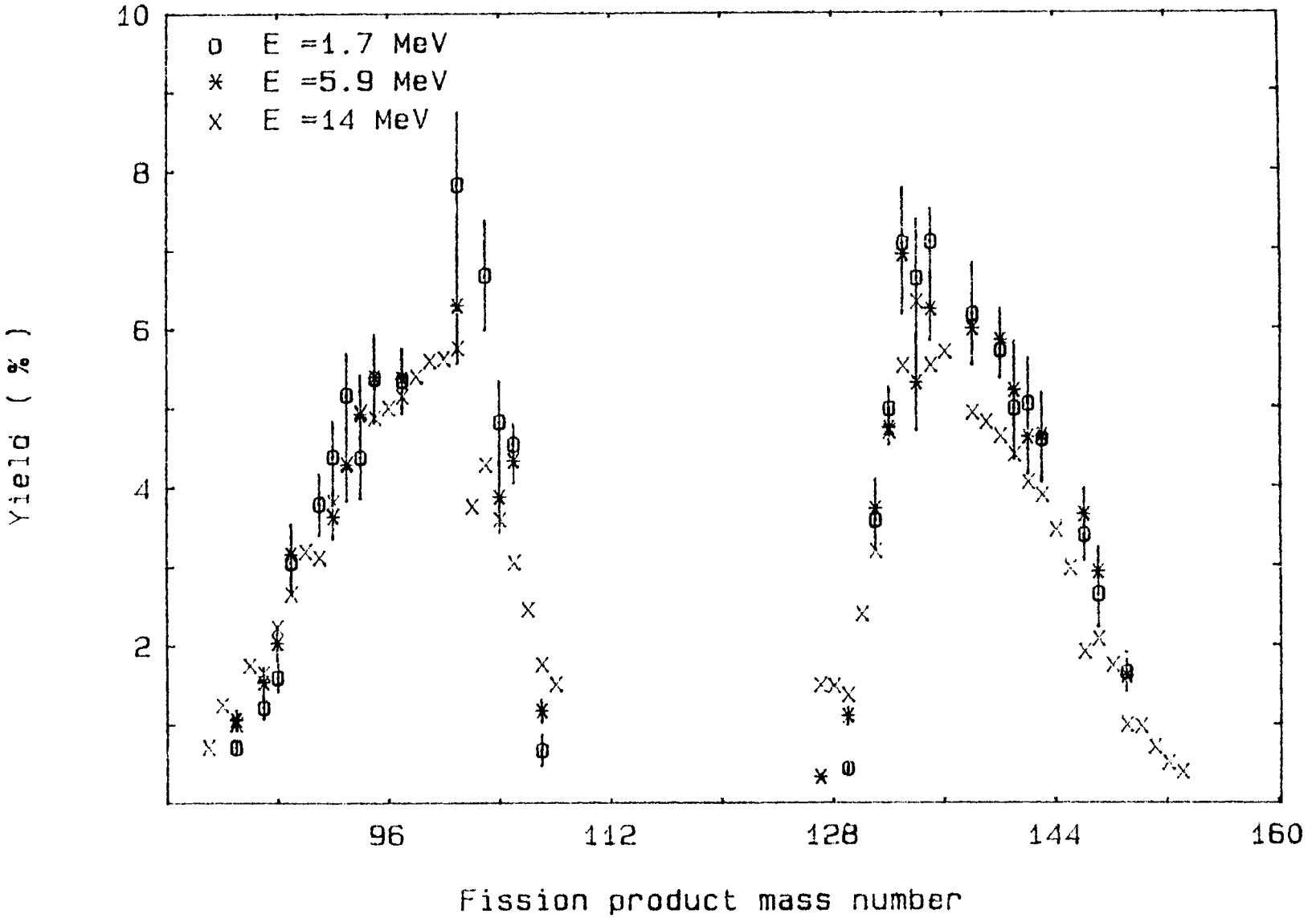

Fig. 5.16 Mass yield curves for fission of ^{238}U ranging from 1.7 to 14 MeV.

Table 5.13

Recommended fission product values based on the experimental values determined here different neutron energies

Fission Product	Neutron Energy (KeV) 1722	2160	3726	4782	5982
85mKr	.71 ± .07	.83 ± .12	.80 ± .02	.99 ± .1	1.06 ± .14
87 Kr	1.22 ± .15	1.06 ± .13	1.38 ± .16	1.52 ± .16	1.54 ± .20
88 Kr	1.6 ± .18	1.48 ± .22	1.77 ± .19	2.0 ± .21	2.04 ± .23
89 Rb	3.05 ± .36	3.02 ± .29	2.93 ± .45	3.65 ± .50	3.15 ± .39
91 Sr(Y)	3.78 ± .40	3.69 ± .33	3.59 ± .22	3.62 ± .38	3.62 ± .29
92 Sr	4.38 ± .46	4.45 ± .47	4.90 ± .51	3.47 ± .38	3.74 ± .38
93 Y	5.16 ± .54	4.55 ± .47	5.23 ± .57	4.11 ± .43	4.28 ± .47
94 Y	4.37 ± .53	4.47 ± .55	4.56 ± .56	4.77 ± .52	4.92 ± .50
95 Zr	5.37 ± .57	5.33 ± .57	5.75 ± .63		5.39 ± .55
97 Zr(Nb)	5.34 ± .42	5.54 ± .58	5.67 ± .40		5.37 ± .38
101Tc	7.83 ± .93	6.99 ± .77	7.49 ± .79	6.56 ± .68	6.30 ± .74
103Ru	6.68 ± .70	6.48 ± .67	6.27 ± .64	5.86 ± .62	
104Tc	4.82 ± .52	4.73 ± .54	4.13 ± .45	5.0 ± .53	3.87 ± .46
105Ru(Rh)	4.54 ± .26	4.36 ± .32	4.20 ± .40	3.71 ± .40	4.33 ± .29
107Rh	.67 ± .20	.82 ± .23	.81 ± .8	.92 ± .2	1.17 ± .15
129Sb	.44 ± .7	.43 ± .05	.62 ± .08	.75 ± .08	1.11 ± .12
131I	3.57 ± .37	3.53 ± .36	3.65 ± .37	3.86 ± .39	3.72 ± .38
132I	4.98 ± .29	5.78 ± .31	4.64 ± .37	4.63 ± .24	4.74 ± .22
133I	7.08 ± .71	6.96 ± .72	6.50 ± .67	6.17 ± .63	6.94 ± .76
134Te	6.64 ± .74	6.54 ± .71	6.11 ± .75	6.28 ± .72	5.31 ± .61
135I	7.1 ± .42	7.14 ± .44	7.0 ± .58	6.64 ± .40	6.25 ± .41
138Cs(Xe)	6.18 ± .65	5.29 ± .56	5.62 ± .41	5.96 ± .62	6.0 ± .45
140Ba(La)	5.72 ± .36	5.76 ± .31	5.56 ± .36	6.14 ± .45	5.85 ± .40
141Ba	4.98 ± .65	4.67 ± .51	4.99 ± .79	5.09 ± .55	5.21 ± .63
142La	5.04 ± .59	4.78 ± .52	5.10 ± .53	3.81 ± .39	4.62 ± .48
143Ce	4.59 ± .55	4.49 ± .49	4.39 ± .45	4.47 ± .46	4.64 ± .55
146Ce	3.38 ± .33	3.86 ± .43	3.6 ± .34	3.86 ± .29	3.64 ± .32
147Nd	2.64 ± .42	2.73 ± .44	2.77 ± .34	2.74 ± .34	2.92 ± .30
149Nd	1.65 ± .25	1.68 ± .26	1.84 ± .22	1.71 ± .22	1.61 ± .20
127Sb				.33 ± .05	.33 ± .05
139Ba				5.33 ± .71	
99 Mo				6.77 ± .70	

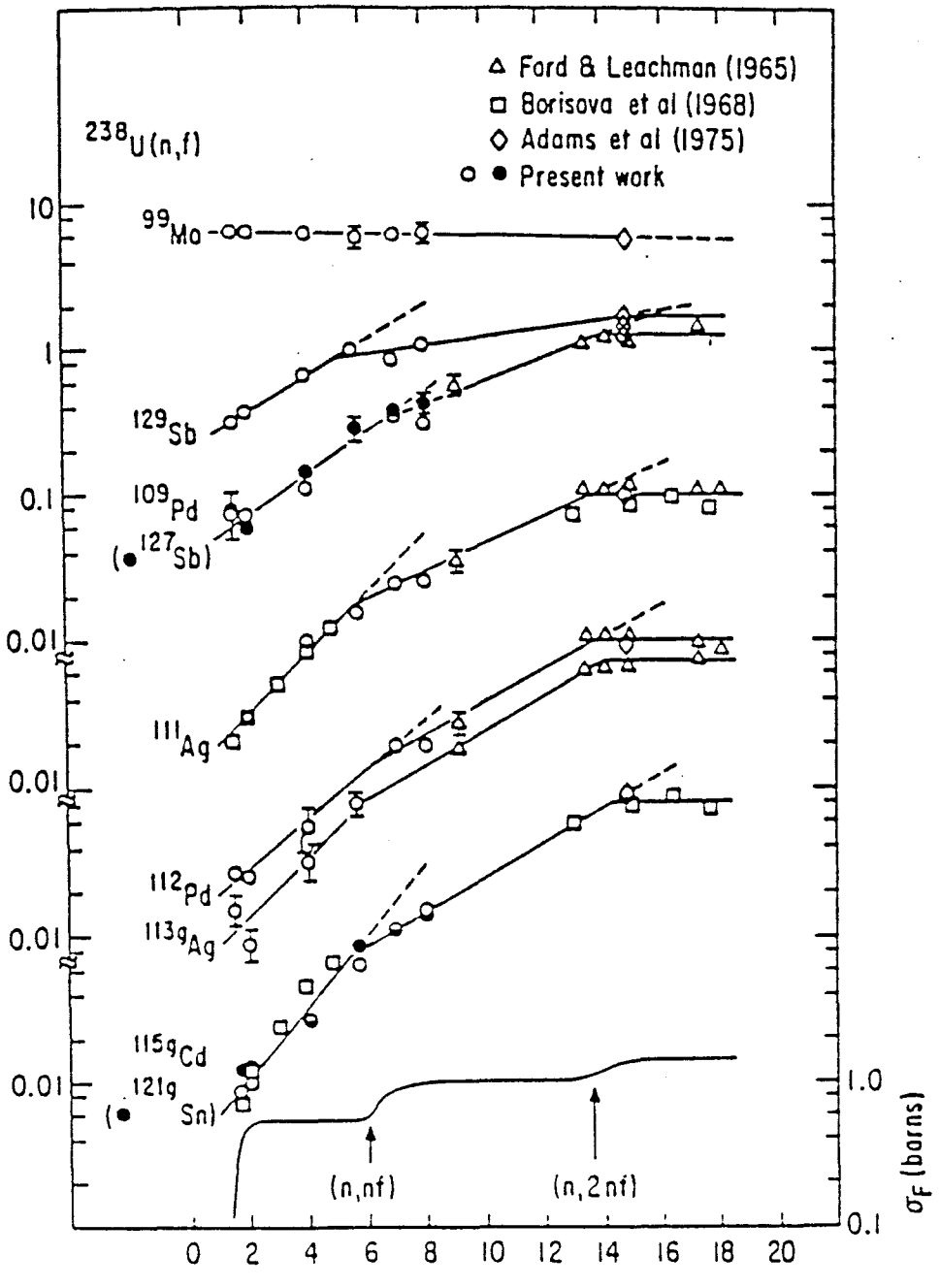

Fig. 5.17 Fission yields and cross section, σ_f, for fission of ^{238}U by monoenergetic neutrons as a function of neutron energy.

fission cross section to the total fission cross sections at a given E_n. The first-chance fission is calculated at E_n and the second- and third chance fissions are calculated at $E_n - \epsilon_n$ and $E_n - \epsilon'_n$ respectively, where ϵ_n and ϵ'_n are the amount of energy removed from the excited coumpound nucleus ^{239}U by the emission of a neutron. Yields calculated for ^{115}Cd from the ^{238}U(n,fission) reaction, with 6.9 and 18 Mev neutrons using equation 5.16 are given in Table 5.14. In contrast to the valley region the yield of fission products in the peak regions are only weakly dependent on the neutron energy and seem to decrease with increasing neutron energy. These reductions, however, are usually not more than 10% over the range 1.75 to 5.98 MeV. The variation of fission yield versus neutron energy for several fission products in these regions are shown in Figure 5.18. The best fit to the data shown in the Fig. 5.11 to 5.16 was determined by the use of an exponential function (using the weighted least-squares technique) of the form

$$Y = Y_0 \exp(bE_n) \qquad 5.17$$

where Y_0 and b are the constants for fission with neutrons ranging in energy from 1.5 to 14 MeV and for the asymetric mass distribution region i.e. the peak regions. In the case of the symetric mass region i.e. the valley region, the occurance of different chance fission is not uniform for this whole range of energies. The behaviour can best be described by dividing the total energy range into two regions, 1.5-6 MeV (first chance) and 6-14 MeV (second chance) and assigning separate values to the constants Y_0 and b for each region. These values are shown in Table 5.15. The plot for b versus mass number is illustrated in Fig. 5.19. The results indicate a 3.5% per MeV decrease in b values in the mass region of 85-106 and a 1.8% per MeV for the mass range 131-149.

It would be an important step forward if one could calculate fission yields for any given neutron spectrum rather than having to determine

Table 5.14

Calculated and measured ^{115}Cd yields for 6.9 MeV and 18 MeV neutron-induced fission of ^{238}U

Energy	$6_h/6f$[a]	$Y_1(E)$[b]	$Y_2(E_n-\epsilon_n)$[g]	$Y_3(E_n-\epsilon'_n)$[f]	$6f_2/6_f$[c,a]	$6f_3/6f$[d]	Y(E) Calculated	Y(E) Experimental
6.9	0.61	0.15	0.09	0	0.39	0	0.101	0.116 ± 0.012
18 MeV	0.61	0.1	0.8	0.1	0.91	0.09	0.798	0.78

a σ_{f_1}, σ_{f_2} determined by extrapolating σ_f from the region of first-ans second-chance fission.

b Y_1 and Y_2 determined by extrapolating the fission yields from the region of first- and second-chance fission

c $\sigma_{f_2} = \sigma_f - \sigma_{f_1}$ where σ_f is the fission cross-section at $E_n = 6.9$ MeV

d $\sigma_{f_3} = \sigma_f - \sigma_{f_1} - \sigma_{f_2}$ where σ_f is the fission cross-section at $E_n = 18$ MeV

g $En-\epsilon_n = 1.5$ MeV for 6.9 MeV

f $En-\epsilon'_n = 5.6$ MeV

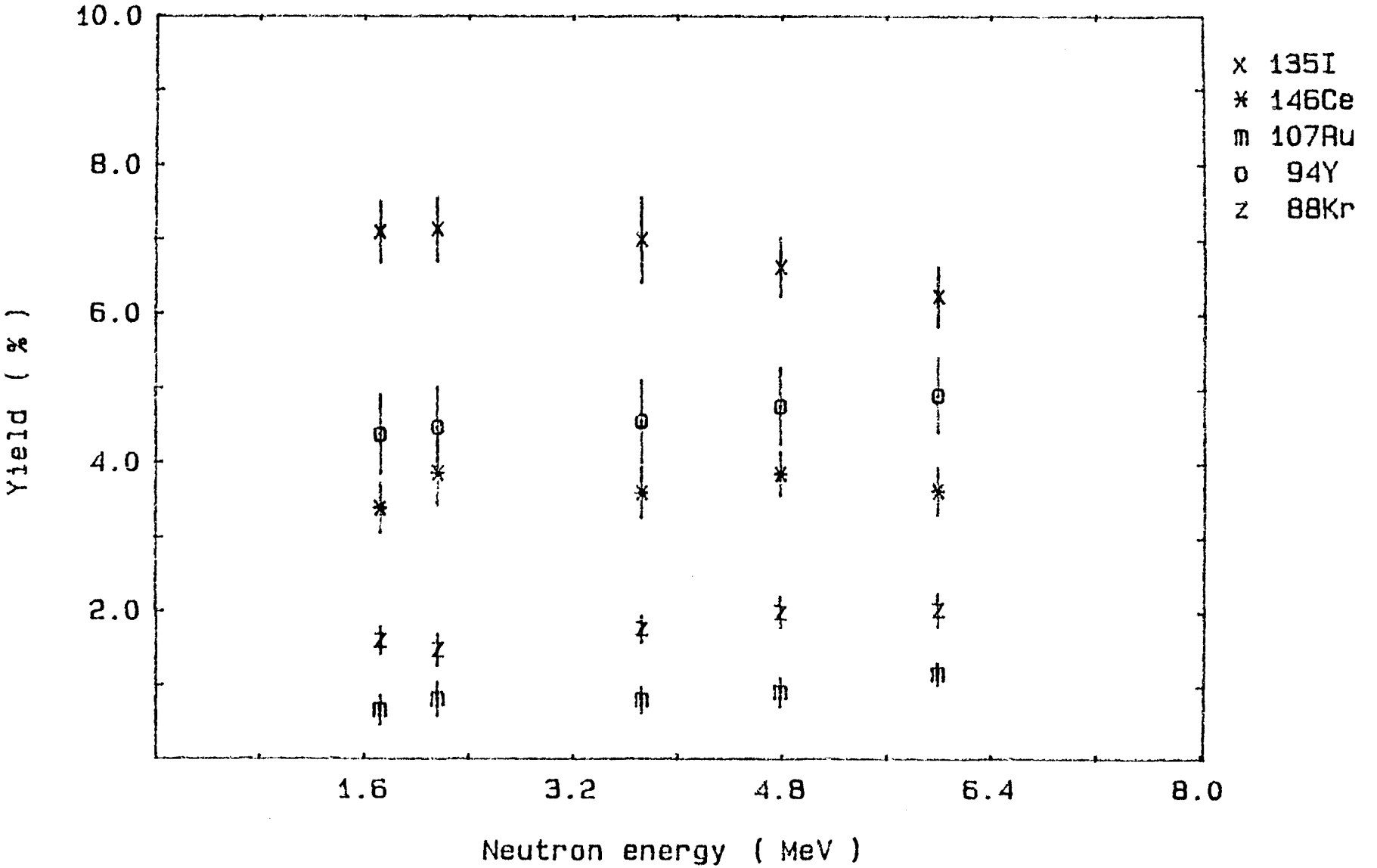

Fig. 5.18 Yield of nuclid as a function of neutron energy for several fission products.

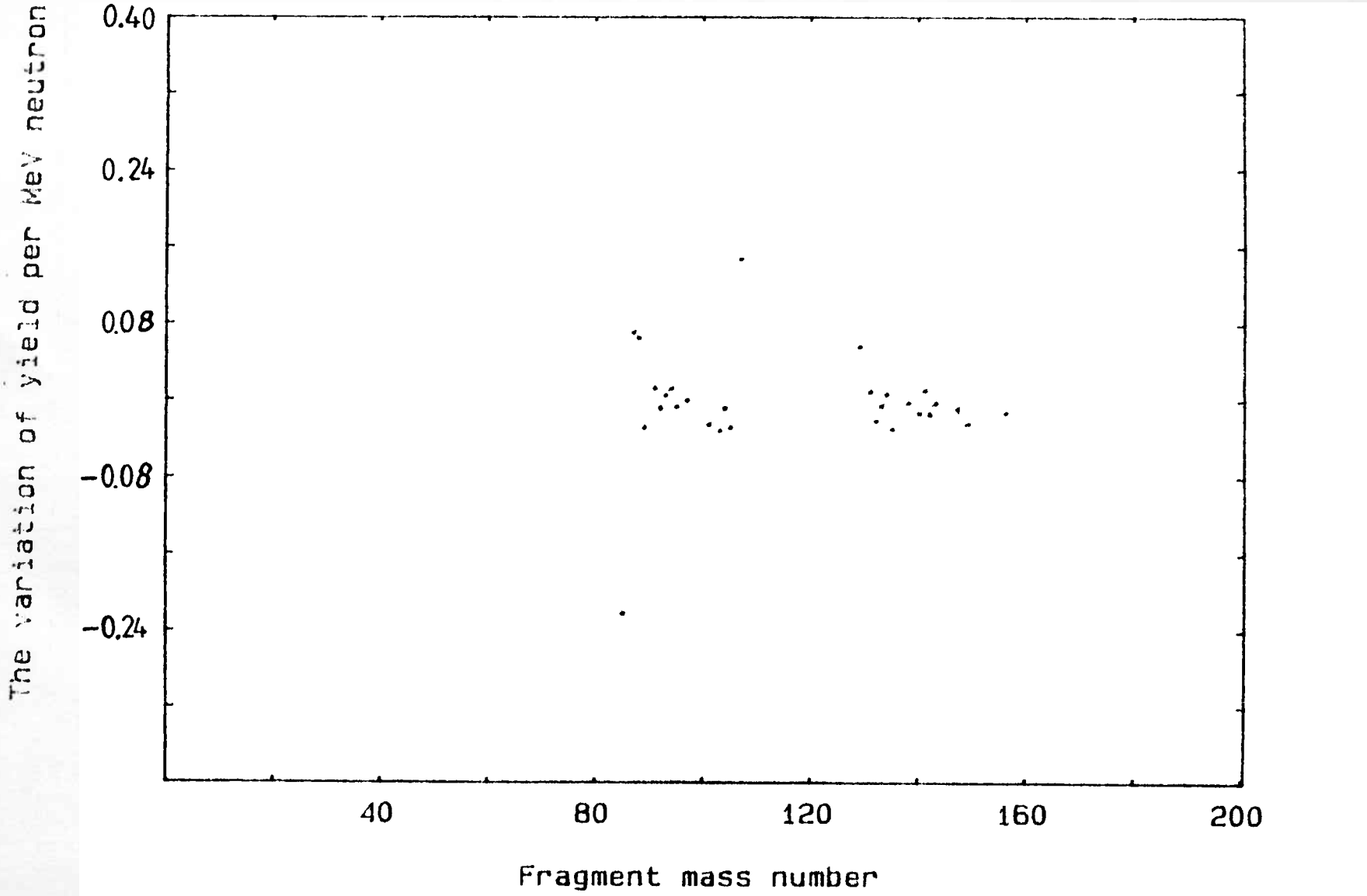

Fig. 5.19 Plot of b versus fission product mass for monoenergetic-neutron-induced fission of ^{238}U.

Table 5.15

The coefficients of Eq. 5.17 derived from a least-squares fit to the experimental data

Nuclide	Y0	b	Nuclide	Yo	b
85mKr	.8867	-.02228	129Sb	.5256	.0565
87 Kr	1.031	.07157	131I	3.514	.00937
88 kr	1.387	.06522	132I	5.410	-.02099
89 Rb	3.395	-.0289	133I	6.945	-.00565
91 Sr	3.542	.0128	134Te	6.254	.00659
92 Sr	4.397	-.00869	135I	7.623	-.0297
93 Y	4.694	.005243	138Cs,Xe	5.819	-.00228
94 Y	4.345	.01241	140Ba(La)	6.022	-.01329
95 Zr	5.557	-.006658	141Ba	4.761	.01079
97 Zr	5.474	-.000023	142La	4.951	-.01443
101Tc	7.803	-.02556	143Ce	4.545	-.00296
103Ru	7.028	-.03168	156Ce	3.782	-.0122
104Tc	4.709	-.00812	147Nd	2.811	-.008277
105Ru(Rh)	4.674	-.0286	149Nd	1.843	-.02368
107Rh	.4855	.1484			

them experimentally, since this involves large expenditure in both time and money. Such imformation is very important in reactor technology. From the values of the constants Y_o and b obtained for each fission product and using the method described here, it is possible to calculate fast fission yields (FFY) by the help of the following relationship

$$FFY = \int_{E_o}^{E_{max}} Y(E)\sigma_f(E)\,\Phi(E)\,dE \Big/ \int_{E_o}^{E_{max}} \sigma_f(E)\,\Phi(E)\,dE \qquad 5.18$$

where

E_o and E_{max} are the fission threshold energy and the maximum energy, respectively of the neutrons in the spectrum.

σ_f is fission cross-section

$\Phi(E)$ is the Watt spectrum of neutrons in a reactor.

Equation 5.18 can be written numerically as

$$FFY = \sum_{i=1} Y(E)\sigma_f(E_i)\,\Phi(E_i) \Big/ \sum_{i=1} \sigma_f(E_i)\,\Phi(E_i) \qquad 5.19$$

The neutron distribution $\Phi(E)$ is described by the following equation

$$\Phi(E) = [\exp(-E_f/T)/(\pi E_f T)^{\frac{1}{2}}]\exp(-E/T)\ Sinh[2(E E_f)^{\frac{1}{2}}/T] \qquad 5.20$$

where E_f is the fragment kinetic energy per nucleon and T represents the temperature of the fragment. The values of T and E_f were found from published data[29,30] and were taken to be 0.965 and 0.533, respectively. Values of the fission cross section were taken from the GEF file[31]. The calculated values of the fast fission yield are listed in Table 5.16 along with experimentally obtained yield by Chen Chun et al[32] and published evaluated values by Crouch[33]. As can be seen from Table 5.16 there is quite good agreement between these predicted and reported ones.

Table 5.16

Predicted fission product yields from ^{238}U for a reactor neutron spectrum and their comparison with published values

Nuclide	Yield		
	This work	Chien chung[32]	Crouch[33]
85mKr	.958	.74	.74
87 Kr	1.34	-	1.59
88Kr	1.75	-	2.37
89 Rb	3.07	3.01	3.06
91 Sr	3.70	4.41	4.13
92 Sr	4.27	-	4.57
93 Y	4.78	4.86	5.18
94 Y	4.36	4.88	5.03
95 Zr	5.43	5.28	5.25
97 Zr	5.47	5.55	5.67
101 Tc	7.15	-	-
103 Ru	6.31	6.38	6.34
104 Tc	4.58	-	-
105 Ru	4.24	3.48	3.95
107 Rh	.85	-	-
129 Sb	.64	-	.54
131 I	3.63	3.19	3.28
132 I	5.04	5.11	5.26
133 I	6.81	6.47	6.60
134 Te	6.40	7.19	7.38
135 I	6.89	6.47	7.19
138 Cs(Xe)	5.77	5.94	6.13
140 Ba	5.75	6.07	6.0

Table 5.16 (continued)

141 Ba	4.94	-	5.55
142 La	4.71	4.86	4.62
143 Ce	4.50	4.68	4.67
146 Ce	3.63	-	3.51
147 Nd	2.73	-	2.61
149 Nd	1.69	-	1.67

References:

1- Cuninghame J.G., In proceedings of the panel and fission product nuclear data (IAEA, Vienna 1974) Vol.1, 353(1973)

2- Ford G.P. and R.B. Leachman, Phys. Rev. 137B, 828(1965)

3- Lyle S.J. and R. Wellum, Radiochim. Acta 13, 167(1969)

4- Harvey J.T., D.E. Adams, W.D. James, J.N. Beck, J.L. Meason and P.K. Kuroda, J. Inorg. Nucl. Chem. 37, 2943(1975)

5- Nagy S., K.P. Flynn, J.E. Gindler, J.W. Meadows and L.E. Glendenin, Phys. Rev. C 17, 163(1978)

6- Malsbury P., Phys. Dept. university of Birmingham, PhD thises (1986).

7- Weaver D., J. Owen, Radiation Centre, Phys. Dept. University of Birmingham proviate communication

8- Gotoh H., H. Yagi, Nucl. Instr. and Meth. 101, 395(1972)

9- Liskien H., F. Arnotte, R. Widera, A. Paulsen, Nucl. Sci. and Engineering 67, 334(1978)

10- Paulsen A., R. Widera, R. Vaninbroukx, H. Liskien, Nucl. Sci. and Engineering, 76,331-335 (1980)

11- Storm E., H.Israel, Nucl. Data Tables A7, 565 (1970)

12- "Reactor Physics Constants", Argonne National Laboratory, USAEC Report ANL. 5800, 2nd ed., 1963.

13- Blackband J., K. Randle, Depatment of Physics Radiation Centre Report BRC 82104,72(1982)

14- Routti J.T., University of California, Lawrence Berkely Laboratory Report UCRL-19452(1969)

15- Koskelo M.J., P.A. Aarnio, J.T. Routti, Nucl. Inst. and Meth. 190, 89(1981)

16- Koskelo M.J., P.A. Aarnio and J.T. Routti, Computer Phys. Communications 24,11(1981)

17- Bevington P.R.,'Data Reduction and Error Analysis for the Physical Science McGRW-Hill, Inc. (1969)

18- Randle K. Radiation Centre Phys. Dept. University of Birmingham private communication

19- Dobreva E., N. Nenoff, Journal of Radioanalytical and Nucl. Chem., 81/1 29(1984)

20- Desoete D., R. Gijbels and J. Hoste, Neutron Activation Analysis, Wiley-Interscience, 1972.

21- Tables of isotopes, Seventh edition, edited by C.M. Lederer and V.S. Shirley published by J. Wiley and Sons, Inc., New York (1978).

22- Nuclear Decay Data for Selected RAdionuclides, edited by M.S. Martin, Oak Ridge National Lab. Report No. ORNL-5114 (1976).

23- Gunnink R., J.B. Niday, R.P. Anderson and R.A. Meyer, Lawrence Livermore Lab. Report No. UCID-15439 (1969).

24- Helmer R.G. and R.C. Greenwood, Nucl. Tech. 25, 258 (1975).

25- Bowman W.W. and K.W. Macmurdo, Al. Data. Nucl. Data Tables 13, 89 (1974).

26- Nuclear Data Sheets 10, 151 (1973).

27- Flynn K.F., Trans Am. Nucl. Soc. 22, 677 (1975)

29- Terrell J., Phys. Rev., 113, 527 (1959)

30- Cranberg L., G. Frye, N. Nereson and L. Rosen, Phys. Rev., 103, 662 (1956)

31- Weaver D.R., Radiation Centre, Physics Department, University of Birmingham Private Communication.

32- Chien Chung, Ming-Yung Woo, J. Radioanal. and Nucl. Chem 109, 117 (1987).

33- Crouch E.A.C., Atomic Data and Nucl. Data Tables 19, 417 (1977).

CHAPTER 6

Ternary Fission Experiments

6. Introduction

The energy characteristics and the emission probabilities of the light charged particles (LCP) (mainly tritons and alpha-particles) emitted in spontaneous ternary fission of Cf-252 and induced by monoenergetic neutrons in U-238, has been studied. The work on ^{238}U involved the 3MV Dynamitron Accelerator in the Physics Department Radition Centre. The neutron energies of 3.6 and 4.12 MeV were obtained via the D(d,n)^{3}He reaction, in the Low Scatter Cell using 900 KeV and 1.4 MeV deuterons respectively.

6.1 Experimental Arrangement

A $\Delta E-E$ counter telescope of two silicon surface barrier detectors (with the thickness of the ΔE detector appropriately chosen) was used to identify the particles emitted in ternary fission and to measure their yield and energy, by means of analogue signal processing. This telescope was located inside a vacuum chamber especialy designed for this experiment.

6.1.1 Vacuum Chamber

The fission reaction and the detection of its LCP in ternary fission were carried out in a chamber of 40 cm diameter with two, independent rotating arms. These two arms were pivoted about the centre of the chamber. Several detectors could be mounted on each arm, with reasonable separation between them. The target assembly for producing neutrons was located inside the chamber at the end of the beam line

and the position of this target assembly was adjustable in distance from the centre of the chamber. The centres of the neutron-producing target and the ^{238}U fission foil were aligned on the axis of the chamber and adjusted to be at the same height and in the same plane, perpendicular to this axis. The ^{238}U fission foil was located at the centre of the chamber. The arms carrying the detectors were placed either side of the fission foil and could rotate in the plane prependicular to that of the foil. The detectors themselves were very carefully adjusted so that their centres were at the same height as those of the neutron target and the fission foil. In addition the detectors on each arm were adjusted to be perpendicular to the axis of the arm and the plane of rotation. Figure 6.1 illustrates the positions of the neutron target, ^{238}U fission foil and the detectors on their arms. Throughout the experiment the chamber was maintained at a working pressure of 10^{-5} torr. In the spontaneus ternary fission of ^{252}Cf, the ^{238}U target was replaced with a thin ^{252}Cf source, keeping all other parameters identical.

6.1.2 The Target Assembly for Neutron Production

The two deuterium targets used in this experiment were obtained from Amersham International plc. They consisted of a deuterated layer of titanium, 1.87 mg/cm^2 thick on a silver backing disc. The specifications of the target as supplied by the manufacturer were as follows:

	support	deposit
material	silver	titanium
dimension	31.7 mm dia	25.4 mm dia
thickness	0.5 mm	4.128 μm

weight of deposit (mg)	total deuterium (cc)	Deuterium:Titanium

Fig. 6.1 The vacuum chamber and telescope used during the irradiation.

A Surface barrier fission detector

B Surface barrier E detector } E-ΔE telescope

C Surface barrier ΔE detector }

(E-ΔE telescope covered with polyethene to reduce damage by fast neutrons)

D Uranium target

E Neutron producing target

M Collimator

N Telescope arm.

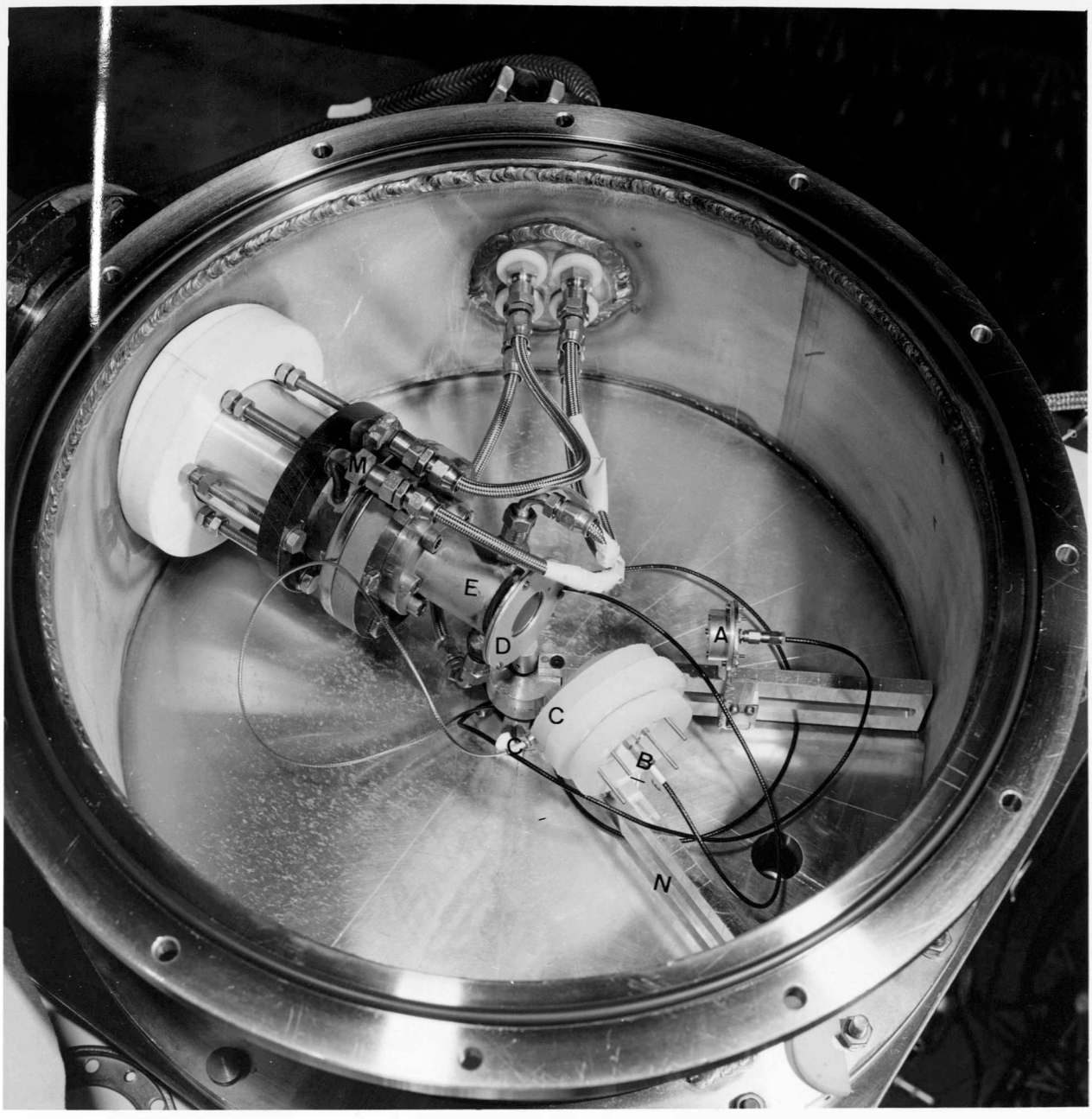
M
E
D
C
C
A
B
N

9.5 2.8 1.5:1

Figure 6.2 illustrates the neutron-producing target assembly employed in the ternary fission experiment. The silver disc was held in position by knife-edge seals from one side and an indium "O"ring from the other side and was cooled by a constant flow of water across the back. The knife-edge produces a vacuum seal at the beam-line side of the target. This type of arrangement, however, does not ensure a vacuum seal into the chanber itself. This was provided by the indium "O"ring. An additional vacuum seal between the target and the chamber was later provided by modifying the upper part of the assembly body to take a Viton "O"ring, as shown in Fig. 6.2. A water-cooled collimator, 1.1 cm diameter was mounted just before this assembly to ensure that the beam strikes only the target and does not impinge on the sides of the target beam tube. Irradiations were carried out with high beam currents (about 200 μA) and with a beam spot size of 1.1 cm, with power densities in the region of 180 to 280 watts cm^{-2}. Power densities, however, can be very much higher if the beam is accidentally focussed during the course of the irradiation. In such cases there is danger of puncturing the target with catastrophic loss of vacuum. Consequently, in order to guard against this eventuality, a pneumatically-operated automatic gate-valve was located before the collimator to afford protection to the rest of the beam transport system in the event of such a failure. In addition, the beam was scanned across the target area with the aid of a variable frequency magnetic field.

6.1.3 The U-238 Foil Target

The target was prepared by the sample preparation group of the Central Bureau for Nuclear Measurments, Geel, Belgium. It was prepared

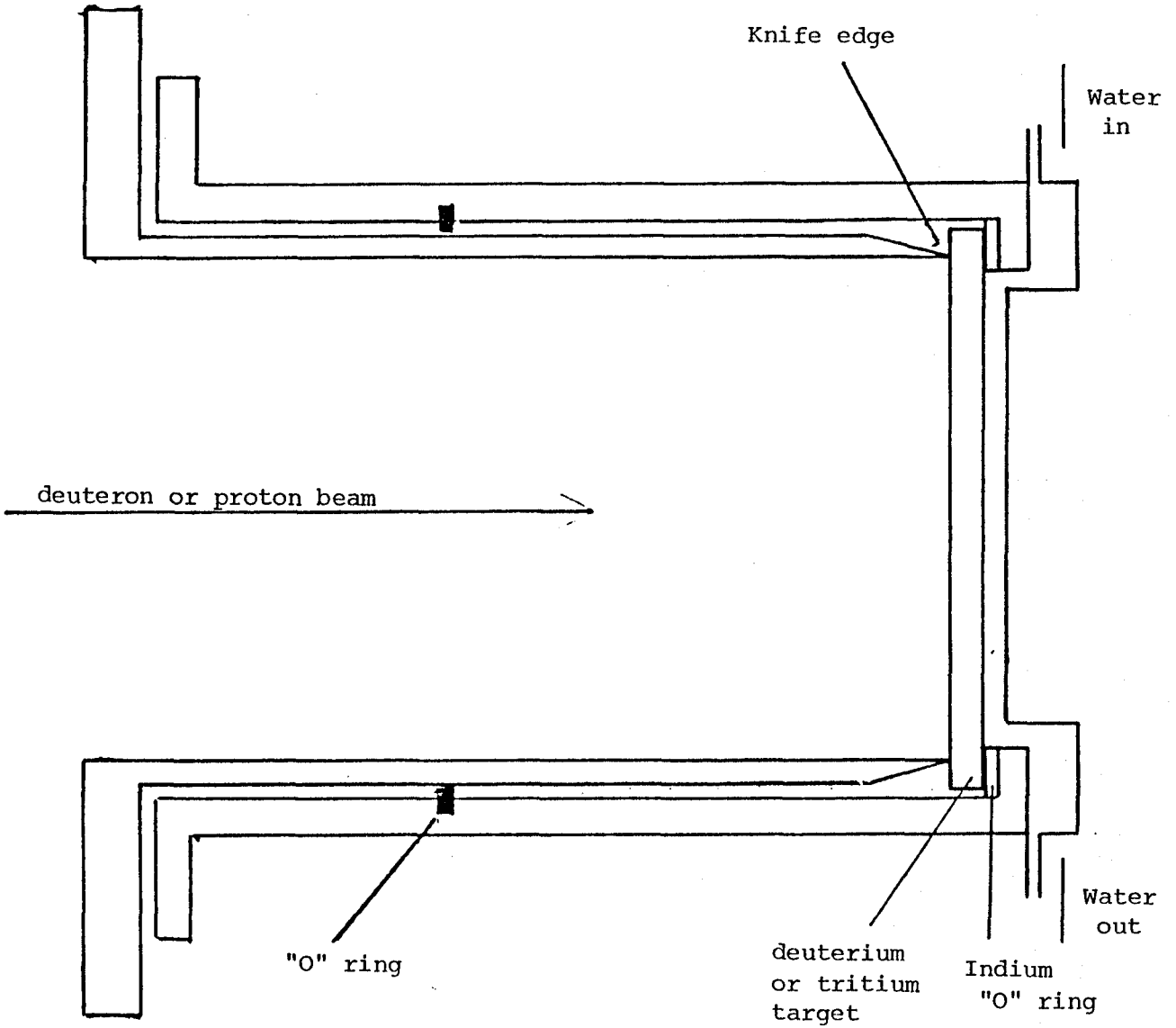

Fig. 6.2 Schematic diagram of neutron producing target systems.

by electrospraying highly depleted ^{238}U to form a very uniform deposit, 500 μg/cm2 thick and 20 mm diameter on a 7 μm thick gold-coated, polymide foil. This target was then mounted on an annular, aluminium ring, 50 mm outside diameter, 30 mm inside diameter and 0.5 mm thick. Finally, this complete target assembly was mounted on a steel pillar in the centre of the chamber where it could be rotated through 360° if necessary and then clamped in position. Figure 6.4 shows the ^{238}U target mounted in its normal position. The target thickness was chosen to satisfy the following requirements:

i) thin enough not to seriously degrade the energy of the LCPs,

ii) thick enough to produce a reasonable number of fission events.

6.1.4 Particle Identification Unit (PIU)

The theory and operation of this electronic system are discussed at length elsewhere[1] so that only a brief summary is given here. The principle of operation of this particle identifier arises from the relationship between the type of charged particle and rate of energy loss during its passage through matter. For non-relativistic particles, the energy loss is approximately given by the Bethe-Livingstone equation[2] which can be stated as:

$$\frac{dE}{dx} = (C_1 MZ^2/E_T)[\log(\frac{C_2 E_T}{MZ^2})] \qquad 6.1$$

where C_1 and C_2 are constants and E_T is the incident energy of a charged particle of mass M and charge Z. If the logarithmic term is neglected, and after some re-arrangement, Equation 6.1 can be expressed as a product

$$\Delta E \times E'_T = \text{constant} \times MZ^2 \qquad 6.2$$

Where $\Delta E (=dE/dX \cdot t)$ is the energy deposited in a thin transmission

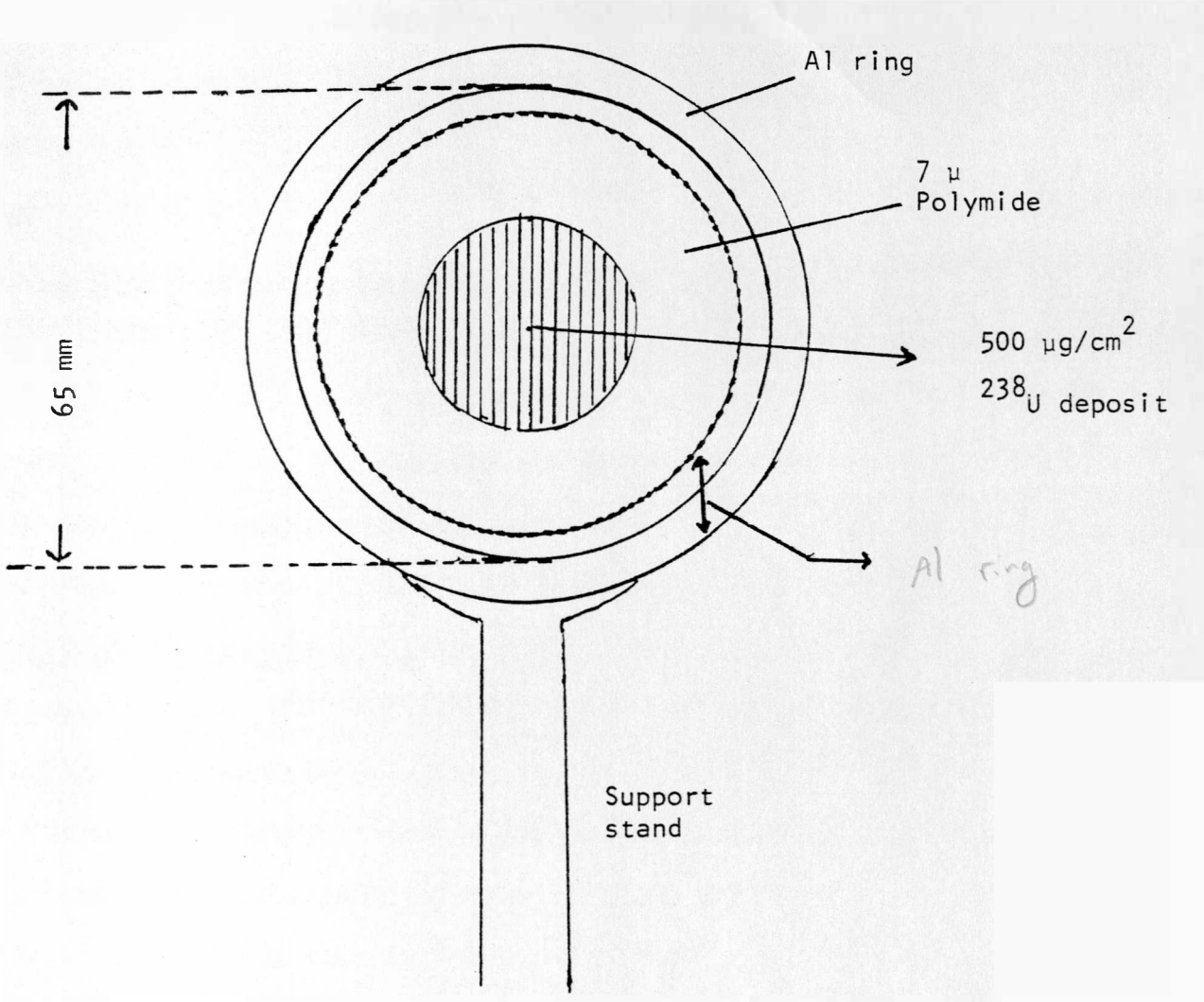

Fig. 6.3 The ^{238}U ternary fission source showing the supporting arrangement.

detector (of thickness t) and E'_T is the energy deposited in a stopping detector, i.e. the product of these signals is proportional to MZ^2. The neglected logarithmic term limits particle identification to a limited range only. A considerable improvement is possible shown by expanding equation 6.1 into a power series for the representation of MZ^2, that is,

$$MZ^2 \simeq \Delta E\ (E'_T + K_0 - K_1\ \Delta E + K_2\ .\ \Delta E^2 - K_3\ .\ \Delta E^3 + \ldots) \qquad 6.3$$

The constants K_0, K_1, K_2 etc., have been evaluated[1] over a very wide range of energies and E'_T detector thickness, K_0 $=7.0\pm0.5$ and K_1 $=0.5\pm.01$ where ΔE and E'_T are measured in units of 1 MeV/volt. The constants K_2 and K_3 are negligible and can be ignored.

In actual operation, ΔE and E'_T signals are supplied to the Particle Identifier unit (PIU). These signals are processed by the PIU which outputs simultaneously a unipolar and a bipolar mass identification pulse. Provision has been made to alter the constants K_0 and K_1 via two heliopotentiometers located on the front panel. These are calibrated in MeV/volt and allow the user to set the appropriate constants after determining the required system gain using an alpha source (see later discussion). For example, if the E_T and ΔE gains are set at 1 Mev/volt then the constants K_0 and K_1 are assigned values of 7.0 and 0.5 respectively. After mass identification, the unipolar output pulse is prepared for digitisation by the data acquisition hardware.

6.1.5 The Electronics

The standard electronic units used with the detector telescope are shown in Fig. 64. Signals from the ΔE and E detectors were first amplified by fast, charge-sensitive preamplifiers (CSP) (Ortec models 142B and 125). These were located adjacent to the vacuum chamber. To minimise r.f. pickup from the Dynamitron oscillator and by -pass earth

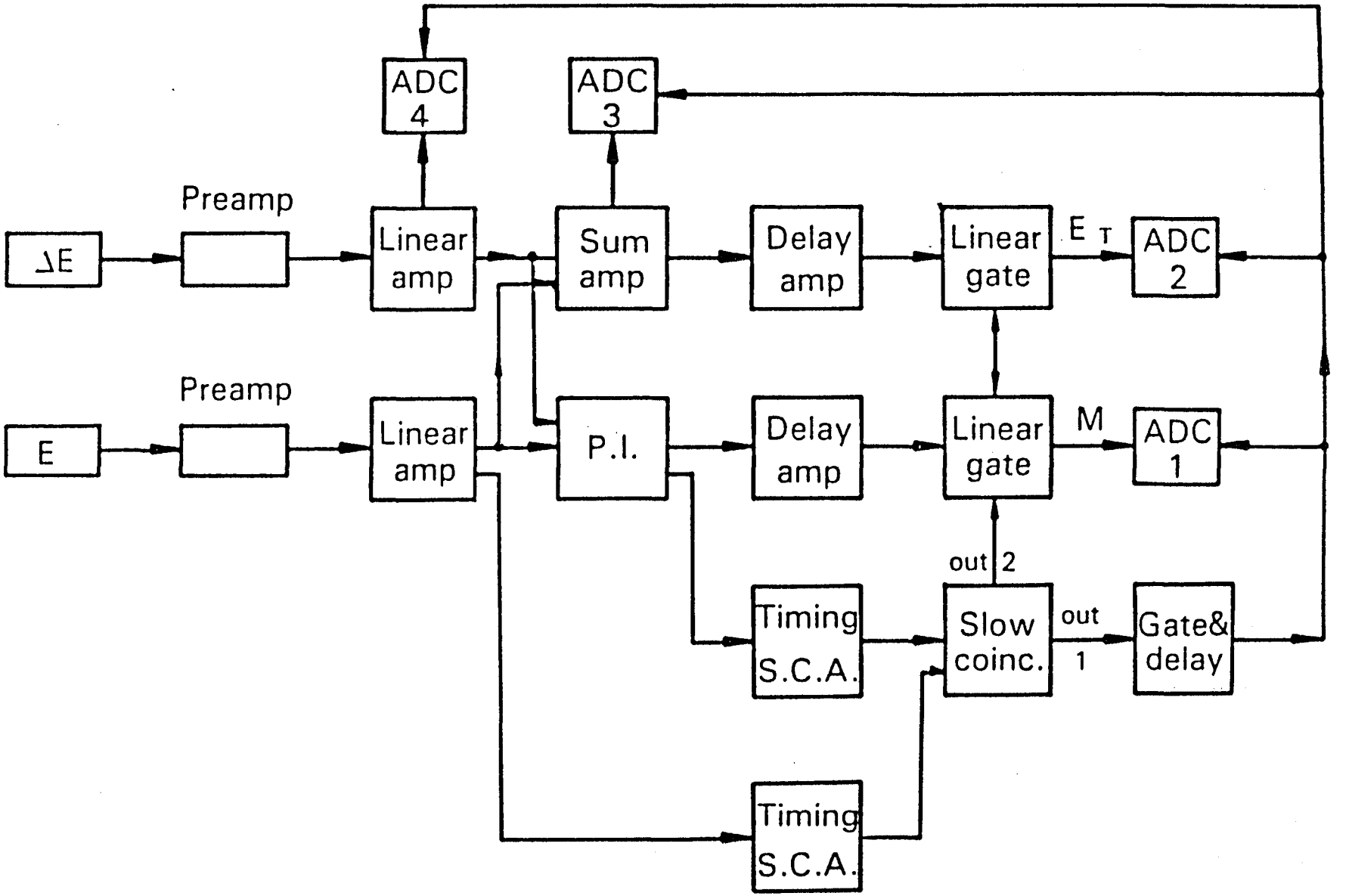

Fig. 6.4 Block diagram of the electronic used with the E-ΔE detector telescope.

loops these preamplifiers were covered with aluminium foil and well grounded by copper strings. The outputs from the CSPs were sent to a distribution panel situated in the Low Scatter Cell and via that to the computer room on the floor above. The bias voltage required for each detector was maintained through the preamplifier box and was produced by standard units. This bias voltages were 4.5 V and 180 V for ΔE and E detectors respectively.

Both the ΔE and E signals were inputs to the Ortec 572 linear spectroscopy amplifiers. The unipolar output signals from these units were routed to both a Canberra 1465A summing amplifier, which produced a signal corresponding to the the total energy and to the PIU, which generated a unipolar signal corresponding to the particle mass. In addition the bipolar signals from the E linear amplifier and the PIU were taken to the Timing Single Channel Analysers (TSCA -Ortec 420A), operated as differential discriminators. The low level thereshold was set at approximately 40 mV and the upper level to 10 V. The TSCA units generated standard, positive logic pulses which were directed into a slow coincidence unit. The output signal from the latter was then used to gate the total energy and mass signals through the Canberra 1451 linear gate units, the output of the linear gates units being sent to ADC1 and ADC2. The coincidence requirement effectively reduces the background and the count rate handled by the data acqustion system by selecting only those events in which a charged particle passed through both ΔE and E detectors. The delay amplifier units (Canberra 1457 and Tennelec 215) were adjusted to ensure that the total energy and mass signals were presented to the linear gates at the correct time. Signals which are presented to the ADCs for digitisation had to satisfy certain timing requirements. Briefly, the coincidence gate pulse to the ADC could start immediately after the input signal arrived at the ADC but must have started before the input signal had

reached its peak[3]. Thereafter, it had to remain until the input signal had passed its peak amplitude. In practice, these requirements were satisfied by adjusting the delays in the delay line amplifiers and the output pulse width from the gate and delay generator. The coincidence output was also sent to the gate and the delay generator unit. On receiving this signal the gate and delay generator itself generated a logic pulse which was used to gate both the mass and energy ADCs. This ensured that both of the ADCs were operating in coincidence. In order to maximize the amount of information gatherd from this experiment we also displayed the ΔE and E_T outputs using a further set of two ADCs (ADC3 and ADC4). This was achieved by taking the output of the ΔE amplifier to ADC3 and that of the summing amplifier to ADC4 and gating these signals via a third output signal from the coincidence unit.

It was essential that the gains of the spectroscopy amplifiers associated with the ΔE and E detectors were identical at the point where the output signals were linearly summed to yield the total energy signal. These gains were matched by observing (on a multichannel analyser) the pulse height spectrum of alpha particles emitted from a weak, americium (Am-241) source located between the ΔE and E detectors. The location of the single, prominent peak in the spectrum for each detector could be identified with the 5.478 MeV alpha particles. The gains on the spectroscopy amplifiers were adjusted so that both alpha peaks were in the same channels. The peak channel position was chosen such that there was sufficient gain to be able to detect the most energetic particle without saturating the amplifiers or the ADCs.

6.1.6 Energy Caliberation of the ΔE-E Telescope

Several standard alpha sources were used for calibration of the ΔE and E detectors in the telescope. The energies of the alpha particles

emitted and the sources used are shown in Table 6.1.

source	alpha-particle energy MeV
^{241}Am	5.478
^{228}Th	5.423
	5.686
	6.288
	6.779
	8.784

6.2 Experimental Conditions

6.2.1 Spontaneus Ternary Fission of ^{252}Cf

The energy spectrum of alpha-particles in the ternary fission of 252Cf has been determined by two, independent methods and that of the triton by just one. In the first method, Long Range Alpha particles (LRA) and tritons were identified by a $\Delta E-E$ telescope. Here, the energy spectrum and the emission probability of both tritons and alpha particles were determined. In the second method, combinations of the cellulose nitrate plastic LR-115 and various thickness of aluminium foil were used to measure the energy spectrum of LRA particles down to a 2 MeV cut-off from the tracks produced in the plastic.

6.2.1.1 Telescope Method

The charged-particles, after passing through a 12 μm Al foil (to remove the fission fragments), were detected in the $\Delta E-E$ telescope mounted in front of the ^{252}Cf source. In order to maximize the amount of information gathered from this experiment, in addition to the

electronic units used in section 6.2.5, we also displayed the ΔE and E_T outputs using a further set of two ADCs (ADC3 and ADC4). This was achieved by taking the output of the ΔE amplifier to ADC3 and that of the summing amplifier to ADC4 and gating these signals via a third output signal from the coincidence unit.

6.2.1.2 Track Counting Method

In this method, LR-115 (type II) cellulose nitrate SSNTDs, which are sensitive to alpha-particles, were used. These detectors were found to give a constant, maximum response for those alpha-particles which have energies lying in the etchable range of approximately 2 to 4.5 MeV. The detector response as a function of alpha-particle energy has been studied, using standard etching conditions. The response changed somewhat from batch to batch, so that every batch had to be calibrated before use. A combination of various thicknesses of aluminium foils was then placed in front of the LR-115 detectors to act as energy degraders for the LRA emission from ternary fission of ^{252}Cf, in order to bring the energy of the alpha-particles within the recording range of the LR-115. The irradiation facilities consisted of two different vacuum chambers: one for alpha irradiations and one for the ^{252}Cf irradiations. A 150nci, ^{241}Am alpha source was used as the calibration standard in the alpha chamber. The primary alpha-particle energies from ^{241}Am are in the range 5.3 to 5.55 MeV. In order to determine the response of the LR-115 detectors for various alpha energies in the range from 1 to 5 MeV, the primary energy was degraded by admitting air at different, known pressures into the alpha chamber. Several pieces of LR-115 detector were exposed to normally incident alpha-particles from a ^{241}Am (150 n ci or 5550 Bq) source. The irradiation chamber is shown in Fig. 6.6. The detector holder as shown

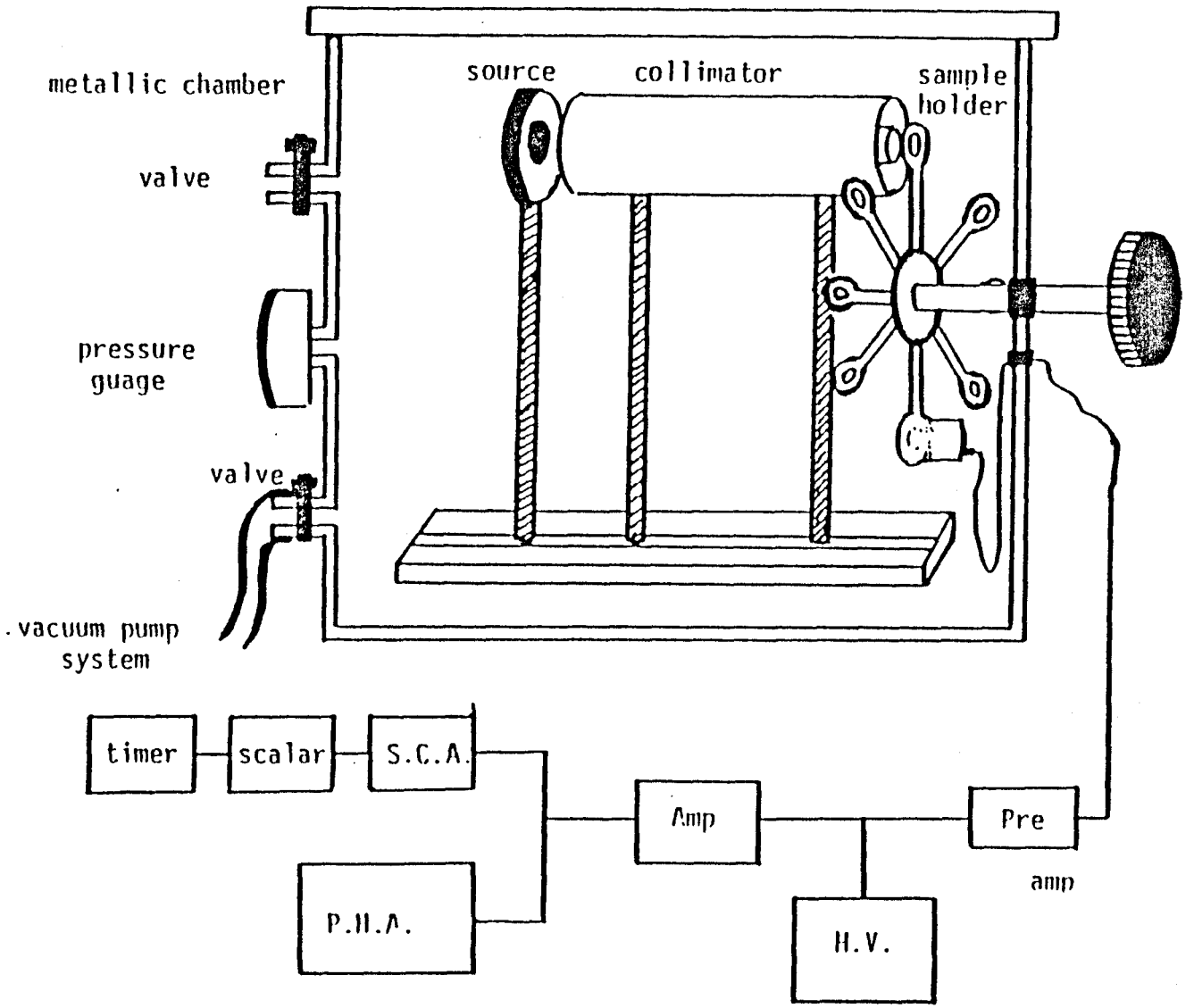

Fig. 6.5 Schematic diagram of the alpha particle irradiation chamber and associated detector electronics.

in Figure 6.5, could be rotated manually from outside the chamber in order to move the plastic detectors, one by one, to face the collimated beam from the source. A mixed source (Am-Pu-Cm) was used for energy calibration of the multichannel analyser. The absolute flux and the energy spectrum of the degraded alpha particle beam over the range 1 to 5 MeV was measured using a surface barrier detector and a multichannel analyser.

The irradiation for LRA particle emission from the ternary fission of ^{252}Cf was carried out in the second chamber. Since the yield of LRA particles was extremely low, the irradiation was continued for several months. After the end of the irradiation, the LR-115 detector was chemically etched. The etching conditions were: 2.5 M NaoH at 60°C for 60 min. For the background determination, the etching time was extended to 120 min.

6.2.2 Ternary Fission of ^{238}U Induced by Monoenergetic, Fast Neutrons

Irradiation were carried out in the Low Scatter Cell of the Radiation Centre. The neutron target assembly was positioned at the closest distance physically posible from the uranium foil (=1.5 cm), which was at an angle of 0 degrees with respect to the incident neutron beam. The ^{238}U foil was viewed at the opposite side by a ΔE-E telescope assembly and a surface barrier, total fission detector of 100 μm thickness. The telescope and fission detectors were arranged at opposite sides of the beam direction and at 30° to this direction, as shown in Fig. 6.6. The ΔE detector was fully depleted, with a thickness of about 50 μm and active area of 75 mm^2. The E detector had a thickness of 800 μm an active area of 400 mm^2. Its initial energy resolution was approximately 36 keV for 6.05 MeV alpha particles. The

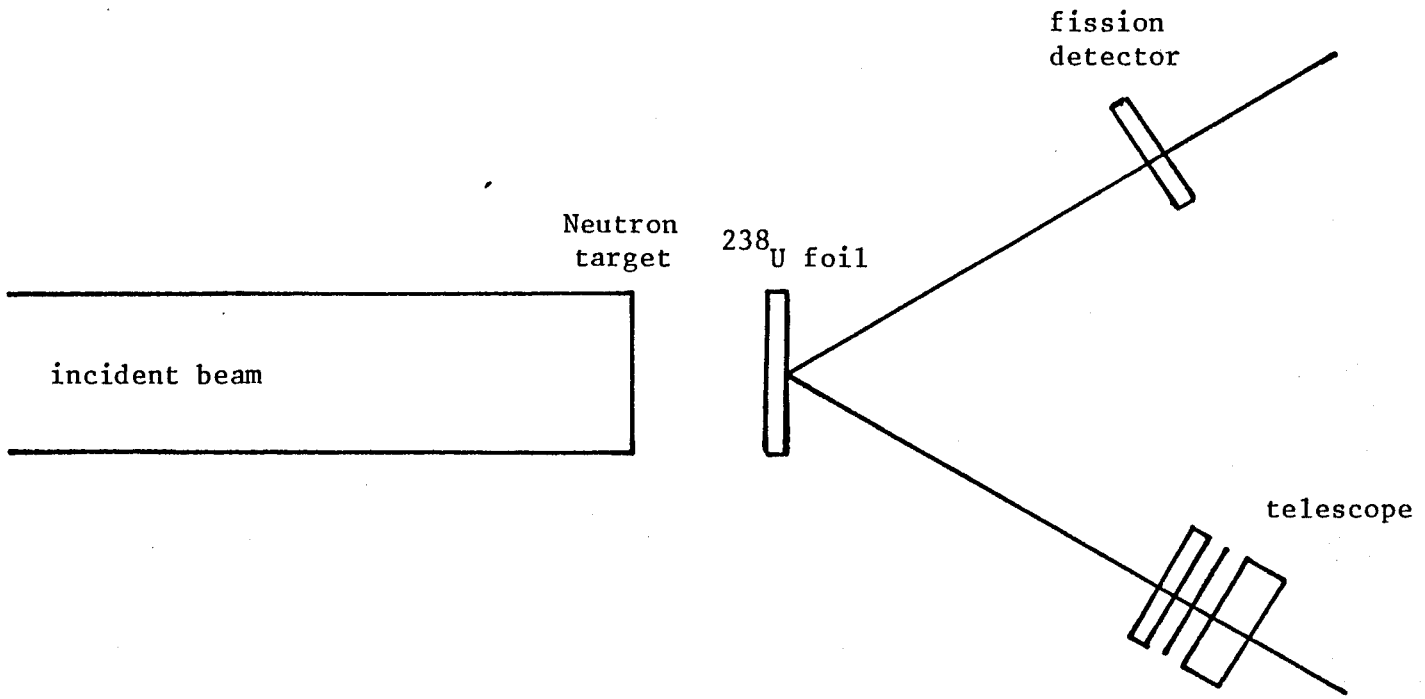

Fig. 6.6 Schematic diagram of arrangement for the ternary fission of ^{238}U experiment.

uranium target to detector distances were 120 mm for the fission detector and 25 to 50 mm for the ΔE–E system. The solid angle acceptance for the telescope varied from 0.12 to .03 steradians, depending on the distance of telescope from target, which was 3.4 millisteradian from the fission detector . The uncertainty in determining these solid angles arose from the uncertainty in the diameter of the detectors, and was estimated to be 2%. A 12 μm Al foil absorber was placed between the target and the ΔE detector in order to prevent the binary fission fragments reaching the ΔE detector. This considerably increases the life time of this detector. Although alpha particles due to radioactive decay of ^{238}U could pass through the Al foil they could not pass through the ΔE detector and so were not recorded by the telescope. Several days of irradiation were required to produce suitable ternary fission events, using a high current deuterum beam of a few handred microamperes. The irradiations in each neutron energy were carried out for 3 days with ≈ 200 microamperes current on the deuterium target. A weak, annular Am–241 alpha source, coated on a stainless steel disc, was permanently mounted between the ΔE and E detectors to continuously monitor their resolution during the course of the irradiation (see Fig. 6.8). The annular design did not interfere with the detection of LCPs in the telescope. The experimental setup was identical to that depicted in Fig 6.5, and will not be described here in detail.

The procedure used for adjusting the thresholds on the various TSCA units and the gains of the spectroscopy amplifiers was designed to reject the overwhelming background without losing the events of interest. The ΔE and E spectroscopy amplifier gains had been set according to the procedure outlined earlier in section 6.2.5 (i.e. gain macthing using the Am–241 alpha source). ΔE and E gain was set at 3.04 MeV/V, which ensured a working energy range of up to 30 MeV

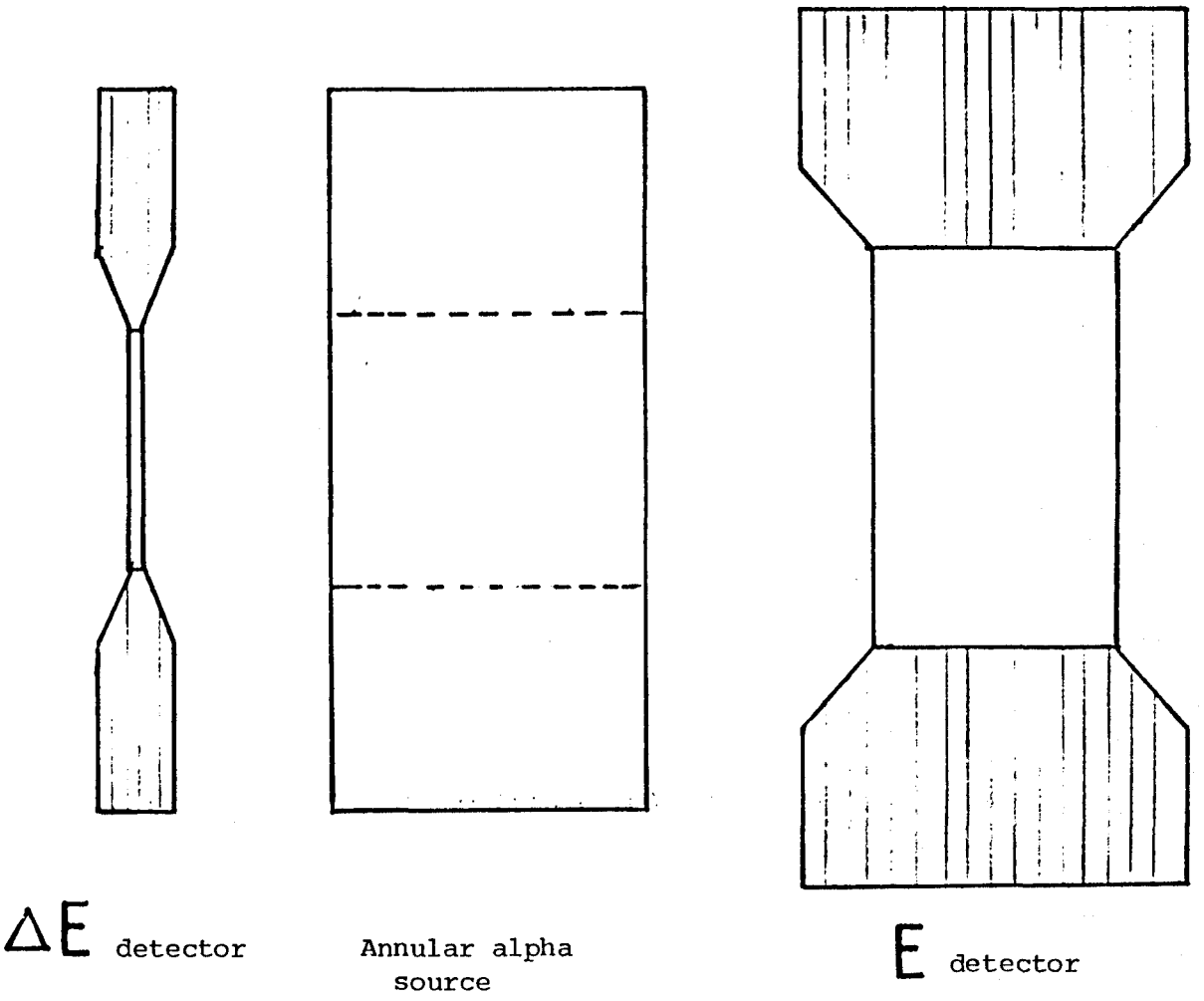

Fig. 6.7 Schematic diagram of the detector telescope with the annular ^{241}Am alpha source in place.

without saturating the amplifiers. Both energy signals where summed in a linear sum amplifier with the ΔE signal presented to the variable gain input. The latter was used to compensate for the difference in gain between the ΔE and E signals. The TSCA upper and lower level discriminators were set to 10 and 0.4 volts for the ΔE detector and set to 10 and 1 respectively for the E detector, which effectively removed much of the unwanted noise pulses. The various delays in the circuit were adjusted with the aid of an external pulser driving the test inputs of the charge sensitive preamplifiers of the ΔE and E detectors simultaneusly. Considerable care was necessary to ensure correct timing of all signals, particularly when summing signals and feeding coincidence units. The resolving time of the coincidence unit was 500 nsec.

6.3 The Data Acquisiation Hardware

The multi-channel analyser facility of the H-P computer was used to produce a three-dimensional representation of the resultant energy-mass distribution . Energy was plotted along the X-axis whilst mass was recorded on the Y-axis; counts were recorded vertically (Z-axis). This was achieved by operating the pairs of ADCs (ADC1-ADC2) in multiparameter mode. In ternary fission of ^{252}Cf the other pairs of ADCs (ADC3-ADC4) were operated in multiparameter mode to record ΔE against E_T. Coincident mass-E_T or ΔE-E_T data pairs were stored in 128x64 channels matrix of a H.P. 2100A computer. Fig. 6.9 shows the working station used during the experiment.

Fig. 6.8 Counting system used during ternary experiment.

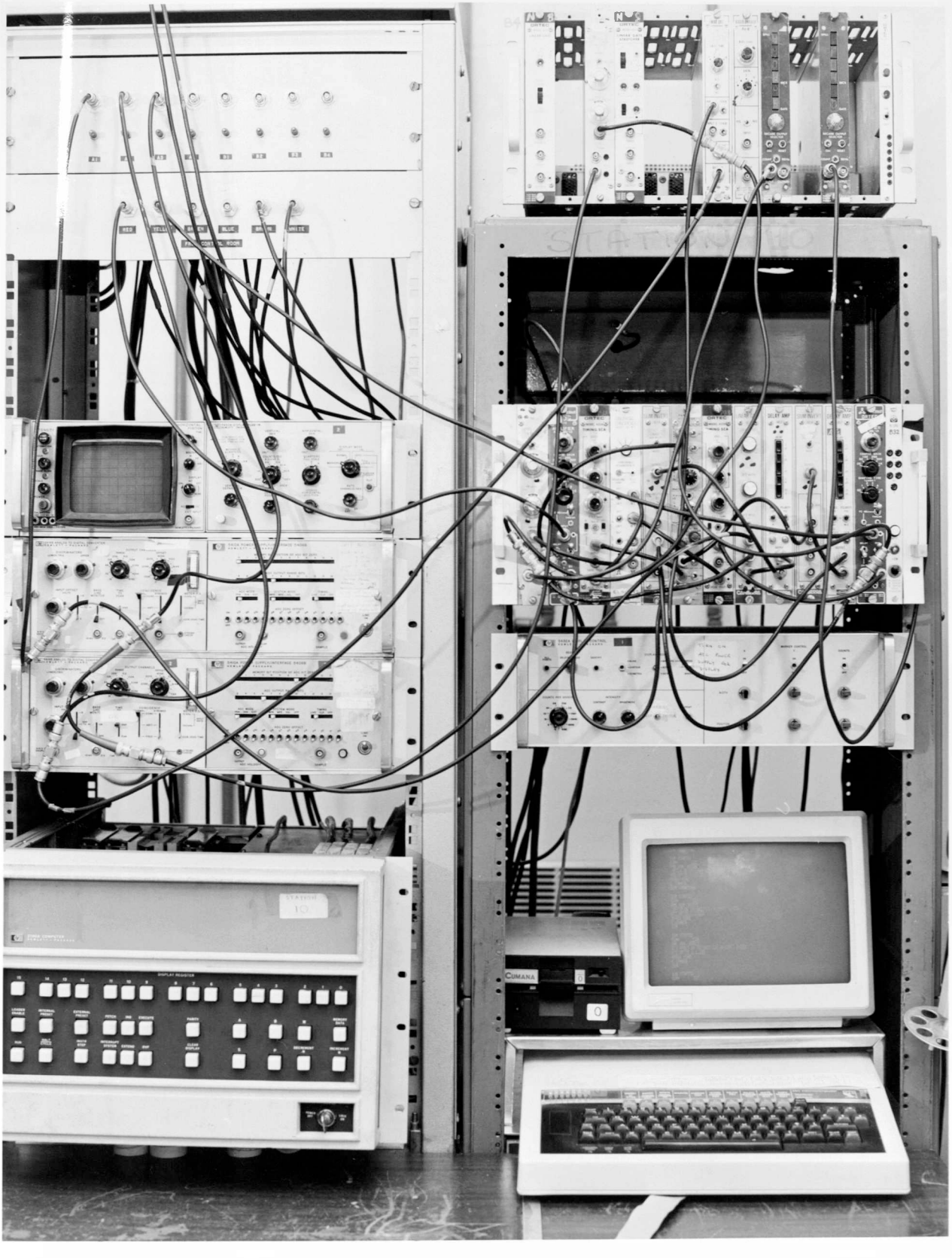
CUMANA

6.4 Results and Discussion

6.4.1 Spontaneous Fission of ^{252}Cf

Figure 6.9 illustrates the three-dimensional plot of particle mass versus total particle energy and figure 6.10 the three-dimensional plot of ΔE versus E for the ternary fission of ^{252}Cf. The energy distribution of the alpha particles and tritons was determined from Figure 6.9. In order to obtain the appropriate energy distribution, it was necessary to sum together all points of a given energy within the mass envelope for each particle. This envelope was in turn estimated from the range-energy relationship for the alpha-particles and tritons. Having then fitted an envelope around the appropriate data, an energy slice was selected and each point on that slice within the envelope was summed to give the total number of particles having that particular energy. This process was repeated for successive energy slices, until the entire energy range, from the low-energy cut-off to the maximum value, was covered. A computer program was written to perform this operation. The resultant distributions are illustrated in Figures 6.11 and 6.12 for the alpha particles and tritons, respectively.

Figure 6.13 shows the background track density versus etching time. This clearly indicates that no tracks are observed for etching times of less than 80 minutes. For longer etching times the background track density increases as a function of etching time. We investigated the response of LR-115 to alpha particles of energies in the range 1-5 MeV, for various etching times; as an example, Figs. 6.14 and 6.15 show track densities versus etching times for 3.5 and 4.8 MeV alpha particle energies, respectively. The irradiation fluence corresponded to 5×10^3 tracks/cm^2. As can be seen from the Figures 6.14 to 6.15,

Fig. 6.9 Mass vs energy spectrum for ternary fission fragments from ^{252}Cf obtained using the Particle Identification Unit (PIU), showing the clear separation of alpha particles (upper part of spectrum) from tritons.

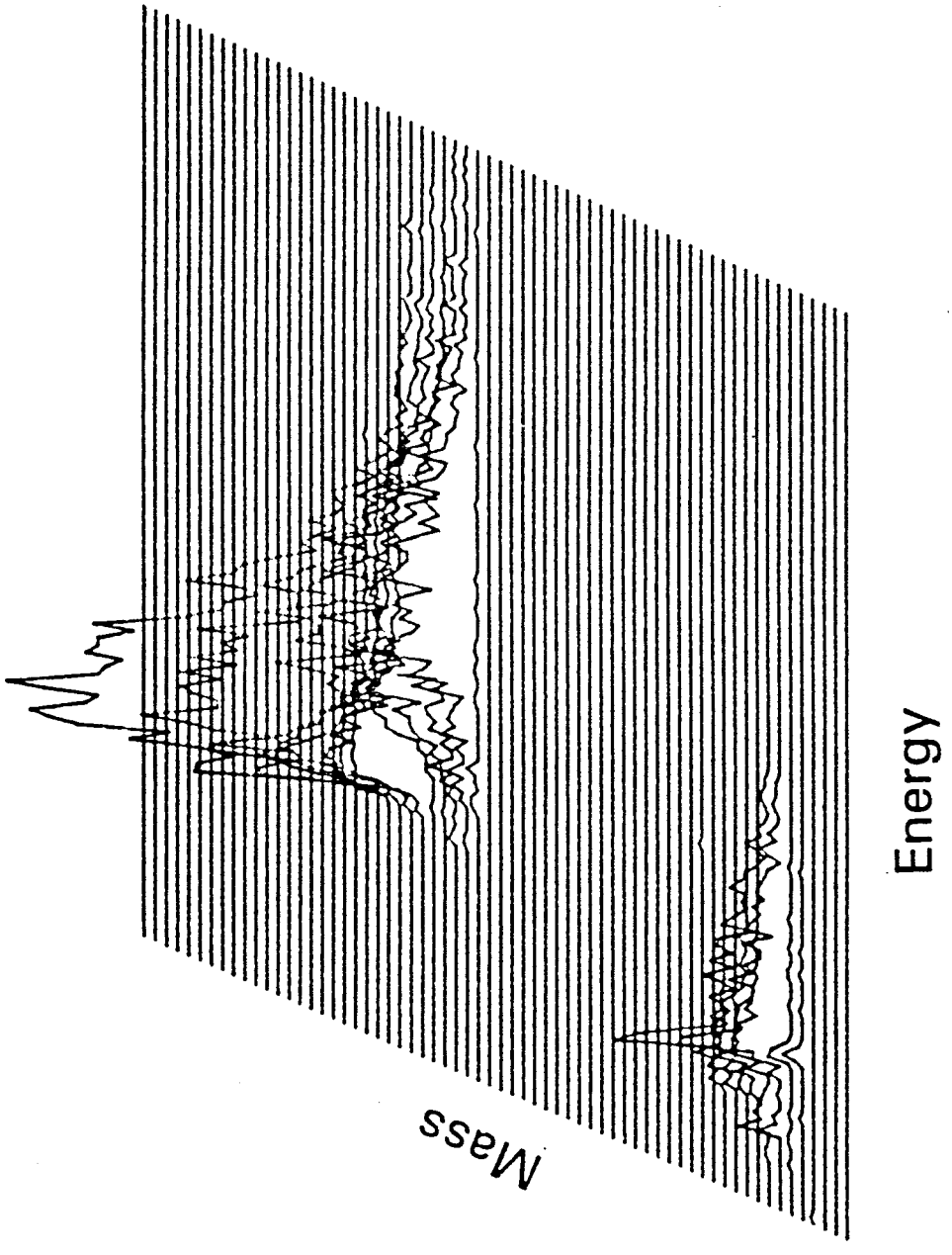

Fig. 6.10 ΔE vs E spectrum of ternary fission fragments obtained using the detector telescope.

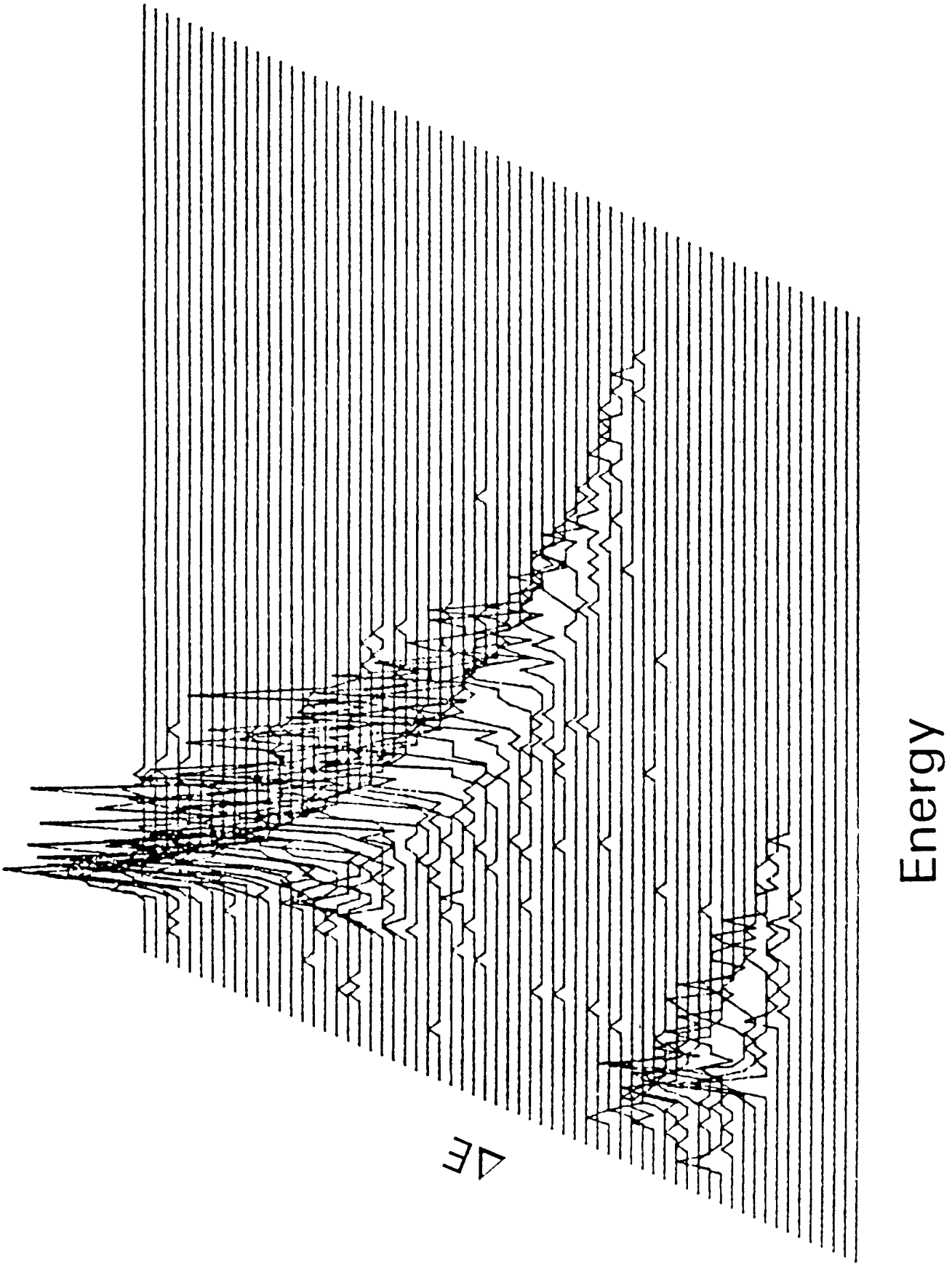

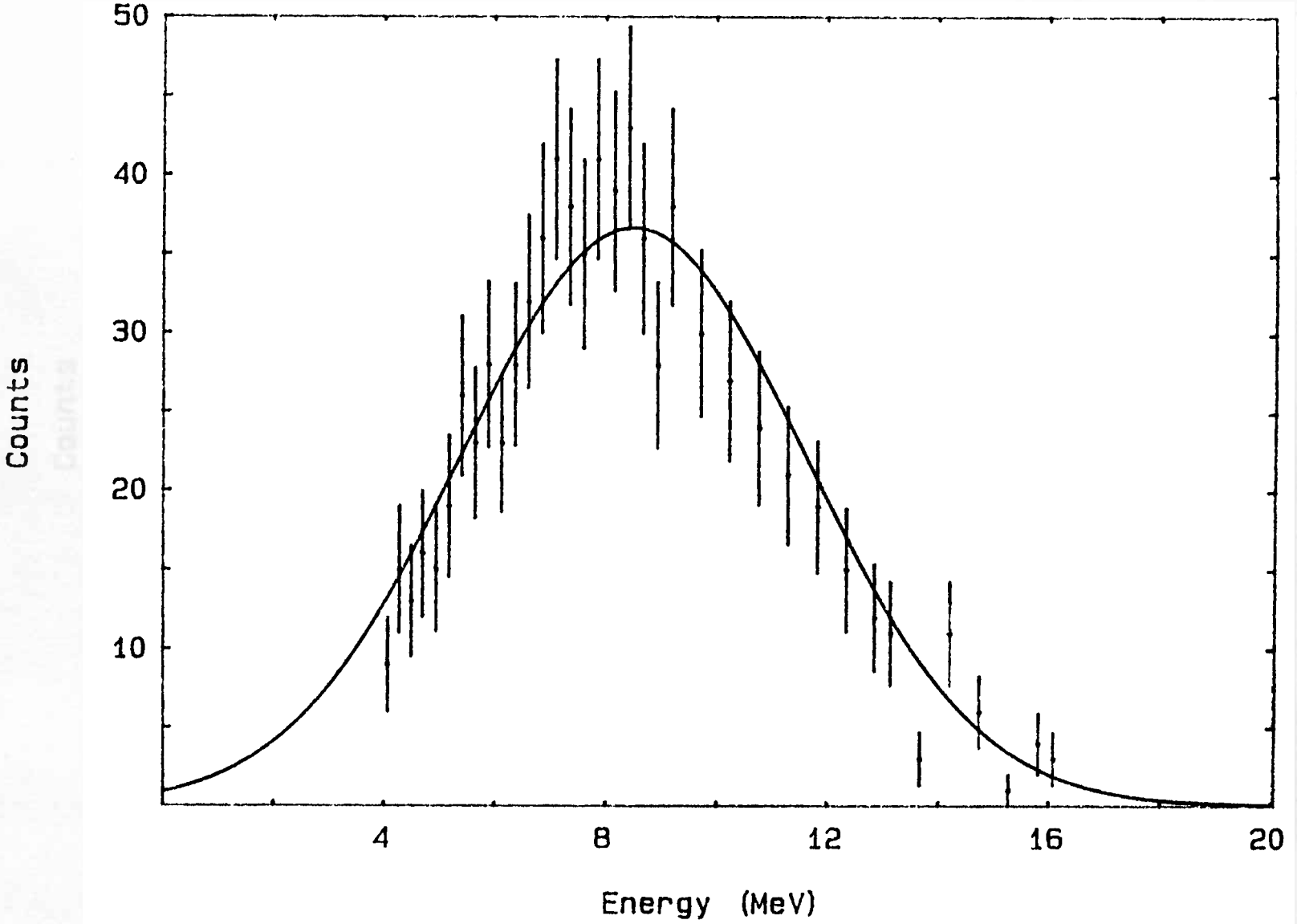

Fig. 6.11 Energy distribution of the identified alpha particles in ^{252}Cf obtained using the detector telescope and PIU.

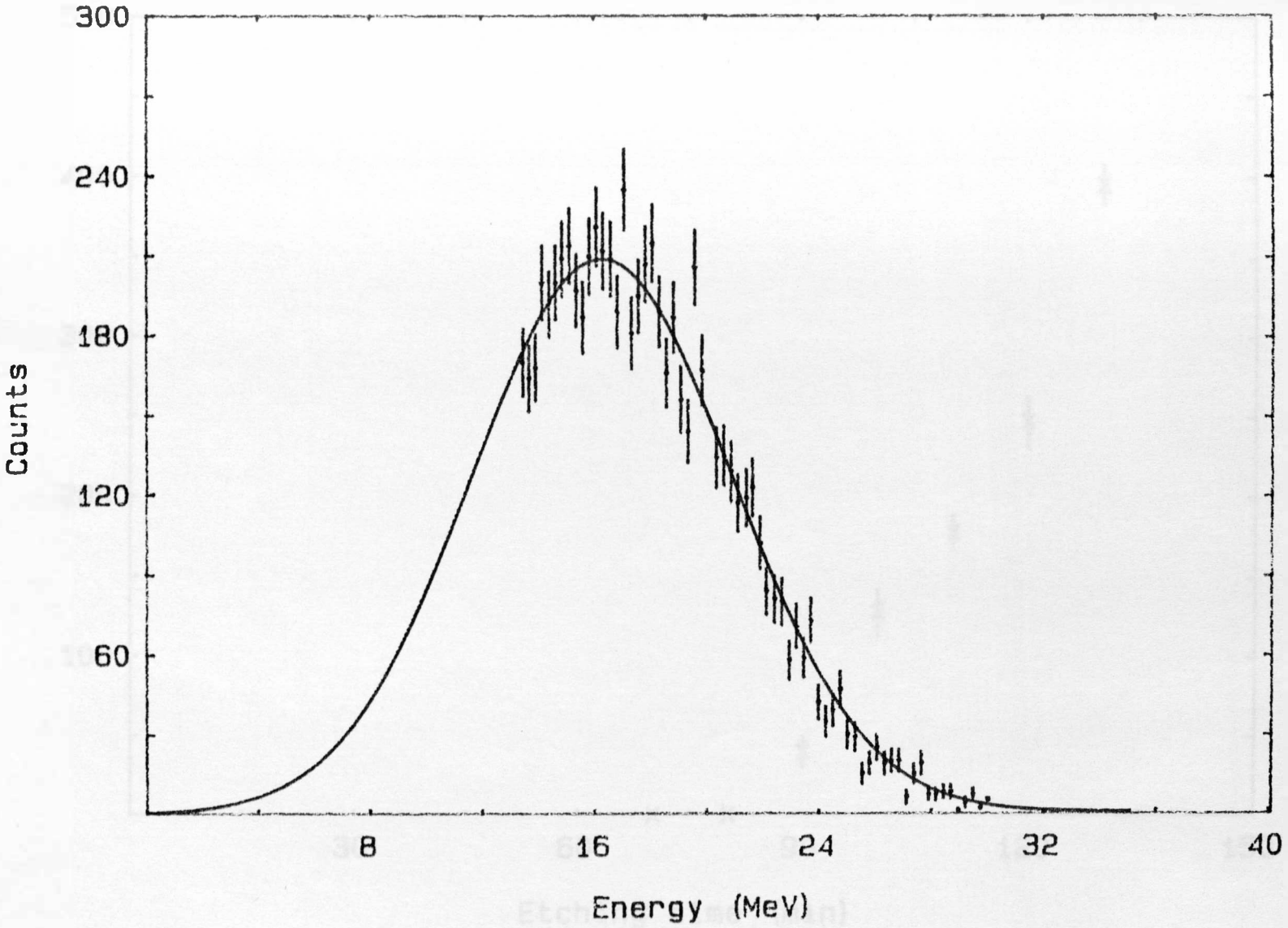

Fig. 6.12 As in Fig. 6.11 for tritons.

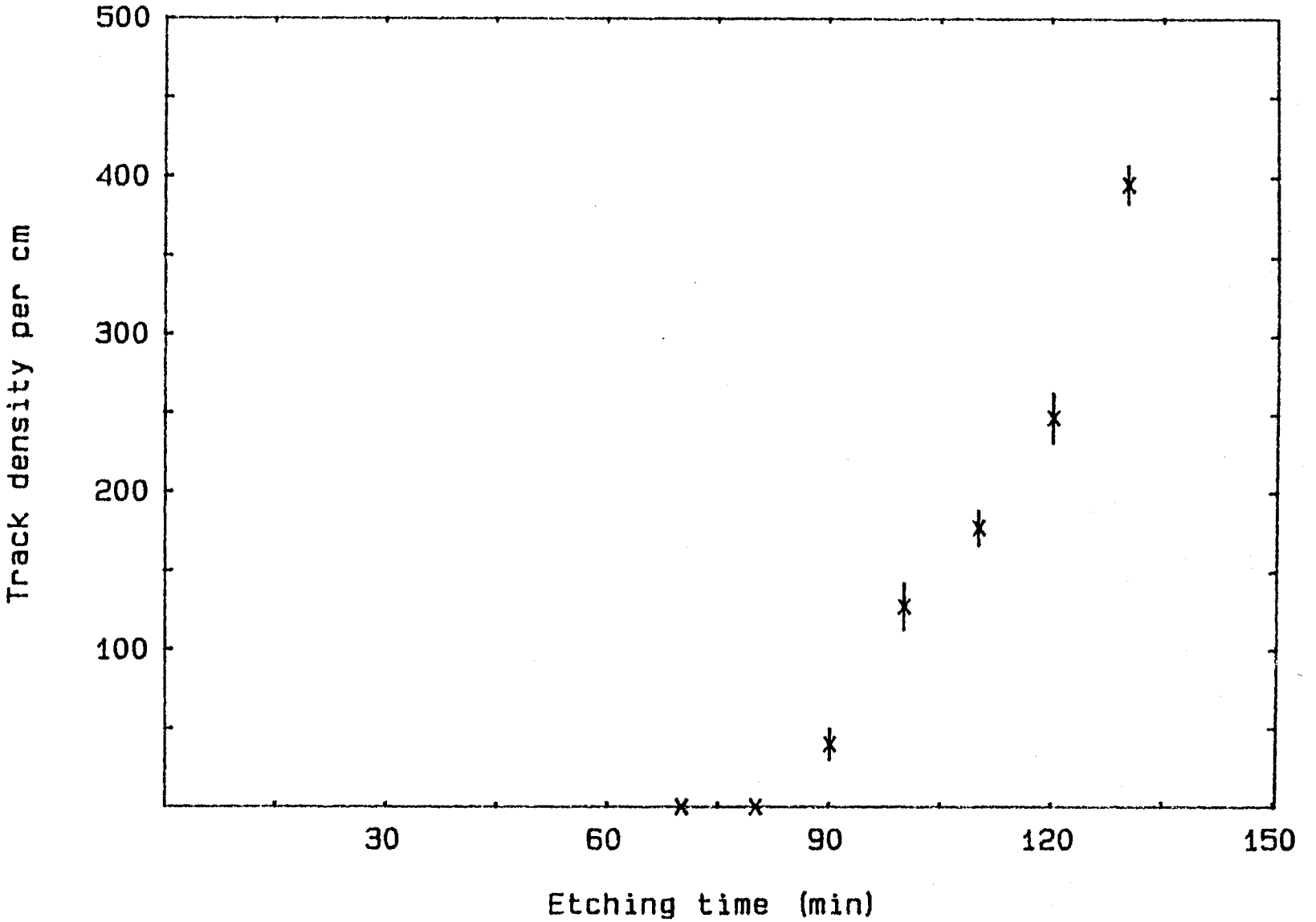

Fig. 6.13 Background track density as a function of etching time for LR115 (type II) cellulose nitrate SSNTD.

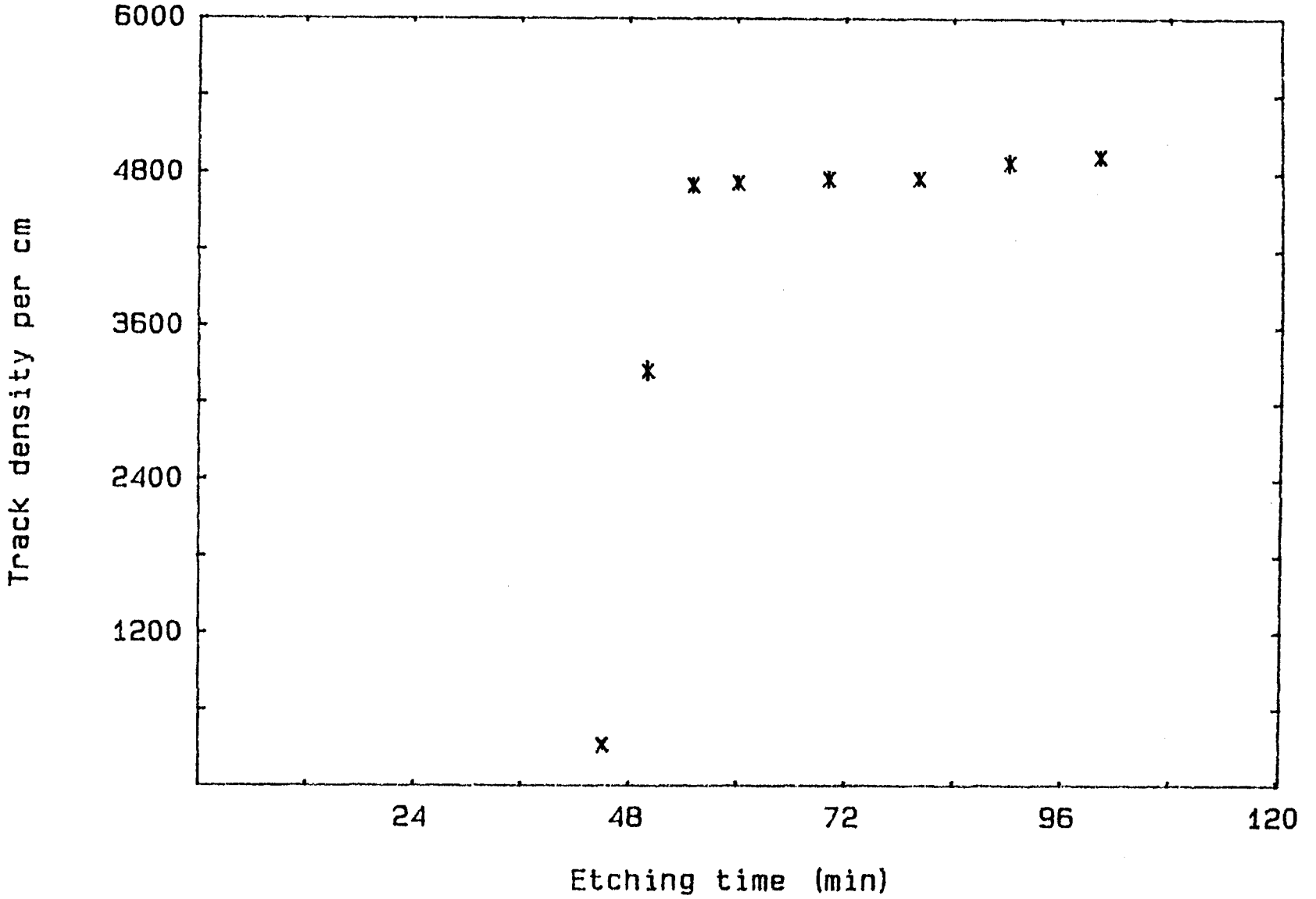

Fig. 6.14 Variation of track density with etching time for 3 MeV alpha particles in the LR115 detector.

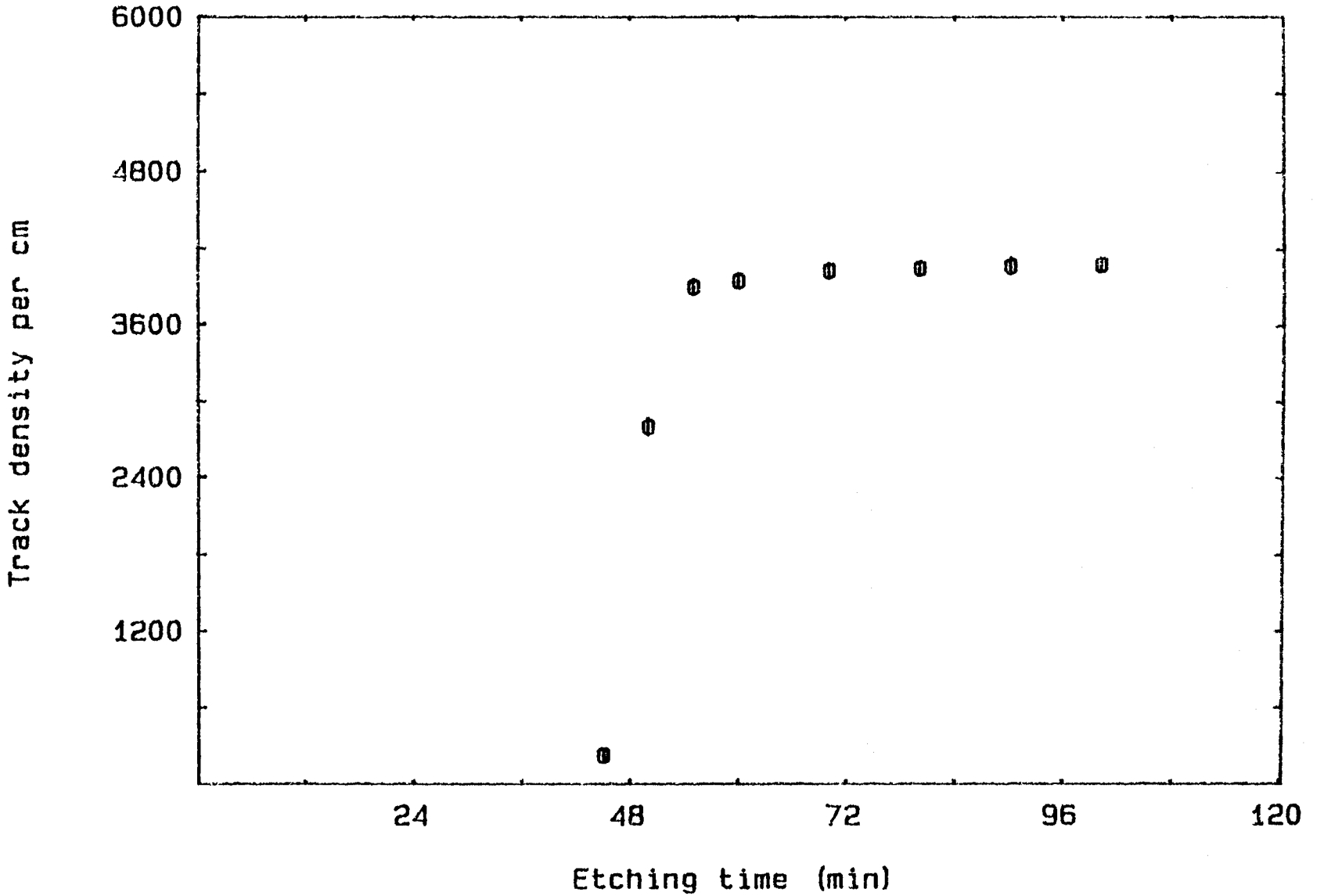

Fig. 6.15 As in Fig. 6.14 for 4.8 MeV.

the track density increases with etching time and reaches a constant value for etching times greater than 50 minutes. There is a further increase after 80 minutes etching time owing to the onset of contributions from background tracks at this time interval. Based on these data an etching time of 60 minutes was chosen. Figure 6.16 shows the detector efficiency versus alpha-particle energy. It is clear from this figure that the detector has a flat response between approximately 2.2 and 4.2 MeV. As a consequence, determinations of LRAs from the spontaneous fission of ^{252}Cf required that their energies be brought into this response range. Aluminium degrader foils were used for this purpose. For a given thickness of Al foil a cut-off energy was calculated based on the standard range-energy relationship for alpha particles[4]. The degraded particles must have a residual energy in the range 2 to 4.2 MeV to be effectively recorded. The ranges corresponding to these energies were then determined and added to the thickness of the Al foil under consideration to give a quantity which may be termed the effective range. These effective ranges were in turn converted to the relevant initial energies of the alpha particles which will produce tracks in the flat-response range of the detector. These data are summarised in Table 6.2 for degrader foils from 30 μm to 300 μm thickness, corresponding to effective alpha-particle energies in the range 7 to 26.8 MeV. Without any degrader foil the effective energies are 2 to 4.2 MeV, which is the energy range giving the flat response in the detector. Thus column 4 of this Table gives the track density for each effective alpha-particle energy (column 7) with the cut-off energy in column 5.

The energy spectrum of LRA-particles emitted in the spontaneous fission of ^{252}Cf using the LR-115 detector is shown in Fig. 6.17. The mean energy and FWHM determined from the energy spectrum obtained from

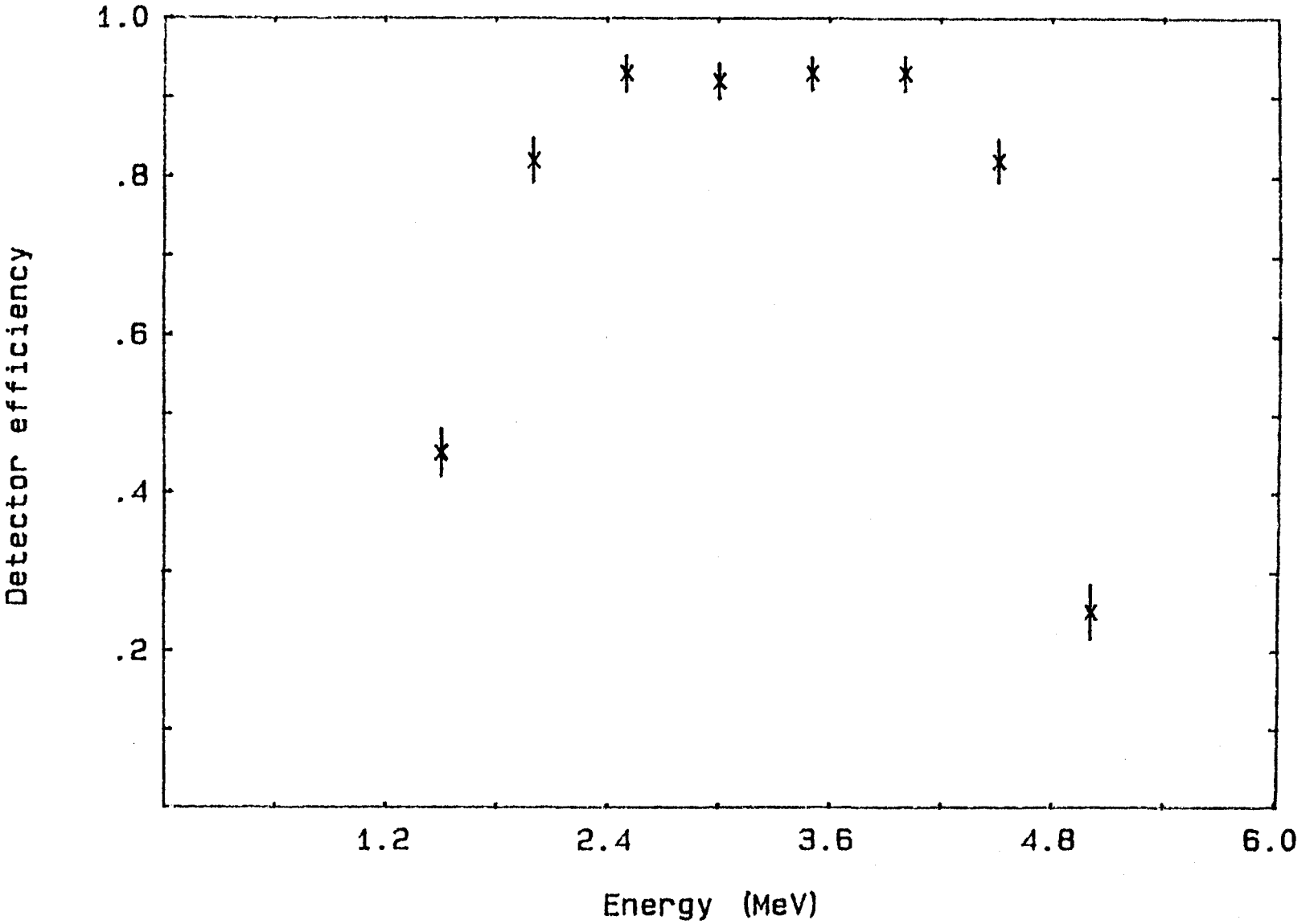

Fig. 6.16 Relative efficiency of the LR115 detector, compared to a surface barrier detector as a function of alpha particle energy.

Table 6.2

The variation of track density in LR115 detectors as a function of Al degrader foil thickness and the corresponding effective alpha-particle energy range.

Thickness of Al degrader foil	Irradiation time (hours)	Etching condition	Track density t/cm^2	Energy cut-Off MeV	Track density normalized to 200h irradition	The energy response for track formation
-	382	2.5M NaOH 60 min	279 ±43	-	146 ±23	2 - 4.2
30μm	290	-	1538 ±139	6.3	1061 ±96	7 - 8.6
50μm	306	-	3214 ±244	8.8	2101 ±160	9.3 - 10.7
70μm	215	-	3683 ±272	10.9	3426 ±253	11.4 - 12.5
100μm	194	-	4548 ±302	13.7	4689 ±312	14 - 15
140μm	244	-	5403 ±310	16.6	4429 ±255	17 - 17.8
170μm	266	-	4364 ±269	18.6	3281 ±202	19.1 - 19.8
200μm	267	-	2829 ±198	20.58	2119 ±148	20.8 - 21.7
250μm	270.5	-	1038 ±124	23.5	767 ±92	23.7 - 24.4
300μm	355	-	336 ±41	26	190 ±23	26.4 - 26.8

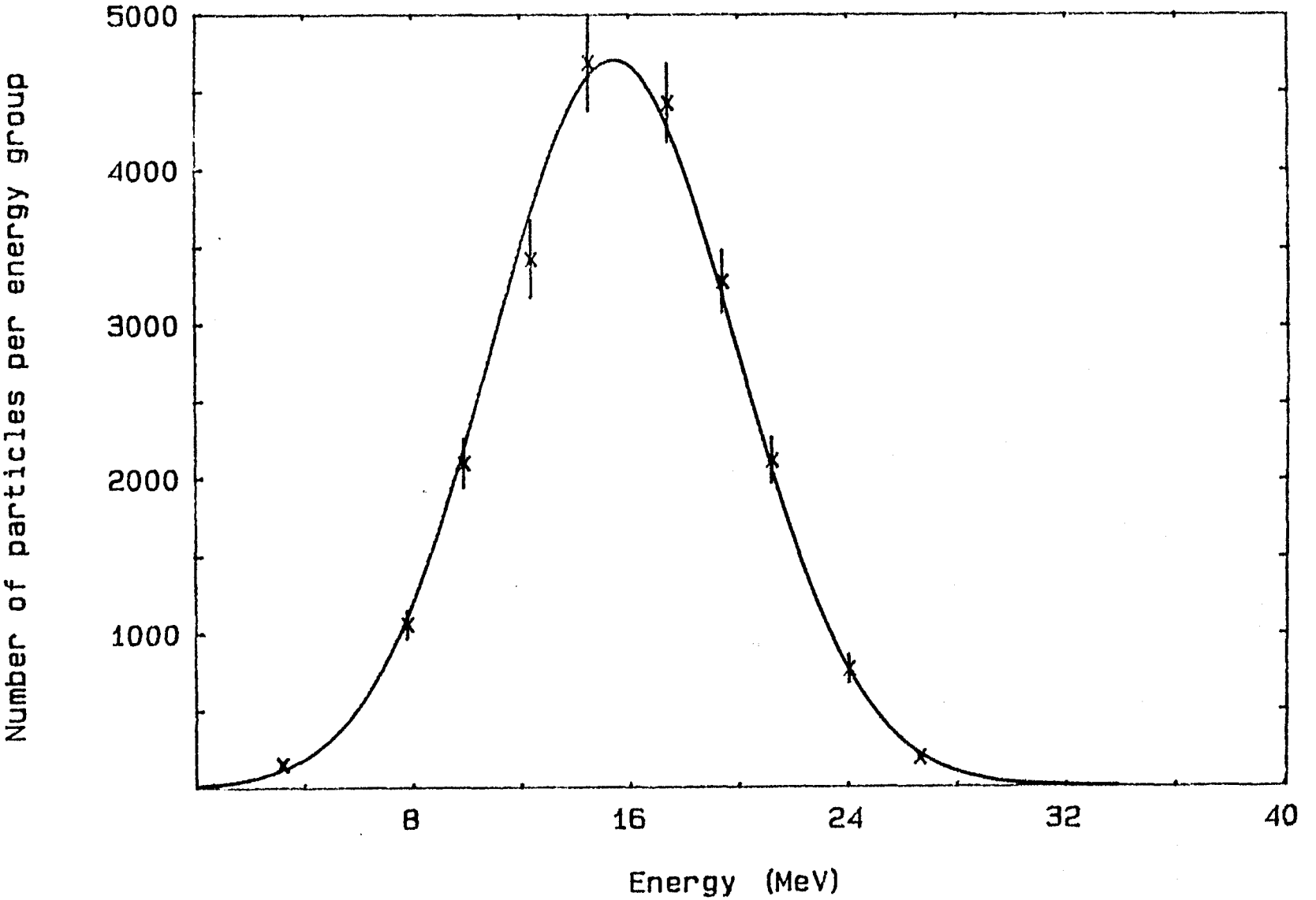

Fig. 6.17 Energy distribution of alpha particles emitted by ^{252}Cf obtained with the LR115 detector.

these experiments and those recently published are shown in Table 6.3, along with an overall mean from the two methods. A Gaussian fit to the data of Fig. 6.17 shows no significant deviation of the data from the curve in the low energy tail. This result agrees with that of Cosper et al.[6] but is in contrast to that obtained by Loveland[12], who found a deviation from a Guassian fit in the low energy tail of the spectrum. As can be seen from Fig. 6.17, there is no evidence for the emission of short-range alpha particles in the ternary fission of ^{252}Cf. This is in contrast to the results of Kugler and Clarke[13], who found the probability for emission of alpha particles ($E_\alpha > 8$ MeV). The use of aluminium degraders with the LR-115 may result in broadening the energy distribution and this may affect the shape of the spectrum in Fig. 6.17. The values obtained for the mean energy of the alpha particles emitted in ternary fission and the FWHM of the Gaussian distribution of their energies obtained in both methods reported here are in excellent agreement with previously reported data. The error values quoted are based on two sources of error (a) that due to the calibration procedure and (b) that due to fitting the Gaussian curve to the experimental data. The latter was by far the larger. The errors from both sources were added in quadrature to give the final, overall error.

In order to obtain the ratio of ^3H to ^4He it was necessary to correct the experimental yields of these particles for losses of low-energy particles in the 12 μm thick, Al stopping foil. The correction was based on the extrapolation of the Gaussian curve to the area under the relevant part of the curve. Thus, the area under the low energy portion, when extrapolated to zero energy gave the necessary correction. The ratio of ^3H to ^4He quoted, namely $(7.6 \pm 0.4) \times 10^{-2}$ is the corrected value. A similar procedure was used to obtain the ratio in the references quoted except for the determination by Raisbeck and

Table 6.3
Values for 4He and 3H from varios sources

Method	^{4}He Mean energy (MeV)	^{4}He FWHM (MeV)	^{3}H Mean Energy (MeV)	^{3}H FWHM (MeV)	yield of ^{3}H / yield of ^{4}He x 100	Reference
ΔE-E	16.0 ± .5	11.5 ± .5	8.0 ± 1.0	6.0 ± 1.0	5.9 ± .2	5
ΔE-E	16.0 ± .2	10.2 ± .4	8.0 ± .3	6.2 ± .6	8.46±.28	6
Coinc-indence***	15	13*	-	-	-	7
ΔE-E	15*	10*	8*	8*	7.0**	8
ΔE-E	15.5	10*	-	-	-	9
ΔE-E	16.1 ±.8	13.0 ± .7	9.0 ± .5	8.2 ± .5	7.4 ± .3	10
ΔE-E	15.6 ±.2	10.3 ± .5	7.7 ± .4	8.2 ± .9	7.7 ± .46	11
SSNTD (LR115)	15.6 ±.8	10.4 ± .6	-	-	-	this work
ΔE-E	16.3 ±.6	11.0 ± .7	8.4 ± .8	6.9 ± .8	7.6 ± .4	this work
Mean value this work	16.0 ± .7	10.7 ± .7	8.4 ± .8	6.9 ± .8	7.6 ± .4	

* Estimated from their data
** Values quoted in Cumpstey and Vass (1979) based on data of Raisbeck and Thomas (1968).
*** coincidence between alpha detector and fission detector

* Estimated from their data

** Values quoted in Cumpstey and Vass (1979) based on data of Raisbeck and Thomas (1968).

*** coincidence between alpha detector and fission detector

Thomas[8]. The values quoted for these workers are in fact values determined by Cumpstey and Vass[10] from the data published by Raisbeck and Thomas[8].

6.4.2 Fast Neutron Fission of ^{238}U

In fission involving fast neutrons, There is always the possibility of the production of low mass particles by reaction other than that of ternary fission. These interfering reactions must be taken into consideration where they are energetically possible. In Table 6.4 are listed the more probable reactions based on the composition of the detector and stopping materials. As can be seen from this Table the Q-value for all the reactions is negative and most of them have a threshold higher than the neutron energies used for the yield measurements. For those cases which are energetically posible, it was possible to prevent the induced charged particles from being counted without at the same time having a significant number of ternary events by using an appropiate lower limit on the TSCA of the E detector. In order to determine chance coincidences a fixed delay time was applied to the output of the TSCA of the E detector. The resultant pulses, along with the output pulses from the other TSCA, which were derived from the ΔE detector, were input to another coincidence unit. The output of this coincidence unit was sent to a scaler and the count in this indicated the chance coincidences.

During the experiment a considerable number of background counts were recorded by the telescope close to the triton and alpha particle regions. The three dimensional spectra of energy versus mass obtained in ternary fission of ^{238}U for alpha particles and tritons are shown in Fig. 6.18. Figure 6.18(a) represents a raw spectrum including background counts and 6.18(b) the same spectrum after removing background counts. The spectrum was recorded continuously throughout

Fig. 6.18(a) Mass vs energy spectrum for ternary fission products from ^{238}U obtained using the Particle Identification Unit (PIU). This figure represents a raw spectrum including background counts.

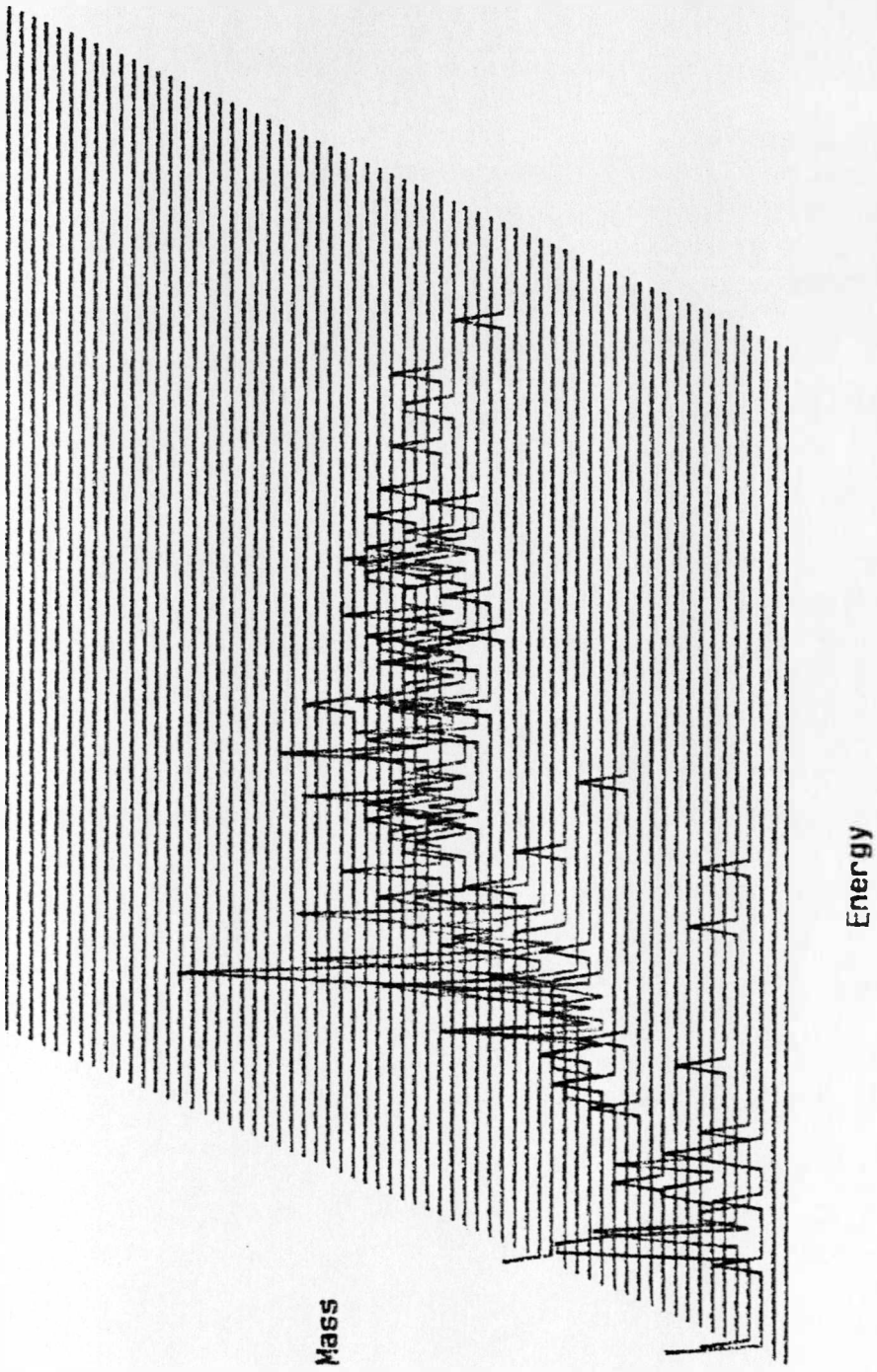

Fig. 6.18(b) Shows the spectrum in Fig. 6.18(a) after removing the background.

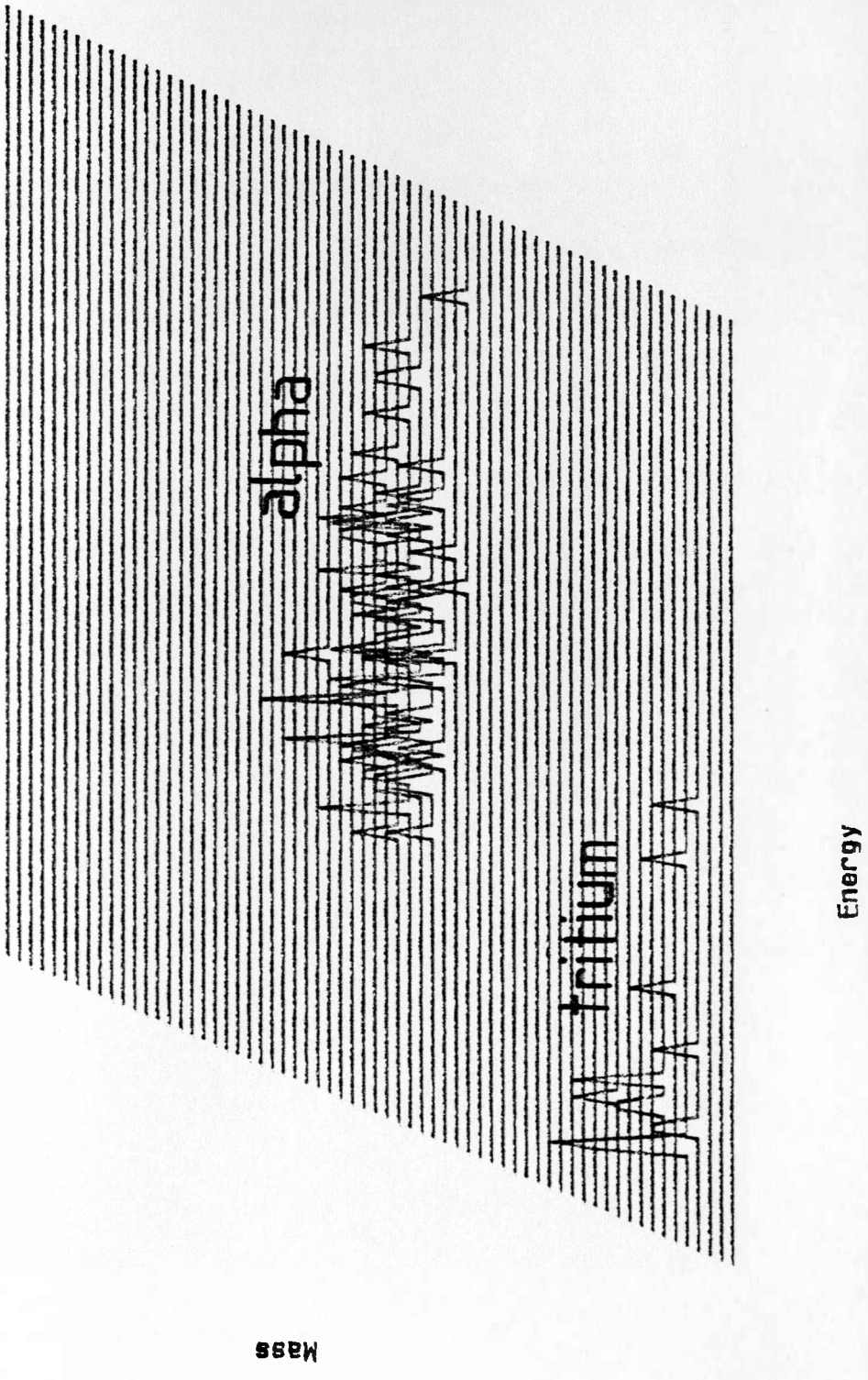

Table 6.4

Possible interfering reactions in the determination of LCPs.

Reaction	Q-value (Mev)	Threshold (MeV)
28Si(n,p)28Al	-3.86	3.928
29Si(n,p)29Al	-2.899	3.928
30Si(n,p)30Al	-7.799	8.0215
27Al(n,p)27Mg	-1.8269	1.89
28Si(n,d)27Al	-9.3613	9.70
29Si(n,d)28Al	-10.1099	10.464
30Si(n,d)29Al	-11.284	11.60
27Al(n,d)26Mg	-6.046	6.273
28Si(n,t)26Al	-16.164	16.749
29Si(n,t)27Al	-11.5779	11.983
30Si(n,t)28Al	-14.462	14.952
27Al(n,t)25Mg	-10.882	11.291
28Si(n,3He)26Mg	-12.1387	12.579
29Si(n,3He)27Mg	-14.168	14.579
30Si(n,3He)28Mg	-16.27	16.827
27Al(n,3He)25Na	-14.69	15.25
28Si(n,4He)25Mg	-2.65	2.749
29Si(n,4He)26Mg	-.034	.036
30Si(n,4He)27Mg	-4.2	4.34
27Al(n,4He)24Na	-3.13	3.24

the experiment but was stored about every two hours. It shows the relatively constant value for the ratio of tritons to alpha particles. The E detector, however, suffered damage durring the irradiation wich resulted in a blurring of the boundaries of the background and triton counts towards the end of the irradiation period. Consequently, these later counts were not included in the final results. Figure 6.19 shows the contribution from background counts to the triton region. Tables 6.5 and 6.6 show the emitted number of LCP detected by the telescope and the total fission events recorded by the fission detector for each neutron energy. The emission probability for alpha particles and tritons relative to the total binary fission events, along with the geometrical counting efficiency (g.c.e.) are also included in these Tables.

Mica detectors were placed adjacent to the ΔE detector and to the fission detector in order to determine the experimental g.c.e. at each detector. The resultant tracks in the mica were etched in 48% HF acid for 13 minutes. From the the track density found in each Mica sheet, the ratio of these densities along with the known angular anisotropy for neutron induced fission of ^{238}U (see Chapter 7), it was possible to determine the g.c.e.. The track density and g.c.e. found from these experiments are shown in Table 6.7. The present data for ternary fission of ^{238}U does not enable us to provide any information about the energy spectra of the particles owing to the poor statistics. Tables 6.8 and 6.9 summarise the reported tritium and alpha yield values for ^{238}U by fast neutron fission.

In the case of tritium, the only reported value which was obtained experimentally, is that of Buzzelli etal[14], who measured the tritium yield after chemical separation and counting using a liquid scintillation counter. Their reported value of 9×10^{-4} t/f is 4 times greater than that theoretically calculated value for tritium[16]. As can be seen

Table 6.5 The alpha and triton yields determined from neutron induced, ternary fission of ^{238}U at E_n = 4.1 MeV

Alpha events	triton events	fission counts	geometry correction	ratio of t/α	alpha yield*	triton yield^t
36	6	4562	6.73	.166		
52	8	6634	=	.153		
61	11	7867	=	.18		
79	13	10177	=	.164		
93	14	12014	=	.150		
102	16	13400	=	.157	1.13±.11	1.77±.44

* yield x 10^{-3}

t yield x 10^{-4}

Table 6.6 As for Table 6.5 but at E_n = 3.6 MeV

Alpha events	triton events	fission counts	geometry correction	ratio of t/α	alpha yield*	triton yield^t
28	6	738	32.159	.214		
64	12	1696	=	.187		
78	16	2096	=	.205	1.15±.13	2.37±.59
102	67	2894	=	rejected this data		

* yield x 10^{-3}

t yield x 10^{-4}

Table 6.7 The solid angle correction (geometry correction) for the fission detector and the telescope obtained from the track densities registered in mica, solid state nuclear track detectors

Neutron Energy (MeV)	Track density in mica attached fission detector	Track density in mica attached telescope	df* cm	dt* cm	geometry correction
3.6	19703	132600	6.5	3	6.73
4.12	5737	184501	12	2.5	32.159

* D_f is the ^{238}U foil-fission detector distance

** D_t is the ^{238}U foil-telescope distance

Table 6.8 Published values for the ratio of binary fission to triton emission in the ternary fission of ^{238}U.

Neutron energy (MeV)	Binary/triton	Method of measurement	Reference
Fast neutron*	434.7±14	experimentally	Buzzelli et al[14]
fast neutron**	1000±29	=	=
fast neutron	384	=	=
fast neutron	9000		Rider et al[15]
fast neutron	3840	calculated	ANL[16]
3.6	5649±1412	experimentally	this work
4.12	4219±1054	=	=

* location of irradiation at lower blanket at 42 cm from core midplane

** location of irradiation at core at 5 cm from core midplane

Table 6.9 As for Table 6.8 but for LRAs.

Neutron energy (MeV)	Binary/LRA	Method of measurement	Reference
fast neutron	645		Rider et al[15]
2.5	1103±28	experimentally	Nagy et al[19]
14	795±35	=	=
2.5	600	=	Soloveva et al[20]
2.5	4550±350	=	Drapchinski et al[21]
14	3750±270	=	=
14	1050±100	=	Porfilovz et al[22]
3.6	884±86	=	this work
4.12	869±98	=	=

Fig. 6.19 As in Fig. 6.18 but showing the blurring of the boundaries of the background and triton counts as a result of damage to the E detector in the high flux neutrons.

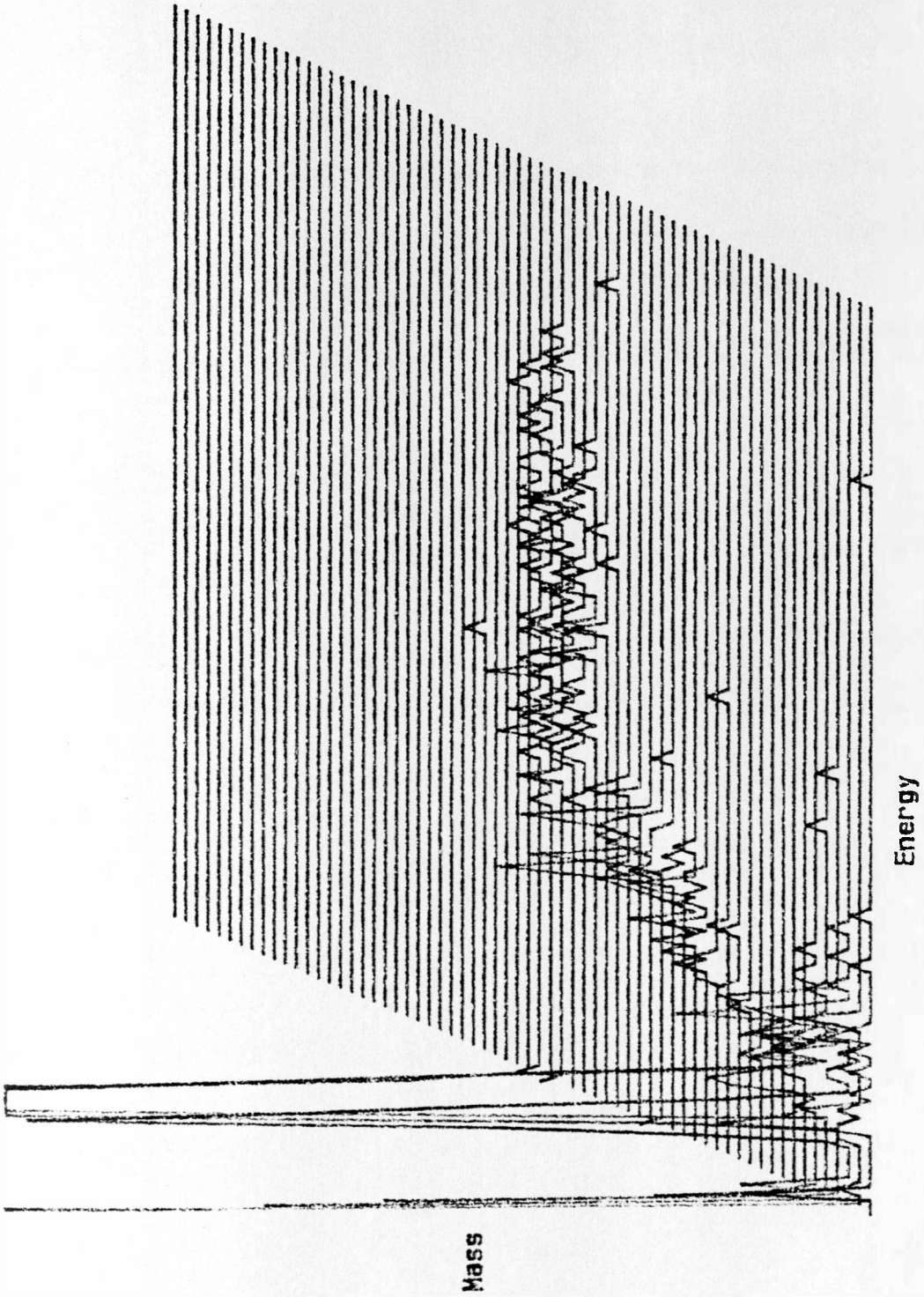

in Table 6.8, our results for tritium are about the value predicted theoretically. Buzzelli etal also quoted a very small error (2.9 to 3.3 %) on their reported values. Such a small errors would not appear to include all the uncertainties in their method. They used a summation method as described in Chapter 3 for calculating the total fission products produced during irradiation. This in itself has more than a 5% uncertainty, because reported uncertainties for fission products resulting from fast neutron induced fission of ^{238}U are at least 5% . Our results for the tritium yield indicate that the value reported by Buzzelli etal may not be purely due to ternary fission but may include some tritium contamination from other sources of tritium production in a fast breeder reactor. The possible sources of tritium production in a fast reactor are now considered.

Tritium is produced by neutron activation of lithium and boron, in addition to ternary fission. Boron and lithium can contribute anywhere from 35 to 80% of the total tritium produced[17], depending on the type of reactor. Boron is used in the control rods in fast reactors and is also used as a chemical shim in the reactor coolant in fast reactors and some light water reactors. Lithium occurs as an impurity in the coolant and fuel. The lithium reactions for tritium production are:

$^{6}Li\ (n,\alpha)^{3}H$

$^{7}Li\ (n,n'\alpha)^{3}H$

The boron activation reactions are as the following

$^{11}B\ (n,t)^{9}Be$

$^{10}B\ (n,t)2^{4}He$

$^{10}B\ (n,\alpha)^{7}Li$

$^{7}Li\ (n,n't)^{4}He$

Most of the tritium is produced by $^{10}B(n,2\alpha)^{3}H$ reaction, because the $^{11}B(n,t)^{9}Be$ reaction and the $^{7}Li(n,n't)^{4}He$ reaction have thershold energies of 9.6 MeV and 2.8 MeV, respectively.

Our results indicate that ratio of tritium to LRA is about 16 to 18 % and this represents nearly three times the amount of tritium as produced in thermal reactions[18]. This much greater rate of tritium production indicates its importance in the development of fast reactors.

It is difficult to establish any neutron energy dependence of the observed yield due to the lack of published data for other neutron energies. Our results, however, for two different neutron energies indicate that the triton yield increases with increasing neutron energy. For the yield of alpha particles in the ternary fission of ^{238}U several data obtained experimentally by other authors[19-22] along with the results obtained in this work are shown in Table 6.9. The reported data are statistically inconsistent and there is considerable spread in the data amounting to a factor of 5. Bearing this in mind we find that our results are in reasonable agreement with those of reference 19. It seems there is a trend of increasing yield with increasing neutron energy. This is indicated by a least-squares line through the data (see Fig 6.20).

This is in contrast with the observation of Fluss etal[23] in the fission of monoenergetic-neutron-induced fission of ^{235}U where they used both a telescope method and radiochemical technique. They found that the tritium yield for ^{235}U by radiochemical method was about (2.0 ± .2)x10-4 for neutron energies from 170 to 700 KeV. This indicates an increase of the tritium yield from thermal energies to 170 KeV of about 2.3 to 2.4 . As mentioned in chapter two, there is some evidence from other fissioning nuclides that the yields of LCP increase with increasing excitation energy (see Fig. 2.14). Although Fig. 2.14 shows this trend to be valid for excitation energies above 15 MeV our results indicate rather the possibility of extention of this curve to lower energies down to about 10.6 MeV. It seems in any case, that the

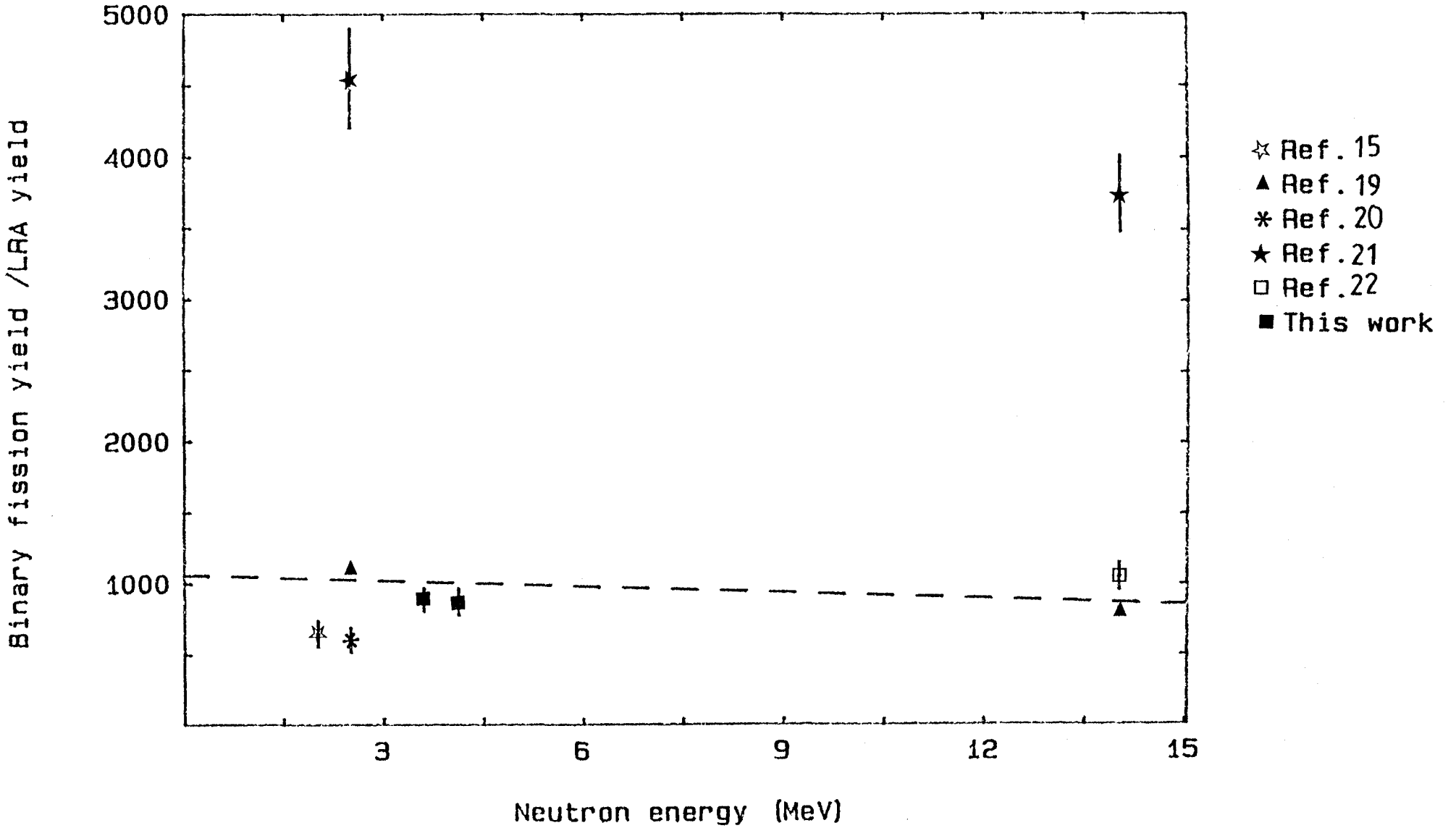

Fig. 6.20 Yield of LRAs from ^{238}U as a function of neutron energy.

yield depends only weakly on excitation energy. The reason for this may be connected with the observation that there is no correlation between the average fragment kinetic energy and initial excitation energy. This observation can be easily interpreted from the fact that the nuclear shape and charge distribution at scission are insensitive to the internal energy of the nucleus. Even accepting this view, there are still many questions left unaswered. One of these is why the rate of LCP emission from nuclides with an excitation energy, E^*, in excess of 15 MeV should be less than that from the nuclide in the ground state ($E^*=0$); see Fig. 6.21. Perhaps the higher yields in spontaneous fission reflect a special feature of this process and should not be considered in any general discussion of the energy dependence of the yield of LCP. The only conclusion from differences in spontaneous fission to fission at all higher excitation energies, is that the nucleus must penetrate rather than climb over the fission barrier.

The production ratio of tritium to alpha (t/α), shown in Tables 6.5 and 6.6 does not seem to depend strongly on the excitation energy of the fissioning nucleus.

According to Wagmens etal[18], the FWHM for the triton and LRA energy distributions increases as Z^2/A increases. As mentioned earlier in chapter two, it has been reported that there is a correlation between LRA/binary fissions and Z^2/A or $4Z-A$. Our result also indicates such a correlation as seen in Figs. 6.22 and 6.23. According to reported experimental results, discussed in chapter two, the actual values of the most probable α-particle energy, $E\alpha$, and triton energy, E_t, are constant for different fissioning nuclides, within experimental uncertainties. Therefore, the question arises as to why this should occur. A possible explanation is given below.

It is clear from trajectory calculations[24] that the initial energies

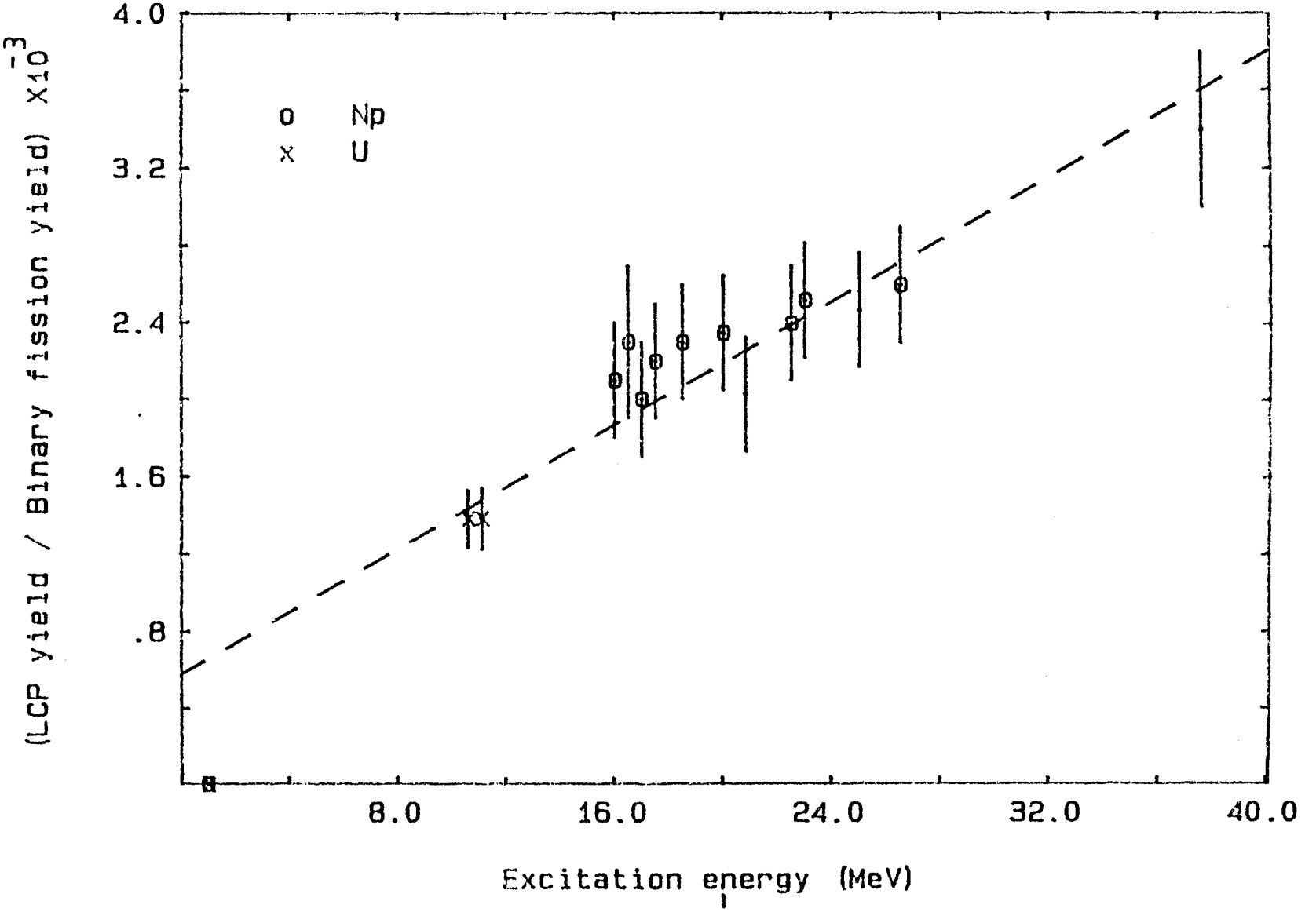

Fig. 6.21 The LCP emission observed in several fissioning nuclides as a function of excitation energy.

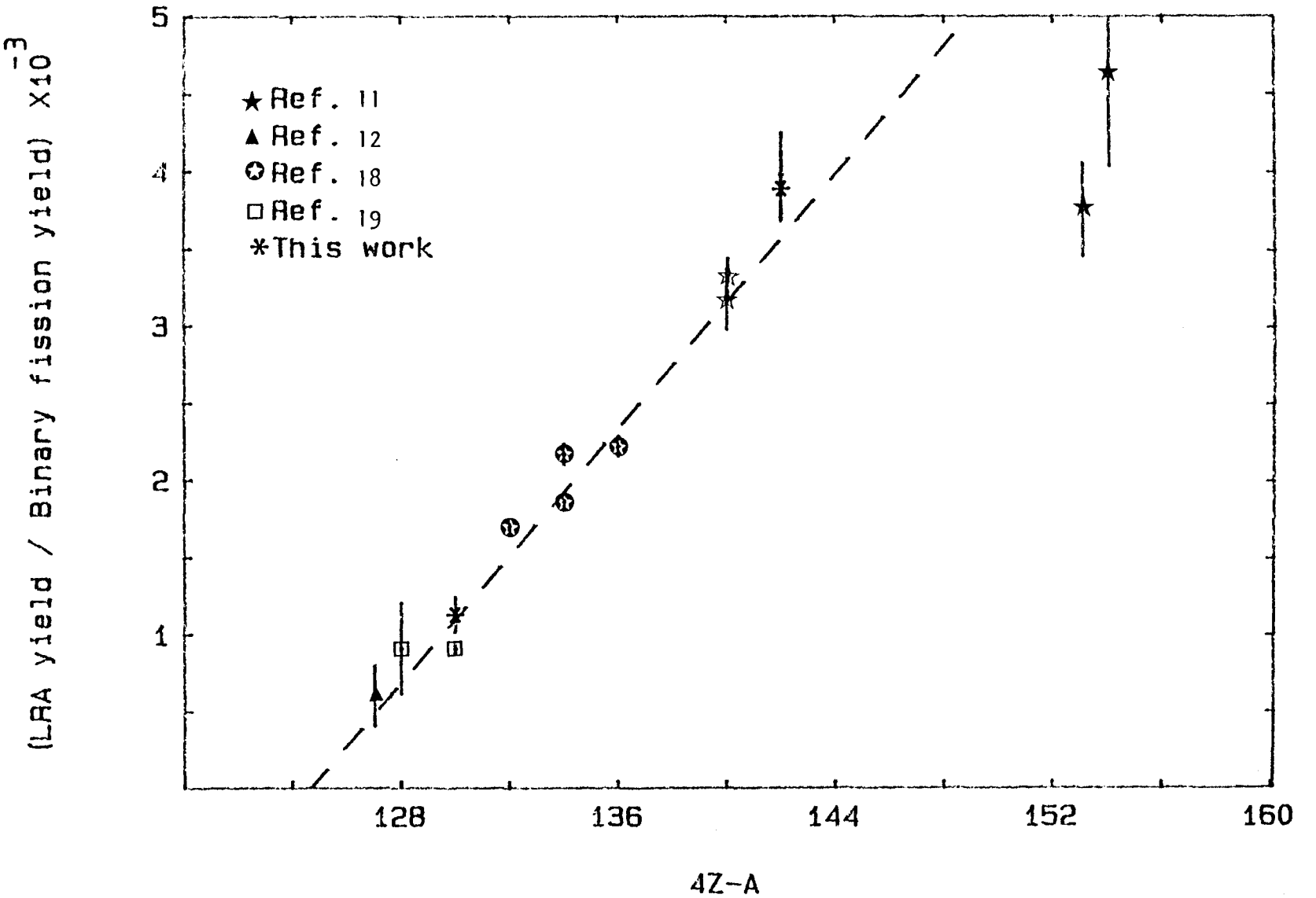

Fig. 6.23 LRA/binary ratio as function of 4Z-A.

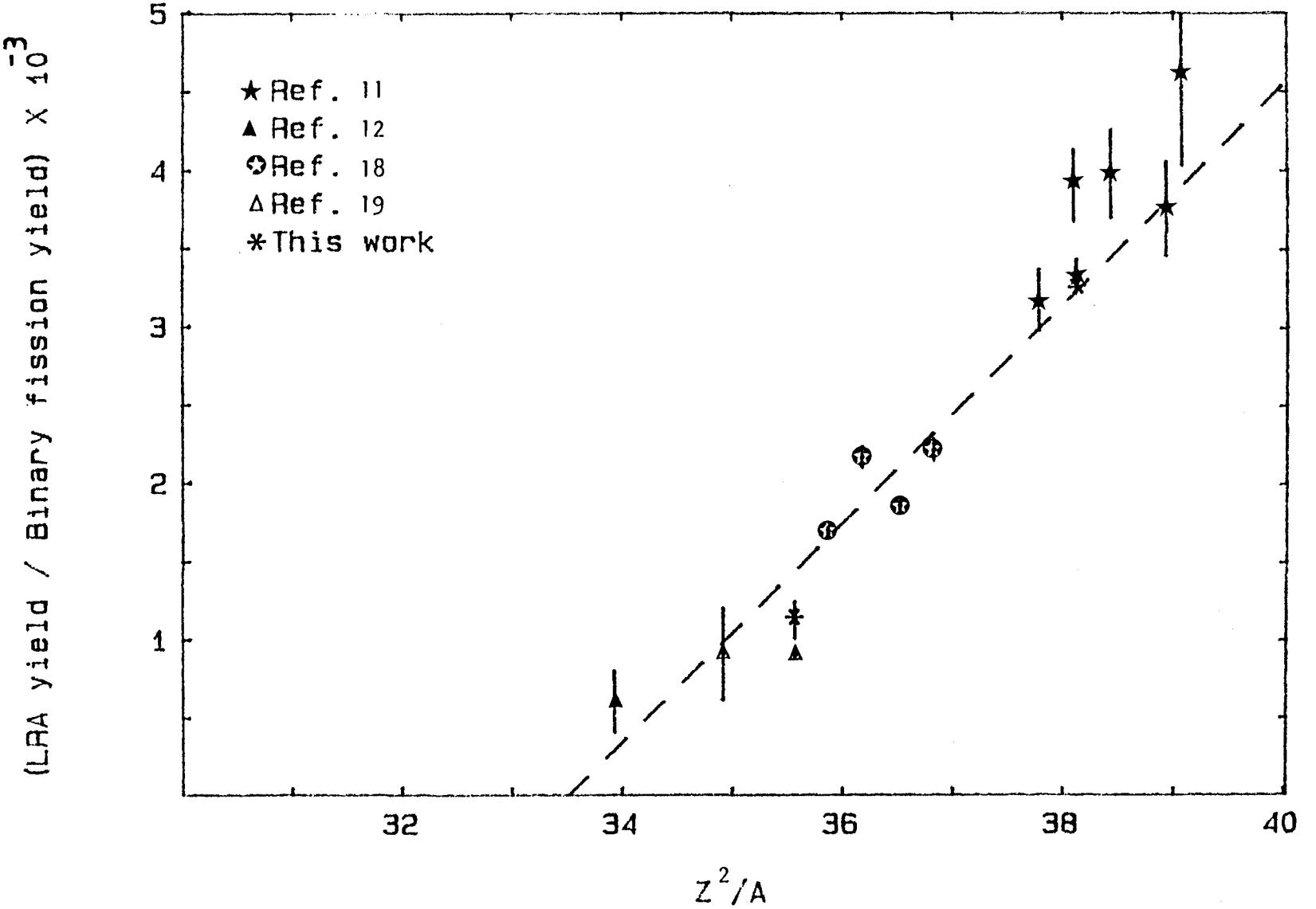

Fig. 6.22 LRA/binary ratio as function of Z^2/A.

of the LRA-particles can be roughly approximated by a Boltzmann distribution with a temperature around 1.5 MeV. In Chapter two it was pointed out that, the most probable angles for emission of LRA with respect to the light fission fragment from $^{235}U(n_{th},f)$ and ^{252}Cf are 81.3^{o} and 84.3^{o}, with a FWHM of 18.5^{o}, respectively. The final energy of LRA particles is affected by their emission angle and the focusing Coulomb field between both fission fragments. As illustrated in Chapter two, E_{α} as a function of angle of emission is simillar for $^{235}U(n_{th},f)$ and ^{252}Cf. With respect to the question posed above, it is assumed that the focusing Coulomb field and the cones in which the LRA particles are emitted are constant. Such an assumption seems reaonable, following the discussion in Chapter two and drawing on the fact of the well-known stability of the heavy fragment peak in the mass distribution. This, in turn is mainly due to the spherical nature of the Z=50 and N=82 shells and to the deformed N=88 shells. Consequently, the mass of the heavy fragment, m_H, remains almost constant. The Coulomb field is strongly depend on charge of heavy fragment, Z_H, but it is required to be constant in order to explain the constancy of E_{α}.

References:

1- England J.B.A., Nucl. Instr. and Meth. 106, 45 (1973)

2- England J.B.A., 'Techniques in Nuclear Structure Physics', Macmillan, 1974

3- Analog to digital converter 5416A/B, Hewlett Packard, 1970.

4- Henk R.P., E.V. Benton USA Naval Radiological Defence Laboratory San Francisco, Report USNRDL (1968)

5- Whetstone S.L. and T.D. Thomas, Phys. Rev. 154, 1174 (1967)

6- Cosper S.W., J. Cerni and R.C. Gatti, Phys. Rev. 154,1193 (1967)

7- Fraenkel Z., Phys. Rev. 156, 1283 (1967)

8- Raisbeck G.M. and T.D. Thomas, Phys. Rev. 172, 1272 (1967)

9- Fluss M.J., S.B. Kaufmann, E.P. Steinbery and B.D. Wilkins, Phys. Rev. C7, 153 (1973)

10 - Cumpstey D.E. and D.G. Vass, in Physics and Chemistry of Fission (Proc. Symp. Vienna, 1978) IAEA, Vienna, 223 (1979)

11- Wild J.F., Baisden P.A., Dougan R.J., Hulet E.K., Loughead R.W. and Landrum J.H., Phys. Rev. C32, 488 (1985)

12- Loveland W., Phys. Rev. C9, 395 (1974)

13- Kugler G. and W.B. Clarke, Phys. Rev. C5, 551 (1972)

14-Buzzelli G.S. Langer, C. Jones, B. Gainey, Transactions, Amc. Nucl. Soc. 24, 458 (1976)

15-Rider B.F., Vallecitos Nuclear Centre, NEDO-12154-3(B) (1980)

16- Argonne National Lab. Chemical Engineering Division Research Highlights, May 1967 -April 1968 ANL-7450, Argonne, Illinois (1968)

17- Tanner J.E. PNL 3563, UC-11, 3 (1981)

18- Wagemans C., P. Dhoundt, P. Schilebeeckx, R. Brissot, Phys. Rev. C33, 943 (1986)

19- Nagy L., T. Nagy, and I. Vinnay, Sov. Jor. of Nucl. Phys., 8 , 257 (1969)

20- Soloveva Z.I., Atomnaya energiya 8,137 (1960)

21-Drapchinskii L.V., S.S. Kovalenko, K.A. Petrzhak, and I.I. Tyutyugin, Atomnaya energiya 16, 144(1964).

22- Perfilov N.A., Z.I. Solovena, and R.A. Filov, Sov. Phys.-JETP 14, 7 (1962)

23- Fluss M.J., N.D. Dudey and R.L. Malewicki, Phys. Rev. C 6 2252 (1972)

24- Radi H., j. Rasmussen, F. Donangelo, L. Canto and L. Oliveira, Phys. ReV. C 26, 2049 (1982)

CHAPTER 7

Angular Distribution of Fragments from the Fission of ^{238}U Induced by Neutrons in the Energy Range 1-19 MeV

7. Introduction

The fission of ^{238}U with neutrons can occur through reactions (n,f), (n,n'f) and (n,2n'f), called first, second and third chance fission[1], respectively, with increasing neutron energy. It has been predicted[2,3] that the ratio, R, of the fission yield at 0^o to that at 90^o with the neutron incidence direction i.e. $R= W(0^o)/W(90^o)$, increases at energies just above the thresholds for (n,f), (n,n'f) and (n,2n'f) reactions and that lower, fission-chance, fission fragments do make a contribution to the angular-distribution anisotropy of higher fission-chance fragments.

Even though the published experimental results[4-6] for the (n,f) and the (n,n'f) reactions confirm that the anisotropy ratio R increases at energies just above the fission thresholds, yet there are disagreements in the reported values of R. No marked increase in the ratio, R has been found[5-8] at $E_n>12$ MeV, where the (n,2n'f) reaction becomes energetically possible. This, however contradicts the expected variations predicted by theoretical calculation.

Our investigation was undertaken with the aim of improving the experimental results on the angular distribution of the fission fragments, as these are important for the compilation of energy-dependent fission cross sections. Variations in the fission fragment angular distribution with neutron energy may be mis-interpreted as changes in the apparent efficiency of the detector. For example, detector efficiency may be affected by changes in the proportion of fragments that fail to emerge from the fission foil with

sufficient energy to appear above the detector bias, or by variations in the fraction of emerging fragments that reach the sensitive volume of the detector. The other aim of our experiments with neutrons of energies E_n>12 MeV was to investigate the behaviour of the anisotropy ratio R when the $^{238}U(n,2n'f)$ reaction sets in. The wellknown discovery of vibrational resonances attributed to the second minimum in the fission potential barrier[1] has permitted a detailed investigation of fission fragment anisotropy leading to more percise determination of quantum number of states involved and this has been successfully used as an important tool for this propose[9-10].

7.1 Experimental Procedure and Results

The targets used for this study were as follows:

1. ^{238}U(of 99.99% purity) with a uniform thickness of 500 $\mu g/cm^2$, prepared by electrospraying the uranium isotope on a gold-coated polyimide foil (7 μm thick), mounted on an aluminium ring.
2. ^{238}U (of 99.98% purity) with a uniform thickness of 1 mg/cm^2 coated on thin foil of polyethylene (3 μm thick).

The beam-spot size at the target was made approximately 11 mm in diameter by using a copper, water-cooled collimater before the target holder. A 4 mm collimater, consisting of a 4 mm diameter in a sheet of paper attached to the target foil effectively restricted the emission area of the target with respect to the detector. This limited the measurement of angular distribution to angles $< 80^o$ with respect to the beam direction.

As the distance of the uranium target from the neutron source was ≈ 10 cm in most of the experiments, this means that the fission fragments could be considered as coming essentially from a point

Table 7.1

Characteristics of the neutron irradiations on the 3 MV Dynamitron at the Radiation Centre, University of Birmingham

Neutron source	Principal neutron energy (MeV)	Energy spread (MeV)	Neutron flux on uranium target ($n.cm^{-2}s^{-1}$)
$^{3}H(p,n)^{3}He$	2.00	1.96 - 2.03	1.09×10^{7}
"	1.85	1.80 - 1.89	1.04×10^{7}
"	1.75	1.71 - 1.80	9.87×10^{6}
"	1.61	1.55 - 1.65	9.31×10^{6}
"	1.55	1.50 - 1.60	8.70×10^{6}
"	1.50	1.46 - 1.56	8.6×10^{6}
"	1.45	1.41 - 1.52	7.90×10^{6}
"	1.41	1.35 - 1.46	7.20×10^{6}
"	1.32	1.27 - 1.37	6.80×10^{6}
$^{2}H(d,n)^{3}He$	5.9	5.83 - 6.02	1.12×10^{7}
"	4.8	4.71 - 4.92	1.07×10^{7}
$^{3}H(d,n)^{4}He$	17.72	17.61 - 17.77	3.11×10^{6}
"	16.58	16.46 - 16.63	3.07×10^{6}
"	15.51	-	"
"	14.71	-	"
"	14.02	-	"
"	13.51	-	"

source. Fragments from the neutron-induced fission of ^{238}U were detected either by means of Lexan* (polycarbonate plastic) detectors or with a muscovite mica track detector.

Irradiation took place in the Low Scatter Cell of the Department of Physics Radiation Center, using the 3 MV Dynamitron facility. Characteristics and parameters of the irradiations, with principal neutron energies, E_n, resulting from (p,T),(D,T) and (D,D) reactions, are presented in Table 7.1. In the case of the $^{3}H(d,n)^{4}He$ reaction, neutrons in the energy range 13.5-16.5 MeV were produced by 950 keV deutrons. The experimental chamber was located in such a way that the angle between the uranium foil and the neutron beam corresponded to the required neutron energy. The reaction-kinetics computer program, "DWKIN[11], was used to calculate the neutron energy at a specified angle, from the (D,T) reaction.

The neutron beam was produced by the bombardment of D and T targets using a collimated beam (10 mm in diameter) of deutrons or protons. The spread in the principal energy of the neutrons from the above reactions is caused by both the thickness of the titanium target on which the deuterium or tritium has been absorbed and the angular spread in the emission of the neutrons. The computer program, "DWFXA"[11], was used to calculate the neutron energy spectra for the circular (disk) neutron target and the circular uranium foil geometry used in these experiments. The neutron energy spread was also calculated by the same program. The contributions to the fission fragments for each principal neutron energy, caused by neutrons with energies other than the principal one are negligible. These latter neutrons arose from deutron-stripping reactions, primarily in the deuterium target cell, and from elastic and inelastic scattering due to the room itself as discussed in chapter Five. Two, different

* Manufactured by the General Electric Co. of USA.

vacuum chambers were used. The first was a small, cylindrical chamber similar to the one used by Chaudhuri et al[12]. The irradiation geometry used with this chamber is illustrated in Fig. 7.1. From Fig. 7.1(b), it is clear that

$$d\sigma = \text{const.} 2\pi \ell . T_d \qquad 7.1$$

where σ is the fission cross section for a given neutron energy, T_d is the track density (number of tracks per cm^2) registered in a detector strip of width ℓ at a distance, r, from the centre of the base of a cylinder of radius R. If θ is the angle between the neutron beam and the direction of the flight of the fission fragment, then the solid angle subtended at θ is as follows

$$\Omega = 2\pi(1-\cos\theta)$$

where Ω is the solid-angle element presented by a given detector strip.

$$d\Omega = 2\pi \sin\theta d\theta \qquad 7.2$$

From Fig. 7.1(b) it follows that

$$r d\theta/\ell = \sin\theta = R/r,$$

i.e.

$$d\theta = \ell \sin\theta/r = \ell.\sin^2\theta/R$$

by substituting the value of $d\theta$ in equation 7.2,

$$d\Omega = (2\pi.\ell/R).\sin^3\theta \qquad 7.3$$

Combining the equations 7.1 and 7.3, the angular distribution of the emission cross section for fission fragments at an angle θ to the neutron-incidence direction is given by the equation[12]:

$$\left(\frac{d\sigma}{d\Omega}\right)_\theta = \text{const.}\ (R^2.T_d/\sin^3\theta) \qquad 7.4$$

Thus the relative angular distribution of fission fragments could be determined by measuring the track density in horizontal strips at different heights from the base line of the detector. With this arrangement we were able to detect fragments at angular intervals of

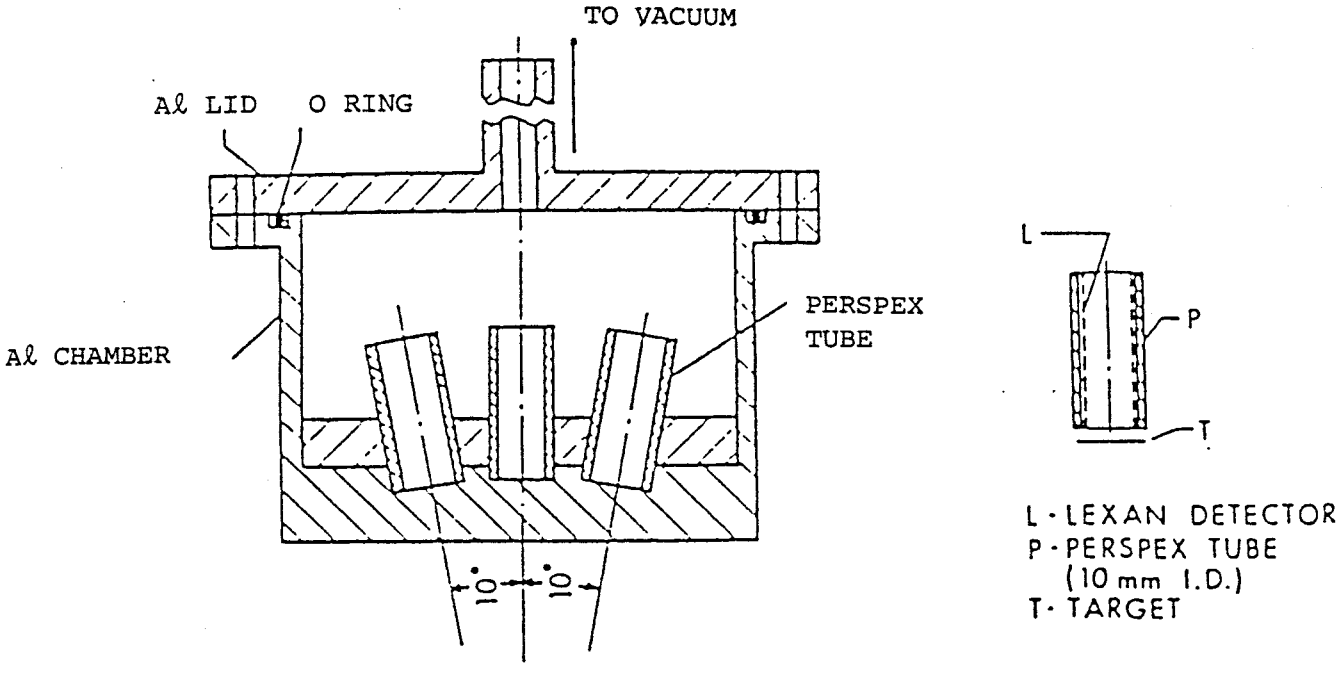

Fig. 7.1(a) Schematic diagram of the "small" cylindrical fission chamber (of diameter 7.5 cm) used in the experiments. Five Perspex tubes are mounted on the base of the Aℓ chamber. The tube positioned co-axially at the centre of the chamber is the one that receives the fission fragments.

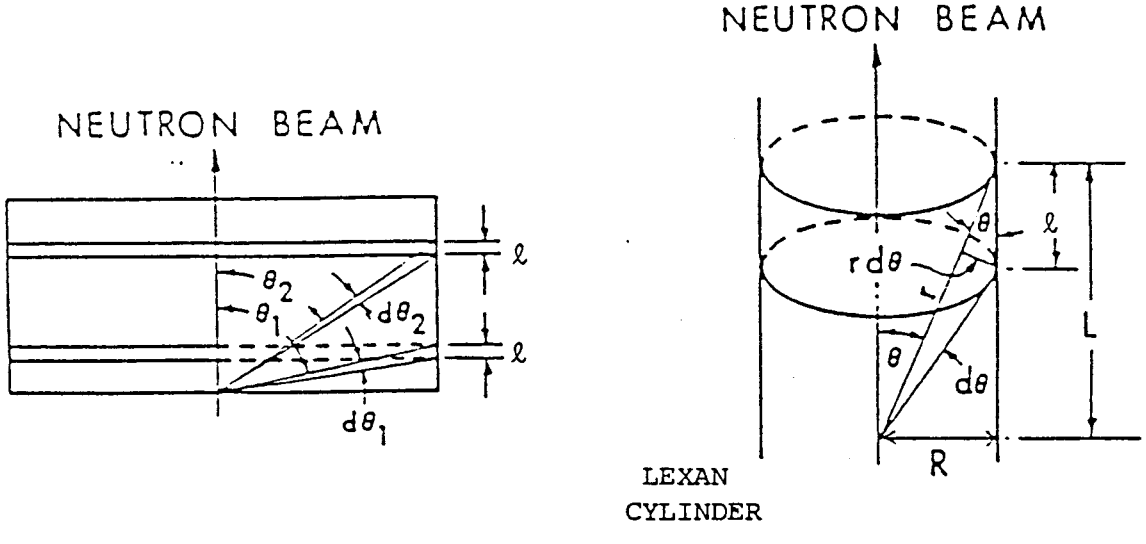

Fig. 7.1(b) Schematic diagram of the track registration geometry. The right-hand diagram shows the position of the Lexan detector inside the cylinder during irradiation. The left-hand diagram shows the unfolded Lexan detector as fixed on the microscope slide. The horizontal strips of width, ℓ, being scanned correspond to a given angle, (θ_1, θ_2), that the fission fragments make with the neutron beam.

≃ 10° over the range 0° to 80°.

The second chamber used in these experiments was one of 40 cm in diameter, which was also used in experiments on the ternary fission of ^{238}U. A photograph of the experimental arrangments with the second chamber is shown in Fig. 7.2. The geometrical disposition of the Lexan and mica detectors (2π-geometry) used here allowed us to detect fragments over the angular range 0° to 180° with respect to the direction of the neutron beam.

After each irradiation, the Lexan foils were etched in 6M NaoH at 60°C, and the mica detectors in 48% HF at room temperature. The etched tracks were counted under an optical microscope.

The normalized, experimental, angular distribution, $W(\theta)$ of the fission-fragment yield is plotted against the laboratory angle θ in Figs. 7.3 and 7.4, where θ is the angle between the neutron axis and the direction of the fission fragment. Only one fission fragment emerges from the target in the forward hemisphere, and is detected; the one moving in the backward direction is not detected. The predominant error in the experimental results is that of the track counting statistics, which, for the cylindrical geometry, varies from 20% at an angle of 10° to 3% at 80°. The errors due to variations in the distance of the U-foil from the fission detectors are small (≃ 1%) and may be neglected in comparison with those of counting statistics. The uncertainty in the emission angle for the cylinderical chamber varied in the range of 1°-3° and for the other chamber was ≃ 2°. The smooth curves drawn in Figs. 7.3 and 7.4 are those obtained by a least-squares fit of the experimental data with an expansion of Legendre polynomials of the form

$$W(\theta) = \sum_{n=0}^{3} A_{2n} P_{2n} (\cos \theta) \qquad 7.5$$

The coefficients of the polynomial for each neutron energy is tabulated in Table 7.2. The values for the anisotropy ratio, R,

Fig. 7.2 Photograph showing the "large" fission chamber (of diameter 40 cm) and the experimental arrangements. a: neutron target, b: uranium foil, c: fission detectors.

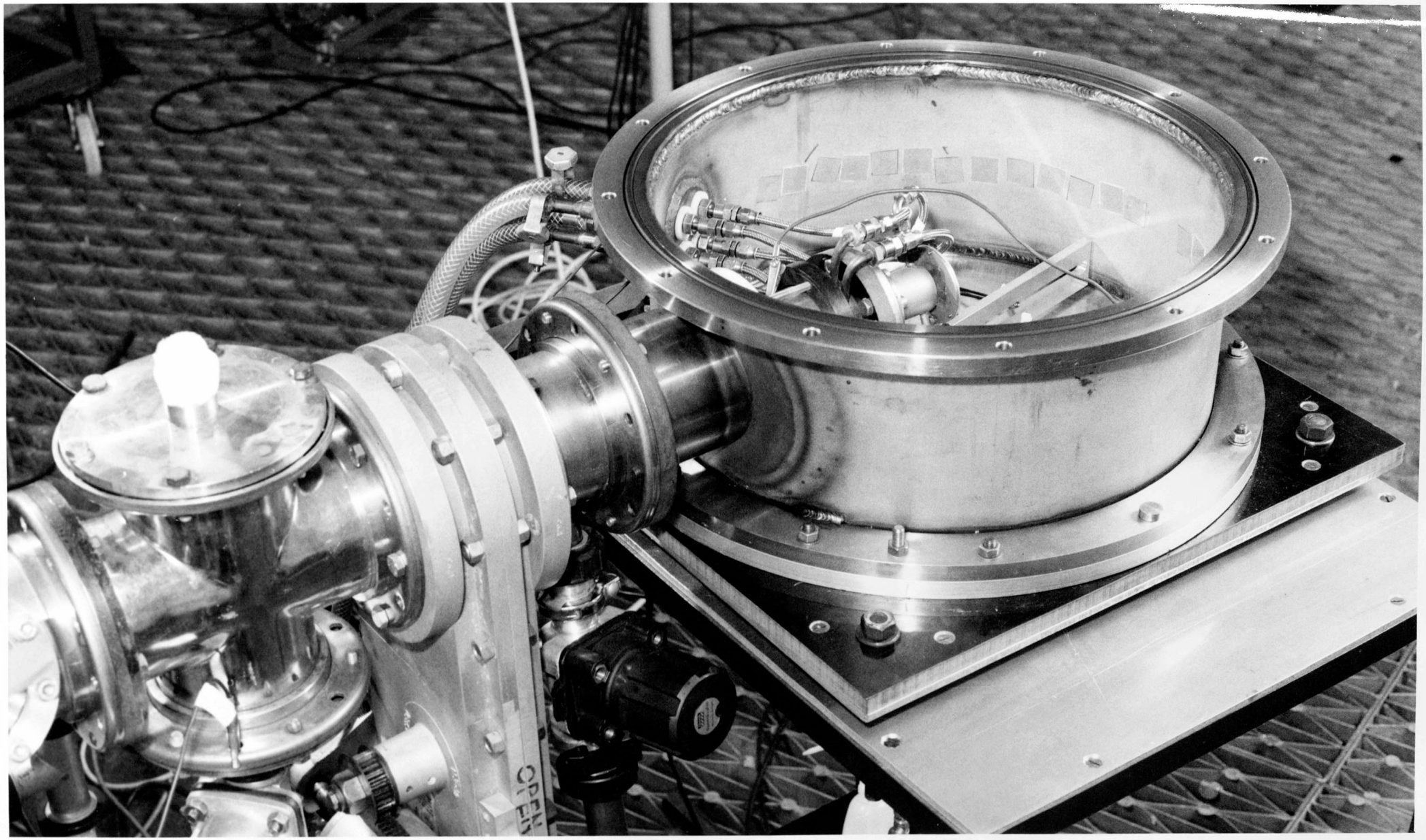

Fig. 7.3 Normalized angular distribution of the fragments, $W(\theta)$, in the fission of ^{238}U with neutrons of energies above the threshold for third-chance fission (n,2n'f), plotted as a function of the lab. angle (θ) of emission. The solid curves are least-squares fits to the experimental data using the function given in Eq. 7.5 for each incident-neutron energy, E_n; the set of coefficients in Eq. 7.5 being different for each energy. Figure a: E_n = 13.5 MeV; b: 14.7 MeV; c: 15.5 MeV; d: 16.6 MeV; e: 17.7 MeV.

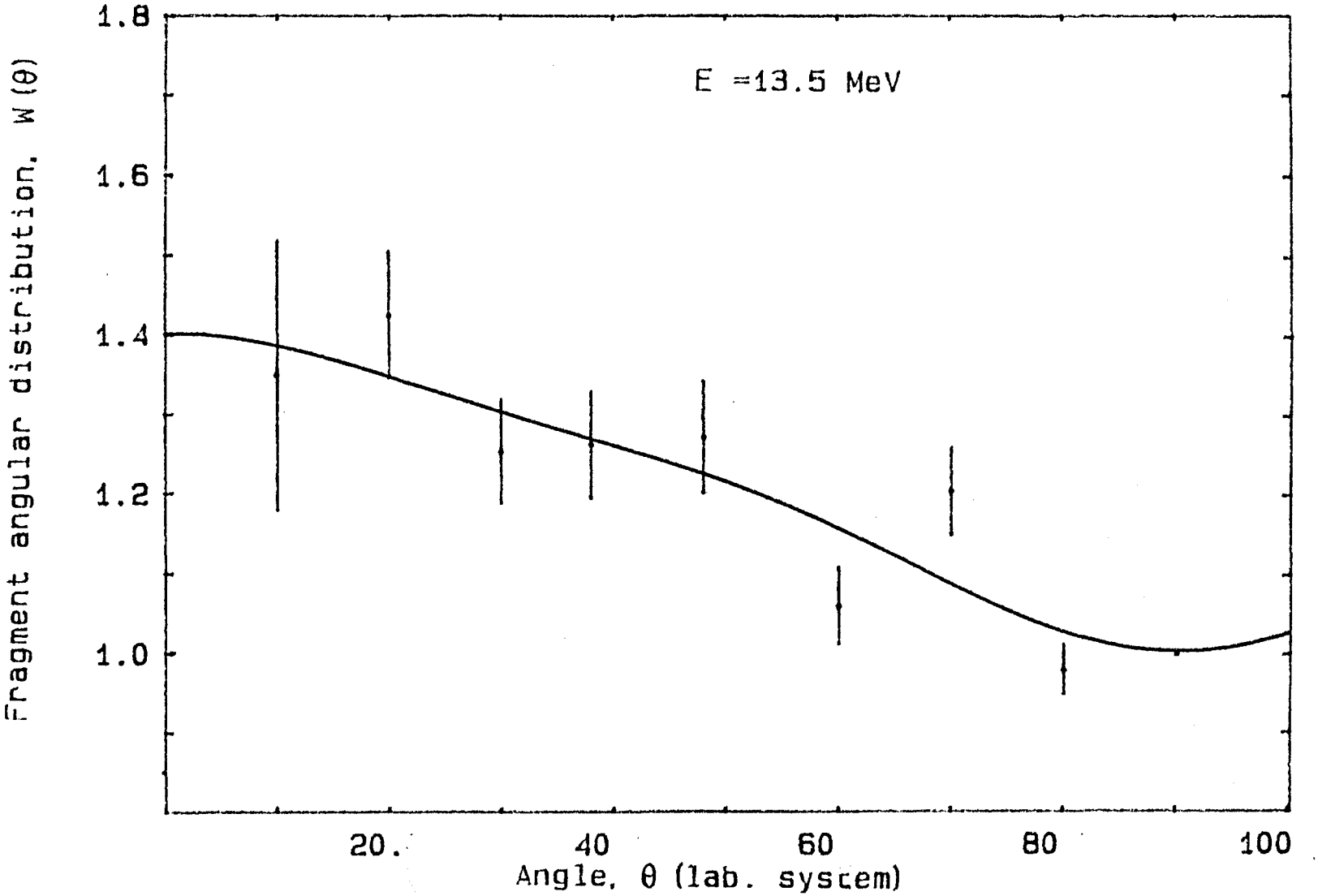
E =13.5 MeV
Fragment angular distribution, W(θ)
1.8
1.6
1.4
1.2
1.0
20.
40
60
80
100
Angle, θ (lab. system)

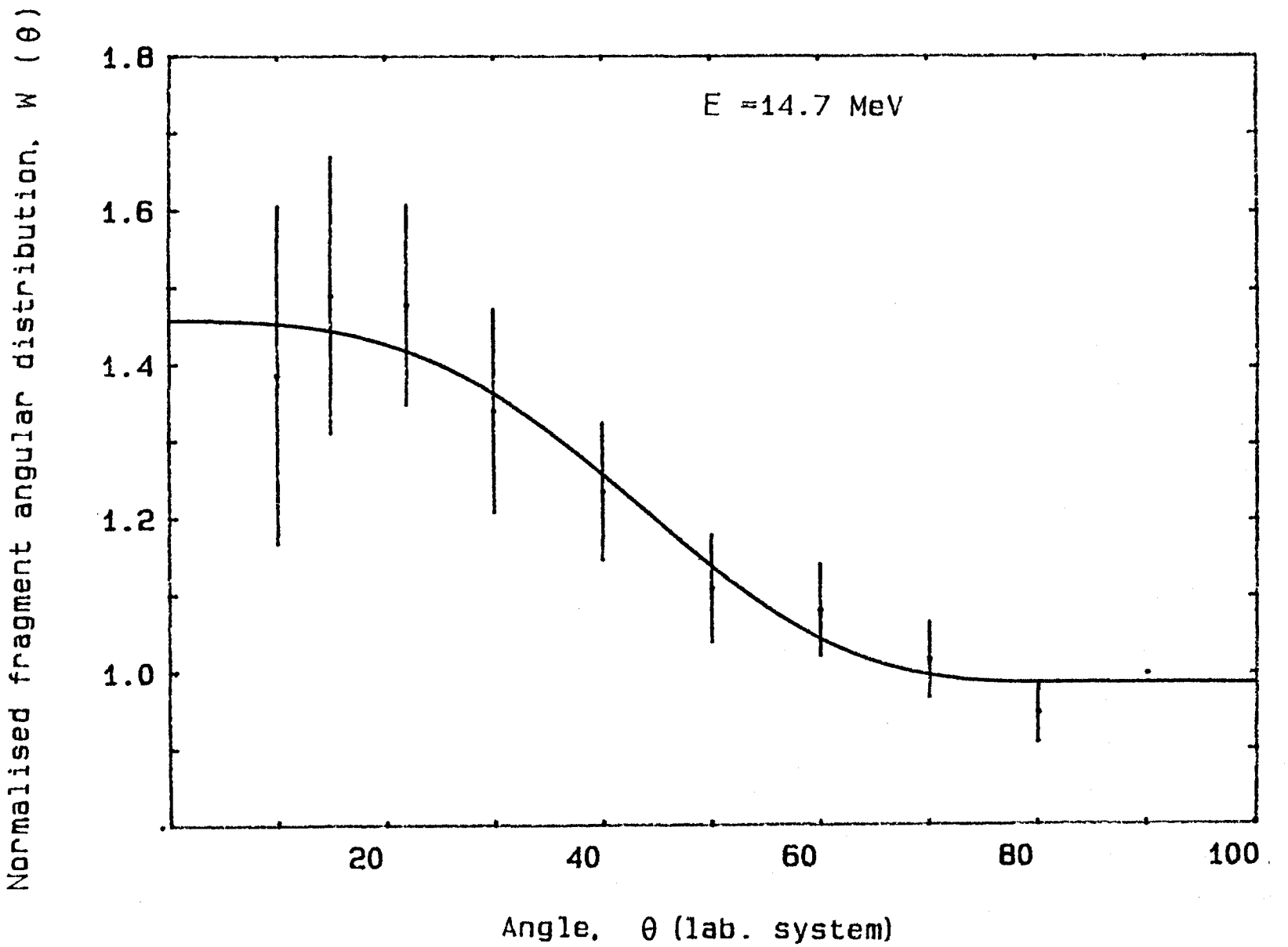
E =14.7 MeV
Normalised fragment angular distribution, W (θ)
1.8
1.6
1.4
1.2
1.0
20
40
60
80
100
Angle, θ (lab. system)

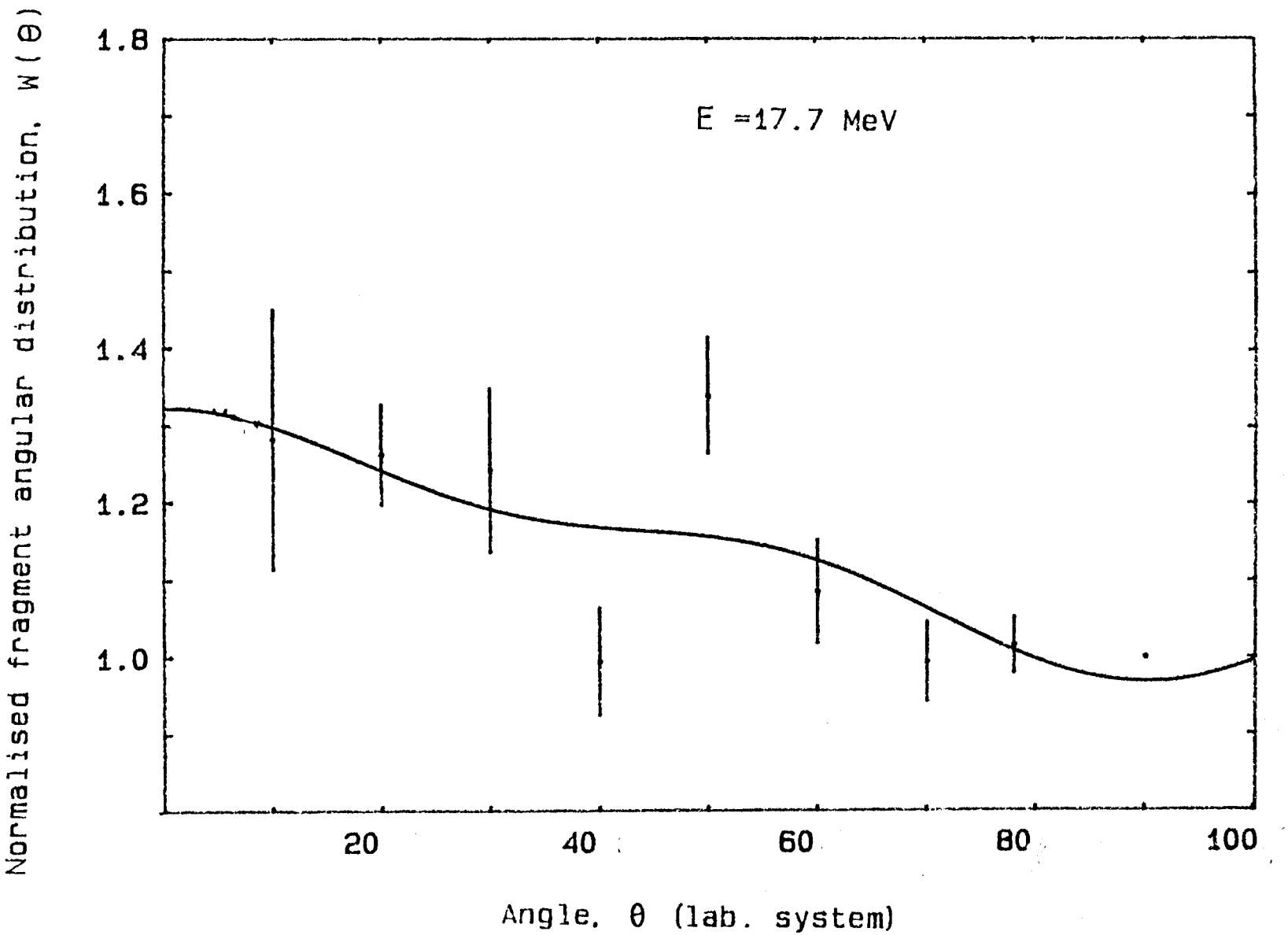
Normalised fragment angular distribution, W(θ)
1.8
1.6
1.4
1.2
1.0
E =17.7 MeV
20
40
60
80
100
Angle, θ (lab. system)

Fig. 7.4 Normalized angular distribution, $W(\theta)/W(90^{o})$, as a function of lab. angle θ, for the emission of fragments from the $^{238}U(n,f)$ reaction, at the following incident-neutron energies, E_n:- Figure a: E_n = 1.30 MeV; b: 1.40 MeV; c: 1.45 MeV; d: 1.50 MeV; e: 1.55 MeV; f: 1.60 MeV; ℓ: 1.75 MeV; m: 1.85 MeV; n: 2.0 MeV; p: 4.8 MeV.

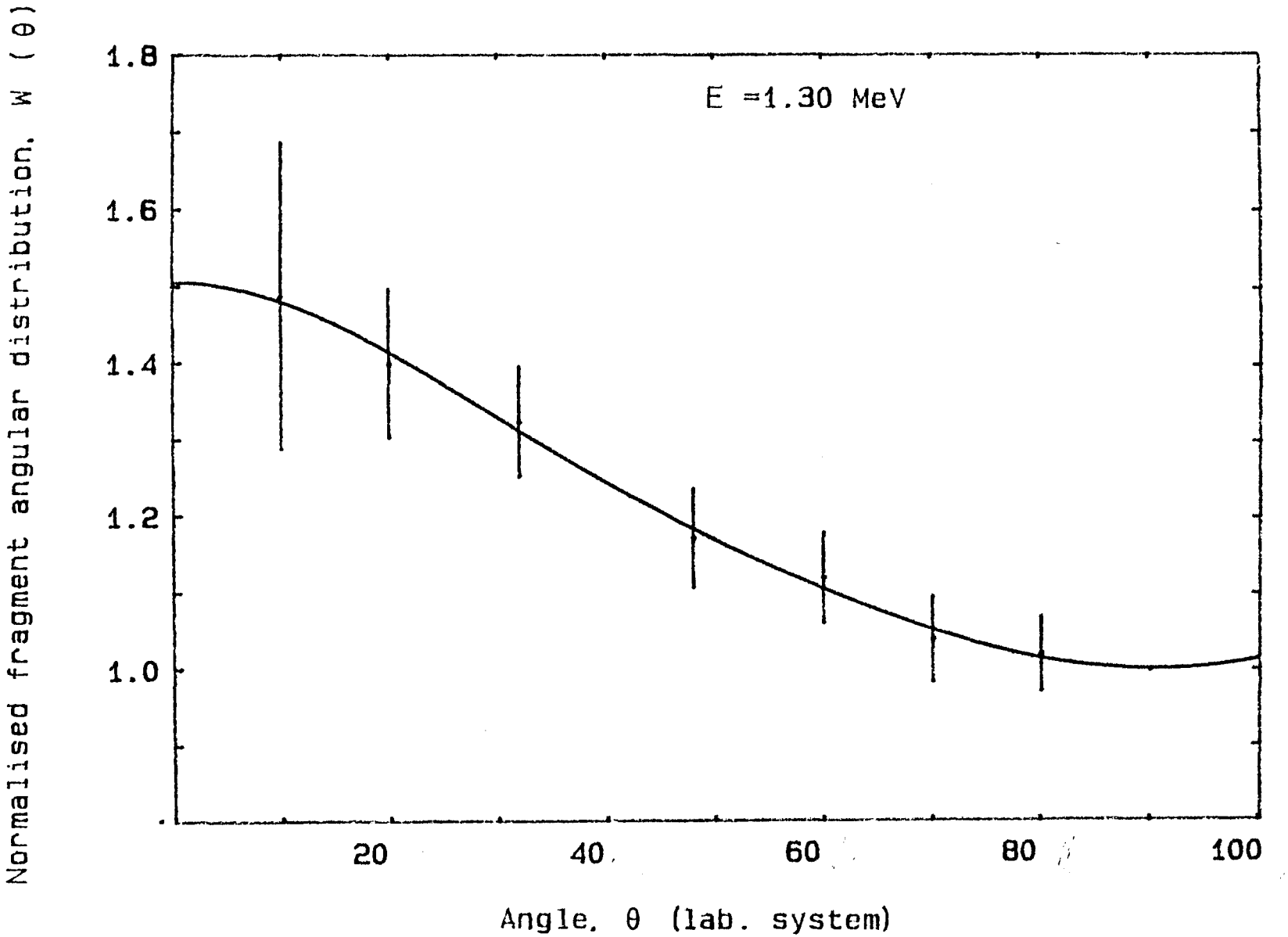
E =1.30 MeV
Normalised fragment angular distribution, W (θ)
1.8
1.6
1.4
1.2
1.0
20
40
60
80
100
Angle, θ (lab. system)

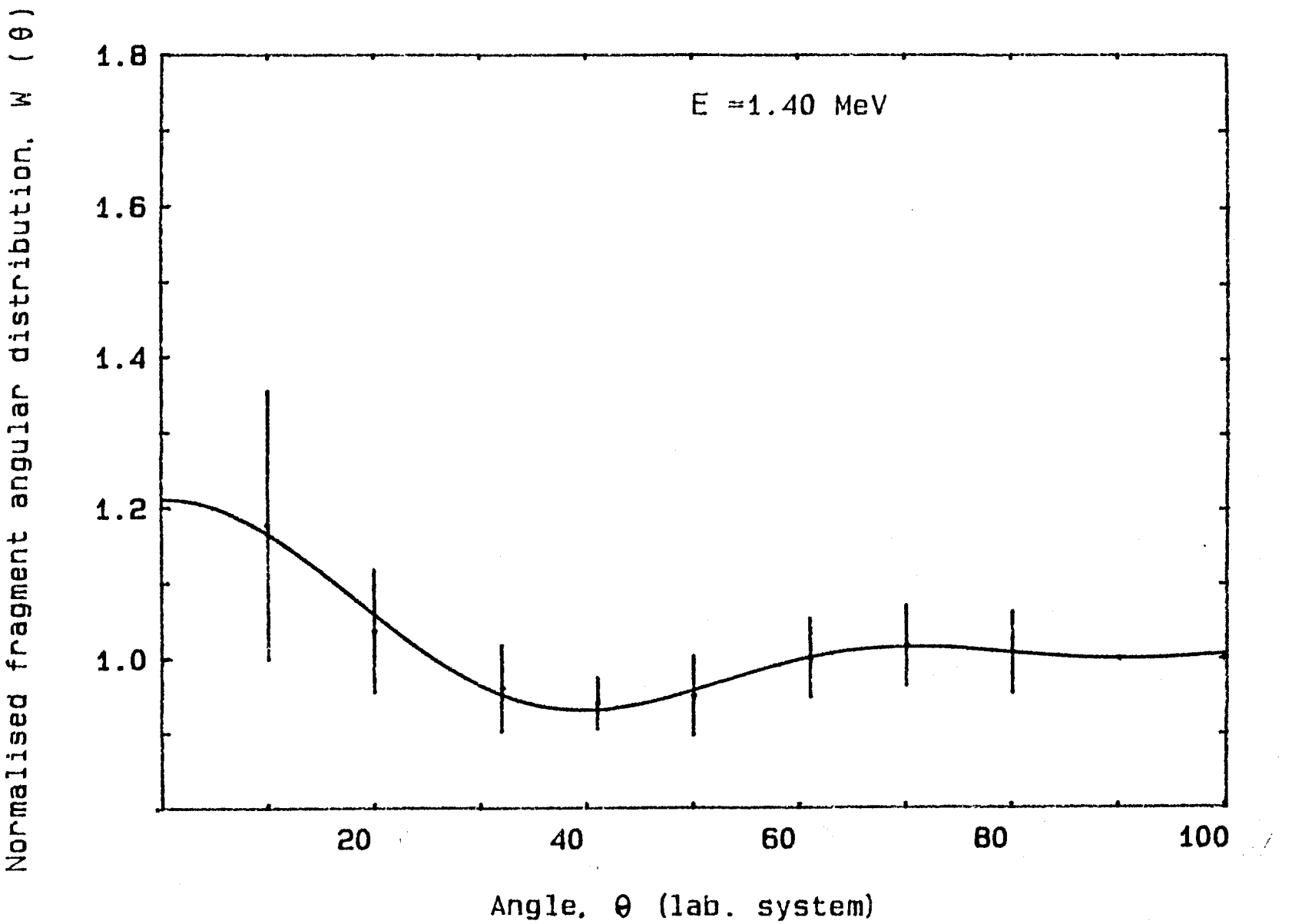
E =1.40 MeV
Normalised fragment angular distribution, W (θ)
1.8
1.6
1.4
1.2
1.0
20
40
60
80
100
Angle, θ (lab. system)

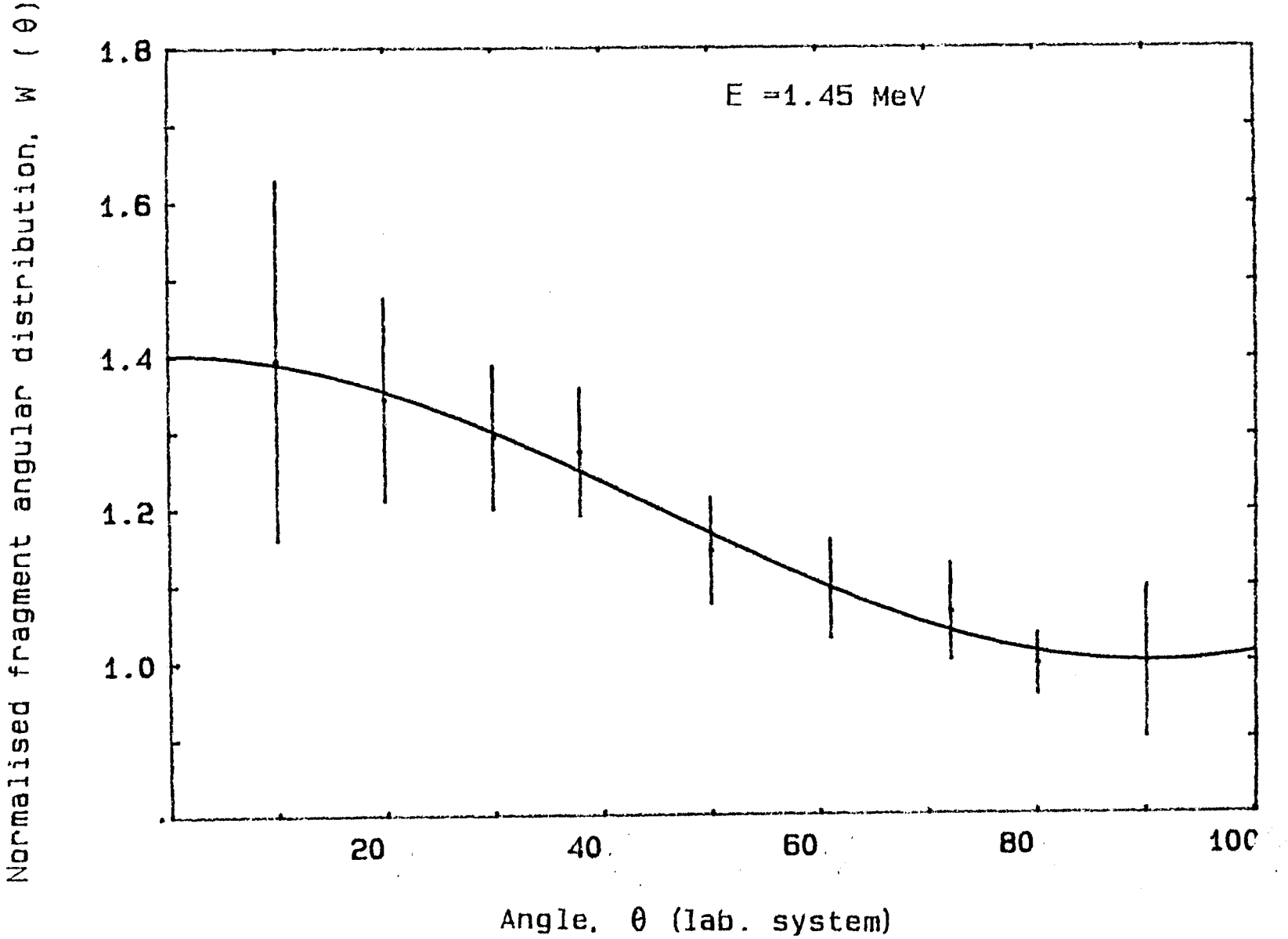
E =1.45 MeV
Normalised fragment angular distribution, W (θ)
1.8
1.6
1.4
1.2
1.0
20
40
60
80
100
Angle, θ (lab. system)

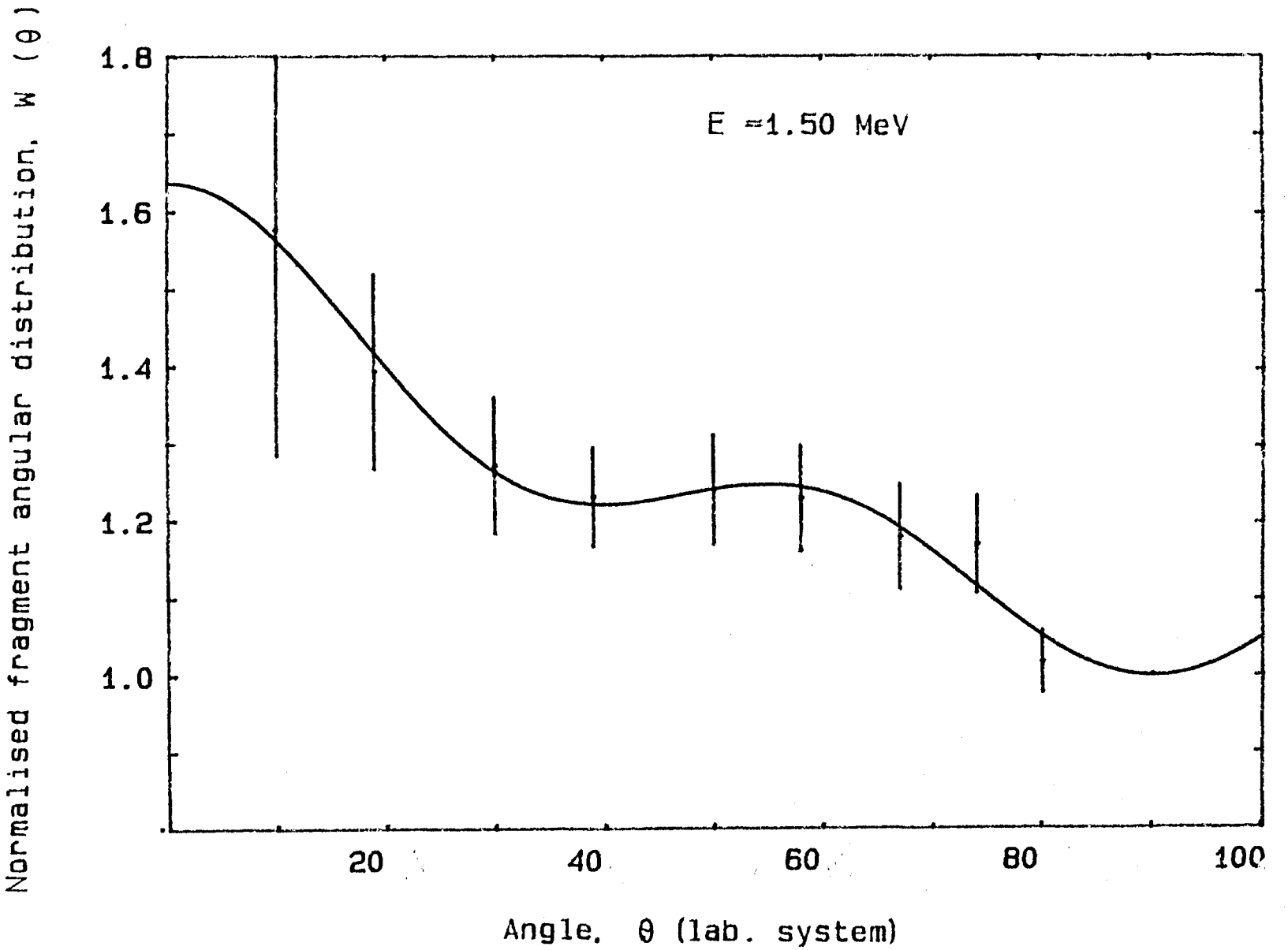
Normalised fragment angular distribution, W (θ)
1.8
1.6
1.4
1.2
1.0
E =1.50 MeV
20
40
60
80
100
Angle, θ (lab. system)

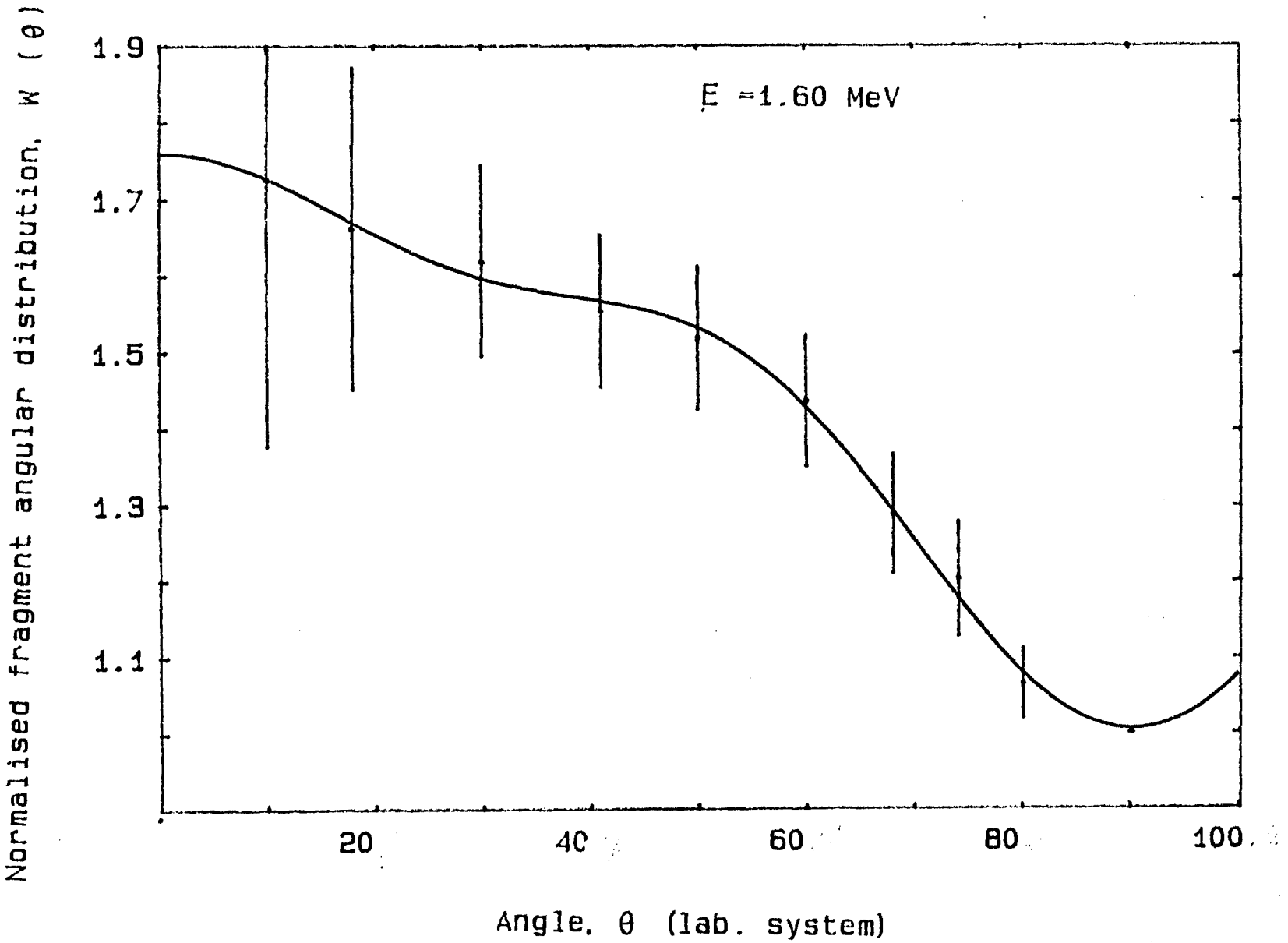
E =1.60 MeV
Normalised fragment angular distribution, W (θ)
1.9
1.7
1.5
1.3
1.1
20
40
60
80
100
Angle, θ (lab. system)

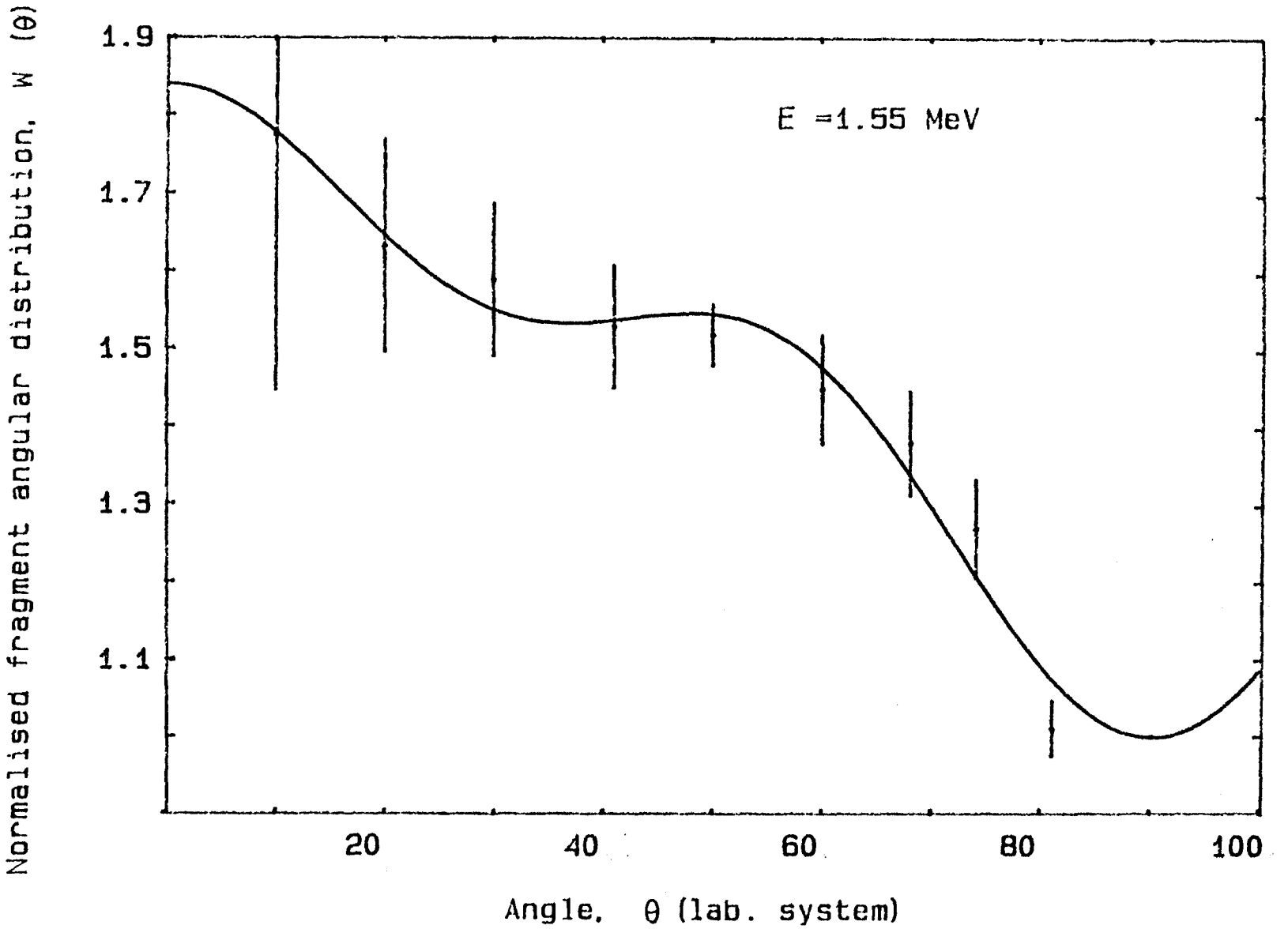
Normalised fragment angular distribution, W (θ)
1.9
1.7
1.5
1.3
1.1
E =1.55 MeV
20
40
60
80
100
Angle, θ (lab. system)

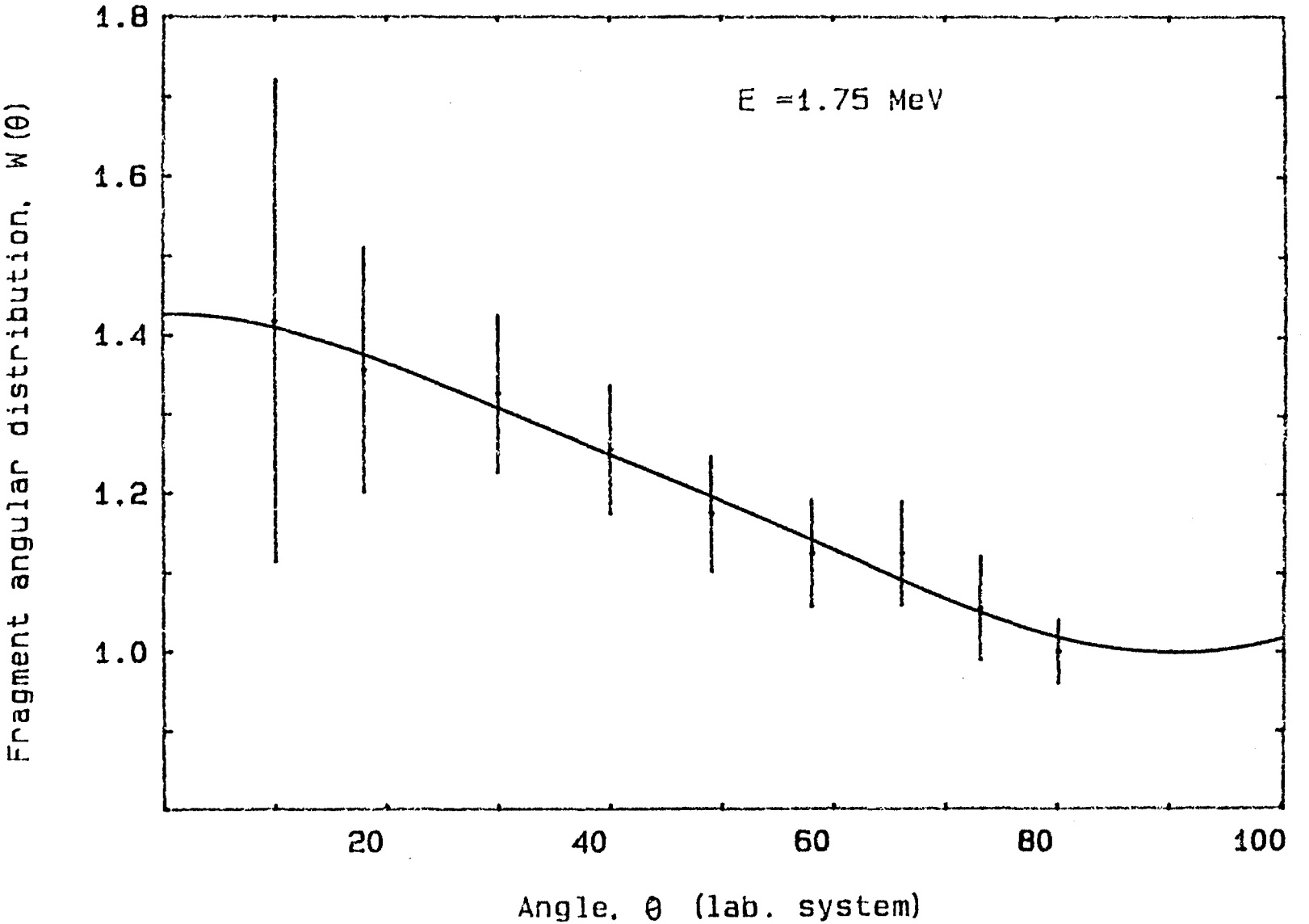
E =1.75 MeV
Fragment angular distribution, W(θ)
1.8
1.6
1.4
1.2
1.0
20
40
60
80
100
Angle, θ (lab. system)

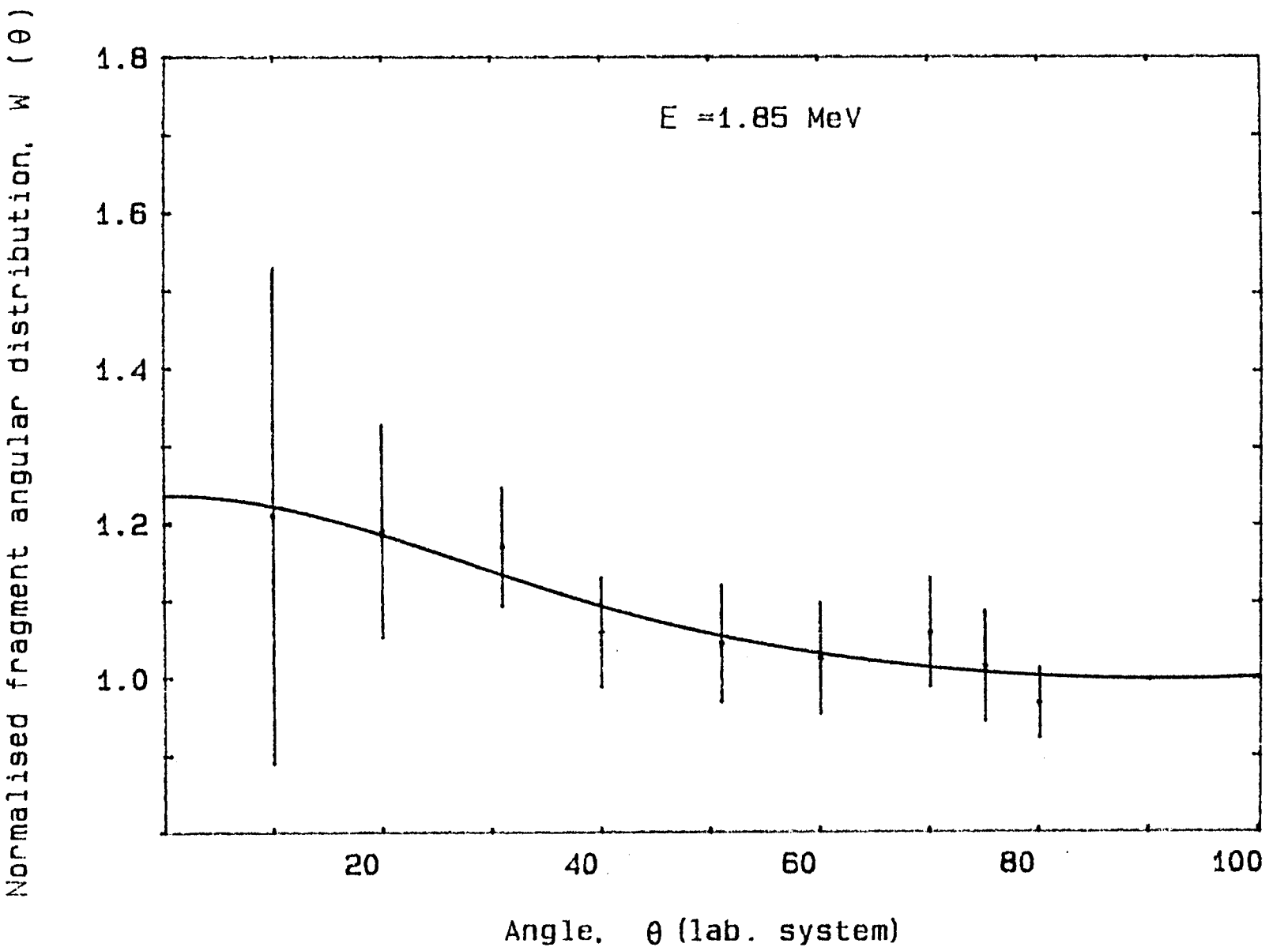
E =1.85 MeV
Normalised fragment angular distribution, W (θ)
1.8
1.6
1.4
1.2
1.0
20
40
60
80
100
Angle, θ (lab. system)

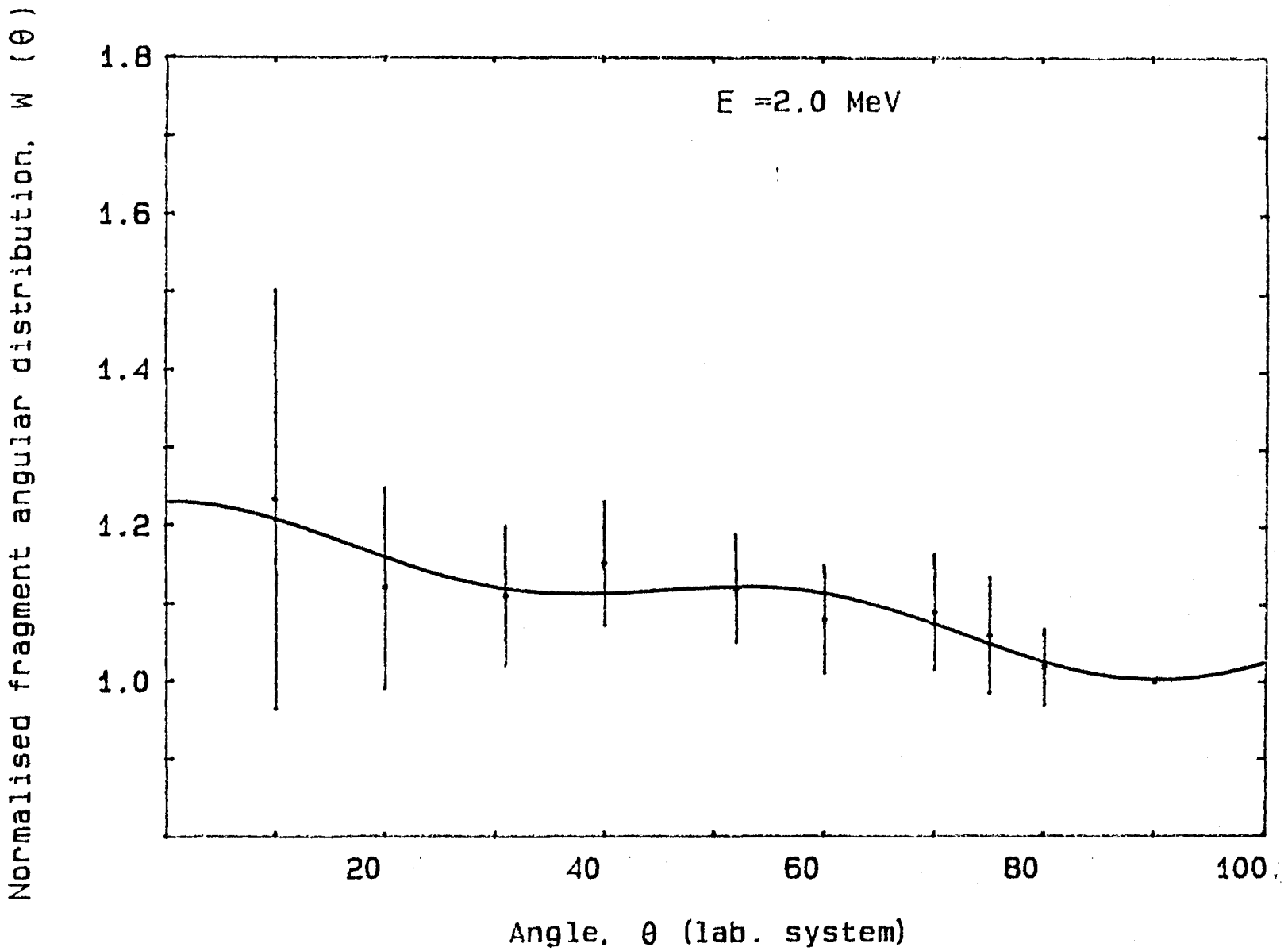
E =2.0 MeV
Normalised fragment angular distribution, W (θ)
1.8
1.6
1.4
1.2
1.0
20
40
60
80
100
Angle, θ (lab. system)

Table 7.2

The Legendre Polnomial coefficients of Eq. , derived from a least-squares fit to the experimental data of the angular distribution of fission fragments as a function of neutron energy.

Neutron Energy (MeV)	Legendre Polnomials Coefficients P(1)	P(2)	P(3)	P(4)
1.30	1.1461216	.3034480	.0345691	.0216566
1.40	.9960147	.0058635	.1053288	.1042639
1.45	1.1345479	.2666371	-.0020147	.0019635
1.50	1.1941078	.2416321	-.0163783	.2172662
1.55	1.3817625	.4324048	-.2305781	.2561544
1.60	1.3709232	.4629985	-.2286484	.1544775
1.75	1.1486993	.2701577	-.0179042	.0257108
1.85	1.0563524	.1350223	.0358401	.0087992
2.0	1.0896284	.0980581	-.0360418	.0785755
13.5	1.1611369	.2524755	-.0513129	.0394398
14.7	1.1215286	.3460683	.0521059	-.0622571
17.7	1.1062275	.1858239	-.0521454	.0824428

deduced from Equation 7.5 are shown in Table 7.3 and, are plotted in Fig. 7.5 together with other published experimental data[5-8,13,14]. The results of our experiments indicate that the anisotropy ratio, R, increases immediately above the fission threshold for the first-chance fissions, as expected theoretically. As far as second-chance fission is concerned we have not been able to get sufficient data due to the limitations neuron energy obtained from the Dynamitron. We could achieve neutrons, from our accelerator, only up to the energy of 6 MeV with D(d,n)He which is close in the lower shoulder of the threshold region for second-chance fission. This provided a brief data only at the lower shoulder of R versus E_n curve. This data is not sufficent enough and as we are not able to encompass the whole span of the two threshold shoulders due to our experimental limitation. We are not, therefore, comparing our results with their publications in this regards. The increase for the third-chance fission is also found to be significant in our experimental results, although it does not closely follow the calculated curves.

7.2 Discussion

Our experimental, angular-distribution results for fission fragments from ^{238}U at $E_n<3$ MeV, shown in Fig. 7.4, can be qualitatively explained on the basis of the theoretical expectation for even-even nuclei, as given by the expression as discussed in appendix 4

$$W^J_{M,K}(\theta) = [(2J+1)/2]\,|d^J_{M,K}(\theta)|^2 \qquad 7.6$$

where

J = is the total angular momentum of the fission fragments,

K = is the projection of J on the nuclear symmetry axis, and

M = is the projection of J on a space-fixed axis (usually the direction of the incident beam).

Table 7.3

Angular anisotropy determined from neutron induced fission of ^{238}U.

Reaction	Neutron energy MeV	Anisotropy angular distribution of fission fragment
(D,P)	1.30	1.485 ± 0.08
	1.40	1.211 ± 0.08
	1.45	1.39 ± 0.09
	1.50	1.634 ± 0.09
	1.55	1.843 ± 0.1
	1.60	1.74 ± 0.12
	1.75	1.41 ± 0.09
	1.85	1.235 ± 0.095
	2	1.22 ± 0.08
(D,D)	5.9	1.61 ± 0.09
(D,T)	13.5	1.385 ± 0.076
	14	1.55 ± 0.13
	14.7	1.462 ± 0.11
	15.5	1.68 ± 0.12
	16.5	1.294 ± 0.09
	17.7	1.33 ± 0.08

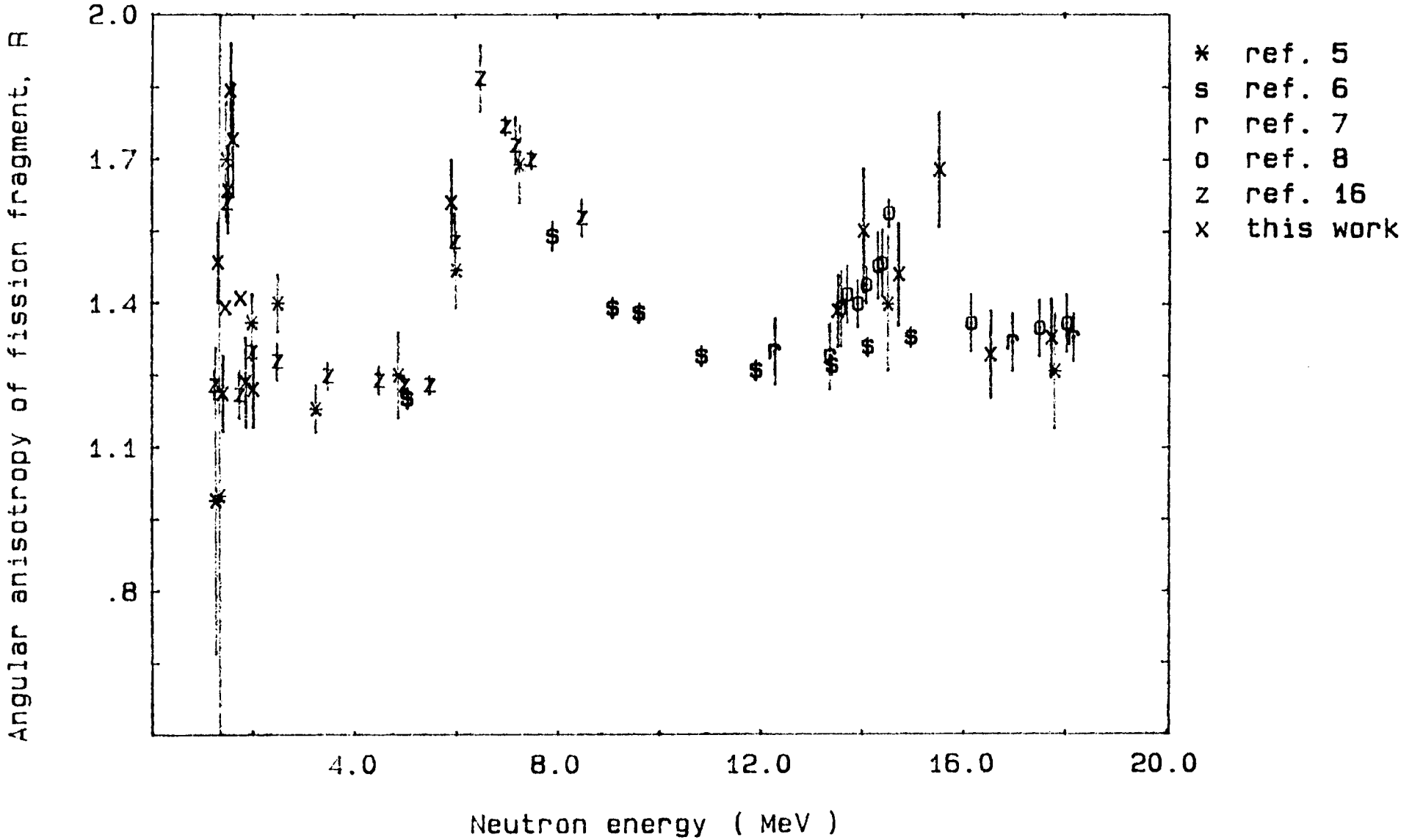

Fig. 7.5 Fission fragment anisotropy, $R = W(0^{o})/W(90^{o})$ as a function of incident neutron energy for ^{238}U.

Each state is characterized by these quantum numbers.

Figure 7.6 shows the theoretical, fission-fragment angular distribution for the neutron fission of even-even targets. From comparison of this with Fig. 7.4, we can exclude the presence of K>3/2 bands; but the K=1/2 bands always seem to be present. This result is similar to that of Nigro et al.[4] and the minimum value of the angular distribution ratio R can be seen in Fig. 7.5 to occur at around E_n=1.40 MeV. This can be explained as being due to the strength of the K=3/2 band at this energy. Thus the sequence of the K-bands for $^{238}U(n,f)$ reaction at neutron energies of 1.2 to 1.6 MeV goes through 1/2, ≠1/2, and back to 1/2, which is in agreement with the suggestion of other authors[4,15].

The fragment anisotropy in the neutron energy range 2 to 5.5 MeV, as shown in Fig. 7.4, remains more or less constant, and then increases sharply at 6.5 MeV, which corresponds to second-chance fission, (n,n'f). In this region of neutron energy, our results (Fig. 7.4) are in agreement with those of Simmons and Henkel[16].

In the energy range 12 MeV ⩽ E_n ⩽ 18 MeV, the three reactions (n,f),(n,n'f) and (n,2n'f) contribute to the fission, so that the angular distribution of the fragments is:

$$W(\theta) = \sum_{i=0}^{2} \gamma_i W_i(\theta) \qquad 7.7$$

where

i= 0, 1 and 2 stand for the first-, second- and third-chance fission, respectively; and

γ_i = is the contribution to the fission yield by the ith chance fission with angular distribution $W_i(\theta)$, and is expressed as

$$\gamma_i = \frac{\sigma_{fi}}{\sum_{i=0}^{2} \sigma_{fi}} \qquad 7.8$$

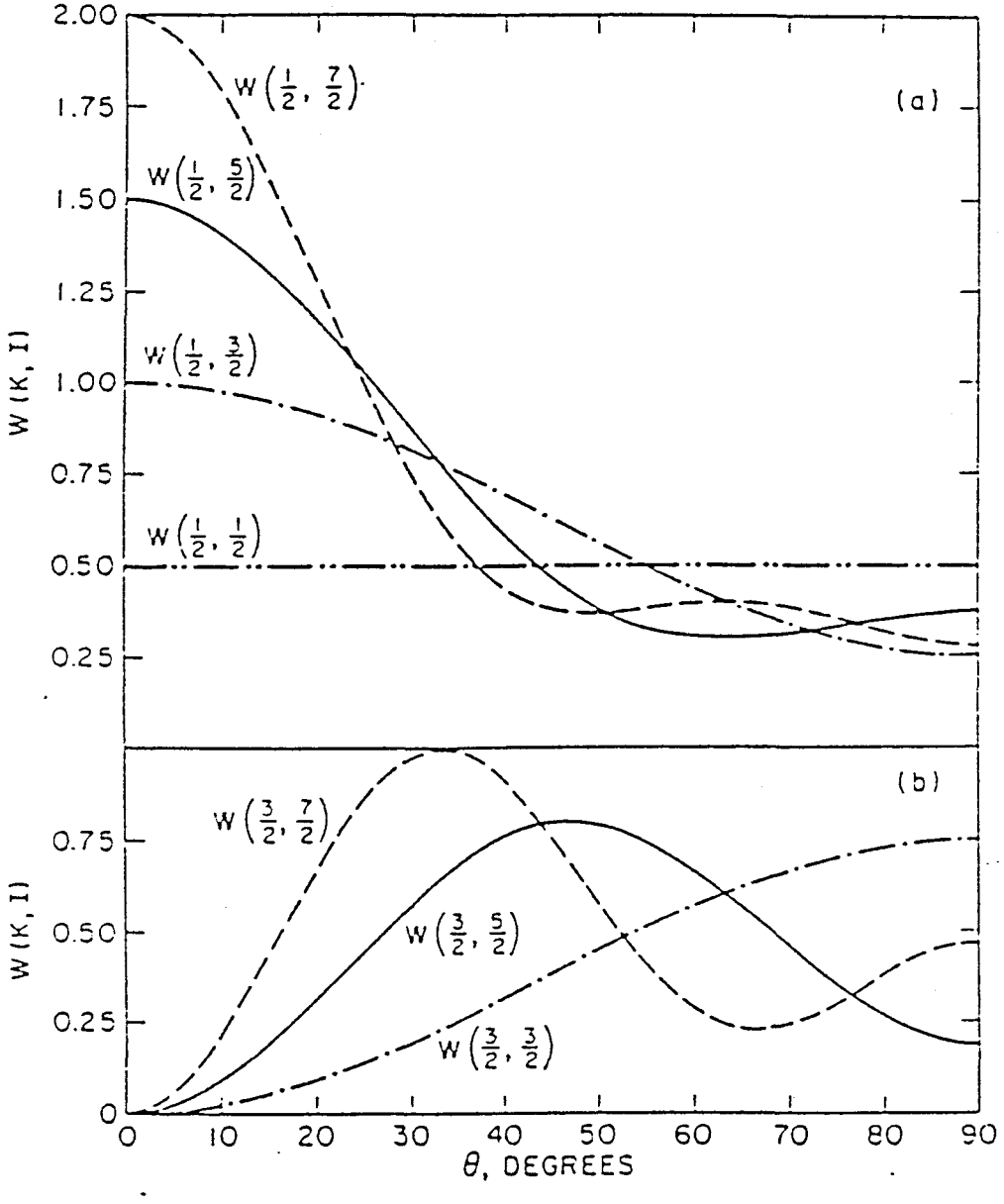

Fig. 7.6 Theoretical fission-fragment angular distributions for neutron fission of even-even targets, calculated from Eq. 7.6 (after ref. 2).

where σ_{fi} is the corresponding fission cross section.

The total anisotropy ratio is given by

$$R(E_n) = \frac{W(0^o)}{W(90^o)} = 1 + \gamma_0 A_0 + \gamma_1 A_1 + \gamma_2 A_2 \qquad 7.9$$

From Fig. 7.5, we deduce that $A_0 = 0.20$ and $A_1 = 0.32$ and these are supported by those deduced from published data[6,12]. A_2 can be calculated from the expression[17]

$$A_2 = \frac{L_m(L_m+2)}{8K_o^2} \qquad 7.10$$

where L_m is the maximum value of the orbital angular momentum, L of the incident neutron and depends on the neutron energy. If we assume that those neutrons that evaporate before fission takes place carry off only a small angular momentum, then L_m may be determined for the initial compound nucleus ^{239}U by means of the expression[2]

$$L_m = (4.2\ E)^{\frac{1}{2}}. \qquad 7.11$$

The value K_o^2 in equation 7.10 is the square of the standard deviation of the Gaussian distribution that is assumed for K; it depends on the excitation energy E_x of the nucleus and on the fissioning species[16] and is given by the expression[2]

$$K_o^2 = T \cdot \frac{\varphi_{eff}}{\hbar^2}$$

where

φ_{eff} = is effective nuclear moment of inertia and

T = is the thermodynamic temperature.

K_o^2 can also be obtained by using the equation of Simmons and Henkel[16] (i.e. $K_o^2 = B_1 + B_2 (E_n - E_f)$, where $B_1 = 0.87 \pm 0.76$; $B_2 = 3.1 \pm 0.25$; and $E_f = 1.25$ MeV). Although these authors had obtained this equation for lower neutron energies, since the behaviour in the equation not expected to change significant at higher energies. The mean excitation energy, E_x, above the fission threshold, E_f, was calculated from the relation[12]

$$E_x = E_n - E_f - w_n \qquad 7.13$$

where w_n is the kinetic energy carried off by the neutrons and can be shown[12] to be equal to 2T. The value of T was taken from experimental data[19]. The experimental and calculated anisotropy values are recorded in Table 7.4, where good agreement is seen to exist between the experimental and theoretical values in the range 14.7 MeV$\leqslant E_n \leqslant$19 MeV. In this energy region the only value of R that is different from the calculated one is at an energy of 15.5 MeV. The increase in the anisotropy ratio, R, just above the energy of third-chance fission is explained by the fact that the emission of a neutron before fission leaves the fissioning nucleus in a state of excitation with access to only a few quantum states. Consequently, there is a strong dependence of the fragment angular distribution on the parameters of these states.

7.3 Summary and Conclusion

On comparison of the experimentally determined angular distribution of fission yields with the theoretical curves predicted by Vandenbosch and Huizenga[2] (see Fig. 7.6), it is clear that, at most neutron energies, the band states of the compound nuclei immediately preceding fission are predominanatly in the $K=\frac{1}{2}$. This conclusion is in agreement with the experimental results of Nigro et al.[4]. The principal exception to this finding appears to occur at neutron energies around 1.40 MeV. At these energies the fission anisotropy ($R= W(0^o)/W(90^o)$) reaches a local minimum and the angular fission distribution exhibits a behaviour characteristic of both $K=\frac{1}{2}$ and K=3/2 band states.

In the neutron energy range $E_n \simeq 2$ to 5 MeV, the fission anisotropy, R, remains approximately constant but it begins to increase at higher energies, peaking at $E_n \simeq 6$ MeV. This corresponds

Table 7.4

Values of parameters used in the calculation of the angular-distribution anisotropy at different incident-neutron energies (see text for explanation of symbols)

E_n (MeV)	L_m	E_x (MeV)	A_2		Calculated R		Experimental R
			a	b	a	b	
17.7	8.622	4.6	0.756	0.545	1.388	1.33	1.33
16.5	8.234	3.4	0.941	0.651	1.427	1.35	1.294
15.5	8.068	2.4	1.22	0.846	1.481	1.39	1.687
14.7	7.857	1.6	1.660	1.180	1.560	1.455	1.462
14.0	7.668	0.9	2.531	1.930	1.549	1.72	1.553
13.5	7.529	0.4	4.25	2.989	1.548	1.89	1.385

a: using the K_o^2 value obtained from the equation of Simmons and Henkel[16]

b: using the K_o^2 value of Nigro and Milone[20]

to the threshold energy for second-chance fission, (n,n'f), and is in agreement with the experimental results of Simmons and Henkel[16]. The anisotropy coefficient A_2 for third-chance fission, determined for several neutron energies above 12 MeV, has been used, together with values of A_0 and A_1 deduced from the literature and from Fig. 7.5, to calculate the total fission anisotropy, R, as a function of neutron energy in the range 13.5-17.7 MeV. Our experimentally determined values of R in this energy range are in good agreement with the theoretical values except at 15.5 MeV, where the experimental value appears to be slightly too high.

References

1. G.D. James, J.E. Lynn, A. Michaudon, J. Rowlands and G. de Saussure. Nuclear Fission and Neutron-induced Fission Cross-sections. Pergamon Press, Oxford, 1981.

2. R. Vandenbosch and J.R. Huizenga. Nuclear Fission. Academic Press, 1973.

3. J.J. Griffin. Phys. Rev. 116 107 (1967).

4. S. Lo Nigro and C. Milone. Nucl. Phy. A151 182 (1970).

5. R.L. Henkel and JU.E. Brolley, Jr. Phys. Rev. 103 1292 (1956).

6. R.B. Leachman and L. Blumberg. Phys. Rev. 137 No. 4B, 814 (1965).

7. V. Emma, S. Lo Nigro and C. Milone. Nucl. Phys. A157 449 (1970).

8. R. Abegg and R. Wagner. Phys. Rev. C. 15, No. 3, 1171 (1977).

9. G. Yuen, G.T. Rizzo, A.N. Behkami and J.R. Huizenga. Nucl. Phys. A171, 614 (1971).

10. G.D. James, J.E. Lynn and L.G. Earwaker. Nucl. Phys. A189, 225 (1972).

11. D.R. Weaver and J.G. Owen, Department of Physics, University of Birmingham. Personal communication.

12. N.R. Chaudhuri, V. Natarajan, R. Sampathkumar, M.L. Sagu and R.H. Iyer. Nucl. Tracks, 3, 69 (1979).

13. J.E. Brolley, Jr. and W.C. Dickinson. Phys. Rev. 94, 640 (1954).

14. E. Barutcugil, S. Inhasz, M. Varnagy, S. Nagy and J. Csikai. Nucl. Phys. A173 571 (1971).

15. W. Lamphene. In: Physics and Chemistry of Fission, Vol. I (IAEA, Vienna, 1965) 63 (1965).

16. J.E. Simmons and R.L. Henkel. Phys. Rev. 120 198 (1960).

17. J.J. Griffin. Phys. Rev. 127 1258 (1962).

18. R.B. Leachman and E.E. Sanmann. Ann. Phys. A18 274 (1962).

19. Y.U.S. Zamiatinin, I.N. Safina, E.K. Gutnikova and N.I. Ivanova. Soviet J. Atomic Energy, 4, 443 (1958).

20. S.L. Nigro and C. Milone. Nucl. Phys. A96, 617 (1967).

CHAPTER 8

HEAVY ION FISSION

8. Introduction

In this chapter, experiments involving the collision of a heavy projectile with a heavy target material are studied. Heavy ion physics is an entirely new area of research in nuclear physics[1,2]. The behaviour of a heavy nucleus under extreme conditions of temperature, density, angular momentum, etc. is a very important aspect of heavy ion physics. Heavy projectiles were used as probes for a deeper insight into the nucleus for the first time by Kaufman and Wolfgang[3,4]. Many concepts, such as friction and nucleon diffusion, which subsequently attained considerable importance were anticipated as a result of their experiments. With the advent of heavy ion accelerators such as UNILAC in Darmstadt, a strong interest emerged for the study of the interactions of very heavy projectiles with heavy targets[5]. Since high linear and angular momenta are associated with energetic, heavy ion collisions, they provide the opportunities to study the transfer of large amounts of mass, energy and angular momentum, along with the subsequent relaxation phenomena and the structure of nuclei at high excitation energies. In heavy ion interactions, the wave length of relative motion at the interaction barrier can be found from the expression[2]

$$\lambda(R) = \left[\frac{M_p + M_t}{M_p M_t} \cdot \frac{20\ \text{MeV}}{E_{cm} - V(R)}\right]^{\frac{1}{2}} \quad \text{fm} \qquad 8.1$$

where

M_p = projectile mass number

M_t = target mass number

E_{cm} = energy in the centre-of-mass system

$V(R)$ = potential energy at the interaction radius R.

The value of $\lambda(R)$ is of the order of 10^{-3} fm, for a heavy projectile with an incident energy of a few GeV as used in these experiments, which is very small compared to the characteristic length of the colliding nuclei (e.g. surface thickness ≈ 2 fm). The collisions can therefore be treated classically.

According to the classical picture[6] shown in Figure 8.1, there are three qualitatively different types of reaction, determined by the impact parameter, b, or the corresponding angular momentum, $l=bp_\infty/h$, where p_∞ denotes the asympotic, initial relative momentum. The impact parameter, b, equals b_{gr} at the interaction radius, R_{int}, and is given by the closest distance of approach between the centres of the nuclei on grazing trajectories. In this condition the nuclear interactions only just begin and there is, therefore, little overall reaction. Under these conditions we expect a reaction to dominate where only a few degrees of freedom of the projectile and target are involved; these are called direct collisions[7]. For impact parameters which are considerably larger than b_{gr}, the nuclear interaction is negligible and the trajectories of these distant collisions are completely determined by the Coulomb field. Only excitations induced by the mutual Coulomb interaction between nuclei[8] can occur along these trajectories. For impact parameters considerably smaller than b_{gr}, we expect a strong disturbance of the projectile and target by their strong, mutual nuclear interaction. Practically all nucleonic degrees of freedom are involved in these close collisions. The interaction time, T_{int}, is the time during which the two colliding nuclei are within the sphere given by the interaction radius R_{int}. This interaction time is considerably larger for a close collision than for a direct reaction. Such a close collision can lead to the formation of a compound nucleus[9]. This compound nucleus has a life

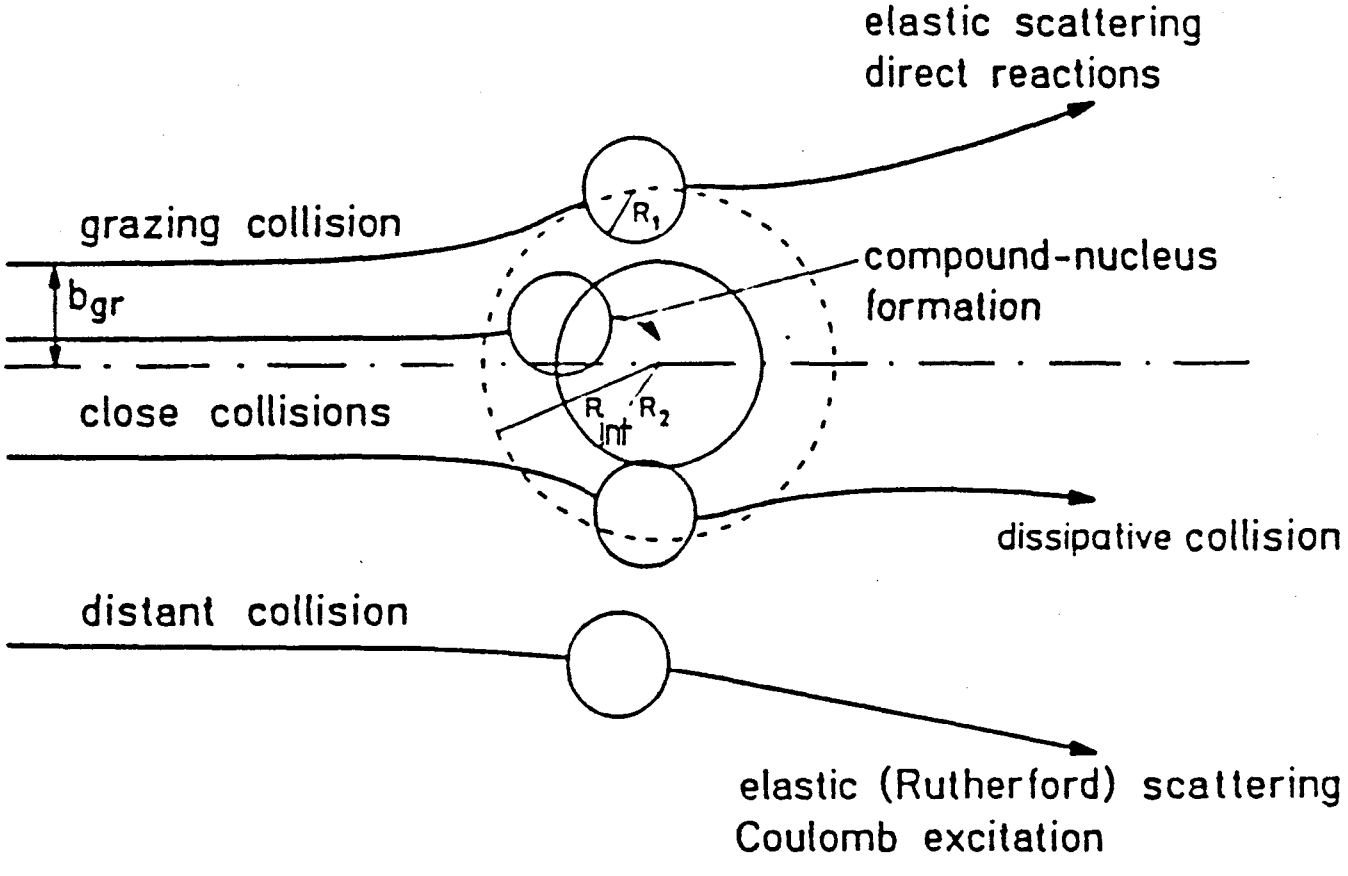

Fig. 8.1 Classical picture of heavy ion reactions, illustrating distant, grazing and close collisions.
R_1 is radius of projectile nuclide, R_2 is radius of target and R_{int} is interaction radius.

time which is large compared to the time-of-flight of the projectile through the interaction region i.e. sphere of radius R_{int}. The highly excited compound nucleus can decay either by emission of light particles or by fission. Very heavy reaction partners, after building a di-nuclear complex, undergo deep inelastic collisions and the process is referred to as a dissipative collision. This process is characterized by[10]:

(i) a strong, non-isotropic angular distribution and therefore rather short interaction times of the order of 10^{-22} to 10^{-20} of a second,

(ii) strong dissipation of relative, kinetic energy and angular momentum,

(iii) transfer of a considerable amount of mass between projectile and target.

There is a smooth transition between direct processes and dissipative collisions. The heavy ion collision based on the concept of the classical impact parameter is shown in Fig. 8.2. In this Figure, the distance of closest approach associated with a given impact parameter is represented by r. There is no nuclear interaction when $r>R_{int}$ and the only phenomena ocurring are Coulomb excitation and elastic scattering of the projectile and the target nucleus. The coulomb barriers for the reactions of interst in this experiment are calculated and shown in Table 8.1. In the case of $r=R_{int}$, where the angular momentum, l, is small, there exists the possibility of inelastic scattering and the exchange of a few nucleons. Conseqently, there is some loss of kinetic energy of relative motion. Most such quasi-elastic events cause three body events in the exit channel. For even smaller values of l, at $r<R_{int}$ the interacting nuclei come into 'solid - solid contact', which allows for a considerable exchange of mass and the damping of the relative, kinetic energy. Such damped

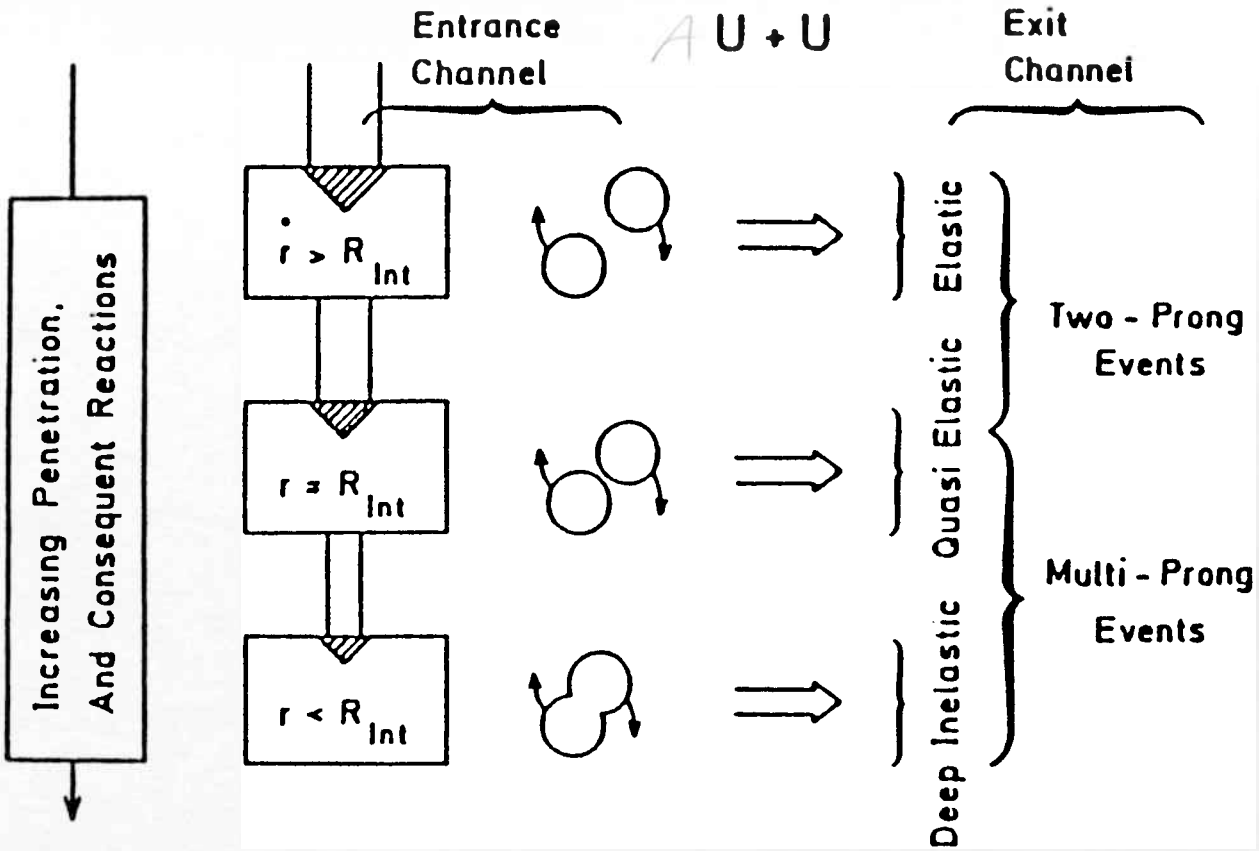

Fig. 8.2 Schematic representation of collisions between complex nuclei based on a classical impact model.

r and R_{int} are the distance of closest approach and the interaction radius, respectively. The characteristics of the reaction are described on the right hand side of the diagram.

Table 8.1

Columb barrier for reaction of interst

parameter Reaction	Radius of target R_Z (fm)	Radius of projectile R_Z (fm)	Columb barrier height* maximum (MeV)	minimum (MeV)
Au(U,U)Au	6.23	6.63	1576.8	812.92
Au(Pb,Pb)Au	6.23	6.33	1472.0	741.87
Au(La,La)	6.23	5.54	1169.15	550.30

*Barrier height = $\frac{Zze^2}{4\pi\epsilon_o r}$

where $R_Z < r < R_Z \pm R_Z$

$R = 1.07\ (A)^{1/3}$

interactions produce more than two heavy fragments in the exit channel.

The mechanisms of multibody events could be explained by I) instantaneous fission induced by Coulomb or nuclear forces[10], II) multibody breakup after fission[12] or III) fission and subsequent fusion[13]. A sequential fission process is, however, the more favoured mode and the one expected for most of these events. Figure 8.3 shows a schematic representation of a sequential fission process yielding three and four particles in the exit channel. In the first step, due to inelastic collisions a certain amount of mass transfer occurs and intermediate nuclei in excited states are formed. One or both of these intermediate nuclei may fission in the second step of the reaction, resulting in three or four particles in the exit channel. There is the possibility for fission of these secondary fragments if they are heavy enough and have sufficient excitation energy, resulting in five or six particles in the exit channel[14]. It was observed later that the interaction of very heavy nuclei (such as ^{238}U, ^{208}Pb, etc.) with similar target atoms resulted in the emission of as many as four or five fragments[15,16].

The reaction pattern of multibody processes is extremely complex and a knowledge of the kinematical correlations between the correlated reaction products is very important. In order to get useful, experimental information on the reaction mechanism underlying such interactions, a complete correlation measurement is required. All the reaction products need to be registered and it is also necessary to obtain all the kinematical variables. The large number of independent, kinematical variables in a multibody process as compared to ordinary binary kinematics make both experimental and theoretical investigations extremely time consuming and difficult. Use of advanced and sophisticated, on-line electronic telescope systems is rather

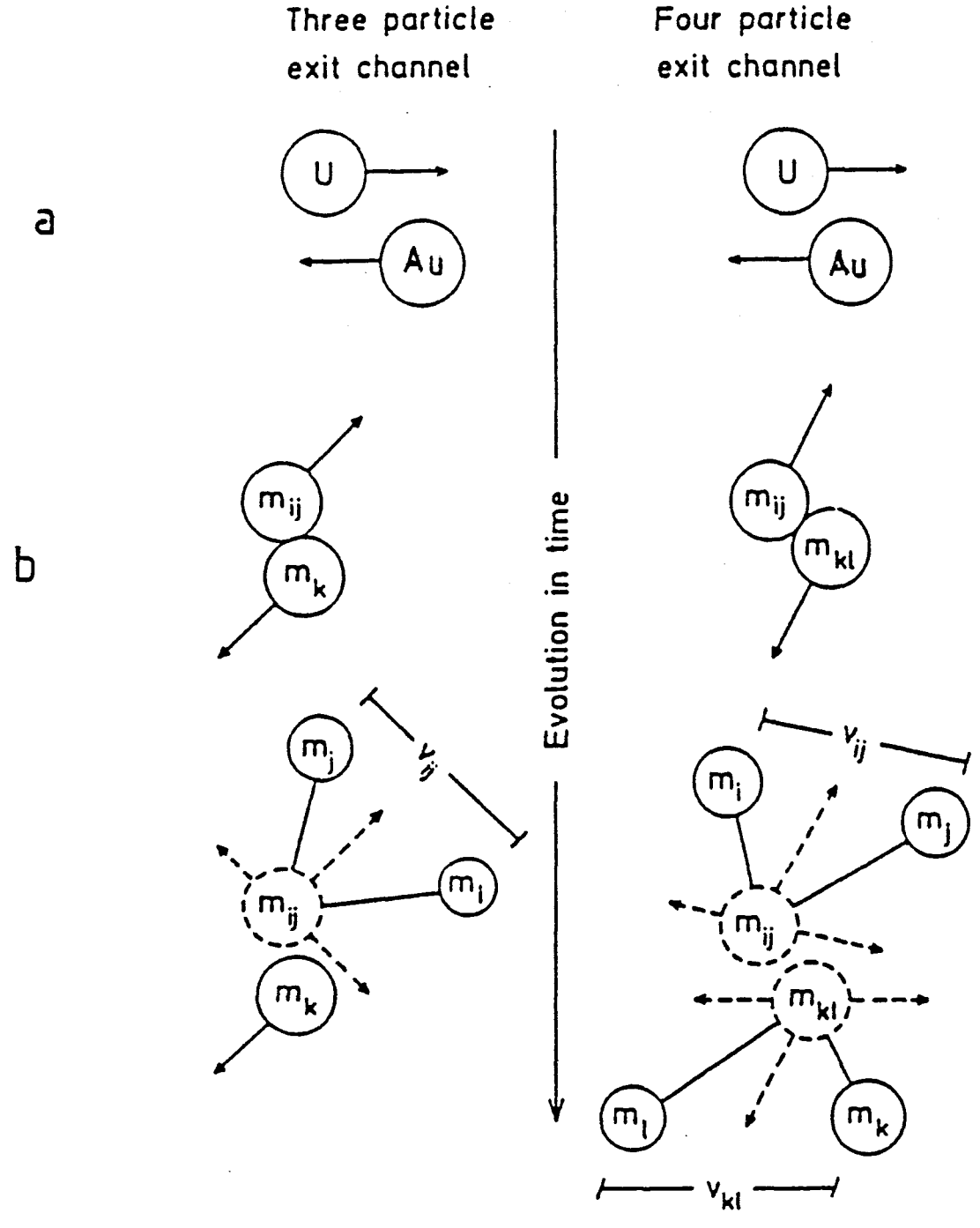

Fig. 8.3 Schematic representation of the sequential fission process in the U + Au reaction.

(a) Projectile and target nuclide before interaction

(b) the first step is an inelastic scattering reaction

(c) on the second step one or both of the interacting nuclides may undergo fission yielding three or four particles in the exit channel. V_{ij} and V_{kl} are the relative velocities between the fission fragments m_i and m_j and m_k and m_l, respectively.

limited. They are mostly restricted to reactions producing up to three outgoing, coincident particles[17]. Very expensive experimental systems are required if coincidence measurements are going to cover a large fraction of the total solid angle. In addition, the data handling is very time consuming and requires a large group of scientists to study such reactions. Solid State Nuclear Track Detectors (SSNTD), therefore, have been used in these experiments to record the particles in the exit channels. They provides a very useful tool for observation of the events when several reaction products are in coincidence. These detectors are very cheap and have almost a 2π-detector geometry. An optical microscope is required to study the fragment tracks produced in the SSNTD.

8.1 Experimental Details

8.1.1 Principle of the Technique and Preparation of the Samples

The muscovite mica ($KAl_3 Si_3 O_{10} (OH)_2$) solid state detector is most extensively used for heavy ion studies. This is due to its favourable track registration characteristics[18], high registration threshold (30 amu) and the ratio, V_t/V_b, of track etch velocity (V_t) to the bulk etch velocity (V_b) is very high. The tracks formed, therefore, are needle-like and act as well-defined vectors in space. CR-39 (allyldiglycol carbonate), is also used as a SSNTD, and this can register particles down to protons. Tracks due to particles with different atomic numbers are developed stepwise by successive etching of CR-39 in 6M NaOH solution at 70°C. The tracks due to heavy ions are revealed in a few minutes while light charges (those from low masses) are made visible only after hours of etching[19].

In these studies we used a gold target of 0.5 to 1 mg/cm^2 thickness

which was vacuum evaporated on to a clean surface of mica or CR-39 using a sputter coating machine. This constituted the target-detector. The target thickness was determined in two ways:

a) weighing the mica or CR-39 before and after the deposition,

b) from the rate of coating in the machine.

The value of the target thickness was a compromise between a reasonable number of reaction events and the energy loss of the projectiles in the target layer. The target-detector assembly was then irradiated with a beam of heavy ions normal to its surface, at Gesellschaft fur Schwerionenforschung (GSI), Darmstadt, West Germany. The fluence of heavy ions was varied from 10^6 to $5x10^6$ ions/cm^2. The projectile ions used in these experiments were 14MeV/amu ^{238}U, 17 MeV/amu ^{208}Pb and 19 MeV/amu ^{142}La. In the case of ^{142}La, by putting mica of approcimately 80 μm thickness in front of the gold target as a degrader foil, its energy was reduced to 9.5 MeV/amu. All the reaction products emitted into the forward, 2π-solid angle, with an angle more than the critical one for track formation and having a mass larger than the thresold for the SSNTDs, produced etchable damage trails. These critical angles were 3^o and 5^o for mica and CR-39, respectively. The main features of the 2π-geometry techniqe as applied in this work are shown in figure 8.4. After the irradiation, the gold was dissolved off with a solution of 3 parts concentrated HCl and 1 part concentrated HNO_3 (aqua regia). The mica samples were etched with 48% hydrofluoric acid at room temperature for 8 minutes, and CR-39 samples were etched in 6M NaOH at 70^{o}C in succesive steps of etching time, starting with an etch of a few minutes. In the case of mica, with this etching time all latent tracks were fully etched.

8.1.2 Features of the Etched Track Detectors

The etched detectors showed a number of characteristic, microscopic

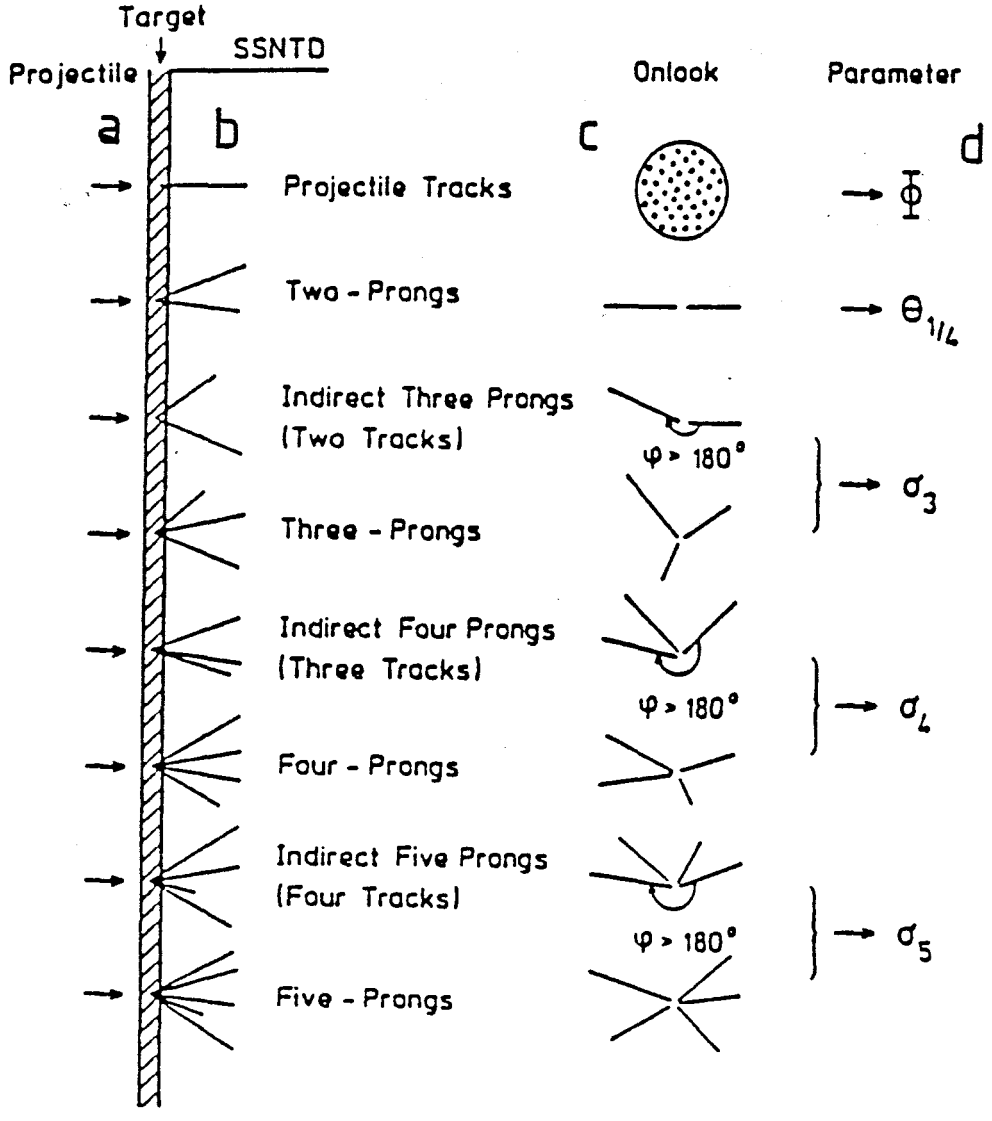

Fig. 8.4 Schematic representation of the 2π geometry technique using mica solid state nuclear track detector (SSNTD) to determine heavy ion collision fragments. The target material is coated on the mica surface.

(a) Projectiles

(b) particles in the exit channel

(c) exit channel tracks projected into the surface plane, viewed perpendicular to that plane

(d) parameters derived from the observed number of tracks and their relation to one another.

features.

i) Black spots

These were tracks of projectiles that had not undergone any interaction with the target material. The projectile fluence could be obtained directly by counting these black spots, and this fluence could be used in the evaluation of absolute reaction cross-sections.

ii) Two-pronged events

These were events with two, correlated tracks emerging from one reaction spot, indicating elastic scattering or inelastic, binary fission reactions.

iii) Three and higher-multiplicity events

Here the projectile or the target, or both, underwent fission. They indicated a multibody break-up or a sequential fission in more than one step. In addition to the usual type of multi-pronged events, some "indirect" events were also found. In these, the largest angle between any two neighbouring tracks in the plane of observation was greater than 180^{o}. This indicated that linear momentum in the plane of observation was not conserved. In such cases we believe that at least one of the fragments that was emitted was not registered. This could be due either to it being a light particle (below the detector threshold) or it was emitted in the backward 2π solid angle. This technique, however was not able distinguish between the tracks of those fragments emitted parallel to or prependicular to the detector surface. Fig. 8.5 shows the relation between the track lengths, L_i and their projected values (l_{ip},p), together with their scattering angles and the corresponding projected angles (Φ_i).

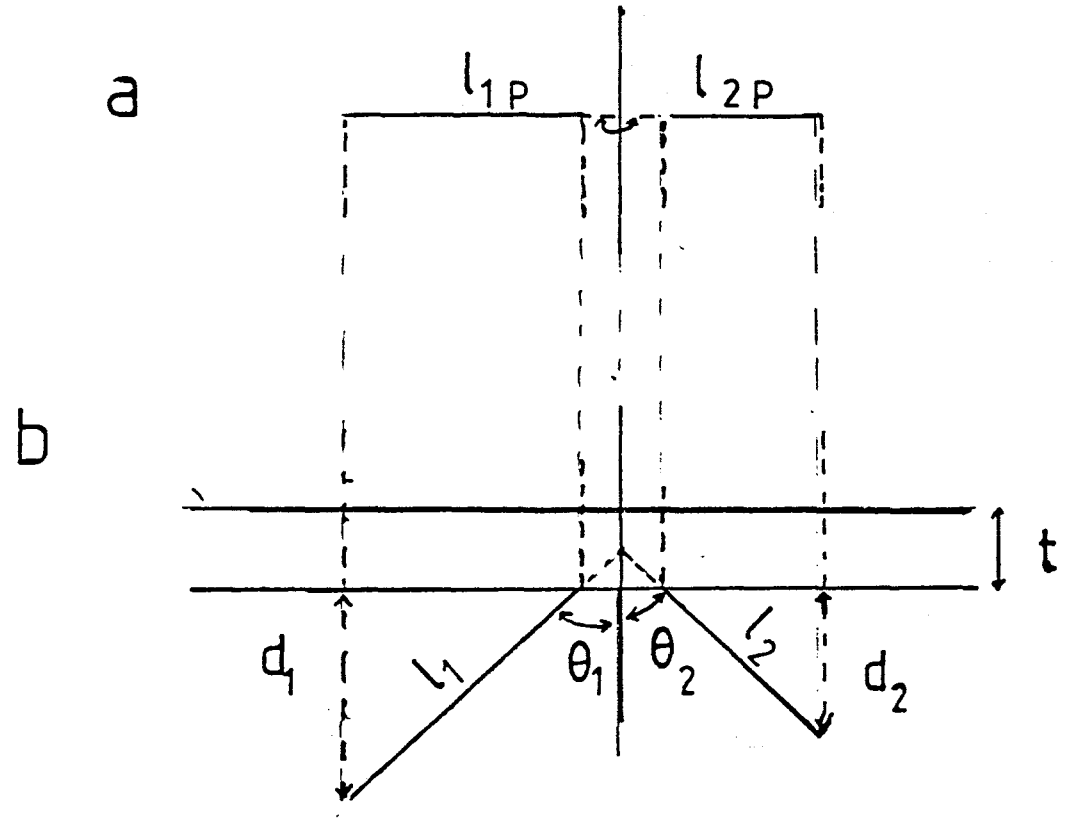

Fig. 8.5 A schematic representation of a typical elastic, two-prong event observed in the U + Au reaction showing (a) the onlook view and (b) edge-on view in the mica. See text for explanation of the parameters shown.

8.2 Analysis of Data

8.2.1 Selection of the Elastic Two-Prong Events

In an elastic reaction the masses of the projectile, M_p and the target, M_t, remain unchanged after the reaction. If the projectile energy in the laboratory system is E_{lab} and after elastic scattering the projectile and target scattering angles in the laboratory system are θ_1 and θ_2, it follows that their laboratory energies, E_1 and E_2, are correlated as

$$\sin\theta_2 = \left(\frac{M_p}{M_t}\cdot\frac{E_1}{E_2}\right)^{\frac{1}{2}} \sin\theta_1 \qquad 8.2$$

where

$$E_1 = \frac{M_p^2}{(M_p+M_t)^2}\left[\cos\theta_1 + \left\{(M_t/M_p)^2 - \sin^2\theta_2\right\}^{\frac{1}{2}}\right]^2 \qquad 8.3$$

$$E_2 = E_{lab} - E_1 \qquad 8.4$$

The above equation can be used for the selection of elastic scattering events. All suspected elastic events were checked for consistency in two ways:

i) both of the measured scattering angles should be correlated in accord with the above equation,

ii) both of the measured track lengths, after converting to the equivalent energy using the standard range-energy relationship data, should also be correlated in accord with the above equation.

The data from elastic, two-prong events were used for calibration purposes (section 8.4). They also provided an independent method of calculating reaction cross sections using the 'quarter point angle' which will be discussed in section 8.3.1.2.

8.2.2 Analytical Treatment of the Multi-Prong Events

Each track is like a well-defined vector, l_i, in space and, corresponding, each of the two-, three-, or four-pronged events are characterized by their correlated two, three, or four track vectors in the exit channel (Fig 8.6).

In order to determine the N particles corresponding to an N-pronged track, it is necessary to know the 3N individual momenta and N individual masses, giving 4N variables to be conserved. Because, however, there is conservation of total momentum and spherical symmetry around the beam axis, the total number of variables reduces to 4(N-1) independent variables. In the measurement of multi-pronged tracks with three dimentional coordinates, it is possible to determine 4, 8 or 11 independent variables for two-pronged, three-pronged or four-pronged events. These independent variables are the track length, the angles with respect to beam direction and the angles between the tracks in the plane perpendicular to the beam direction (Fig. 8.6). These measured variables are enough for two- and three-pronged events. For four-pronged events, however, we need 12 independent parameters. The missing parameter can be supplied by consideration of conservation of mass during the experiments. The correlated fragment masses, M_i and velocities, V_i, from an indiviual multi-pronged event are calculated on the basis of the measured correlated track length, l_i and track direction, e_i. To do this, we need to solve, event by event, the coupled equations

$$\sum_{i=1}^{N} MV(\ell_i, m_i)\, \vec{e}_i = \vec{P}_{in} \qquad (N = 2,3,4) \qquad 8.5a$$

and

$$\sum_{i=1}^{N} M_i = M_p + M_t \qquad 8.5b$$

where P_{in} is the incident linear momentum and M_p and M_t are the

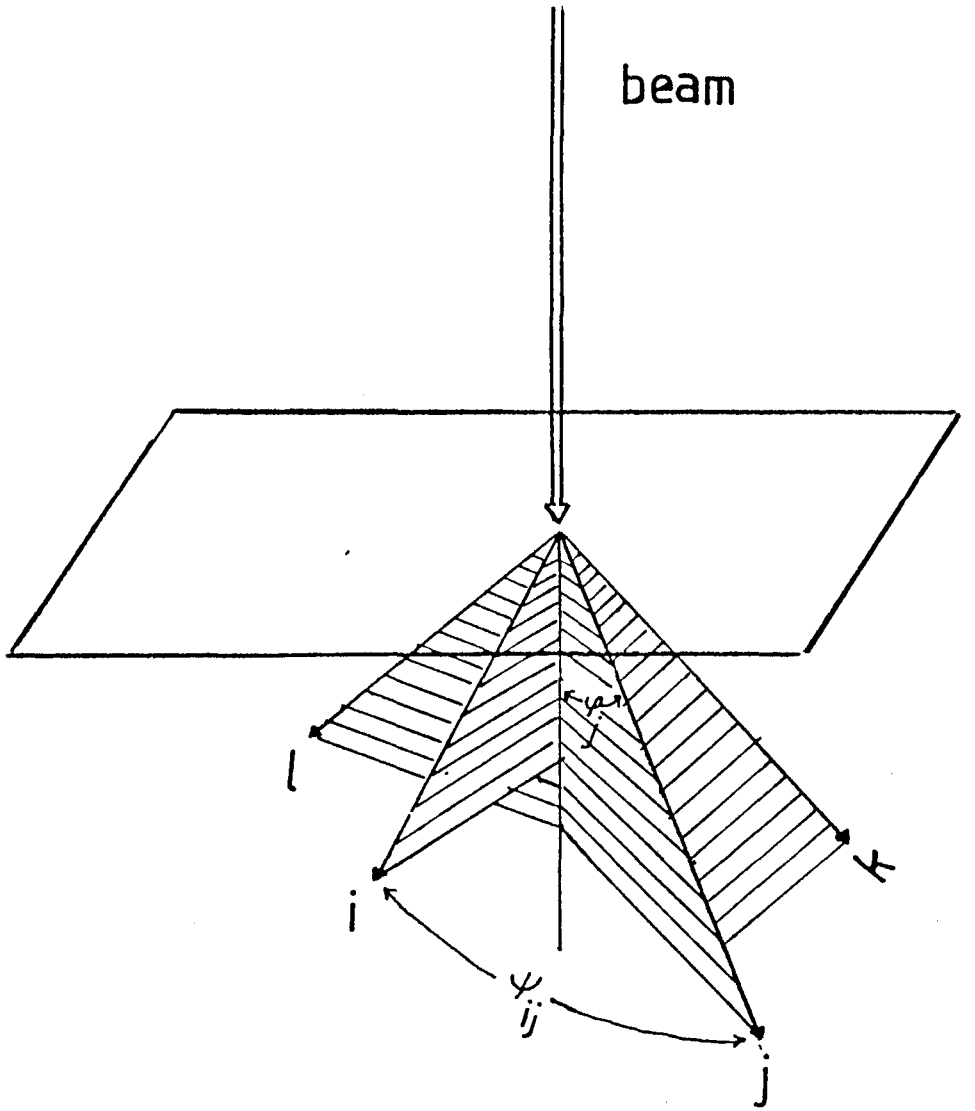

Fig. 8.6 The schematic representation of a four-prong event viewed edge-on. See text for explanation of the parameters shown.

masses of projectile and target, respectively. Equation 8.5 can be solved for individual fragments arising from two-, three-, and four pronged events as follows[20]:

a) two pronged events

$$M_i = \frac{| \vec{P}_{in} |}{V_i \sin \psi_i (\cot \psi_i + \cot \psi_j)} \qquad (i, J=1,2) \qquad 8.6a$$

b) three pronged events

$$M_i = \frac{\vec{P}_{in}(\vec{e}_j x \vec{e}_k)}{V_i e_i . (\vec{e}_j x \vec{e}_k)} \qquad (i,j,k=1,2,3;\ \text{cycl.}) \qquad 8.6b$$

c) four pronged events

$$M_i = \frac{(\vec{P}_{in} - M_{tot} V_4 \vec{e}_4)((v_j \vec{e}_j - V_4 \vec{e}_4) \times (V_k \vec{e}_k - V_4 \vec{e}_4))}{(V_i \vec{e}_i - V_4 \vec{e}_4)((V_j e_j - V_4 e_4) \times (V_k e_k - V_4 e_4))} \qquad (i,j,k=1,2,3;\ \text{cycl.}) \qquad 8.6c$$

where $V_i = V_i(\ell_i, M_i)$ 8.6c

$V_i(l_i,M_i)$ is an empirical relationship between track length, mass and velocity. This relationship was found to be a bi-variable polynomial, expressed as

$$V_i(l_i, M_i) = \sum_{i=0}^{4} \sum_{J=0}^{2} A_{ij}\ T_i\ (L_{cap})\ T_j\ (M_{cap}) \qquad 8.7$$

By substitiuting Equation 8.7 in to Equation 8.6a,b or c one can solve Equation 8.6a,b or c for a given coefficient of A_{ij}, for a given e_i and knowing P_{in}. To do this a computer program was developed which is listed in Appendix 5.

8.2.3 Determination of the Coefficients for the Range-Energy Relationship

Equation 8.7 is a bivariate polynomial of degree K in L and P in M. This polynomial is represented by a double Chebyshev series, with arguments Mcap and Lcap. This fit has a better physical basis and

causes less error during the analytical process than the polynomial fitting

used by Gottschalk et al. It is a well-known proposition in mathematics[21] that the nth Chebyshev polynomial, $T_n(x)$, is a solution of

$$(-X^2)\frac{d^2T_n}{dx^2} - X\frac{dT_n}{dx} + n^2T_n = 0$$

Thus

$$T_n(x) = {}^{n}/_{2}\sum_{k=0}^{(n/2)} \frac{(-1)^k(n-k-1)!}{k!\,(n-2k)!}\,(2x)^{n-2k}$$

If $X=\cos\theta$ then $T_n(\cos\theta)=\cos n\theta$ and

$$\left.\begin{aligned} T_0(x)&=1\\ T_1(x)&=x\\ T_2(x)&=2x^2-1\\ T_3(x)&=4x^3-3x\\ T_4(x)&=8x^4-8x^2+1 \end{aligned}\right\}$$

In order to have such simple case as above, the values of Mcap and Lcap must lie in the range, -1 to +1. These are related to the original variables M and L by the transformation

$$Mcap = \frac{2M-(M_{max}+M_{min})}{(M_{max}-M_{min})}$$

$$L\,cap = \frac{2L-(L_{max}-L_{min})}{(L_{max}-L_{min})}$$

In order to do this surface fitting to the data the subroutine E02CAF in the NAG library was used[22]. This routine fits Equation 8.7 to the set of data points ($L_{r,s}$, M_s, $V_{r,s}$), with weights $W_{r,s}$ for s=1,2,---,N and r=1,2,--,L_s. That is, the data points are on lines $L=L_s$ but the M values may be different on each line. The values of K and P are chosen by the user. In fact, this routine forms an approximation to the weighted, least-squares Chebyshev series surface fit to data arbitrarily distributed on lines parallel to one independent co-ordinate axis.

The M_{max} and M_{min} are set by the routine to the largest and smallest value of L_s, respectively but since L_{max} and L_{min} are functions of L, they are set by the user. For this routine, only the values of L_{max} and

L_{min} at each $L=L_S$ are required. For each s(=1,2,--,N, L_{maxs}), the value must not be less than the largest $L_{r,s}$ on the line $Y=Y_S$ and similarly, L_{mins} must not be greater than the smallest $L_{r,s}$.

In the double Chebyshev series, $T_i(L_{cap})$ is a Chebyshev polynomial of the first kind, of degree i, with the arguments Lcap and $T_j(M_{cap})$ similarly defined. The standard convention, however, followed in this routine is that coefficients in the above expression which have either i or j zero are written as 0.5 $A_{i,j}$, instead of simply $A_{i,j}$ and the coefficients with both i and j = zero are written as 0.25 $A_{i,j}$.

The routine first obtains the Chebyshev series coefficients, $C_{s,i}$, (i = 0,1,--,K), of the weighted least-squares polynomial curve fit of degree K, using the soubroutine E02ADZ. The same subroutine is then called K+1 times to fit each Cs,i, (s = 1,2,---,n) to a polynomial of degree P in Mcap, for each i, (i = 0,1,---,P). The resulting coefficients are the required $A_{i,j}$. Appendix 5 includes the listing of this routine and input and output data obtained for this work.

8.3 Results and Discussion

8.3.1 Reaction Cross Section

The reaction cross section is one of the basic parameters in heavy-ion interaction studies. It was determined by two, independent methods for the ^{197}Au(U,U)^{197}Au reaction as follows:

I) from direct observation of multi-prong events,

II) from angular distributions of two-pronged events attributed to elastic scattering.

For the Au(Pb,Pb)Au and Au(La,La)Au reactions only the second method was employed.

8.3.1.1 Reaction Cross Section Determined from the Direct Observation of Multi-prong Events

The total number of direct plus indirect events, N_i, for a particular multiplicity,i , the measured fluence, (Φ), of the projectile and the available number of target nuclei, A, can be used to determine the reaction cross section from the expression

$$\sigma_i = \frac{N_i}{\Phi . A}$$

where σ_i is given in cm^2.

The total number of observed, inelastic events producing three- or higher multi-pronged events, with the resulting cross sections for all reactions under study, registered by mica and CR-39 are shown in Table 8.2. The reaction cross section σ_{3+4} in Table 8.2 is the total cross section for three- and four-prong events. This result has been compared with published, experimental results[20] for the Au(U,U)Au reaction at 9.0 Mev/amu and 16.7 Mev/amu energies, using the mica and CR-39 detectors in Fig.8.7. As can be seen from this Figure, σ_3 increases with increasing projectile energy but σ_4 appears to decrease with increasing energy in the mica detector. In the case of the CR-39 detector, the results indicate that it remains almost constant with increasing energy. These results indicate that the value of σ_4 is larger in CR-39 than in mica. This is due to the lower threshold of CR-39, which is able to register light particles down to protons. If one of the prongs in real, four pronged events was to correspond to a particle with mass less than 30, the mica detector would register it as a three pronged event. The reduction of σ_3 in CR-39 relative to mica may be due to contributions from some four-pronged tracks to three-pronged ones in the mica detectors.

Table 8.2

The cross section of three- and four-pronged events in the U + Au reaction at different projectile energies, using mica and CR-39 detectors.

Energy MeV/amu	Detector	σ_3 (mbarn)	σ_4 (mbarn)
9.0	Mica	1750 ± 150	500 ± 100
14.0	"	3008 ± 373	360 ± 113
16.7	"	3300 ± 350	300 ± 100
14.0	CR-39	2610 ± 242	912 ± 271
16.7	"	2700 ± 200	1000 ± 200

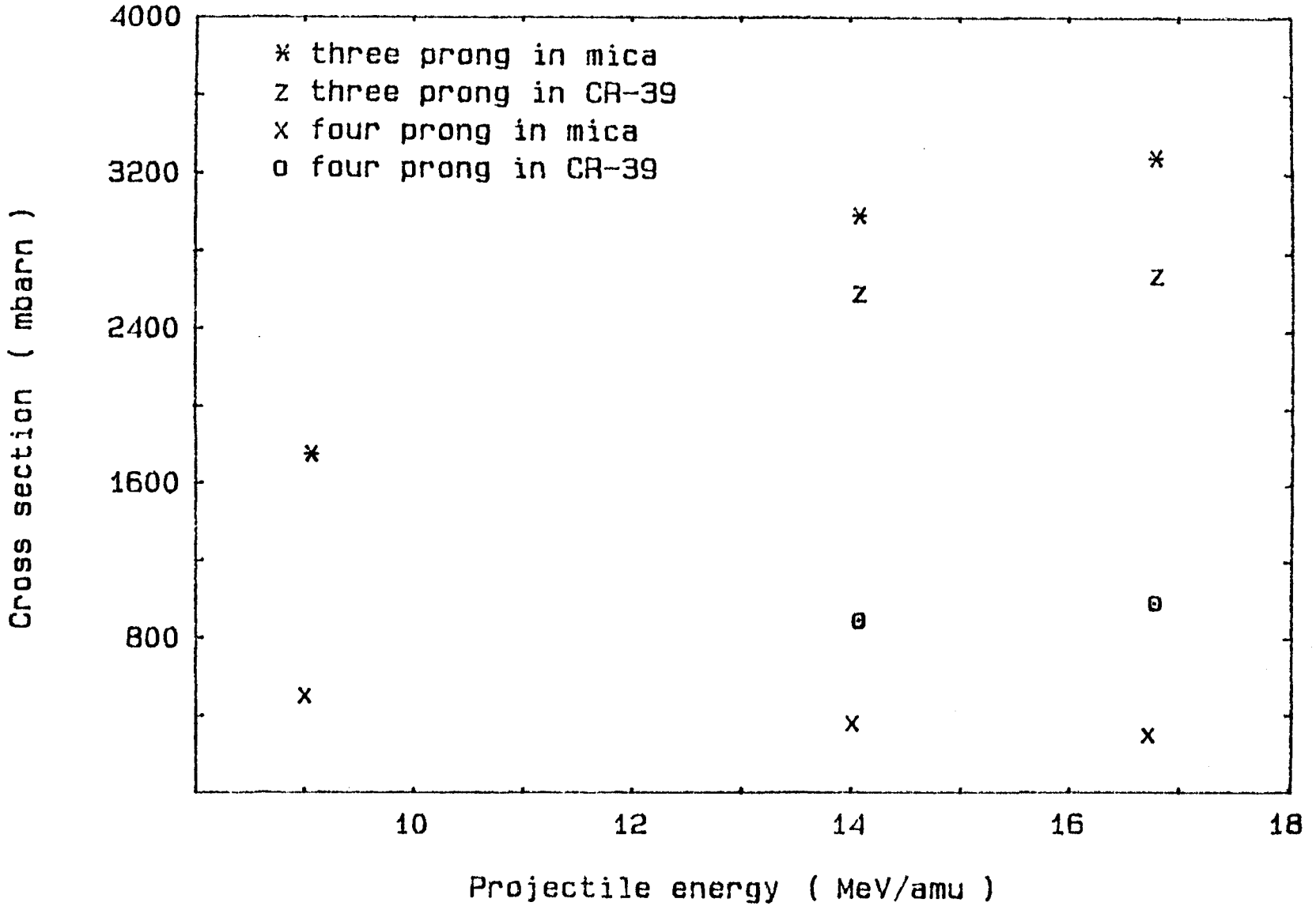

Fig. 8.7 Cross sections of four- and three-prong events for U & Au reaction as function of projectile energy.

8.3.1.2 Reaction Cross Section
Determined Through Elastic Scattering

The elastic scattering events were determined by the procedure explained earlier for the selection of these events. As a typical example of measured track parameters, Figs. 8.8 and 8.9 show two-pronged events colinear in the plane of observation, the track length distribution and the distribution of angles between the beam direction and track length, for the Au(Pb,Pb)Au reaction. The uncertainties in the measurement of individual tracks is about 1.5 μm in the length estimate and 3^{o} in the determination of the angle. Frahn[23] has shown that the Coulomb field deflects the scattered particles in such a manner that angular distributions in elastic nucleus-nucleus scattering exhibit a striking similarity to Fresnel diffraction in optics. The requirements for this Fresnel diffraction are, $l_{gr} \sin\theta_{gr} > 1$ or $l_{gr} >> 1$, which are easily fulfilled for heavy ion, elastic scattering. l_{gr} is the angular momentum equivalent of the impact parameter, bgr, with a scattering angle of θ_{gr}.
In the case of Rutherford scattering, for which $l > l_{gr}$, Fresnel diffraction is described by the following expression for the elastic scattering cross section

$$\frac{d\sigma}{d\sigma_R} = \tfrac{1}{2}\{[\tfrac{1}{2} - S(y)]^2 + [\tfrac{1}{2} - C(y)]^2\}$$

where S(y) and C(y) are the Fresnel integrals σ_R is the Rutherford cross section and the argument, y, is defined by

$$y = \left(\frac{l_{gr}}{\pi \sin\theta_{gr}}\right)^{\frac{1}{2}} (\theta - \theta_{gr})$$

It is clear that for $\theta = \theta_{gr}$ and $y = 0$, $d\sigma / d\sigma_R = 0.25$ and therefore θ_{gr} is called the 'quarter point angle', i.e. the angle where the

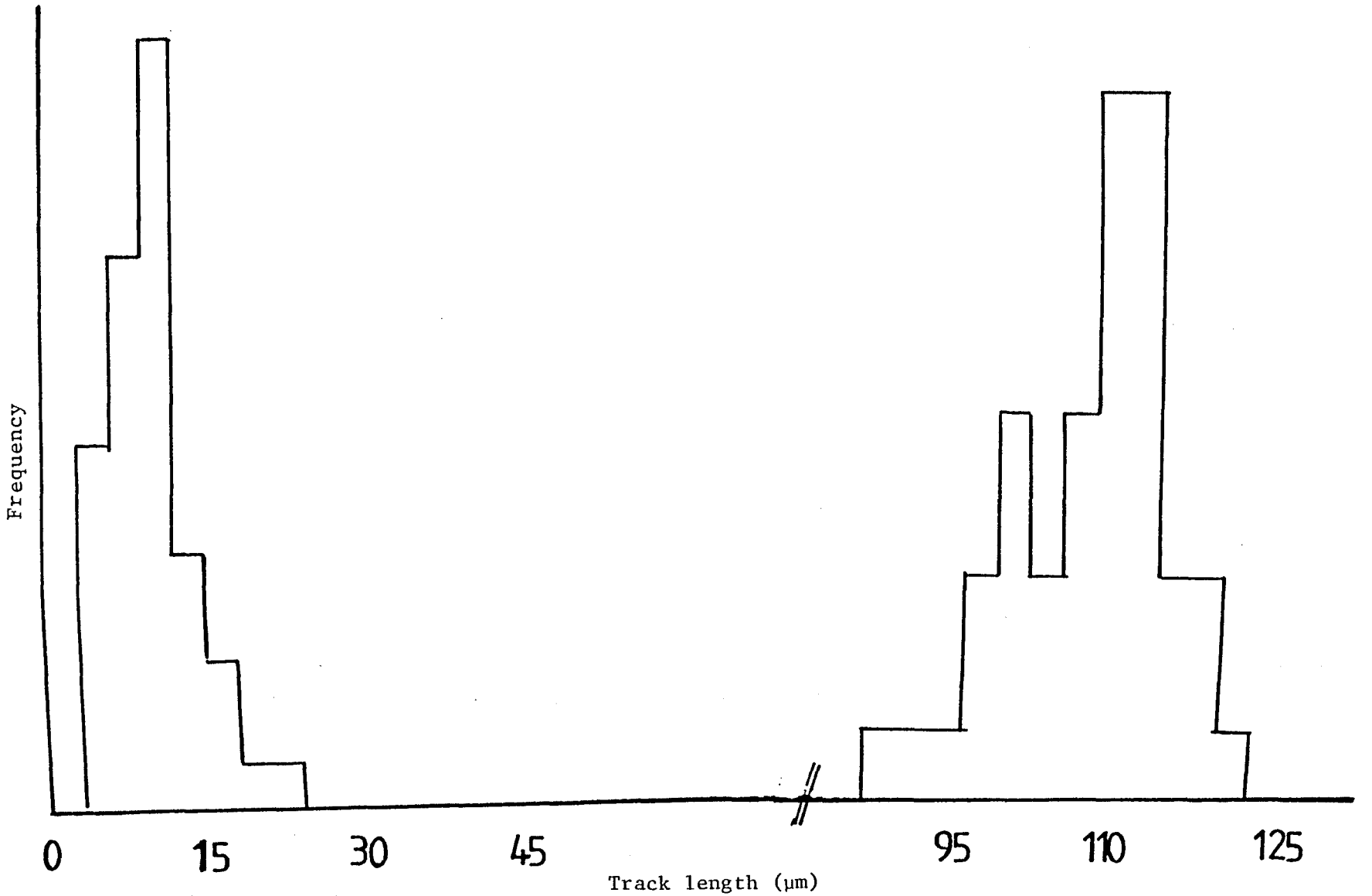

Fig. 8.8 The distribution of track lengths for two prong events viewed as in 8.4(c). A long track length indicates as a fragment scattered in the forward direction (relative to the beam direction). Conversely, a short track length refers to a fragment recoiling through about 80^{o}.

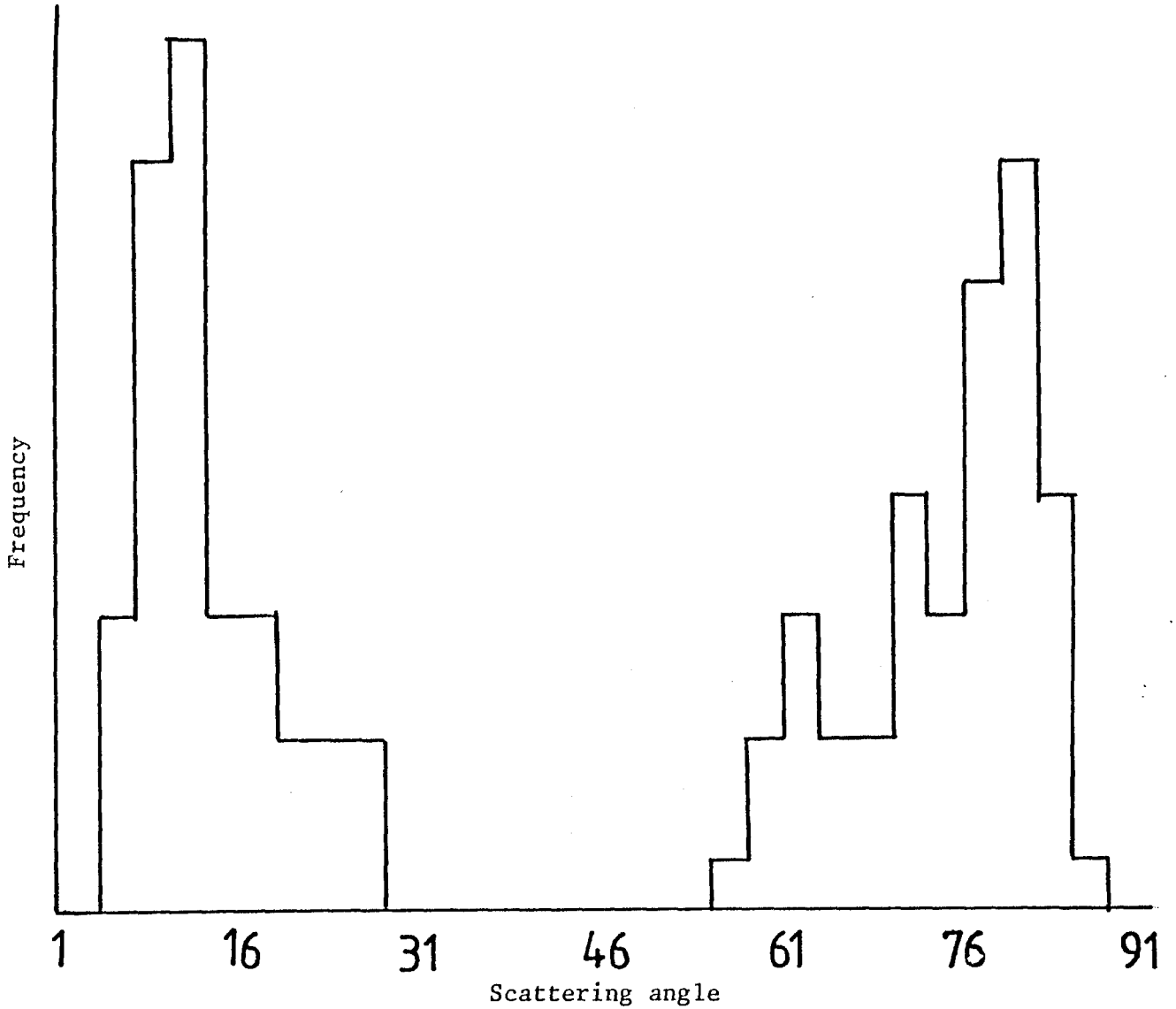

Fig. 8.9 The distribution of angles, θ_{lab}, in the Ph & Au reaction for two-pronged events colinear in the plane of observation. θ_{lab} is the angle of scattering in the lab system between the incident beam and fragment track direction.

elastic scattering cross section is one quarter of the Rutherford value. The quarter-point-angle can be used for computing the total reaction cross section as follows[24]

$$R_{int} = \eta\lambda\ (1+\mathrm{cosec}(\tfrac{1}{2}\theta_{\frac{1}{4}})) \qquad 8.8$$

where λ is the asymotic wavelength and η is the Sommerfeld parameter. These parameters can be obtained as follows

$$k = 1/\lambda = .2187\ M_t(M_p\ E_{ict})^{\frac{1}{2}}\ /(M_t + M_p)$$

$$\eta = 0.15746\ Z_pZ_t\left(\frac{M_p}{E_{int}}\right)^{\frac{1}{2}}$$

or

$$M_o = (M_t.M_p)/(Mt+M_p) \qquad 8.9$$

$$\lambda = \left(\frac{2M_oE_{cm}}{\hbar^2}\right)^{\frac{1}{2}}$$

$$\eta = \frac{Z_p.Z_te^2}{\hbar v}$$

$$R_o = R_{int}\ (M_p^{1/3} + M_t^{1/3}) \qquad 8.10$$

$$l_{max} = \eta\ \cot(\tfrac{1}{2}\theta_{\frac{1}{4}}) \qquad 8.11$$

$$\sigma_R = \pi\ \lambda^2\ (l_{max} +0.5)^2 \qquad 8.12$$

The Rutherford scattering cross section was determined from

$$\frac{d\sigma}{d\Omega} = \frac{b^2}{16} \cdot \frac{1}{\sin^4(\theta/2)} \qquad 8.13$$

where b is the collision diameter and is calculated using

$$b = \frac{Z_pZ_t\ e^2M_p}{4\pi\epsilon_oME_{int}}$$

The values of the collision diameter along with other parameters for the reactions used in this work are shown in Table 8.3.

By using the value of $d\Omega$ from Eq.7.2 in Eq. 8.13, and its integration fron angles θ_1 to θ_2 we obtain

$$d\sigma = \frac{\pi b^2}{16}\ [\mathrm{cosec}^2(\theta_{1/2}) - \mathrm{cosec}(\theta_{2/2})$$

Table 8.3

Collision diameters and reduced masses for the heavy ion reductions investigated.

Parameter / Reaction	Reduce mass μ^{**}	Projectile energy (E_{in}) (MeV)	Collision diameter b (fm)
Au(U,U)Au	107.78	3332	6.93
Au(Pb,Pb)Au	101.17	3536	5.42
Au(La,La)Au	81.49	1320.5	4.65

$$*b = \frac{Zze^2\mu p}{4\pi\epsilon_o\mu_o E_{in}}$$

$$**\mu = (M_p.M_t)/(M_p+M_t)$$

The ratios of the experimentally observed elastic scattering cross sections to the Rutherford scattering cross section were used to obtain a curve showing the variation of $\sigma_{exp}/\sigma_{Rut}$ versus scattering angle. The quarter-point-angle ($\theta_{.25}$) was determined from this distribution. Figures 8.10, 8.11 and 8.12 show the variation of experimental to Rutherford cross sections versus the scattering angle (in the centre of mass system) for the scattering of ^{238}U, ^{208}Pb and ^{139}La ions by a ^{197}Au target. The values obtained for the quarter-point-angles were used in Eqs. 8.8 to 8.12 to yield values of the total cross-sections and of other reaction parameters. The results are summarised in Table 8.4.

8.4 Calibration of the Detector for the Velocity, Mass and Track Length Relationships

There are two ways to determine the coefficients, $A_{i,j}$ in Eq. 8.7, and are considered below.

i) External Calibration

In this method the mica is irradiated with well-defined, heavy ions. Measurement of track lengths then results in a velocity-track length correlation for those well-defined, heavy ions. We have not used this method.

ii) Internal calibration

In this method the two-pronged events originating from elastic scattering and fission fragments produced in the thermal neutron induced fission of uranium are used for calibration. In the case of elastic scattering we used colinear, two-pronged tracks to define an elatic scattering events. Since we know the masses of the particles involved and their energies from the track lengths it is therefore possible to determine the coefficient of $A_{i,j}$ using Equation 8.7. To

Fig. 8.10 The ratios of the experimental to the Rutherford cross sections as a function of the C.M. scattering angles, θ_{CM}, for two-prong events resulting from a 14 MeV/amu beam of U on a gold target.

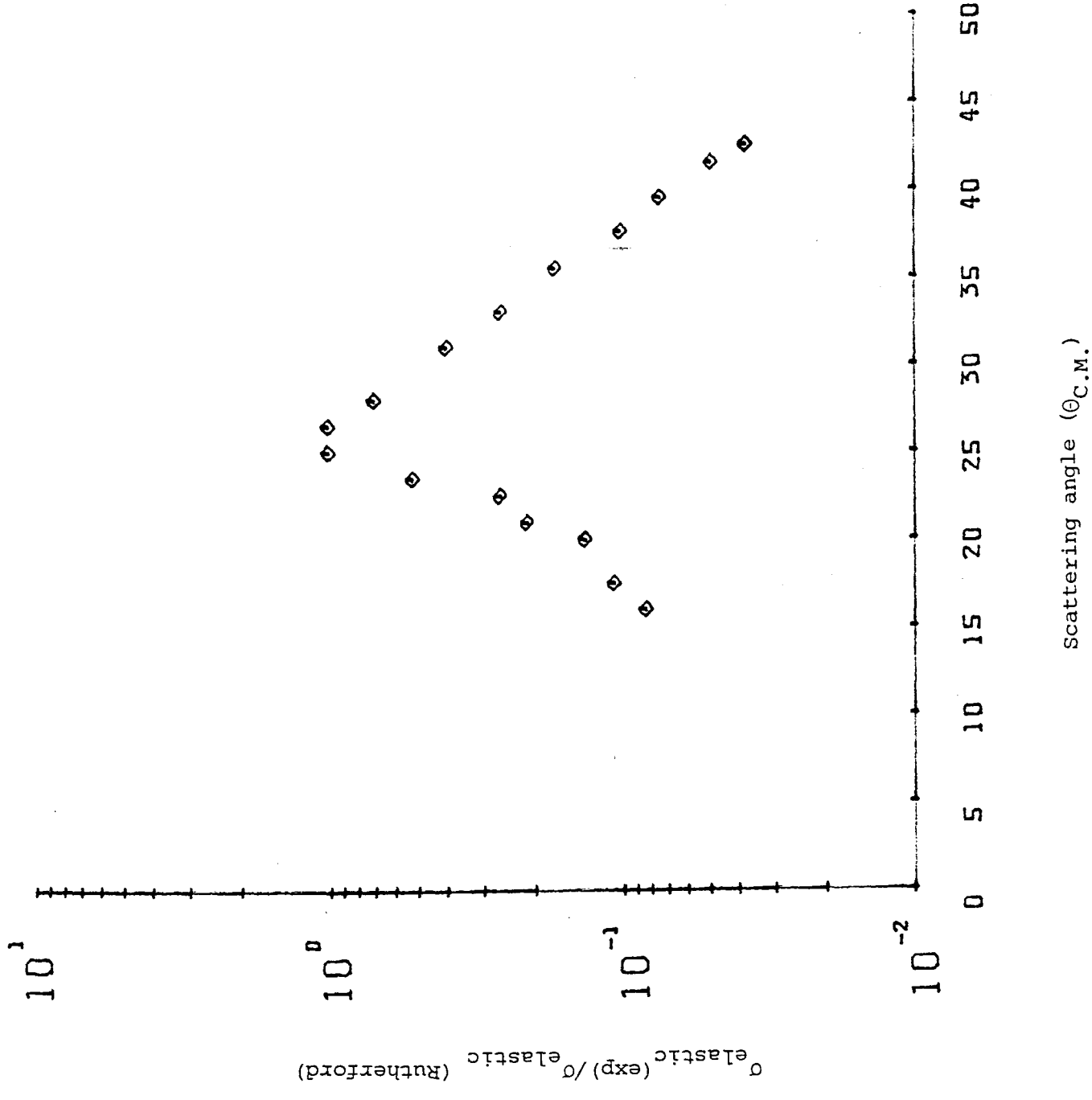

Fig. 8.11 Same as Fig. 8.10 but for 17 MeV/amu ^{208}Pb on a gold target.

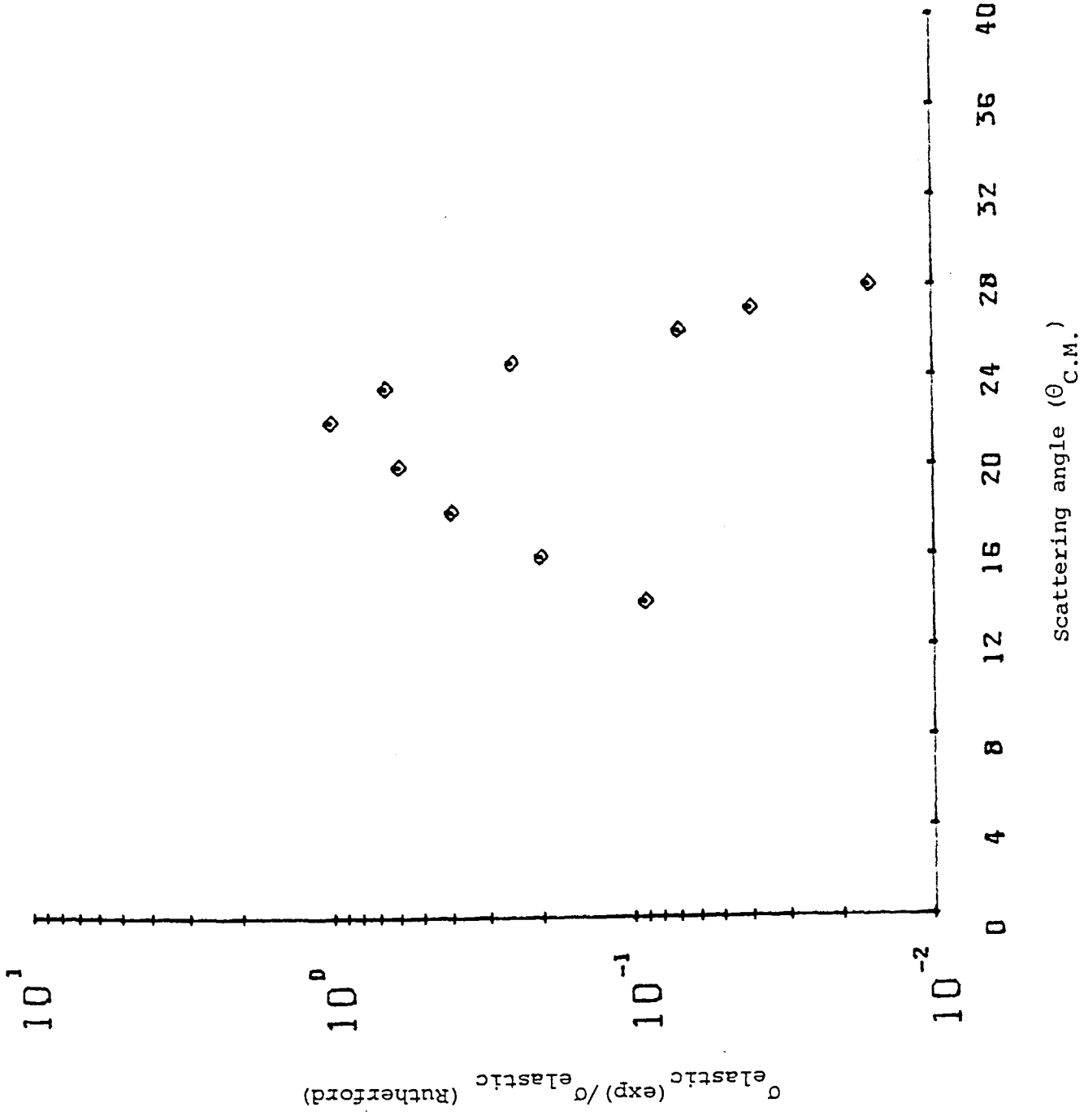

Fig. 8.12 Same as Fig. 8.10 but for 9.5 MeV/amu ^{139}La on gold target.

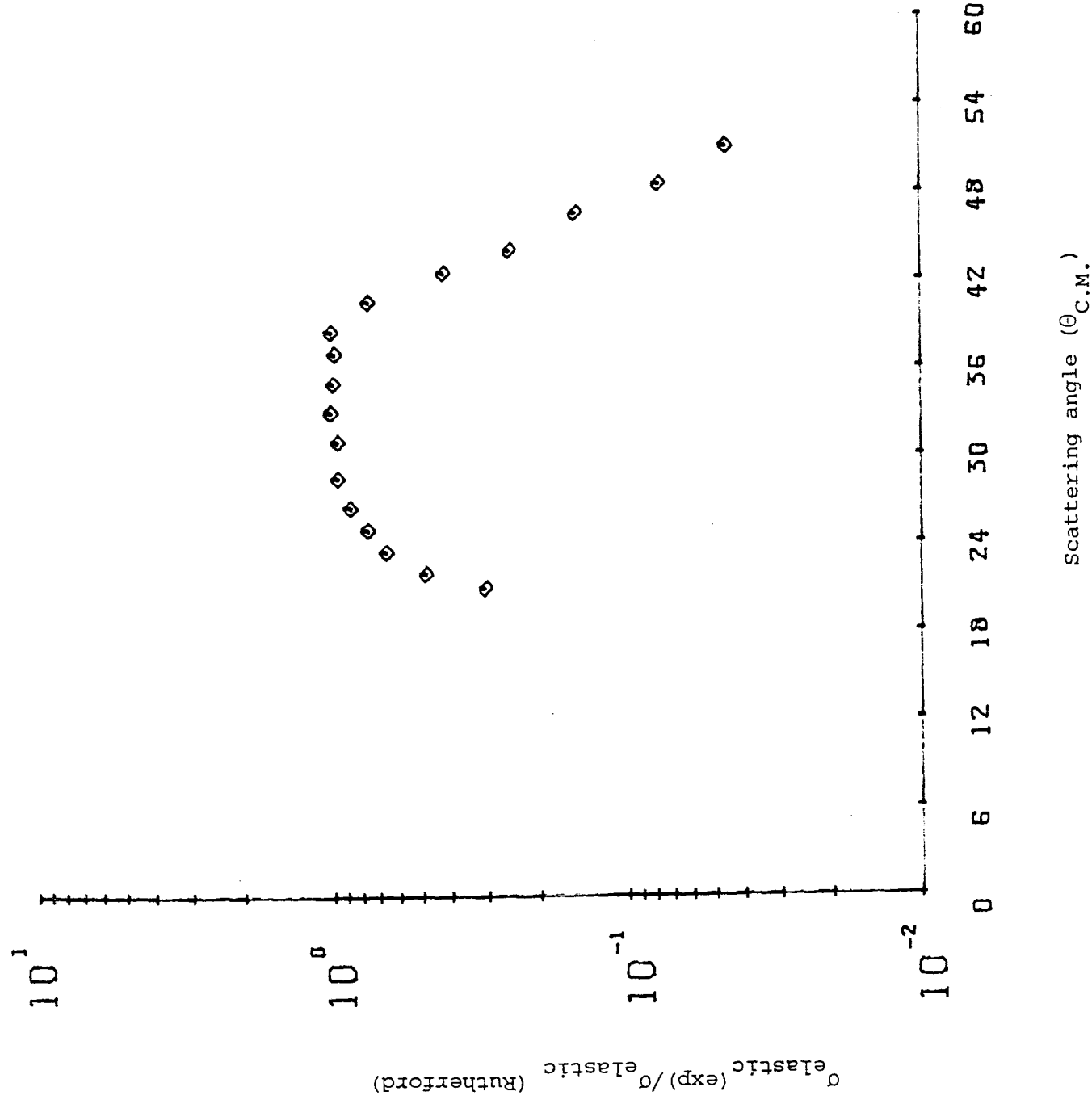

Table 8.4 The reaction parameters derived from heavy ion bombardment of gold with U, Pb and La at specific energies. For an explanation of the meaning of the symbols used refer to the text.

parameter / Reaction	θ_{14} C.M.	R_{in} fm	R_o fm	Projectile energy (MeV) C.M.	Projectile energy (MeV) Lab.	θ_{14} lab.	η	L_{max}	λ	σ_R mbarn
Au(U,U)Au	33.1	17.1	1.42	1508.9	3332	14.9	305.8	1029	.01133	4280.8
	(31.7)*					(14.3)*				4686*
Au(Pb,Pb)Au	24.9			1719.9	3536		247.4	1120.5	.01096	4743
	(23.8)*					(11.6)*				
Au(La,La)Au	44.1			774.2	1320	26	230.03	567.9	.01820	336.3

* Ref. 24

check that the calculated coefficient is indeed the correct one it is only necessary to see that it gives rise to two maxima in a plot of mass versus number of events.

The best set of coefficients in Eq. 8.7, obtained from data for U(Au,Au)U are shown in Table 8.5. In this equation, V(L,M) is in $fm/10^{-23}s$, L is in mg/cm^2 and M is the atomic mass.

These coefficients are used for the analyses of masses and velocities from the track data, using Eqs. 8.6 and 8.7, and thence the total kinetic energy loss (TKEL). The yield distribution of two pronged events corresponding to elastic scattering is plotted versus TKEL in Fig. 8.13 for U ion beams on a gold target. It is clear that they peak around a value of TKEL = 0 MeV.

The distribution of total mass in the two-pronged and three-pronged track is shown in Fig. 8.14 for a U projectile. It is clear from Fig. 8.14 that mass distributions have peaks around the sum of projectile and target masses. Fig. 8.15 shows fragment mass distribution for elastic scattering events in Au(U,U)Au rection (E_{lab} = 3332 MeV). This indicates a narrower peak for light fragments (Au nuclide) but a broader peak for the heavy fragment (U nuclide). This is a somewhat unexpected result, since it would be expected that the projectile moving in an essentially forward direction would produce a long track and hence a sharp peak whereas the recoil fragment (Au nuclide), scattered through about 80^o has a much shorter length. In order to explain the present curves in Figure 8.15, may accept there is higher uncertainty in the measurement of angle and length of track in depth rather than in the top surface.

References:

1 Bass R., Nuclear reactions with heavy ions. Springer, Berlin, Heidelberg, New york (1980)

2 Deubler H.H., Dietrich K., Hofmann H., Statistical theory of heavy

Table 8.5 The set of coefficients obtained from Eq. 8.7 (see text for further information).

4.6093D-01	8.7704D-02	3.5060D-01	3.3468D-01	1.2341D-01
2.4023D-02	1.2659D-02	-2.5316D-03	-9.6931D-03	-4.7102D-03
-6.6536D-04	-2.8186D-04	2.9712D-04	3.0611D-04	3.5247D-04

Fig. 8.13 The distribution of TKEL for two-pronged, elastic scattering events from the U & Au reaction. The Gaussian fit to the data peaked around zero MeV TKEL. The centroid of the peak is actually at 2.0 MeV and the value of σ derived from the Gaussian fit was 39.22 MeV.

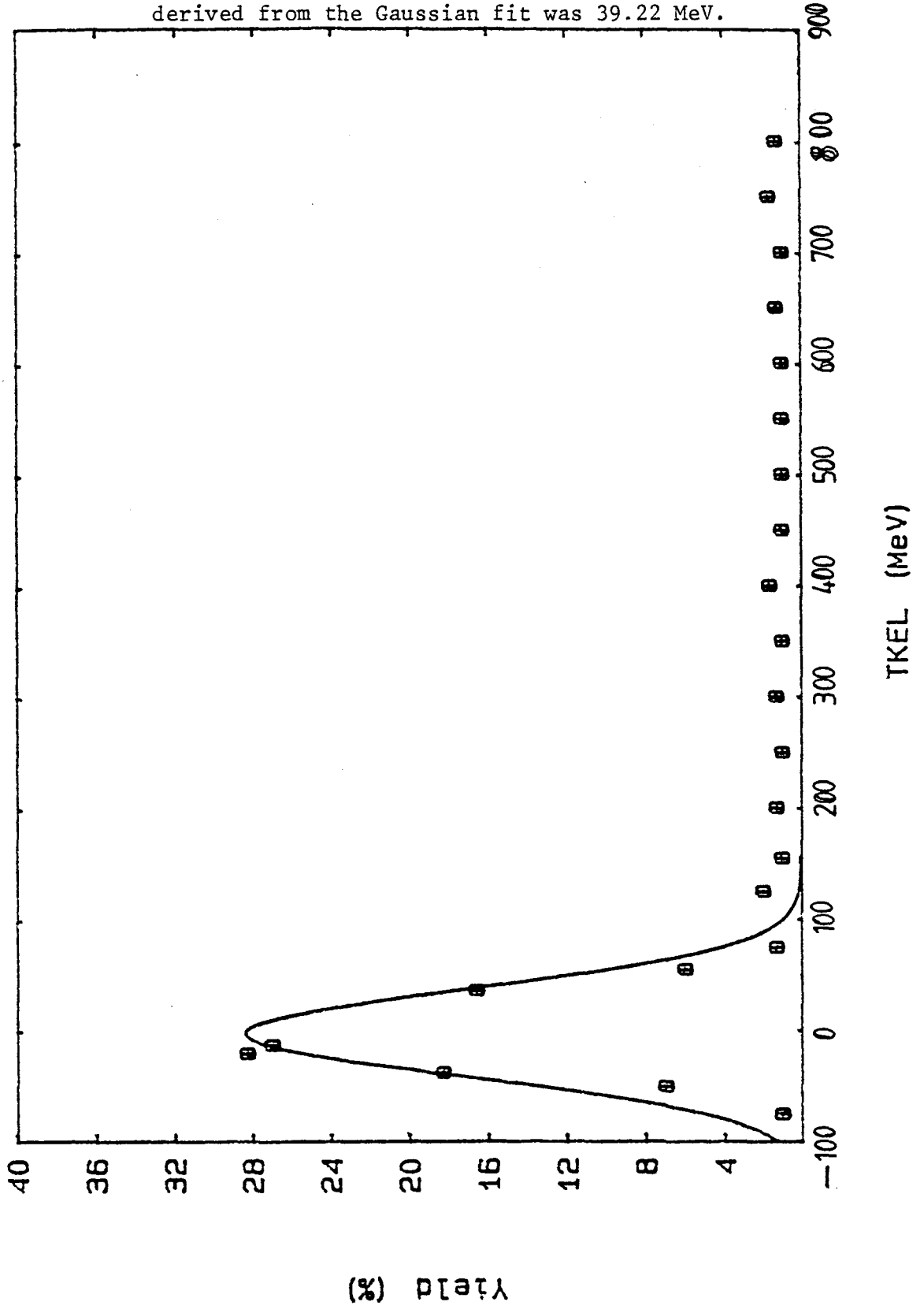

Fig. 8.14 Distributions of calculated total mass in the two- and three-body exit channels from the U & Au reaction. The solid lines refer to Gaussian fits with (a) $\sigma_{2\text{-prong}}$ = 41 amu and (b) $\sigma_{3\text{-prong}}$ = 78.9 amu, respectively.

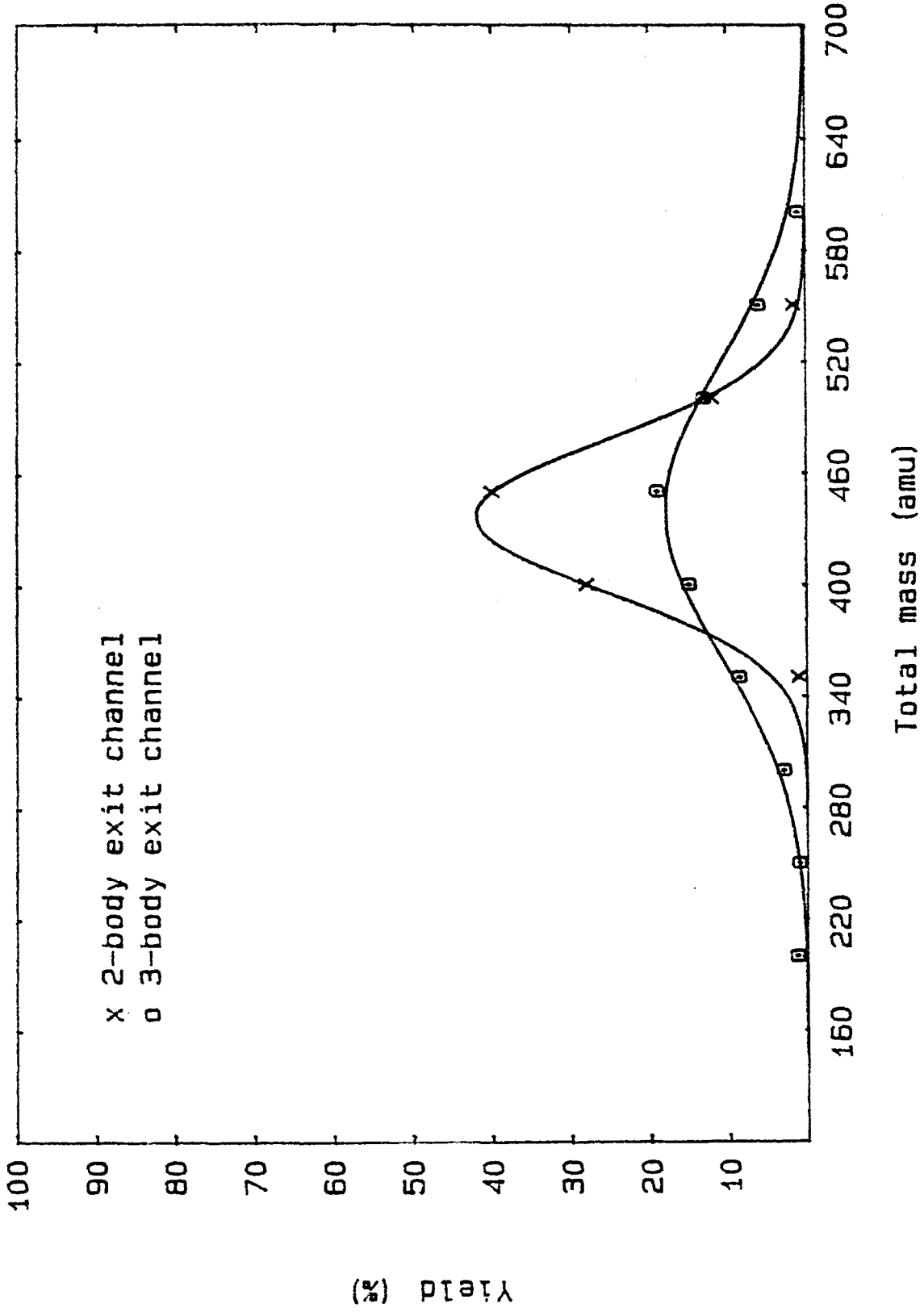

Fig. 8.15 Distribution of individual fragment masses of two-pronged events resulting from elastic scattering in the Au + U reaction. From the Gaussian fit for light and heavy masses, the centroid of the peaks are at 198.66 and 240.66 amu. These values are very close to the initial masses of the target and projectile, respectively. The experimental dispersion determined from the

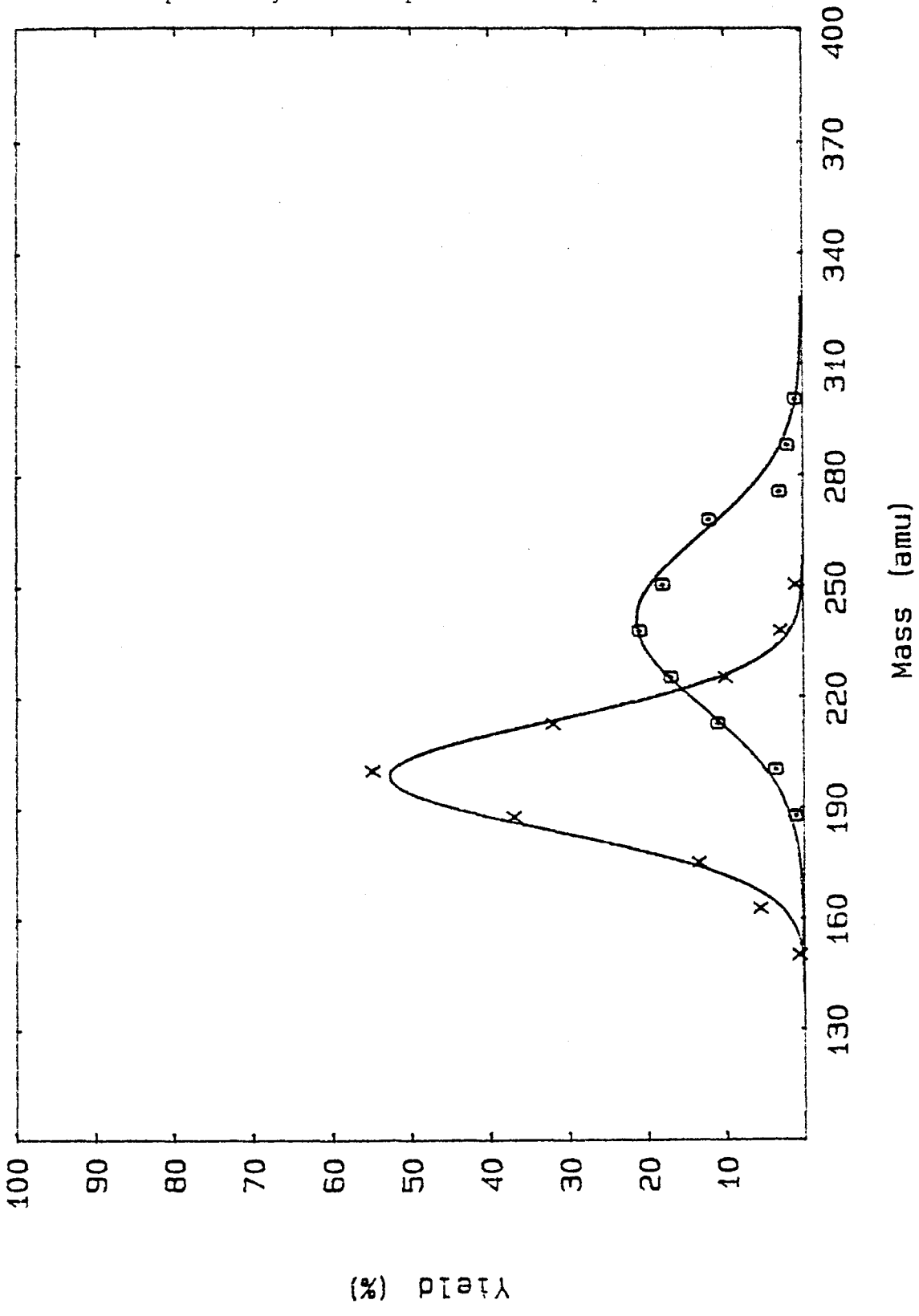

Gaussian fits are, σ_L = 14.89 amu and σ_H = 23.39 amu.

ion reactions. Heavy Ion collisions, volume 2, chapter 5, edited by R. Bock. North-Holland, Amsterdam, New york, Oxford (1980)

3 Kaufmann r., Wolfgange R., Phys. Rev. Lett. 3, 232-234 (1959)

4 Kaufmann R., Wolfgang R., Phys. Rev. Lett. 121, 192-205 (1961)

5- GSI-scientific report J-1-77

6 Norenberg W., Basic concepts in the description of collisions between heavy nuclei, Heavy IOn Collissions, volume 2, chapter 1, edited by Bock R., North-Holland, Amsterdam, New york, Oxford (1980)

7 Richter A. and C. Toepffer, Elastic and Inelastic heavy ion scattering. Heavy Ion Collisions, volume 1, chapter 1-2, edited by R. Bock. North-Holland, Amsterdam, New york, Oxford (1980)

8 Pelte D. and D. Schwalm, In-beam gamma-ray spectroscopy with heavy ions, Heavy Ion Collisions, volume 3, chapter 1, edited by R. Bock, North-Holland, Amsterdam, New York, Oxford (1980).

9 Lefort M., The critical distance of approach. Heavy Ion Collisions, volume 2, chapter 2-3, editted by R. Bock (1980)

10 Mosel U., Fusion and fission of heavy nuclei. Heavy Ion Collisions, volume 2, chapter 4, editted by R. Bock (1980)

11 Oberacker V., Holmtt., Scheid W., Phys. Rev. C 10, 1917(1974)

12 Diehl H., Greiner W., Nucl. Phys. A 229, 29(1974)

13 Deubler H.H., Dietrich K., Phys. Lett. 62 B, 369(1976)

14 Gottschalk P.A., Vater P., Becker H.j., Brandt R., Grawert G., Fiedler G., Haag R., Rautenberg T., Phys. Rev. Lett. 42, 359(1979)

17 Glassel P., Harrach D.V., Specht H.j., Grodzins L. Z., Phys. Rev. 310, 189(1983).

15 Debeauvais M., J. Ralarosy, J. Tripier, S. Jokic, Nucl. Tracks 8, 515(1984)

16 Vater P., E.U. Khan, R. Beckmann and R. Brandt, Nuc. Tracks 8, 541(1984)

18 Fleischer R.L., Price P.B., Walker R. M., Nuclear Tracks in Solids.

University of California Press(1975)

19 Khan E.N., Vater P., Brandt R., Khan H.A., Jamil K., Khan N.A., Sial M.A. communications CEA-N-2406 , 40 (1984)

20 Gottschalk, P.A., P. Vater, H.J. Becker, R. Brandt, G. Grawert, Phys. Rev. c27, 2703 (1983)

21- Clenshaw C.W. and J.G. Hayes. J. Inst. Maths. Applicas., 1, 164 (1965)

22- Curve and Surface fitting, NAGFLIB:1635/0:MK7 (1978)

23- Frahn W.E. Phys. Rev. Lett. 26, 568(1971)

24- Wilcke W.W., Birkelvnd J.R., Wollersheim H.J., Hoover A.D., Huizenga J.R., Schroder W.U., Tubbs L.E., Atomic Data and Nuclear Data Tables 25, 389(1980)

CHAPTER 9

Conclusions and Suggestion for Further Work:

This work has been mainly concerned with various aspects of fission in ^{238}U to gain both a better insight into the mechanism of fission but also to try and enhance the data base for fission in this nuclide. We did, however, extend the project to a brief study of ternary events in the spontaneous fission of ^{252}Cf as both an initial test of the equipment and electronics and to try and solve a specific problem. Also we considered heavy ion reactions other than those involving ^{238}U so as to provide data for a further understanding of these very high momentum reactions.

We have been able to determine the absolute cumulative yield of 33 fission products at five neutron energies. In very many cases there was only one previously published value for the fission yield and often these data were reported with dubious or unsupported error estimates. These new data allowed us to establish an emperical equation between yields of fission products and neutron energy. This equation was then used for the prediction of reactor neutron fission yields. The predicted fission yields were in good agreements with reported values.

The angular distribution of the products of binary fission were determined from monoenergetic neutron induced fission of ^{238}U in first-, second- and third-chance fission. A least-squares fit, based on an expansion of the Legendre polynomials of degree three of the even terms was applied to the experimental data. The values of the anisotropy ratio, R, were deduced from the best-fit distributions. In first-chance fission, on comparing the experimentally determined angular distributions of the fission yields with those predicted

theoretically, it was clear that, at most neutron energies the bands of the compound nuclei immediately preceding fission were predominantly in the K=1/2 states. The principal exception to this finding appeared to occur at neutron energies around 1.40 MeV. At these energies the fission anisotropy, R, reached a local minimum and the angular fission distribution exhibited a behaviour characteristic of both K=1/2 and K=3/2 band states. In the neutron energy range E_n=2 to 5 MeV, the fission anisotropy, R, remained approximately constant but began to increase at higher energies, peaking at E_n=6 MeV. This corresponds to the threshold energy for second-chance fission, (n,n'f). In the neutron energy range above 12 MeV, where third-chance fission is energetically possible, there are also contributions from first- and second- chance fission. The anisotropy coefficient, A_2, for third-chance fission for neutron energies above 12 MeV was calculated and used for determing the total fission anisotropy, R, as a function of neutron energy in the range 13.5-17.7 MeV. Our experimentally determined values of R in this energy range were in good agreement with the calculated values, except at 15.5 MeV, where the experimental value appears to be slightly too high.

We then turned to the question of ternary fission. The yields of tritons and alpha particles from ^{238}U and ^{252}Cf were determined by detector telescope techniques. The determination of the yield of tritons in the monoenergetic-neutron-induced fission of ^{238}U was very difficult and these measurements provided the first experimental determination of this parameter. The experiment produced a rather unexpected result for tritons in that the yield was found to be 16 to 18 % of alpha-particles. If this is confirmed it indicates that tritium production is not as high as reported by Buzzelli etal[1] for the reactor-neutron-induced fission of ^{238}U[2] but is three times higher than his figure for its production in the

thermal-neutron-induced-fission of $^{235}U^{2}$. This high yield of tritium will require serious consideration for the development of fast breader ractors in which natural uranium is used as the fuel. This high yield of tritium also gives rise to an increase environnmental hazard for such reactors as compared with thermal ones. The determination of LRA particle yields in the fission of ^{238}U in this work indicates that there is a better correlation of LRA particle yield with Z^2/A than that previously reported by Harphern[3]. The results for LRA particle yield obtained in our experiments and the other reported data, discussed in Chapter six indicate a weak dependence of yield with excitation energy.

Although the telescope technique produced reasonably accurate data, its operation in the high neutron flux resulted in the E detector suffering damage quite rapidly. Due to the small size of the ΔE detector, the statistical error in the determination of triton and LRA particle yields was high. Any further investigations of triton yield due to ternary fission of fertile material would seem to require the development of alternative detector systems. Such a system could be based on double ionsation chambers as suggested by reference 4. These chambers would have the distinct advantage of not suffering from neutron damage. In adition it would be possible to make the fertile foil the window in such chambers and so provide a large solid angle for the detection.

With the present design of vacuum chamber used in the ternary experiments it would be possible to determine the mass distribution of fission products in fertile and fissile materials by time of flight techniques.

In the ternary fission study of ^{252}Cf, the yield and energy spectra and their FWHM for tritons and LRA-particles were determined by the detector telescope techniques. The energy spectrum of LRA in Cf had a

cut-off energy due to the thickness of the ΔE detector. The LR115 Solid State Nuclear Track detector, with a combination of Al degrader foils was used to determine the lower tail of the LRA-particle energy distribution down to energies of less than 2 MeV. The energy spectrum obtained by this method showed a clear Gaussian distribution and there was no significant deviation from this distribution. This result shows that the suggestion of the emission of low energy alpha-particles accompanying the LCPs in the ternary fission of ^{252}Cf is not correct. It indicates also that there is no need to apply a 6% correction to the LRA-energy spectrum to allow for the yield of these particles as suggested by reference 5 in investigation of the LRA-energy spectrum obtained in thermal neutron-induced fission of ^{235}U.

The CRAY version of the computer code, GD, originally obtained from the Los Alamos National Lab.[6], was modified and several subroutines in the program completly re-written to make it executable on the μVAX-II computer in the Physics Department Radiation Centre. This program takes into account the complete decay and growth of nuclides in a given chain and could be used for the determination of independent fission yields.

It was established in the work on heavy-ion fission (Chapter 8) that an emperical relationship exists between the velocity, mass and track length in mica detectors. This would then enable one to determine chain yields of fission products. In addition the relationship could be modified to take into account the atomic numbers of the fission products. Such a modification would allow the determination of independent fission yields for fission products having very short half-lives (less than one second). These short half-life fission products cannot be determined by current techniques. In Chapter eight, the interaction of heavy ions such as U, Pb and La with a gold target was studied. These are beleived to be the fist such

studies undertaken here. Several computer programs were developed for the analysis of the data. Mica and CR-39 solid state track detectors in 2π-geometry were used for identifying the fission products. The spherical co-ordinates of the correlated tracks were measured, event by event and these were used in the analyses of data. The experimental, total reaction cross sections were determined using two, independent methods for a 14 MeV/amu uranium beam on a gold target. The total number of ternary and quarternary events yielded cross sections of 3360 mbarn and 3500 mbarn with the mica and CR-39 detector, respectively. The quarter point angle was used to obtain a total reaction cross section of 33.1°, 24.9° and 44.1° for the bombardment of the gold target with uranium, ^{208}Pb and ^{139}La, respectively from the elastic scattering data. These experimentally determined cross sections were found to be in good agreement with the theoretical reaction cross section. The cross sections obtained by CR-39 and mica for uranium on the gold target were not the same due to the difference in the registration threshold of the two detectors. This result suggests that light particles having masses between 4 amu and 30 amu have a high probability of emmision in this reaction. The colliding nuclei exchange a large amount of mass in these reactions. This exchange is correlated with a large fraction of relative kinetic energy which is dissipated into intrinsic excitation energy. Therefore, two highly excited, intermediate nuclei are created. These intermediate nuclei rotate, due to the angular momentum transfer during a grazing collision and may undergo fission in a second step. As a result the three or four pronged tracks were produced. Sometimes, however, neither intermediate nuclei undergoes fission and this therefore results in just a two pronged track, equivalent to a binary fission event. Any theoretical model that is developed should address itself to the following questions. What is the correlation between

energy damping in fission, mass exchange and angular momentum transfer? What kind of forcess cause these exchanges and what are the time scales of the different reaction steps?

There are inherent limitations with the technique used here. The accuracy of the method is limited because of the uncertainties in the kinematical determination of masses and energies due to the inherent range-energy relationship of the reaction products in the stopping material (SSNTD). Consequently, the method does not yield quantitative results with high accuracy. The main advantage of the technique, however, is in its ability to show the gross features of heavy ion reactions. Higher accuracy will require the use of sophisticated, electronic telescope devices such as those described in Chapter six for the determination of LCPs in the ternary fission of ^{238}U.

References:

1- Buzzelli G.,S.Langer, C. Jones, B. Gainey, Transactions, Amc. Nucl. Soc. 24, 458(1976)

2- Wagemans, P. Dhoundt, P. Schilebeeckx, R. Brissot, Phys. ReV. C33, 943(1986)

3- Halpern I., Annu. Rev. Nucl. Sci. 21,245.

4-

5- Caitucoli F., B. Leroux, G. Barneau, N. Carjan, T. Benfoughal, T. Doan, F. El Hage, A. Sicre, M. Asghar, P. Perrin and G. Siegert, Z. Phys. A298, 219 (1980).

6- Ford G.P., Los Alamos National Laboratory, Los Alamos, New Mexico, private communication.

Appendix 1

Calculation of Solid angle:

In the general case of extended sources, the solid angle Ω is defined by

$$\Omega = \frac{\text{number of particles per second emitted inside the space defined by the contours of the source and the detector aperture}}{\text{number of particles per second emitted by the source}}$$

Having a plane source of area A_S which emitting s_o particles/cm².sec, isotropically, is located a distance d away from a detector with an aperture equal to A_d (see Figure app1-1). Applying the definition given by equation app1-1 for the two differential areas dA_S and dA_d and integrating, one obtains

$$\Omega = \frac{\int_{A_d}\int_{A_S} (S_o dA_S/4\pi r^2) dA_d(\vec{n}.\vec{r}/r)}{S_o A_S} \qquad \text{app 1-2}$$

where n is a unit vector normal to the surface of the detector aperture. since n.r/r = cos ω, Eq. app1-2 takes form

$$\Omega = \frac{1}{4\pi A_S} \int_{A_S} dA_S \int_{A_d} dA_d \frac{\cos\omega}{r^2} \qquad \text{app 1-3}$$

consider a disc source parallel to a detector with a circular aperture (see Fig. app1-2). The Eq. app1-3 becomes in terms of Bessel function[1]

$$\Omega = s \int_0^\infty d_x\, e^{-xz} \frac{J_1(x)}{x} J_1(xs) \qquad \text{app 1-4}$$

where s= R_d/R_S, Z= d/R_S, and $J_1(X)$ = Bessell function of the first kind. If R_d/d and R_S/d are less than 1, the following algebraic is obtained for solid angle

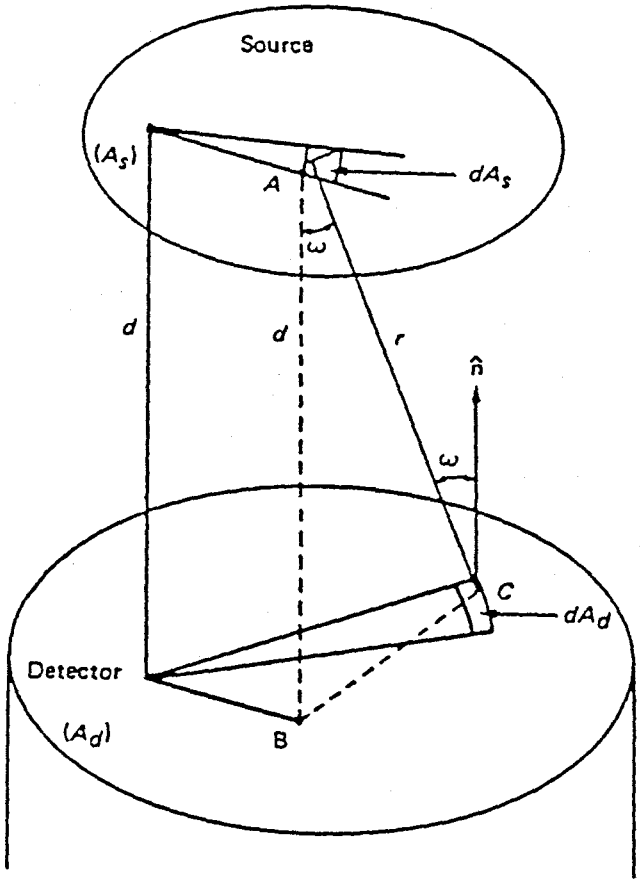

Fig. App 1-1 Definition of the solid angle for a plane source and a plane detector parallel to the source.

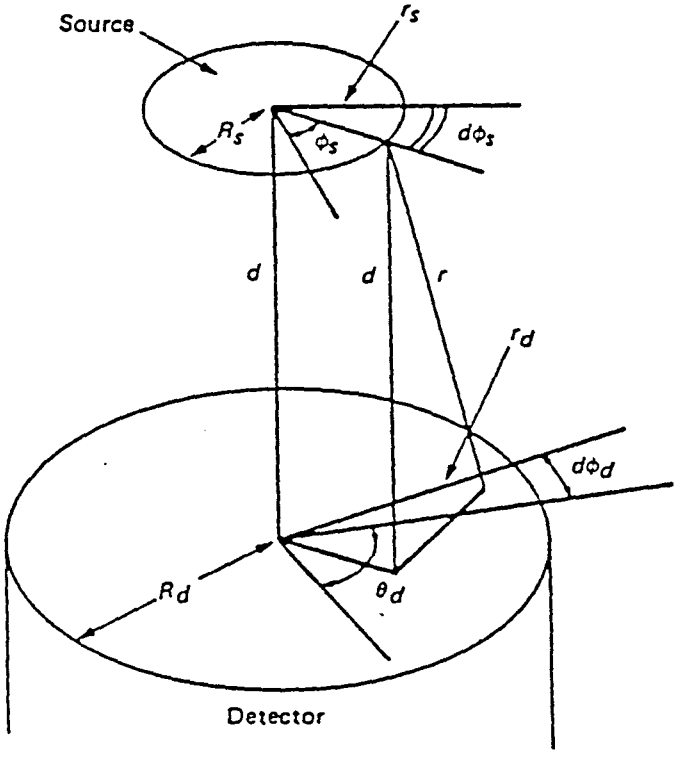

Fig. App 1-2 A disk source and a detector with a circular aperture.

$$\Omega = \frac{\omega^2}{4}\{1 - \frac{3}{4}(\psi^2+\omega^2) + \frac{15}{8}(\frac{\psi^4+\omega^4}{3} + \psi^2\omega^2) - \frac{35}{16}[\frac{\psi^6+\omega^6}{4} + \frac{3}{2}\psi^2\omega^2(\omega^2+\psi^2)]\}$$

where $\theta = R_s/d$ and $\omega = R_d/d$. In the case of two non-parallel discs, an approximate expression for solid angle is as following

$$\Omega = \frac{\omega^2}{4}\{1 - \frac{3}{4}[(\psi^2+\omega^2(1+\sin^2\theta)] + \frac{15}{8}[\frac{\omega^2+\psi^2}{3} + \psi^2\omega^2+\omega^2(1+\frac{1}{4}\omega^2+\frac{2}{3}\psi^2)\sin^2\theta]\}$$

where θ is the angle between the planes of the two discs.

Reference:

1 Ruby L. and J. B. Rechen, Nucl. Instr. Meth. 58,345 (1968)

Appendix 2

```
      DOUBLE PRECISION AMAT(6,12),YEXSUM(6),COEFF(6),XPT(6),WK
     1,XPON1,XPON2,XPON3,AII,AKI
C
C    RUN,AFSJO,LU,LUOUT,IRR
C    IRR=0 RUN WITHOUT IRRADIATION TIME
C    IRR=1  =   WITH       =        =
C                  DATA        IS        READ        IN        FORM
X(I),Y(I),YMSD(I),XST(I),XIR(I),AMASS(I),FCR(I)
C                          X(I),Y(I),YMSD(I)
C                      OR X(I),Y(I)
      DIMENSION X(64),Y(64),YCALC(64),YMSD(64),XST(64),YM(64)
      DIMENSION AMASS(64),XIR(64), IH(5),RLAM(6),HL(6)
      DIMENSION FCR(64),ACT(64),ACTI(64),YE(64),YED(64),A(6)
      DIMENSION RADT(3),RFAC(3),RDEC(3),SATF(3),TXCT(6),PRDR1(6)
      DIMENSION PRDR2(6),TPROD(6),GRY(6)
      CHARACTER*30 NAME
      DATA AMAT/72*0.0D0/,YEXSUM/6*0.0D0/,COEFF/6*0.0D0/
      DATA X/64*0.0/,Y/64*0.0/,YCALC/64*0.0/,YMSD/64*1.0/
C
      LUIN=5
      LUOUT=3
      IRR=IH(3)
      OPEN(UNIT=3,FILE='AFEXP.DAT',STATUS='NEW')
      WRITE(LUIN,11)
   11 FORMAT('$NO. OF HALF-LIVES    ')
      READ(*,*)NHL
      DO 22 I=1,NHL
      WRITE(*,18)I,I
   18 FORMAT(' HALF-LIFE ',I,' GAMMA RAY YIELD',I )
      READ(*,*)HL(I),GRY(I)
   22 CONTINUE
    GRY(I+1)=1
C  11 FORMAT('$HALF-LIF1,HALF-LIFE2,HALF-LIFE3   ')
C       READ(LUIN,*)HL(1),HL(2),HL(3)
      DO 13 JJ=1,NHL
      RLAM(JJ)=0.693/HL(JJ)
      WRITE(LUIN,191)RLAM(JJ),HL(JJ)
      WRITE(LUOUT,191)RLAM(JJ),HL(JJ)
  191 FORMAT(2X,F12.6,4X,F12.6)
   13 CONTINUE
C     ABSOLUTE CONTING EFFICIENCY  CALCULATION DATA
      A(1)=120.8E-4
      A(2)=6.151E-4
      A(3)=284.7E-4
      A(4)=4.754E-3
      A(5)=-5.915E-3
      A(6)=5.798E-4
      WRITE(LUIN,188)
  188 FORMAT(2X,'GAMMA RAYS ENERGY (KEV)  ')
      READ(LUIN,*)Z
      CEFF=0
      DO  3 I=1,3
      CEFF=CEFF+A(2*I-1)*EXP(-A(2*I)*Z)
    3 CONTINUE
      WRITE(LUIN,12)
   12 FORMAT('$BRANCHING RATIO  ')
      READ(LUIN,*)BR
```

```
      WRITE(LUIN,189)
  189 FORMAT('$IF YOU SUPPLIED IRRADITION TIME TYPE 1 ELSE  0
')
      READ(LUIN,*)IRR
      WRITE(LUIN,192)CEFF,BR
  192 FORMAT(2X,F6.5,4X,F6.3)
      WRITE(LUOUT,192)CEFF,BR
C       PROGRAM TO FIT THE AMPLITUDE OF SIX PREDETERMINED
EXPONENTIALS
C     TO EXPERIMENTAL FISSION YIELD DATA
C
C   256 POINTS MAXIMUM
C
C   RLAM=DECAY CONSTANT OF NUCLID
C   XIR(K)=IRRADITION TIME
C   X(K)=DECAY TIME
C   AMASS(K)=WEIGHT OF FOIL IN GRAMMMS
C   XST(K)=COUNTING TIME
C   FCR(K)=RATE OF TOTAL FISSION PODUCTION
      WRITE(LUIN,10)
   10 FORMAT('$DATA INPUT MODE?'/' 0 = THIS TERMINAL'/
     1' 1 = DATA FILE')
      READ(LUIN,*)LUDIN
      IF(LUDIN.NE.1)GOTO 100
      WRITE(LUIN,20)
   20 FORMAT('$DATA FILE NAME  ')
      READ(*,FMT='(Q,A)')LN,NAME(1:LN)
C      READ(LUIN,30)NAME
C  30 FORMAT(3A2)
      LUDIN=2
      OPEN(UNIT=LUDIN,FILE=NAME(1:LN),STATUS='OLD')
      GOTO 200
  100 IF(LUDIN.EQ.0)LUDIN=LUIN
  200 WRITE(LUIN,40)
   40 FORMAT('$NO. OF PTS  ')
      READ(LUIN,*)NPTS
      WRITE(LUIN,831)
  831 FORMAT('$TIMESTEP OPTION (0=CONSTANT,1=VARIABLE) ')
      READ(LUIN,*)ITSOP
      IF(ITSOP.EQ.0)WRITE(LUIN,892)
  892 FORMAT('$TIMESTEP (SECS) ')
      IF(ITSOP.EQ.0)READ(LUIN,*)XSTCON
      XSTCON=XSTCON/NPTS
      DO 675 I=1,NPTS
      IF(ITSOP.EQ.0)XST(I)=XSTCON
  675 CONTINUE
      NXP=NHL
C       WRITE(LUIN,50)
C   50 FORMAT('$NO. OF EXPONENTIALS TO FIT (<=6) ')
C       READ(LUIN,*)NXP
      WRITE(LUIN,55)
   55 FORMAT('$S.D. AVAILABLE (1=YES,0=NO)  ')
      READ(LUIN,*)ISDOP
      IF((LUDIN.EQ.5).OR.(LUDIN.EQ.25))WRITE(LUIN,60)
   60 FORMAT('$INPUTING DATA')
      IF(LUDIN.EQ.LUIN)WRITE(LUIN,70)
   70 FORMAT('$ENTER DATA FROM KEYBOARD')
      DO 300 I=1,NPTS
      IF(LUDIN.EQ.LUIN)WRITE(LUIN,80)I
   80 FORMAT('$POINT ,I3,')
```

```
C
IF(ISDOP.EQ.1.AND.ITSOP.NE.0)READ(LUDIN,*)X(I),Y(I),YMSD(I),XST(I)
C     1,AMASS(I)
C       IF(ISDOP.EQ.1.AND.ITSOP.EQ.0)READ(LUDIN,*)X(I),Y(I),YMSD(I)
C       IF(ISDOP.NE.1.AND.ITSOP.NE.0)READ(LUDIN,*)X(I),Y(I),XST(I)
C       IF(ISDOP.NE.1.AND.ITSOP.EQ.0)READ(LUDIN,*)X(I),Y(I)
        IF(ISDOP.NE.1) GO TO 85
        IF(ITSOP.NE.0) GO TO 83
        READ(LUDIN,*)X(I),Y(I),YMSD(I),AMASS(I)
        WRITE(LUIN,2502)X(I),Y(I),YMSD(I),AMASS(I)
 2502 FORMAT(2X,F7.2,2X,G13.5,2X,F6.2,4X,F7.5)
        GO TO 300
  83    IF(IRR.EQ.1) GO TO 84
        READ(LUDIN,*)X(I),Y(I),YMSD(I),XST(I),AMASS(I)
        WRITE(LUOUT,2503)X(I),Y(I),YMSD(I),XST(I),AMASS(I)
 2503 FORMAT(2X,F7.2,2X,G13.5,2X,F6.2,2X,F8.3,3X,F7.5)
        GO TO 300
  84    READ(LUDIN,*)X(I),Y(I),YMSD(I),XST(I),XIR(I),AMASS(I),FCR(I)

WRITE(LUOUT,2504)X(I),Y(I),YMSD(I),XST(I),XIR(I),AMASS(I),FCR(I)
 2504 FORMAT(2X,F7.2,2X,G13.5,2X,F6.2,2X,F6.2,2X,F8.3,2X,F6.5,2X,G13.6)
        GO TO 300
  85    IF(ITSOP.NE.0) GO TO 86
        READ(LUDIN,*)X(I),Y(I)
        WRITE(LUOUT,2505)X(I),Y(I)
 2505 FORMAT( 2X,F7.2,2X,G13.5)
        GO TO 300
  86    IF(IRR.EQ.1)GO TO 87
        READ(LUDIN,*)X(I),Y(I),XST(I),AMASS(I)
        WRITE(LUOUT,2507)X(I),Y(I),XST(I),AMASS(I)
 2507 FORMAT(2X,F7.2,2X,G13.5,2X,F6.2,4X,F7.5)
        GO TO 300
  87    READ(LUDIN,*)X(I),Y(I),XST(I),XIR(I),AMASS(I),FCR(I)
        WRITE(LUOUT,2506)X(I),Y(I),XST(I),XIR(I),AMASS(I),FCR(I)
 2506 FORMAT(2X,F7.2,2X,G13.5,2X,F6.2,2X,F8.3,2X,F6.5,2X,G13.3)
  300 CONTINUE
C
        WRITE(LUIN,809)
  809 FORMAT('DATA INPUT FINISHED')
C
        M=NXP+1
        DO 900 K=1,NPTS
        YM(K)=Y(K)/AMASS(K)
        WK=1.0/YMSD(K)
        WK=WK*WK
        WRITE(LUIN,2501)YM(K),Y(K),AMASS(K)
 2501 FORMAT(2X,G17.6,2X,G13.5,2X,F6.5)
        DO 342 JJ=1,M
        XPT(JJ)=0.0
        IF(JJ.EQ.M)GOTO 17
        XPON1=RLAM(JJ)*X(K)
        WRITE(LUIN,2509) XPON1
 2509 FORMAT(2X,G13.5)
        XPON2= RLAM(JJ)*XST(K)
        IF(IRR.EQ.0) GO TO 16
        XPON3=RLAM(JJ)*XIR(K)
        IF(XPON1.LT.20.0)XPT(JJ)=DEXP(-XPON1)*(1.0-DEXP(-XPON2))*
       1(1.0-DEXP(-XPON3))*(GRY(JJ)/RLAM(JJ))
        GO TO 341
```

```
IF(XPON1.LT.20.0)XPT(JJ)=DEXP(-XPON1)*(1.0-DEXP(-XPON2))*(GRY(JJ)
     1/RLAM(JJ))
      GOTO 341
   17 XPT(JJ)=1.0
  341 CONTINUE
      WRITE(LUIN,2508)XPT(JJ)
 2508 FORMAT(2X,G13.5)
  342 CONTINUE
      DO 800 I=1,M
      AMAT(I,I+M   )=1.0
      DO 600 J=1,M
      AMAT(I,J)=AMAT(I,J)+WK*XPT(I)*XPT(J)
  600 CONTINUE
      YEXSUM(I)=YEXSUM(I)+WK*YM(K)*XPT(I)
  800 CONTINUE
  900 CONTINUE
C
C
      WRITE(LUIN,2500)YEXSUM(I)
 2500 FORMAT(2X,F17.6)
C
      DO 130 I=1,M
      AII=AMAT(I,I)
      DO 111 J=1,2*M
      AMAT(I,J)=AMAT(I,J)/AII
  111 CONTINUE
      DO 120 K=1,M
      IF(K.EQ.I)GOTO 120
      AKI=AMAT(K,I)
      DO 110 J=1,2*M
      AMAT(K,J)=AMAT(K,J)-AKI*AMAT(I,J)
  110 CONTINUE
  120 CONTINUE
  130 CONTINUE
C
C
C
      DO 210 I=1,M
      DO 201 J=1,M
      COEFF(I)=COEFF(I)+AMAT(I,J+M   )*YEXSUM(J)
  201 CONTINUE
      IF(I.NE.M) WRITE(LUOUT,205)COEFF(I),I
      IF(I.EQ.M) WRITE(LUOUT,206)COEFF(I)
C 205 FORMAT(2X,G13.6,4X,'EXP(-RLAM(',I1,')*X)')
     205  FORMAT(2X,G17.6,4X,'CONCENTRATION  OF  NUCLID  WITH
RLAM(',I1,')')
  206 FORMAT(2X,G13.6,4X,'BGRND LEVEL')
  210 CONTINUE
C
C
C
      WRITE(LUOUT,305)
  305 FORMAT(1X,//8X,' XDATA',6X,'YDATA',6X,'YCALC',9X,'DIFF'
     1,5X,'DIFF/SD'/)
      CHISQ=0.0
      DO 320 K=1,NPTS
      DO 432 JJ=1,M
      XPT(JJ)=0.0
      IF(JJ.EQ.M)GOTO 77
      XPON1=RLAM(JJ)*X(K)
```

```
      XPON2=     RLAM(JJ)*XST(K)
      IF(IRR.EQ.0) GO TO 76
      XPON3=RLAM(JJ)*XIR(K)
      IF(XPON1.LT.20.0)XPT(JJ)=DEXP(-XPON1)*(1.0-DEXP(-XPON2))*
     1(1.0-DEXP(-XPON3))*(GRY(JJ)/RLAM(JJ))
      GO TO 431
                                                                  76
IF(XPON1.LT.20.0)XPT(JJ)=DEXP(-XPON1)*(1.0-DEXP(-XPON2))*(GRY(JJ)
     1/RLAM(JJ))
      GOTO 431
   77 XPT(JJ)=1.0
  431 CONTINUE
  432 CONTINUE
      DO 310 J=1,M
      YCALC(K)=YCALC(K)+COEFF(J)*XPT(J)
  310 CONTINUE
      CHISQ=CHISQ+((YCALC(K)-YM(K))/YMSD(K))**2
      DIFF=YCALC(K)-YM(K)
      SD=DIFF/YMSD(K)
      WRITE(LUOUT,315)X(K),YM(K),YCALC(K),DIFF,SD
  315 FORMAT(3X,5(G12.2,2X))
  320 CONTINUE
      CHIDOF=CHISQ/(NPTS-M   )
C
      WRITE(LUOUT,986)
     986  FORMAT(2X////10X,'COV  MATRIX  (NOT  MULTIPLIED  BY
CHISQ/DOF)'//)
      DO 973 I=1,M
      WRITE(LUOUT,405)(AMAT(I,J),J=M+1,2*M)
  405 FORMAT(6(1X,G12.2,3X))
  973 CONTINUE
      WRITE(LUOUT,987)
  987 FORMAT(2X////10X,'COV MATRIX (MULTIPLIED BY CHISQ/DOF)'//)
      DO 430 I=1,M
      DO 420 J=M+1,2*M
      AMAT(I,J)=CHIDOF*AMAT(I,J)
  420 CONTINUE
  430 CONTINUE
      DO 974 I=1,M
      WRITE(LUOUT,405)(AMAT(I,J),J=M+1,2*M)
  974 CONTINUE
      WRITE(LUOUT,435)CHIDOF
  435 FORMAT(1X//1X,'CHISQ/DOF = ',G15.6)
      ZFAC=CEFF*BR
      IF(IRR.EQ.0) GOTO 998
      DO 999 I=1,NXP
C       ZFAC(I)=GRY(I)*CEFF*BR
      ACT(I)=COEFF(I)/ZFAC
      WRITE(LUIN,2516)ACT(I)
 2516  FORMAT(2X,'ACT=',G13.5)
      ACTI(I)=ACT(I)
      WRITE(LUIN,2517)ACTI(I)
 2517 FORMAT(2X,'ACTI=',G13.5)
      YE(I)=ACTI(I)/FCR(I)
      WRITE(LUIN,2518)YE(I)
 2518 FORMAT(2X,'YE(I)=',F8.6)
      YED(I)=YE(I)*100
      WRITE(LUOUT,440)I,ACTI(I)
  440 FORMAT(1X//1X,'ACTIVITY PER GARAMM (',I1,')=',G15.6)
      WRITE(LUOUT,445)I,YED(I)
```

```
  445 FORMAT(1X//1X,'YIELD OF NUCLIDE(',I1,')=',G15.6)
  999 CONTINUE
      GO TO 131
c       in the case of two stage irradiation
  998  WRITE(*,23)
   23  FORMAT('$TYPE IN FISSION CHAMBER COUNT RATES IN EACH
STAGE ')
      READ(*,*)FCR1,FCR2
      WRITE(*,32)
     32   FORMAT('$TYPE IN FIRST IRRADIATION TIME(MINS),WAIT
TIME(MINS)
     1,SECOND IRRADIATION TIME (MIN)')
      READ(*,*)RADT(1),RADT(2),RADT(3)
      DO 122 I=1,3
      RFAC(I)=RLAM(I)*RADT(I)
      RDEC(I)=EXP(-RFAC(I))
      SATF(I)=(1.0-RDEC(I))
      ALF=FCR1/FCR2
      AB=RDEC(2)*RDEC(3)
      AC=ALF*AB*SATF(1)
      AD=AC+SATF(3)
  122 CONTINUE
      DO 131  I=1,NXP
      ZFAC=CEFF*BR
      TXCT(I)=COEFF(I)/ZFAC
      ACT(I)=TXCT(I)
      PRDR2(I)=ACT(I)/AD
      PRDR1(I)=ALF*PRDR2(I)
      TPROD(I)=(PRDR1(I)*RADT(1))+(PRDR2(I)*RADT(3))
      TFC=(FCR1*RADT(1))+(FCR2*RADT(2))
      YE(I)=TPROD(I)/TFC
      YED(I)=YE(I)*100
      WRITE(LUOUT,445)I,YED(I)
  131 CONTINUE
      STOP
      END
```

Appendix 3

The basic discovery of the technique known as solid state nuclear track detection (SSNTD) goes back to 30 years ago when, first Young[1] described the etched shallow pits of fission fragments in lithium fluoride, and then Silk and Barns[2] published transmission electron micrographs (TEM) of linear damage trails in thin mica sheets which had previously been bombarded by fission fragments from ^{238}U fission. Most of the early development work was carried out by a pioneering team consisting of Fleischer, Price and Walker[3], all then working at the General Electric Laboratories at Schenctady, New York.

Etching Procedure

In order to reveal the latent tracks produced due to the charged particles or fission fragment, a polymer degrader (etchent), is used, which removes the damaged part of the material more rapidly than the undamaged part. This enhances the dimension of tracks, which helps to distinguish the tracks more easily under an optical microscope. The etchant solution (NaOH, KOH, HNO_3, etc.) is set to the required temperature, and in order to avoid rapid changes of the solution normality through the evaporation of water, the solution beaker should

be covered. The process should be continous, because interrupted etching is different from continuous etching. For isotropic etching, samples are usually fixed in springs, and these springs are then put in the etchant. After finishing the etching , the samples should be washed in running water for some 10–30 min. The water quickly stops any further etching and removes any etchant from the tracks. Finally, samples are washed in distilled water using an ultrasonic bath.

References:

1 Young D.A., Nature 182, 375–377

2 Silk E.C.H., R.B. Barners, Phil. mag. 4, 970 (1959)

3 Fleischer R.L., P.B. Price and R.M. Walker, Nuclear Tracks in solids. University of Californica press 1975.

Appendix 4

Fission Angular distribution:

In 1956 a suggestion was made by A. Bohr that low energy fission may be understood in terms of a few levels in the transition nucleus. When the excitation energy of the compound nucleus is approximately equal to the fission barrier, fission occurs through one or only a few channels. A study of fission fragment angular distribution provided some information on the properties of these transition levels. Let us assume that fission fragments separate along the nuclear symmetry axis and that K (the projection of J on the nuclear symmetry axis) is a good quantum number in the passage of a nucleus from its transition state to the configuration of separated fragments, the directional dependence of such fission fragments resulting from a transition state with quantum numbers J, K and M is uniquely determined. The relationship between J, M and K is schematically illustrated in Fig app 4.1.

Where

M= is the projection of J on a space-fixed axis which usually is the beam direction.

J= is the total angular momentum.

The quantum number J and M are conserved in the entire fission process and they are fixed, but K is free and has no restriction.

As mentioned earlier in chapter two, in moving from the original compound nucleus, which is smilar to a ground state nucleus, to the saddle point or transition state of the compound nucleus undergoes many vibrations which result changes in its shape, and redistribution of its energy and angular momentum in various ways. Although the value of K of compound nucleus is not truely the same in transition state as that in the ground state, but as the exact estimation of K value in transition state is not possible, the best approximation and of course

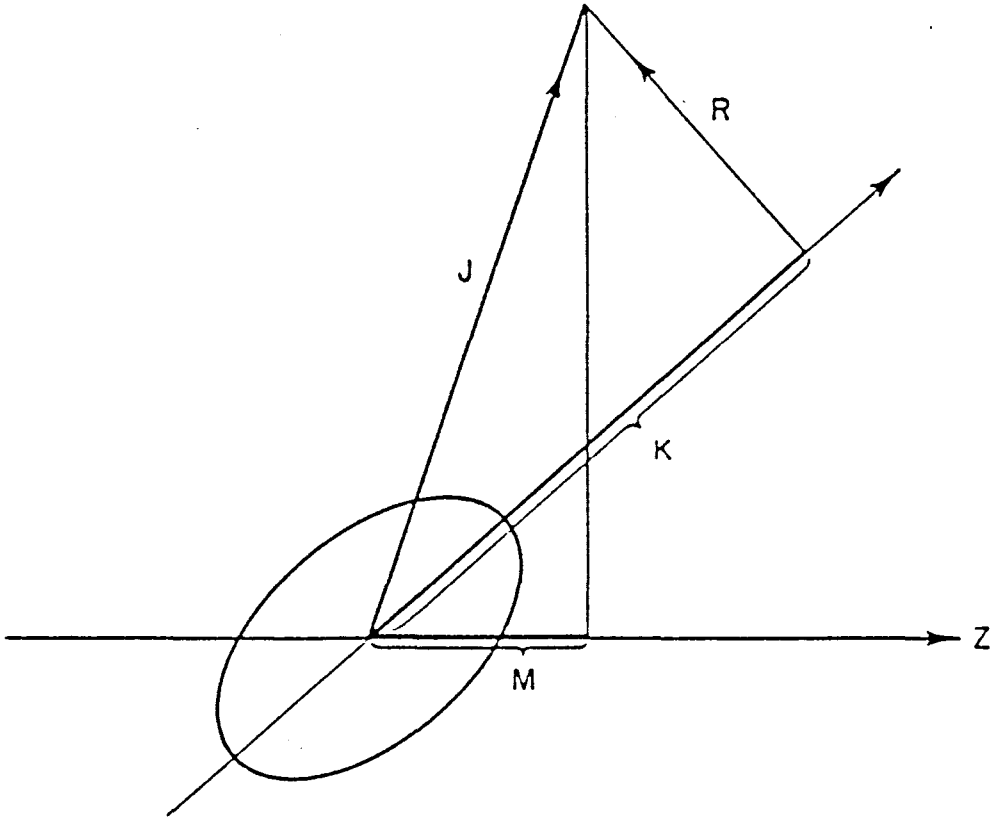

Fig. App. 4-1 Angular momentum coupling scheme for a deformed nucleus.

$\vec{J}$ = total angular momentum

m = the component of $\vec{J}$ on the beam direction (Z axis)

k = the component of $\vec{J}$ along the nuclear symmetry axis.

the most logical one, is to asume transition state value same as ground state value. To calculate the angular distribution of fission fragment at saddle point or in the near vicinity and the subsequent stages.

The probability of emitting fission fragments from a transition state with quantum number J, M, K at an angle θ is given by[1]

$$P^{J}_{M,K}(\theta) = [(2J+1)/4\pi R^2] \; | d^{J}_{M,K}(\theta) |^2 \; 2\pi R^2 \sin\theta d\theta \qquad \text{app 4-1}$$

$P_{M,K}(\theta)$ represents the probability emission of fission fragments at angle θ in to the conical volume defined by angular increament dθ

The Eq. app 4.1 can be rewritten as

$$P^{J}_{M,K}(\theta) = [\tfrac{1}{2}(2J+1)] \; | d^{J}_{M,K}(\theta) |^2 \sin\theta \qquad \text{app 4-2}$$

This probability distribution only depends on the $d^{J}_{M,K}(\theta)$ function and is independent of the polar angle, the angle of rotation about the symmetry axis, and the moments of inertia. It depends only on the angle θ between the beam direction and fission fragment direction.

The $d^{J}_{m,K}(\theta)$ function is defined by the relation[2]

$$d^{J}_{M,K}(\theta) = \{(J+M)!\,(J-M)!\,(J+K)!\,(J-K)!\}^{\frac{1}{2}} \times$$

$$\sum_{x} \frac{(-1)^{M}[\sin(\theta/2)]^{K-M+2x}[\cos(\theta/2)]^{2J-M+M-2x}}{(J-K-x)!\,(J+M-x)!\,(x+K-M)!\,K!} \qquad \text{app4-3}$$

for x = 0,1,2,3

The angular distribution $W^{J}_{M,K}(\theta)$ is obtained by dividing the probability for emitting fission fragments at angle (θ) as defined in Eq. App4-3 by sinθ

$$W^{J}_{M,K}(\theta) = [(2J+1)/2] \; | d^{J}_{M,K}(\theta) |^2$$

This formula assume that the fragments are emitted along the axis of symmetry of the deforming nucleus.

References:

1- Wheeler J.A. In "fast neutron physics" (J.B. Maraion and J.L.Fowler eds.), pt. II, p. 2051. Wiley, New York (1963).

2- Lamphere R.W., Nucl. Phys. 38, 561(1962)

APPENDIX 5

```
      OPEN(5, FILE ='CYBAF.DAT', FORM ='FORMATTED', BLANK ='ZERO')
       OPEN(6, FILE ='CYBAF.RES', FORM ='FORMATTED')
C      E02CAF EXAMPLE PROGRAM TEXT.
C      MARK 7 RELEASE. NAG COPYRIGHT 1978.
C      N.B. ARRAY DIMENSIONS (AND VALUES OF NA, NX AND NW) MUST BE
C      INCREASED FOR LARGER PROBLEMS.
C      .. LOCAL SCALARS ..
       DOUBLE PRECISION RESID, YMAX, YR
       INTEGER I, IFAIL, J, K, KP1, L, MI, MJ, N, NA, NIN, NOUT, NW,NX,
      * R, T
C      .. LOCAL ARRAYS ..
       DOUBLE PRECISION A(100), F(400), FF(400), TITLE(7), W(400),
      * WORK(1500),X(400), XMAX(20), XMIN(20), Y(20)
       INTEGER M(20)
C      .. SUBROUTINE REFERENCES ..
C      E02CAF, E02CBF
C      ..
       DATA NIN, NOUT /5,6/
       NA = 100
       NX = 400
       NW = 1500
       READ (NIN,99999) TITLE
       WRITE (NOUT,99995) (TITLE(I),I=1,6)
C      INPUT THE NUMBER OF LINES Y = Y(I) ON WHICH DATA IS GIVEN,
C      AND THE REQUIRED DEGREE OF FIT IN THE X AND Y DIRECTIONS
   20  READ (NIN,99998) N, K, L
       IF (N.EQ.0) STOP
       KP1 = K + 1
       MJ = 0
C      INPUT Y(I), THE NUMBER OF DATA POINTS ON Y = Y(I) AND THE
C      RANGE OF X-VAUES ON THIS LINE, FOR I = 1,2,...N
       DO 40 I=1,N
          READ (NIN,99997) Y(I), MI, XMIN(I), XMAX(I)
          M(I) = MI
          MJ = MJ + MI
   40  CONTINUE
C      TERMINATE PROGRAM IF THE ARRAYS HAVE NOT BEEN DECLARED
C      LARGE ENOUGH TO CONTAIN THE DATA
       IF (NX.GE.MJ) GO TO 60
       WRITE (NOUT,99994) MJ
       STOP
C      INPUT THE X-VALUES AND FUNCTION VALUES, F, TOGETHER WITH
C      THEIR WEIGHTS, W.
   60  READ (NIN,99996) (X(I),F(I),W(I),I=1,MJ)
       IFAIL = 1
C      EVALUATE THE COEFFICIENTS, A, OF THE FIT TO THIS SET OF DATA
       CALL E02CAF(M, N, K, L, X, Y, F, W, NX, A, NA, XMIN, XMAX, Y,1, Y,
      * 1, WORK, NW, IFAIL)
       IF (IFAIL.EQ.0) GO TO 80
       WRITE (NOUT,99993) IFAIL
       GO TO 20
   80  MI = 0
       WRITE (NOUT,99991)
       DO 140 R=1,N
          IFAIL = 1
          T = MI + 1
          MI = MI + M(R)
          YR = Y(R)
```

```
         YMAX = Y(N)
         IF (N.EQ.1) YMAX = YMAX + 1.0D0
C     EVALUATE THE FITTED POLYNOMIAL AT EACH OF THE DATA POINTS
C     ON THE LINE Y = Y(R)
         CALL E02CBF(T, MI, K, L, X, XMIN(R), XMAX(R), YR, Y(1),YMAX,
     *    FF, A, NA, WORK, NW, IFAIL)
         IF (IFAIL.EQ.0) GO TO 100
         WRITE (NOUT,99992) IFAIL
         GO TO 20
C     OUTPUT THE DATA AND FITTED VALUES ON THE LINE Y = Y(R)
  100    DO 120 I=T,MI
            RESID = FF(I) - F(I)
            WRITE (NOUT,99990) YR, X(I), F(I), FF(I), RESID
  120    CONTINUE
         WRITE (NOUT,99987)
  140 CONTINUE
C     OUTPUT THE CHEBYSHEV COEFFICIENTS OF THE FIT
      WRITE (NOUT,99989)
      T = 0
      DO 160 J=1,KP1
         R = T + 1
         T = R + L
         WRITE (NOUT,99988) (A(I),I=R,T)
  160 CONTINUE
      GO TO 20
99999 FORMAT (6A4, 1A3)
99998 FORMAT (3I5)
99997 FORMAT (D15.5, I5, 2D15.5)
99996 FORMAT (3D15.5)
99995 FORMAT (4(1X/), 1H , 5A4, 1A3, 7HRESULTS/1X)
99994 FORMAT (40H NX IS TOO SMALL. IT SHOULD BE AT LEAST , I5)
99993 FORMAT (22H E02CAF FAILURE NUMBER, I3)
99992 FORMAT (22H E02CBF FAILURE NUMBER, I3)
99991 FORMAT (50H0    DATA Y         DATA X         DATA F         FITT,
     * 20HED F       RESIDUAL F)
99990 FORMAT (1P5D14.4)
99989 FORMAT (34H0CHEBYSHEV COEFFICIENTS OF THE FIT)
99988 FORMAT (1H0, 1P5D14.4)
99987 FORMAT (1X)
      END
E02CAF EXAMPLE PROGRAM DATA
    5     2     4
         90.         4          10.1            11.70
        100.         4          11.61           13.0
        134.         5           7.8             8.6
        197.         4           8.5            14.0
        208.         5         109.            114.0
          10.67       91.8              1.0
          10.96       92.7              1.0
          11.26       93.6              1.0
          11.66       95.4              1.0
          11.72       92.0              1.0
          12.18       94.               1.0
          12.40       95.               1.0
          12.72       96.               1.0
           8.13       69.01             1.0
           8.18       69.68             1.0
           8.36       70.35             1.0
           8.45       71.02             1.0
           8.59       71.69             1.0
```

```
      8.7        72.0          1.0
     10.5       112.58         1.0
     13.1       161.39         1.0
     13.4       188.93         1.0
    109.4      3347.           1.0
    110.39     3374.           1.0
    111.6      3423.0          1.0
    112.6      3463.0          1.0
    113.5      3496.0          1.0
0
```

E02CAF EXAMPLE PROGRAM RESULTS

DATA Y	DATA X	DATA F	FITTED F	RESIDUAL F
9.0000D+01	1.0670D+01	9.1800D+01	9.1827D+01	2.6739D-02
9.0000D+01	1.0960D+01	9.2700D+01	9.2626D+01	-7.4373D-02
9.0000D+01	1.1260D+01	9.3600D+01	9.3664D+01	6.3973D-02
9.0000D+01	1.1660D+01	9.5400D+01	9.5384D+01	-1.6340D-02
1.0000D+02	1.1720D+01	9.2000D+01	9.1989D+01	-1.1460D-02
1.0000D+02	1.2180D+01	9.4000D+01	9.4066D+01	6.5594D-02
1.0000D+02	1.2400D+01	9.5000D+01	9.4925D+01	-7.4878D-02
1.0000D+02	1.2720D+01	9.6000D+01	9.6021D+01	2.0744D-02
1.3400D+02	8.1300D+00	6.9010D+01	6.9159D+01	1.4933D-01
1.3400D+02	8.1800D+00	6.9680D+01	6.9457D+01	-2.2317D-01
1.3400D+02	8.3600D+00	7.0350D+01	7.0482D+01	1.3157D-01
1.3400D+02	8.4500D+00	7.1020D+01	7.0967D+01	-5.3237D-02
1.3400D+02	8.5900D+00	7.1690D+01	7.1686D+01	-4.4921D-03
1.9700D+02	8.7000D+00	7.2000D+01	7.2987D+01	9.8657D-01
1.9700D+02	1.0500D+01	1.1258D+02	1.0987D+02	-2.7059D+00
1.9700D+02	1.3100D+01	1.6139D+02	1.7209D+02	1.0701D+01
1.9700D+02	1.3400D+01	1.8893D+02	1.7995D+02	-8.9812D+00
2.0800D+02	1.0940D+02	3.3470D+03	3.3451D+03	-1.9370D+00
2.0800D+02	1.1039D+02	3.3740D+03	3.3781D+03	4.0553D+00
2.0800D+02	1.1160D+02	3.4230D+03	3.4217D+03	-1.2940D+00
2.0800D+02	1.1260D+02	3.4630D+03	3.4605D+03	-2.4572D+00
2.0800D+02	1.1350D+02	3.4960D+03	3.4976D+03	1.6330D+00

CHEBYSHEV COEFFICIENTS OF THE FIT

4.4325D+02	8.9003D+02	2.3479D+03	2.4390D+03	9.4520D+02
5.2878D+01	3.9463D+01	2.1140D+01	6.0249D+00	2.7554D-01
2.3511D+00	1.9162D+00	8.4342D-01	-1.5511D-01	1.2527D-01

E02CAF EXAMPLE PROGRAM DATA

```
    5     2     4
         90.        4          2.87          3.334
        100.        4          3.308         3.705
        134.        5          2.222         2.451
        197.        4          2.422         3.99
        208.        5         31.065        32.49
```

```
   3.040      0.14029      1.0
   3.123      0.14097      1.0
   3.209      0.14166      1.0
   3.323      0.14301      1.0
   3.340      0.1332       1.0
   3.471      0.13467      1.0
   3.534      0.13539      1.0
   3.625      0.13610      1.0
   2.317      0.0996       1.0
   2.331      0.10019      1.0
   2.382      0.10064      1.0
   2.408      0.10112      1.0
   2.448      0.10160      1.0
   2.479      0.08397      1.0
   2.992      0.10501      1.0
   3.733      0.12572      1.0
   3.819      0.13603      1.0
  31.179      0.55722      1.0
  31.461      0.55946      1.0
  31.806      0.56351      1.0
  32.09       0.56679      1.0
  32.34       0.56949      1.0

0
```

E02CAF EXAMPLE PROGRAM RESULTS

DATA Y	DATA X	DATA F	FITTED F	RESIDUAL F
9.0000D+01	3.0400D+00	1.4029D-01	1.4031D-01	1.8983D-05
9.0000D+01	3.1230D+00	1.4097D-01	1.4092D-01	-5.2784D-05
9.0000D+01	3.2090D+00	1.4166D-01	1.4171D-01	4.5480D-05
9.0000D+01	3.3230D+00	1.4301D-01	1.4300D-01	-1.1679D-05
1.0000D+02	3.3400D+00	1.3320D-01	1.3319D-01	-7.9013D-06
1.0000D+02	3.4710D+00	1.3467D-01	1.3472D-01	4.5028D-05
1.0000D+02	3.5340D+00	1.3539D-01	1.3534D-01	-5.1456D-05
1.0000D+02	3.6250D+00	1.3610D-01	1.3611D-01	1.4329D-05
1.3400D+02	2.3170D+00	9.9600D-02	9.9747D-02	1.4746D-04
1.3400D+02	2.3310D+00	1.0019D-01	9.9975D-02	-2.1466D-04
1.3400D+02	2.3820D+00	1.0064D-01	1.0074D-01	1.0257D-04
1.3400D+02	2.4080D+00	1.0112D-01	1.0110D-01	-2.4286D-05
1.3400D+02	2.4480D+00	1.0160D-01	1.0159D-01	-1.1081D-05
1.9700D+02	2.4790D+00	8.3970D-02	8.4348D-02	3.7842D-04
1.9700D+02	2.9920D+00	1.0501D-01	1.0397D-01	-1.0376D-03
1.9700D+02	3.7330D+00	1.2572D-01	1.2980D-01	4.0820D-03
1.9700D+02	3.8190D+00	1.3603D-01	1.3261D-01	-3.4228D-03
2.0800D+02	3.1179D+01	5.5722D-01	5.5707D-01	-1.5215D-04
2.0800D+02	3.1461D+01	5.5946D-01	5.5978D-01	3.2267D-04
2.0800D+02	3.1806D+01	5.6351D-01	5.6339D-01	-1.1526D-04
2.0800D+02	3.2090D+01	5.6679D-01	5.6661D-01	-1.8175D-04
2.0800D+02	3.2340D+01	5.6949D-01	5.6962D-01	1.2648D-04

CHEBYSHEV COEFFICIENTS OF THE FIT

4.6093D-01	8.7704D-02	3.5060D-01	3.3468D-01	1.2341D-01
2.4023D-02	1.2659D-02	-2.5316D-03	-9.6931D-03	-4.7102D-03
-6.6536D-04	-2.8186D-04	2.9712D-04	3.0611D-04	3.5247D-04

```
      this program analyse the heavy ions fission data
       double precision aldk,laldk
       real mv,asum,am,coff,sum,vlm,ad,qa,qb,qc,ap,ae,tel
       real ve,vve abcd,qd,qk,qq,akcd,makd,abma,bsum
       real labma,lmakd
       dimension e(4,3),tl(5),tm(3),l(5),m(4),ad(4),am(4),coef(4,5)
       dimension coff(4),aw(4),ta(10),mv(4),vlm(4),sum(4),ll(4)
        dimension qa(4),qb(4),qc(4),aldk(4)
       dimension qd(4),qk(4),qq(4),abcd(4),akcd(4),makd(4)
       dimension ae(4),ab(4),abma(4),ve(4,3),vve(4,3)
       dimension lmakd(4),labma(4),laldk(4)
       coef(1,1)= 4.6093E-1
       coef(1,1)=.25*coef(1,1)
       coef(1,2)=8.7704E-2
       coef(1,3)=3.5060E-1
       coef(1,4)=3.3468E-1
       coef(1,5)= 1.2341E-1
       coef(2,1)= 2.4023E-1
       coef(2,2)= 1.2659E-2
       coef(2,3)= -2.5316E-2
       coef(2,4)= -9.6931E-3
       coef(2,5)= -4.7102E-3
       coef(3,1)= -6.6536E-4
       coef(3,2)= -2.8186E-4
       coef(3,3)= 2.9712E-4
       coef(3,4)= 3.0611E-4
       coef(3,5)= 3.5247E-4
       luout=3
       open(unit=3,file=' aprongy.dat',status='new' )
       write(*,99)
       write(luout,99)
   99  format(' what is: mass number  incident energy(MeV) of projec.')
       read(*,*) mp,ep
       write(luout,*)mp,ep
       write(*,11)
       write(luout,11)
   11  format(2x,' no of prongs')
       read(*,*)nhl
       write(luout,*)nhl
       write(*,98)
       write(luout,98)
   98  format(' what is mass number of target ')
       read(*,*)mt
       write(luout,*)mt
       do    22      i=1,nhl
       write(*,18)i
       write(luout,18)i
```

```
   18 format(' initial mass ',i2)
      read(*,*) m(i)
      write(luout,*) m(i)
   22 continue
      do 23  i=1,nhl
      write(*,19)i
      write(luout,19)
   19 format(' angles with beam direction 'i2)
      read(*,*)ta(i)
      write(luout,*)ta(i)
      ta(i)=((2*3.1415)/360.)*ta(i)
   23 continue
      write(*,13)
      write(luout,13)
   13 format( ' no of relative angles')
      read(*,*)lkj
      write(luout,*)lkj
      lkj=lkj+4
      if (lkj .eq. 0) goto 12
      do 34  i=5,lkj
      write(*,35)i
   35 format( ' relative angle for each prong from prong 1',i2)
      read(*,*)ta(i)
      ta(i)=((2*3.1415)/360.)*ta(i)
   34 continue
   12 do 43 i=1,nhl
      write(*,44)i
      write(luout,44)
   44 format(' prongs length(micro mitter)',i2)
      read(*,*)l(i)
      write(luout,*)l(i)
   43 continue
c     for ith prongs
      do     100    jj=1,nhl
      i=jj
      if (nhl .eq. 2) goto 3
      if (nhl .eq. 3) goto 3
      abma(i)=1.0E+8
   25 m(i)=m(i)+1
      labma(i)=abma(i)
      do  300  ii=1,nhl
      i=ii
    3 write(*,*)i
      tl(1)=1
      den=2.5
      l(i)=.1*den*l(i)
c     l(i) in the unit of (mgrm/ cm**2)
      tl(2)=l(i)
      ll(i)=l(i)*l(i)
      tl(3)=2*ll(i)-1
      tl(4)=4*l(i)*ll(i)-3*l(i)
      tl(5)=8*(ll(i)**2)-8*ll(i)+1
      e(1,1)=cos(ta(1))
      e(1,2)=sin(ta(1))
      e(1,3)=0
      e(2,1)=cos(ta(2))
      e(2,2)=sin(ta(2))*cos(ta(5))
      e(2,3)=sin(ta(2))*sin(ta(5))
      e(4,1)=cos(ta(4))/1.
      e(3,1)=cos(ta(3))
```

```
      e(3,2)=sin(ta(3))*cos(ta(6))
      e(3,3)=sin(ta(3))*sin(ta(6))
      e(4,2)=sin(ta(4))*cos(ta(7))
      e(4,3)=sin(ta(4))*sin(ta(7))
c     coef(i,j) for i=1,3 and j=1,5 are calibration coefficent
c     this value supplied from E02CAF program
      if (nhl.eq.4) goto 15
      aldk(i)=1.0e-18
      makd(i)=1.0
    5 m(i)=m(i)+1
      if (nhl .eq. 2) goto 16
      laldk(i)=aldk(i)
      if (nhl.eq.3) goto 15
   16 lmakd(i)=makd(i)
   15 tm(1)=1
      tm(2)=m(i)
      tm(3)=2*m(i)*m(i)-1
      vlm(i)=0
      do 10 k=1,nhl
      sum(k)=0
      do  20  j=1,5
      coff(k)=coef(k,j)*tl(j)
      sum(k)=coff(k)+sum(k)
   20 continue
      aw(k)=tm(k)*sum(k)
      vlm(i)=vlm(i)+aw(k)
      write(*,*)vlm(i)
      write(luout,*)vlm(i)
c     vlm(i) in the unit of fm/10e-23 sec.
   10 continue
c     ad(i)=e(i)*(e(j)xe(k))
c     do 100    i=1,3
      if (nhl.eq.4) goto 601
      if (nhl.eq.2) goto 701
      j=i+1
      if(j.eq.4) j=1
      k=j+1
      if (k.eq.4) k=1
      qb(i)=e(i,1)*(e(j,2)*e(k,3)-e(j,3)*e(k,2))
      qa(i)=-e(i,2)*(e(j,1)*e(k,3)-e(j,3)*e(k,1))
      qc(i)=e(i,3)*(e(j,2)*e(k,2)-e(j,2)*e(k,1))
      ad(i)=qa(i)+qb(i)+qc(i)
      ap=(1.6E-20)*(sqrt(2.*ep*mp))
      am(i)=abs(ap)*(e(j,2)*e(k,3)-e(j,3)*e(k,2))
      mv(i)=m(i)*(vlm(i))*ad(i)
      mv(i)=(1.661E-19)*mv(i)
      aldk(i)=am(i)-mv(i)
      aldk(i)=abs(aldk(i))
      write(*,*)am(i),mv(i),aldk(i)
      am(i)=abs(am(i))
      write(*,*)m(i),aldk(i)
      write(luout,*)m(i),aldk(i)
c     if (aldk(i).gt. .03*am(i)) goto 5
      if (laldk(i) .lt. aldk(i)) goto 5
c      if (aldk(i) .lt. .03*am(i)) goto 5
      write(*,*)laldk(i),aldk(i)
      write(*,321)
      write(luout,321)
  321 format('accepted mass for this energy')
      write(*,*) m(i)
```

```
      write(luout,*)m(i)
c     for four prongs calculation
  601 if (nhl.eq.3) goto 101
  300 continue
      i=jj
      if (i .eq. 4) goto 119
      do  630  ij=1,4
      do  631  iii=1,3
      ve(ij,iii)=vlm(ij)*e(ij,iii)
  631 continue
  630 continue
      do  641 iii=1,3
      do  640 ij=1,3
      vve(ij,iii)=ve(ij,iii)-ve(4,iii)
      write(*,*)vve(ij,iii),ij,iii
  640 continue
  641 continue
      j=i+1
      if (j.eq.4) j=1
      k=j+1
      if (k.eq.4) k=1
      tmass=mp+mt
      qa(i)=(ap-tmass*ve(4,1))*(vve(j,2)*vve(k,3)-vve(j,3)*vve(k,2))
      qb(i)=tmass*ve(4,2)*(vve(j,1)*vve(k,3)-vve(j,3)*vve(k,1))
      qc(i)=-tmass*ve(4,3)*(vve(j,1)*vve(k,2)-vve(j,2)*vve(k,1))
      abcd(i)=qa(i)+qb(i)+qc(i)
      abcd(i)=(1.6E-4)*abcd(i)
      qd(i)=vve(i,1)*(vve(j,2)*vve(k,3)-vve(j,3)*vve(k,2))
      qk(i)=-vve(i,2)*(vve(j,1)*vve(k,3)-vve(j,3)*vve(k,1))
      qq(i)=vve(i,3)*(vve(j,1)*vve(k,2)-vve(j,2)*vve(k,1))
      akcd(i)=qd(i)+qk(i)+qq(i)
      write(*,*)qd(i),qk(i),qq(i),akcd(i)
      makd(i)=m(i)*akcd(i)
      makd(i)=(1.6E-3)*makd(i)
      abma(i)=abcd(i)-makd(i)
      abma(i)=abs(abma(i))
      write(*,*)abcd(i),makd(i),abma(i)
      write(*,*)m(i),abma(i)
      write(luout,*)m(i),abma(i)
c     if (abma(i) .gt. .1*abcd(i)) goto 25
      if (abma(i) .lt. labma(i)) goto 25
      write(*,660)
      write(luout,660)
  660 format(' accepted mass for this pronge ')
      write(*,*) m(i)
      write(luout,*)m(i)
      if ( i .ne.4) goto 101
  119 bsum=0
      do 118  kk=1,3
      bsum =m(kk)+bsum
  118 continue
      m(i)=tmass- bsum
      if (nhl.eq.4) goto 101
  701 j=i+1
c     for two prongs calculation
      if (j.eq.3) j=1
      ab(i)=sin(ta(i))*((cos(ta(i))/sin(ta(i)))+(cos(ta(j))/sin(ta(j))))
      mv(i)=ab(i)*vlm(i)*m(i)
      mv(i)=(1.6E-19)*mv(i)
      ap=(1.6E-20)*(sqrt(2.*ep*mp))
```

```
      makd(i)=mv(i)-(ap)
      makd(i)=abs(makd(i))
      write(*,*)mv(i),ap,makd(i)
      write(*,*)m(i),makd(i)
      write(luout,*)m(i),makd(i)
      if (lmakd(i).gt.makd(i)) goto 5
c     if (makd(i) .gt. .1*abs(ap)) goto 5
      write(*,702)
      write(luout,702)
  702 format('accepted mass number for this prong')
      write(*,*) m(i)
      write(luout,*)m(i)
  101 ae(i)=m(i)*(vlm(i)**2)/2.
      ae(i)=ae(i)*100
      write(*,122)
      write(luout,122)
  122 format(' energy of prongy in Mev ')
      write(*,*)ae(i)
      write(luout,*)ae(i)
  100 continue
c     Q-value for fission about 180 MeV
      asum= 180
      do 200 j=1,nhl
      asum=ae(j)+asum
  200 continue
      tel=ep-asum
      write(*,121)
      write(luout,121)
  121 format( 'Total energy loss')
      write(*,*)tel
      write(luout,*)tel
      stop
      end
```